TECHNISCHE UNIVERSITÄT MÜNCHEN

Fakultät für Chemie

Regulation and Mechanistical Interplay of the HSP-90 and HSC-70 Chaperone Systems in *Caenorhabditis elegans*

Lukas Maximilian Schmauder

Vollständiger Abdruck der von der Fakultät für Chemie der Technischen Universität München zu Erlangung des akademischen Grades eines

Doktors der Naturwissenschaften (Dr. rer. nat.)

genehmigten Dissertation.

Vorsitzender:	Prof. Dr. Johannes Buchner
Prüfer der Dissertation:	1. apl. Prof. Dr. Klaus Richter
	2. Prof. Dr. Matthias Feige

Die Dissertation wurde am 25.10.2021 bei der Technischen Universität München eingereicht und durch die Fakultät für Chemie am 16.02.2022 angenommen.

Abstract

The heat shock response plays an essential role in mediating a cellular response to a multitude of stress conditions. Molecular chaperones were found to be key figures in this response, pivotal for dealing with all kinds of physiological stress and to sustain various intracellular processes. For this reason, elements of the heat-shock response are found across all organisms, from simple organisms like bacteria, through to model organisms like nematodes and up to complex vertebrates such as humans.

The regulation of the heat shock response is a complex task governed by transcriptional activators, called heat shock factors. These activators bind to heat shock elements localized throughout the genome, inducing the expression of heat shock genes. HSF-1 is the most prominent of these transcriptional factors, responsible for the expression of most related genes. In the present work, a small cluster of upregulated heat shock genes was determined during heat shock conditions and the interaction between their respective heat shock elements and the DNA-binding domain of HSF-1 was characterized to be a guided cooperative interaction. Tetrameric and pentameric heat shock elements were discovered, complementing the already suggested trimeric heat shock elements. The approach employed in this work may open up new possibilities to investigate complex multi-step binding reactions.

Even though the heat shock response is mostly well-studied, still parts of it, especially in the model nematode *Caenorhabditis elegans*, remain to be unknown. Here, the underlying mechanism behind the suppression of a locomotion defect in *C. elegans*, called the *head-bent* phenotype, is investigated. In order to do so, the four known suppressor variants, D233N, S321F, A379V, and D384N of the molecular chaperone HSC-70 were studied with regard to their interaction with the HSP-40 like co-chaperones DNJ-12 and DNJ-13 as well as the nucleotide exchange factors BAG-1 and UNC-23. While nucleotide exchange factor binding has almost no impact on the chaperone activity of most mutants, D233N and A379V showed a significantly reduced interaction in combination with the HSP-40 like co-chaperones. Here, this reduced interaction with DNJ-13 *in vivo* leads to the suppression of the severe *head-bent* phenotype.

Of all the various heat shock proteins, HSP-90/DAF-21 is certainly the most extensively studied. Together with one of its kinase-specific cofactors CDC-37, it ensures the stable folding of many client kinases as well as their activation during maturation. HSC-70

represents another important molecular chaperone, which is also involved in protein folding and degradation, where it associates with one of its cofactors, HSP-40. Both chaperone systems, HSP-90 and HSC-70, are crucial for the correct function of proteins and therefore the survival of the cell itself. Thus, the question arises whether their individual cofactors may interact among each other within these complex protein networks. To answer this most fascinating question, a vast array of methods was employed, eventually yielding a specific interaction between the HSP-90 cofactor CDC-37 and DNJ-13, a HSC-70 cofactor of the HSP-40 family. Dimeric DNJ-13 binds to a CDC-37 monomer and its presence is capable of promoting the complex formation of HSP-90 and CDC-37 and modulating the nucleotide-dependent effects. Hence the interaction between HSP-90 cofactors and HSP-40 proteins provides evidence for a more intricated interaction between the HSP-90 and HSC-70 chaperone systems during client processing

Interestingly, the complete absence of HSP-90 leads to an arrest of development in certain larval stages of nematodes, once more showing the importance of chaperones for various kinds of biological processes, even on phenotypic level. The inhibition of UNC-45, another chaperone and cofactor of HSP-90, was found to similarly stall nematode growth during the development of muscle-specific functions.

Nevertheless, nematode development is an enormously complex process and it is therefore a highly complicated task to define the cause of this arrest. RNAi treatments against *hsp-90/daf-21* and *unc-45*, together with subsequent in-depth transcriptional analyses, were performed and mapped to the developmental state from embryo to adult nematode. This revealed an arrest of development close to the L4 larval stage for *hsp-90* RNAi, whereas *unc-45* RNAi led to an arrest at a young adult stage. Developmental processes are found to be misregulated upon depletion of the respective chaperone and the generated “clique map”, together with its clique-specific assignments, might be a valuable tool for further genome-wide research in *Caenorhabditis elegans*.

This thesis focuses thereby on providing a more comprehensive view of *Caenorhabditis elegans* heat shock machinery by elaborating the role of various chaperones and their cofactors.

Zusammenfassung

Die Hitzeschock-Antwort spielt eine essenzielle Rolle in zellulären Reaktionen und ihrem Umgang mit einer Vielzahl von Stresskonditionen. Molekulare Chaperone stellen hierbei die Schlüsselelemente im Umgang mit physischem Stress dar und erhalten somit eine Vielzahl an intrazellulären Prozessen aufrecht. Aus diesem Grund finden sich Elemente der Hitzeschock-Antwort in allen Organismen, von den kleinsten Bakterien, über Nematoden bis hin zu Menschen.

Die Regulierung der Hitzeschockreaktion gestaltet sich als sehr komplex und wird von transkriptionellen Aktivatoren, sogenannten Hitzeschock Faktoren, ausgeführt. Diese binden an sich über das Genom erstreckende Hitzeschock-Elemente und induzieren dabei die Expression von Hitzeschock-Genen. HSF-1 ist der bekannteste unter diesen transkriptionellen Faktoren und für die Expression der meisten dieser Gene verantwortlich. Diese Arbeit befasst sich unter Anderem, mit einer kleinen Gruppe an verstärkt regulierten Hitzeschock-Genen, welche auf ihre Interaktion mit der DNA-bindenden Domäne von HSF-1 hin untersucht wurde. Hierbei wurde eine kooperative Interaktion zu den hier entdeckten tetra- und pentameren Hitzeschock Elemente gefunden. Es ist weiterhin denkbar, dass der hierzu verwendete Ansatz neue Möglichkeiten bieten könnte, um komplexe mehrschrittige makromolekulare Interaktionen zu untersuchen.

Obwohl die Hitzeschock-Antwort weitestgehend erforscht ist, sind Teile davon, vor allem in Hinsicht auf den das Modelsystem *Caenorhabditis elegans*, noch immer unbekannt. Im Rahmen dieser Arbeit wurde daher der Unterdrückungsmechanismus eines Bewegungsdefekts untersucht. Vier bekannte HSC-70 Varianten, welche in der Lage sind die Ausprägung dieses defizitären Phänotyps erfolgreich zu verhindern, wurden zusammen mit den HSP-40 ähnlichen Co-Chaperonen DNJ-12 und DNJ-13, sowie den Nukleotid-Austauschfaktoren BAG-1 und UNC-23 hinsichtlich ihrer Interaktion charakterisiert. Während die Nukleotid-Austauschfaktoren vernachlässigbare Auswirkung auf die Chaperon-Aktivität der meisten Varianten hatten, wiesen sowohl D233N als auch A379V eine stark reduzierte Interaktion mit beiden HSP-40 ähnlichen Co-Chaperonen auf. Darüber hinaus führt diese verminderte Interaktion mit DNJ-13 zu einer erfolgreichen Unterdrückung des Bewegungsdefekts *in vivo*.

HSP-90/DAF-21 ist das bei Weitem am gründlichsten erforschte Hitzeschock-Protein und in Zusammenspiel mit einem seiner Kinase-spezifischen Cofaktoren CDC-37, ist es

sowohl für die stabilen Faltung vieler Substratkinasen verantwortlich als auch an ihrer Aktivierung beteiligt. HSC-70 ist ein weiteres wichtiges molekulares Chaperon, welches sowohl während der Proteinfaltung involviert als auch im Zusammenspiel mit Co-Chaperonen wie beispielsweise HSP-40, beim Abbau von Proteinen beteiligt ist. Die beiden Chaperon-Systeme HSP-90 und HSC-70 sind essenziell für die korrekte Funktion von Proteinen und daher für das Überleben der Zelle unerlässlich. Es stellt sich allerdings die Frage, ob die Cofaktoren beider Systeme innerhalb dieser großen Proteinstrukturen miteinander interagieren können. Im Zuge dieser Arbeit konnte eine spezifische Interaktion zwischen dem HSP-90 Cofaktor CDC-37 und DNJ-13, einem HSC-70 Cofaktor der HSP-40 Familie, nachweisen werden. Hierbei konnte gezeigt werden, dass ein DNJ-13 Dimer an einen CDC-37 Monomer bindet und darüber hinaus die Formation eines HSP•90•CDC-37 Komplexes begünstigt, indem es Nukleotid-abhängige Effekte moduliert. Diese Interaktion, lässt eine komplexere Wechselwirkung zwischen dem HSP-90 und HSC-70 Chaperon-System während der Prozession ihrer Substrate vermuten als bisher angenommen.

Interessanterweise führt die Abwesenheit von HSP-90 zu einem Stopp in der Entwicklung bestimmter Larvenstadien in Nematoden und unterstreicht damit die Relevanz von Chaperonen. Die Inhibierung von UNC-45, einem weiteren Chaperon und Cofaktor von HSP-90, führt zu einem vergleichbaren Wachstumsstopp, während eines für die Entwicklung von muskelspezifischen Funktionen wichtigen Zeitpunkt. Um herauszufinden, wodurch diese ausgelöst werden, wurden sowohl RNAi Experimente gegen *hsp-90/daf-21* und *unc-45*, als auch eine ausführliche Analyse des Transkriptoms durchgeführt. Hierbei konnten sowohl *hsp-90* RNAi als auch *unc-45* RNAi eine Vielzahl an Genegruppen induzieren respektive inhibieren. Ein Abgleich mit den Entwicklungs-stadien von *C. elegans* zeigte einen Abbruch nahe des L4 Larvenstadiums für *hsp-90* RNAi und einen Stopp in einem frühen Erwachsenenstadiums für *unc-45* RNAi. Entwicklungsprozesse zeigten sich folglich fehlreguliert und die durch das Auswerte-verfahren generierte „*Clique Map*“ kann zusammen mit den gruppenspezifischen Zuordnungen ein leistungsfähiges Werkzeug für die genomweite Forschung in *C. elegans* darstellen.

Zusammenfassend beschäftigt sich diese Arbeit damit, einen detaillierten Einblick in den Hitzeschock-Mechanismus von *Caenorhabditis elegans* zu geben, indem sie die Rolle verschiedener Chaperone und ihrer Cofaktoren untersucht.

Publications

Parts of this thesis have been published in peer-reviewed journals as listed below:

Schmauder L, Richter K[2].

***hsp-90* and *unc-45* depletion induce characteristic transcriptional signatures in coexpression cliques of *C. elegans*.**

Sci Rep. 2021 Jun 18;11(1):12852. doi: 10.1038/s41598-021-91690-6. PMID: 34145311; PMCID: PMC8213770

Papsdorf K[1], Sima S[1], Schmauder L[1], Peter S, Renner L, Hoffelner P, Richter K[2].

***head-bent* resistant Hsc70 variants show reduced Hsp40 affinity and altered protein folding activity.**

Sci Rep. 2019 Aug 16;9(1):11955. doi: 10.1038/s41598-019-48109-0. PMID: 31420580; PMCID: PMC6697693

Parts of this thesis have been accepted and are currently in press in peer-reviewed journals as listed below:

Schmauder L, Absmeier A, Barkovits K, Marcus K, Richter K[2].

Nematode CDC-37 and DNJ-13 form complexes and can interact with HSP-90

Accepted manuscript, in press at Scientific Reports, 2021 Oct 18; doi: 10.1038/s41598-021-00885-4.

PhD candidate

[1] these authors contributed equally

[2] corresponding author

Parts of this thesis have been submitted as manuscripts in peer-reviewed journals as listed below:

Schmauder L[1], Sima S[1], Ben Hadj A, Cesar R, Richter K[2].

Binding of the HSF-1 DNA-binding domain to multimeric *C. elegans* consensus HSEs is guided by cooperative interactions.

Submitted manuscript currently in revision at Scientific Reports, 2021 Oct 21;

Research topics that are not covered in this thesis:

Sima S, Barkovits K, Marcus K, Schmauder L, Hacker SM, Hellwig N, Morgner N, Richter K[2].

HSP-90/kinase complexes are stabilized by the large PPIase FKB-6.

Sci Rep. 2021 Jun 11;11(1):12347. doi: 10.1038/s41598-021-91667-5. PMID: 34117308; PMCID: PMC8196007

Sima S, Schmauder L, Richter K[2].

Genome-wide analysis of yeast expression data based on *a priori* generated co-regulation cliques.

Microb Cell. 2019 Jan 22;6(3):160-176. doi: 10.15698/mic2019.03.671. PMID: 30854393; PMCID: PMC6402361.

PhD candidate

[1] these authors contributed equally

[2] corresponding author

Table of Contents

1. Introduction

1.1. Proteostasis

Cellular homeostasis describes an equilibrium of chemical and physical conditions, which is internally maintained by a self-regulated system. This process is essential for all kinds of organisms, and even minor imbalances potentially decide over life and death [1,2]. It is therefore crucial that, even under constantly changing environmental conditions, cellular homeostasis is maintained.

Most biological functions in the cell depend on the coordinated interaction of its proteins, the proteasome [2]. Protein homeostasis, or proteostasis, plays a major and crucial role in the overall equilibrium of the cell, and the maintenance of the proteome must be guaranteed by a network of cellular components [3]. This proteostasis network (Figure 1) responds to various stress conditions and includes pathways like the heat shock response (HSR) [4] and the unfolded protein response (UPR) [5,6].

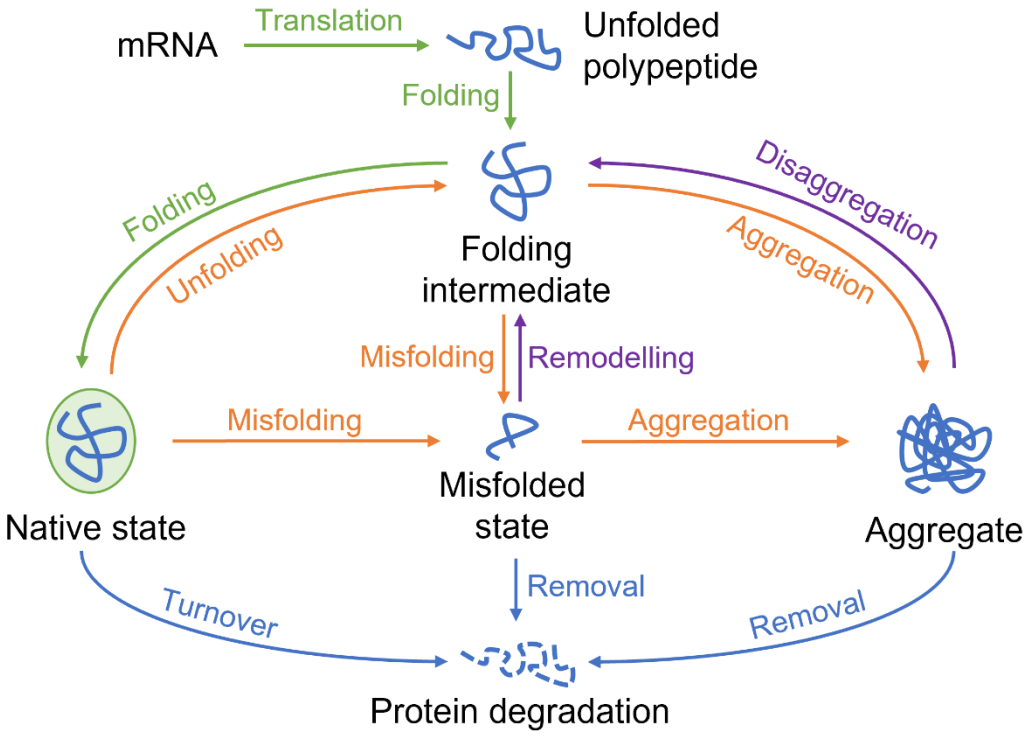

Figure 1: Proteostasis network, adapted from [2]. Protein synthesis and folding (green), general conformational maintenance (purple) and degradation (blue) counteract the harmful generation of unfolded proteins or aggregates (orange), therefore guaranteeing cellular homeostasis.

Exceeding the proteostasis capacity leads to the cytosolic accumulation of misfolded proteins and the formation of protein aggregates [7]. Although not being necessarily harmful to the cell [8], aggregates often interfere with key cellular pathways [9], eventually resulting in proteotoxicity and even diseases like Alzheimer or Parkinson [10-12]. In order to counteract this kind of proteotoxicity, the proteostasis network needs to prevent aggregate formation, execute disaggregation or at least sequestrate these aggregates, if the proteostasis capacity is limited [2,13,14].

These processes are mostly mediated by molecular chaperones, which function as key players of the proteostasis network, thereby contributing a significant proportion to the proteostasis capacity of the cell [15]. They not only provide protection for affected proteins during stress conditions, but also aid in general protein folding, degradation, and the maintenance of conformational stability during normal conditions [16-18].

In sum, the proteostasis network is essential for all aspects of protein synthesis, functionality of both proteins and cell, thereby resulting in a direct impact on the lifespan and stress resilience of an organism [19].

1.2. Protein synthesis and folding

Protein synthesis plays a central role in the maintenance and fidelity of the proteome and the cell itself [20]. Based on a mRNA transcript, linear amino acid (AA) polymers are synthesized by ribosomes [21]. In order to obtain their functionality, these primary structures need to fold into their native three-dimensional structure [22]. ANFINSEN's dogma, a thermodynamic hypothesis of protein folding, postulates that the native form of a protein, simultaneously is also its energetically best conformity [23]. Therefore, a local minimum of free energy ensures the attainment of the native form, compared to other folding possibilities (Figure 2) [3].

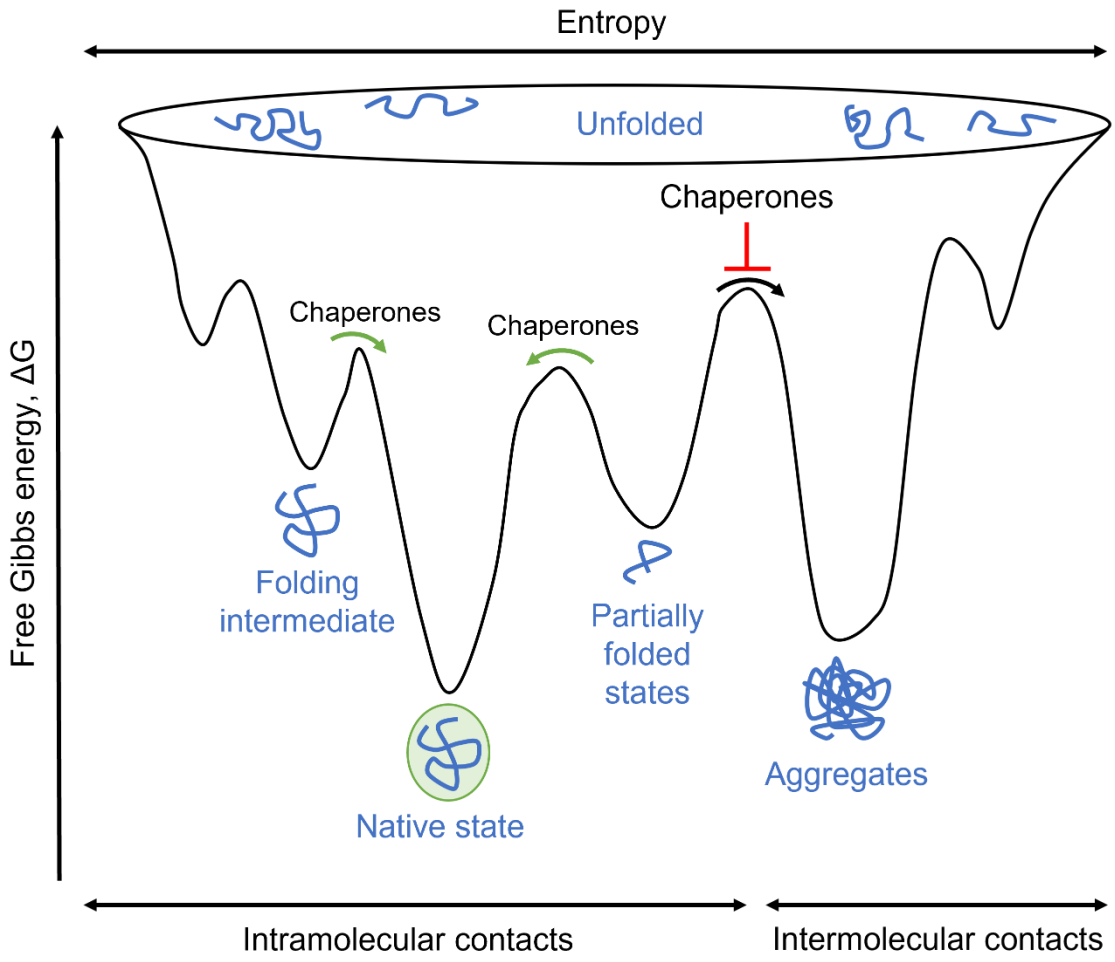

Figure 2: Schematic illustration of a protein folding funnel. Unfolded polypeptides can take various routes towards their native state, which is characterized by low free energy (ΔG) resulting in low entropy. Chaperones inhibit aggregate formation (red inverse T) and help partially folded proteins and folding intermediates, which are kinetically trapped, to reach their final and correct structure (green arrows). Adapted from [3].

While this is true for many freshly synthesized proteins, large proteins with complex structures still remain at a high risk of misfolding and aggregation [7,22], therefore relying on molecular chaperones in order to efficiently fold in a biologically relevant timescale, or even to fold at all [24]. In the process of maintenance, these chaperones participate during and after the translation of the *de novo* synthesized proteins, which prevents misfolding and therefore aggregation. Furthermore, they also prevent the premature folding of the newly synthesized proteins, if they are destined for the incorporation into organelles, like the endoplasmic reticulum or cellular membranes [15,25].

1.3. Molecular chaperones

Molecular chaperones are often defined as proteins, which interact and thereby aid their clients to obtain a functionally active form, as well as protecting them from the impact of environmental stress [15,24].

Heat shock proteins (Hsps) are the most prominent group of molecular chaperones and despite their name, their expression and function are not only limited to heat, but to all sorts of stress like ultraviolet radiation or toxins, and help to keep the cell and its functions alive [26,27]. They recognize unfolded, unstable, or aggregated polypeptides and assist them during *de novo* folding, mediate re-folding, and prevent aggregation [28-30]. Hsps are highly conserved molecular chaperones and are named after their respective molecular weight. The various families of heat shock proteins are genetically not related and their interaction with clients and co-chaperons varies widely [26,27]. Still, the five major families consist of Hsp100, Hsp90, Hsp70, Hsp60 and the small heat shock proteins. Altogether they protect and maintain protein homeostasis [31]. Therefore, Hsps not only serve important roles during stress conditions, but are also necessary under normal conditions. In contrast to most other enzymes, these chaperones need to work at specific stoichiometric ratios to successfully decrease the concentration of non-native client proteins [32]. Even though there is a broad range of highly different substrates, they all share a common feature: Non-native, misfolded proteins exhibit an increased exposure of hydrophobic residues, which are recognized by molecular chaperones [33,34]. Most chaperones depend on adenosine triphosphate (ATP) to function, and both their affinity to clients as well as their own structure is controlled by the binding and hydrolysis state of ATP [24,26,27]. Small heat shock proteins in contrast do not have an ATPase activity and are also called holdases [31]. Together with a multitude of co-chaperones and other cofactors, these chaperone complexes ensure the degradation of unfolded or aggregated polypeptides [31].

Altogether, molecular chaperones fulfill many essential tasks within the proteostasis network, making them an invaluable asset for the proteostasis capacity of the cell.

1.4. Heat shock factor 1

The induction and expression of molecular chaperons, in particular the heat shock proteins, is coordinated by the highly conserved heat shock factor 1 (HSF-1) on transcriptional level [35,36]. Together with the heat shock proteins Hsp40, Hsp70 and Hsp90, it forms a densely linked interaction network upon heat shock [37]. This ubiquitous transcription factor binds to heat shock elements (HSEs) throughout the genome, which, apart from molecular chaperones, also include components of the ubiquitin proteasome. Therefore, HSF-1 is not only responsible for the maintenance of proper protein structure but also for the degradation of damaged proteins and the recycling of amino acids [1,35,38]. Furthermore, HSF-1 is also involved in processes not related to the HSR, like cellular proliferation [39,40], female meiotic division [41], transcription in general [42], placenta development [43], and the regulation of multicellular organism growth [13,44].

Even though the entire structure of HSF-1 could not be resolved yet, hence complicating the association of structure and biological function, the mechanism of interaction between the DNA-binding domain (DBD) of HSF-1 and HSEs is studied to a certain degree [45,46]. Structurally, HSF-1 (Figure 3) consists of a DBD, leucine zipper domains flanking a central regulatory domain (RD) and two C-terminal transactivation domains (TADs). Monomeric HSF-1 can form complexes with Hsp90 [47] and Hsc70 [48], preventing the trimerization and activation of HSF-1 [49]. Under stress conditions, these monomers are released from the protecting chaperone complexes and start to form HSF-1 trimers, which is mediated by leucine zipper domains, flanking the central RD. Subsequent phosphorylation triggers the translocation into the nucleus [50]. This allows the highly conserved N-terminal DBD of each HSF-1 monomer to be orientated next to each other, which recognize and bind to repeated sequences of the 5'-nGAAn-3' pentameric sequence motive close to the transcription start site of target genes [51], eventually leading to the transcription of the respective gene [52]. Even though the exact mechanism of regulation through HSF-1 is not clear yet, the RD has been shown to be capable of sensing heat [53] and transcriptional activation is not only mediated by the two C-terminal TADs [54], but also by extensive post translational modifications (PTMs) [55], like phosphorylation [56] or deacetylation [57]. Figure 3 represents a comprehensive summary of both structure and role of HSF-1 in the heat shock response [58].

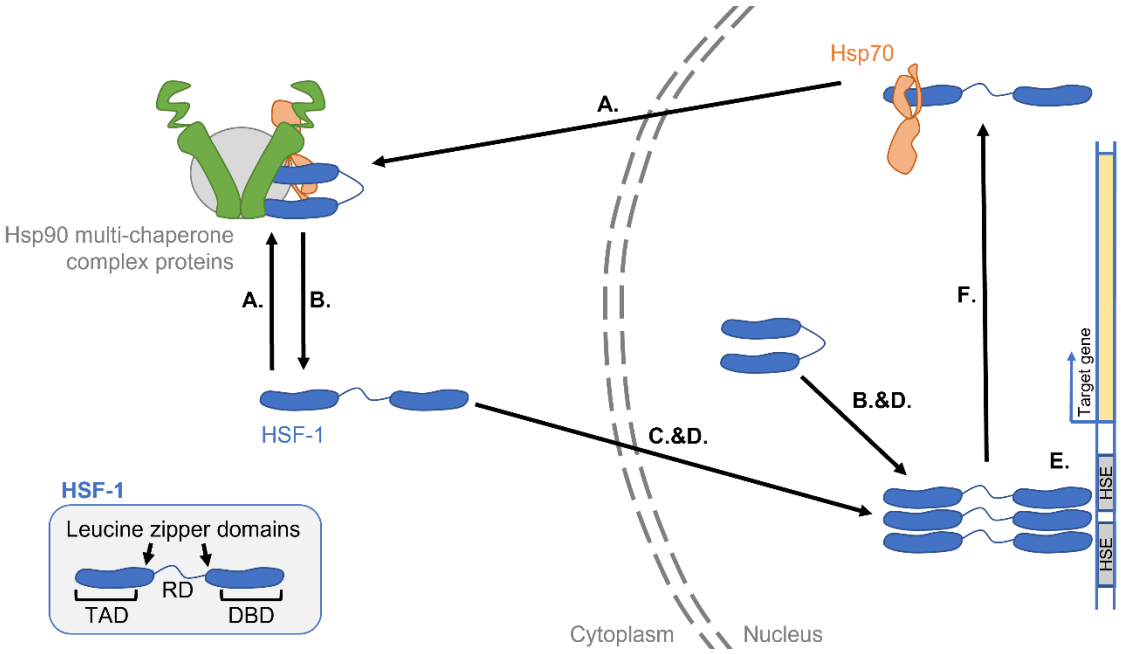

Figure 3: The structure and role of HSF-1 in the heat shock response. The structure of monomeric HSF-1 is schematically shown in the lower left part. It consists of the C-terminal transactivation domain (TAD), a central regulatory domain (RD), which is flanked on both sides by leucine zipper domains, and lastly the N-terminal DNA binding domain (DBD). **A)** The Hsp90 multi-chaperone complex both inhibits and inactivates free HSF-1 monomers. **B)** Release and thereby activation of HSF-1 is mediated upon stress conditions, posttranslational modification, or other chemical activators. **C)** Active HSF-1 monomers translocate into the nucleus of the cell, **D)** where they are able to trimerize. **E)** These trimers then bind to target HSEs, thereby inducting the expression of the respective genes. **F)** Hsp70 inhibits the function of HSF-1 in the attenuation phase, while it transports HSF-1 into the cytoplasm where it once again **A)** is bound by the Hsp90 multi-chaperone complex. Adapted from [58].

In contrast to more than five different HSF proteins in mammals [59], there is only a single copy gene of HSF-1 found in the nematode *Caenorhabditis elegans* (*C. elegans*) [60]. This circumstance simplifies this highly complex regulatory system and therefore enables a more isolated study of HSF-1 [61] and its role in in the context of the HSR, which is still not entirely understood. Nevertheless, it appears clear that HSF-1 plays a crucial role in this early, rapid, and essential defense mechanism of the cell, against different kinds of environmental stress conditions.

1.5. Heat shock protein 90

One of the most extensively studied heat shock proteins is Hsp90. It is ubiquitous under normal cellular conditions and gets overexpressed under stress [27]. Overall, it accounts for 1% of all cellular proteins, which makes it the most abundant soluble cytosolic protein and eventually affecting approximately 10-20% of the proteome [62,63]. By affecting the HSR and assisting with protein folding and maturation of important regulators like steroid hormone receptors, transcription factors and kinases, it plays a crucial role in a multitude of organisms [4,26,27].

Hsp90 forms a homodimer (Figure 4), that interacts at the C-terminal domain (CTD) [26]. Besides the CTD, a Hsp90 monomer consists of two more domains, namely the N-terminal domain (NTD), which mediates the binding of ATP, and the middle domain (MD), responsible for ATP hydrolysis and the binding of its clients [64]. A C-terminal Met-Glu-Glu-Val-Asp (MEEVD) motif is responsible for the interaction with tetratricopeptide repeat (TPR) domain containing co-chaperones [65]. Dimerization at the C-terminus plays an important role in the function of Hsp90 [26]. While the binding of ATP to the N-terminal domain leads to a conformational change of the dimer to a catalytic competent state [31,64], the hydrolysis of ATP leads to a release of ADP and phosphate as well as another change back into its open conformation. This mechanism is called molecular clamp [26,27,31].

Hsp90 relies heavily on the interaction with a cohort of co-chaperones, like Cdc37 or Fkbp51/Fkbp52, to ensure proper client processing [66,67]. Cdc37 alone plays a crucial role in kinase maturation (Figure 4) and Hsp90•Cdc37 complexes perform a wide range of functions. For instance, maintaining the kinase Cdk4 in a folded confirmation, and thereby preventing its aggregation, until its activation is required [68]. Despite the crystal structure of a Hsp90•Cdc37•Cdk4 complex being resolved [69], together with a vast number of biochemical studies, the detailed mechanism of kinase association to the Hsp90•Cdc37 complex remains unknown.

In contrast to Cdc37, the TPR domain containing large prolyl isomerases Fkbp51 and Fkbp52, are not only involved in steroid receptor processing, but also help to stabilize the large Hsp90•Cdc37•kinase complexes [70].

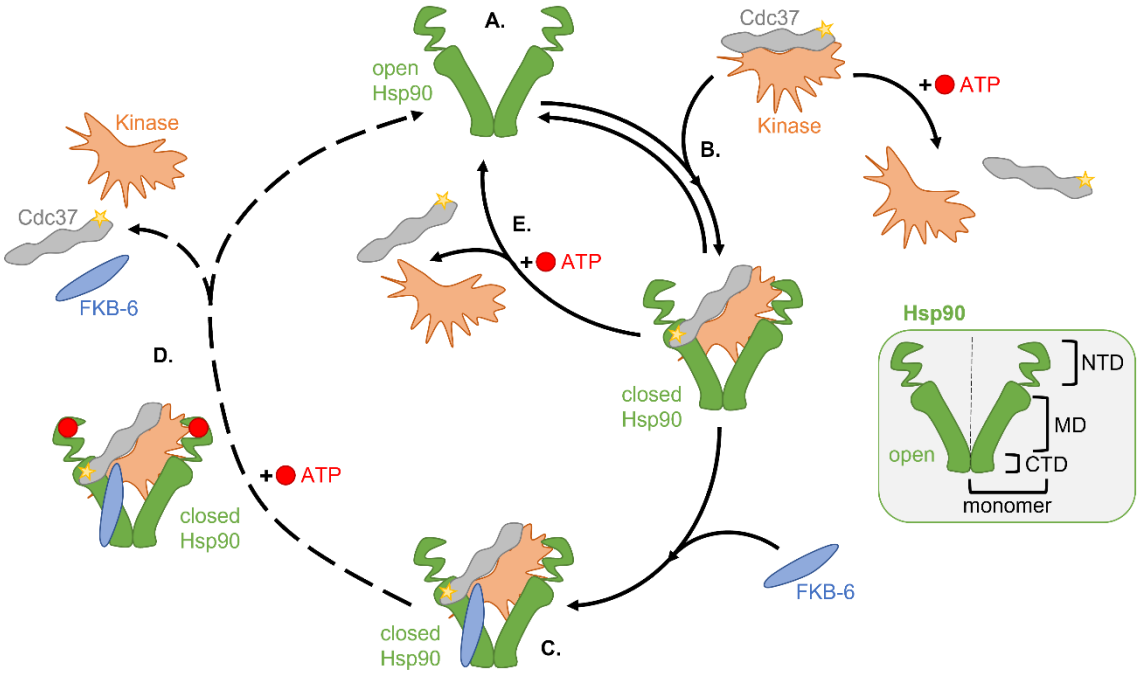

Figure 4: Schematic representation of Hsp90-mediated kinase maturation and its structure. The schematical structure of a Hsp90 homodimer is shown in the green box on the right. A Hsp90 homodimer is made up of two Hsp90 monomers, each consisting of a N-terminal domain (NTD), a middle domain (MD) and a C-terminal domain (CTD), where both monomers are also able to dimerize. A) Hsp90 B) Cdc37 presents client kinases to Hsp90 C) FKB-6 then binds to Hsp90•Cdc37•kinase complex, D) thereby preventing the dissociation of this closed multi-chaperone complex upon binding ATP. D) & E) Eventually ATP hydrolysis leads to the complete dissociation of the complex. Adapted from [70].

A central role of Hsp90 in the regulation of the HSR itself, is expressed by the binding of HSF-1 and thereby causing the inactivation of the latter [49,71,72]. Upon the detection of misfolded proteins or in general, when chaperone function is needed, HSF-1 is released and the transcription of HSPs is thereby induced [27,73].

There are differences between heat shock proteins of a protein family in between species and therefore it is not given, that all of them are equal in their development and biological function. Still, they share large homology, and it is possible to compare systems. In *C. elegans* Hsp90 is known as DAF-21 (HSP-90) and shares 85% homology with its human counterpart [74], where it ensures the longevity of *C. elegans*, whilst being essential for the development of gonads, vulva and oocyte maturation [75-77]. Therefore, mutations or the inhibition of this highly crucial chaperone interfere with several pathways and even induce embryonic and early larval lethality [78]. RNA interference (RNAi) experiments

against *hsp-90/daf-21* reduce not only the motility and arrest the development of nematodes [79,80], but also induce the HSR thus clearly demonstrating the significance of HSP-90 regarding the innate immune response [21,76,81]. This is due to the fact, that the innate immune response in nematodes is directly coupled to the HSR, which on the other hand is known to be suppressed by HSP-90 [82,83].

Since the molecular chaperone Hsp90 interacts with a vast array of proteins, it is therefore also of interest in medical research. There is a large potential in cancer therapy, since many of Hsp90s clients are important pieces of oncogenic signaling and neurodegenerative diseases like Alzheimer's disease and Parkinson's disease [84-87], therefore making it an interesting potential therapeutic target.

1.6. Heat shock cognate 70

Heat shock protein 70 (Hsp70) are ubiquitous classes of chaperones and, like Hsp90, they depend on ATP to fulfill their function [88]. In mammalian cells, there are two classes of Hsp70 chaperones, the heat shock cognate 70 (Hsc70) and Hsp70 itself [89]. Despite Hsc70 being expressed constitutively, Hsp70 is only induced upon either the depletion of Hsc70 or during various kinds of stress [89], while both share an identity of 85% [89]. Together with their co-chaperones, including the heat shock protein 40 (Hsp40) family, they contribute to the folding of polypeptides, protect proteins against aggregation, and even promote degradation of misfolded proteins and aggregates through autophagy or via the proteasome [90-92]. Clients are presented to Hsc70/Hsp70 by the co-chaperone Hsp40, which then interacts with the ATP bound Hsc70/Hsp70 conformation and thereby also improves the ATP turnover of those chaperones [93]. Nucleotide exchange factors (NEFs) on the other hand compete with Hsp40 for the accessibility of Hsp70, resulting in the release of the client and bound nucleotides [94]. Unfortunately, only few details of the Hsp40 mechanism are known yet. In any case the interaction with both Hsp40 and NEFs increases the ATP turnover of Hsc70, thus simultaneously improving the folding of its clients (Figure 5) [95-98].

Both Hsc70 and Hsp70 consist of three domains (Figure 5), the N-terminal binding domain (NBD), the substrate binding domain (SBD), and the C-terminal domain. Interestingly, the helical domain of the C-terminus functions as a lid, covering the substrate binding groove of the SBD [97,99-103]. While this part of the structure varies widely between organisms, both the NBD and SBD are highly conserved. Interaction with Hsp40 and TPR domains of NEFs is mediated by an Glu-Glu-Val-Asp (EEVD) motif at the C-terminus of the chaperone [104,105].

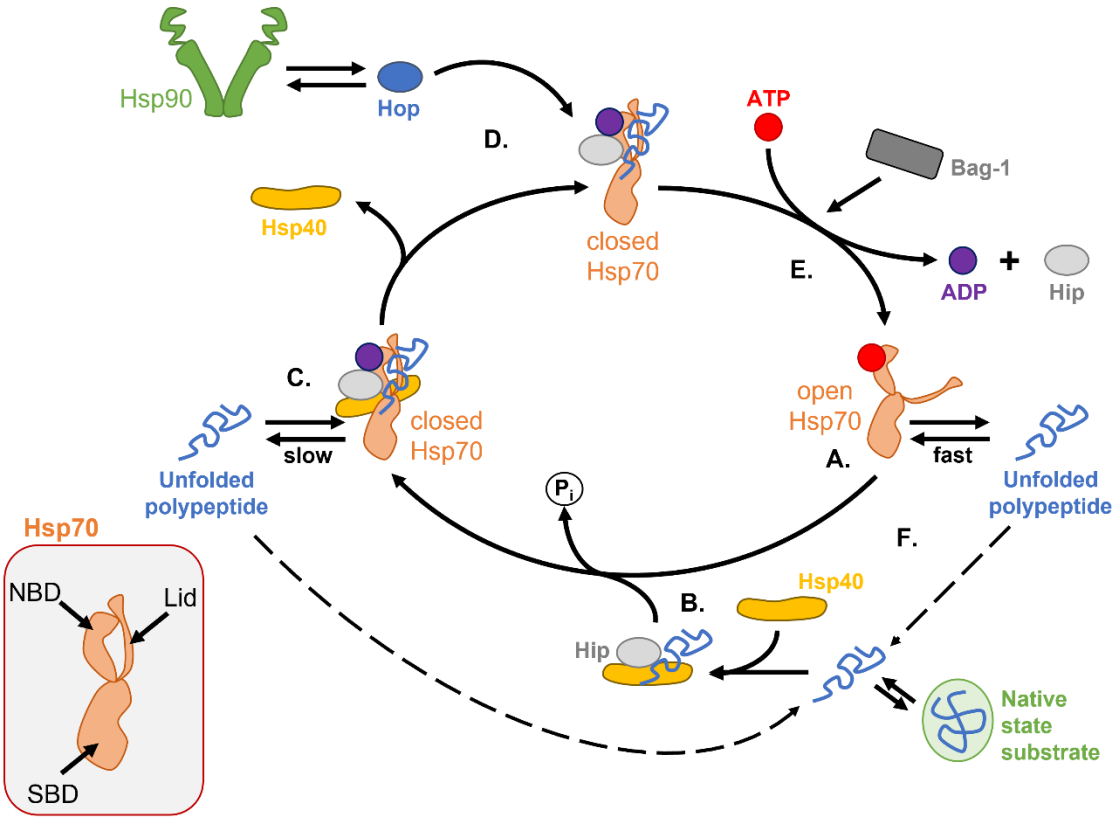

Figure 5: Schematic representation of the Hsp70 cycle and its structure. The structure of Hsp70 is schematically shown in the orange box at the bottom. It consists of a N-terminal binding domain (NBD), a substrate binding domain (SBD), which when in its closed state (as depicted), is covered by its C-terminal lid domain. A) In the open state of Hsp70, ATP is bound, and the substrate binding groove is accessible to unfolded polypeptides with a high exchange rate of low affinity. B) Alternatively, unfolded polypeptides also get bound by Hsp40, which are then presented to Hsp70. Hsp40 then facilitates the hydrolysis of ATP, thereby inducing the conformational change of Hsp70 into its closed state. C) In this, now ADP-bound state, Hsp70 exhibits a slow exchange rate with high affinity for its substrate. D) Hsp40 then leaves the chaperone complex and the coupling to other chaperones like Hsp90 is mediated by Hop, leading to a transfer of the clients to the Hsp90 system. E) Finally, Nucleotide exchange factors, like Bag-1, mediate the release of ADP and Hip, while Hsp70 again changes its conformation into the open state, thereby releasing the substrate if it was not transferred to the Hsp90 system. F) Eventually, if this substrate is not properly folded after release, it is either rebound by Hs70, or alternatively Hsp40. Adapted from [106].

Heat shock protein 1 (HSP-1 or HSC-70), is the only Hsc70 orthologue in the nematode *C. elegans*, alongside the three Hsp70-like proteins (HSP-70, F44E5.4 and F44E5.5) [107-109]. Here, the Hsp40-like J-domain containing cofactors DNJ-12 and DNJ-13 together with the NEFs BAG-1 and UNC-23 directly influence the ATP turnover of Hsc70 [97,110,111]. However, when compared to other organisms, like *E. coli* or mammals, the Hsp70/Hsp40 system of *C. elegans* is only little investigated. Overexpression of Hsc70 results in a locomotion defect, titled the *head-bent* phenotype [111], which resembles conditions of muscular dystrophy through the disruption of muscle attachment [112,113], and is phenocopied by mutations of *unc-23*, a co-chaperone of Hsc70 [112,114]. Interestingly, four suppressor variants of Hsc70, namely D233N, S321F, A379V and D384N, were found to confer resistance to these mutations within *unc-23* [112,115], and up until now, the mechanism behind this rescue was not fully understood. Since HSC-70 is the only protein of its class in nematodes, a RNAi mediated knockdown results in increased protein aggregation [116] and arrests nematode development at an early larval stage [117]. Altogether, these drastic findings demonstrate the importance of HSC-70 and show it performing essential and non-redundant functions *in vivo*.

1.7. Cell division cycle 37

In sharp contrast to its name, cell division cycle 37 (Cdc37), does not perform any cell cycle checkpoint role [118]. Instead, it functions as a specific co-chaperone of Hsp90 and its role as signal transduction molecule is required for the stable folding of a wide range of kinase clients during their maturation [68,119-123]. The interaction between Cdc37 and Hsp90 inhibits the ATP hydrolysis of the latter, denying the release of bound folded proteins and therefore extending the interaction between both chaperone and client [67].

The ubiquitous Cdc37 consists of three structural domains (Figure 6), namely the N-terminal (NTD), central and C-terminal domain (CTD) [124]. Binding to kinase clients is initiated by NTD residues [69,123]. Then, the central domain of Cdc37 interacts with the N-terminus of Hsp90, inhibiting the ATPase-activity of Hsp90, and by transitioning into the

middle domain of Hsp90, also blocking the N-terminal ATP binding site of Hsp90 [69,125-128]. Thus, Hsp90 is held in an open conformation for the loading of kinase clients onto it, assisted by Cdc37 [125,126]. The binding of Aha1, resembling another co-chaperone of Hsp90, results in the dissociation of Cdc37 from the chaperone complex, changing Hsp90 into its closed ATPase active conformation once more [66,67,122]. Eventually, this process leads to a fully maturated kinase. If Cdc37 is depleted, kinases can, instead of forming a stable ternary complex with Hsp90 and Cdc37, also associate with the Hsp40/Hsc70 system, leading to degradation by the proteasome [129]. Posttranslational modifications, like the dephosphorylation of Cdc37, by the serine/threonine protein phosphatase 5 (PP5), has been shown to impact and regulate the activity of Cdc37, thereby affecting interaction with Hsp90 [130,131]. Even though nematode Cdc37 (CDC-37) shares a significant homology with its human homolog, both utilize a different interaction site on Hsp90 (Figure 6).

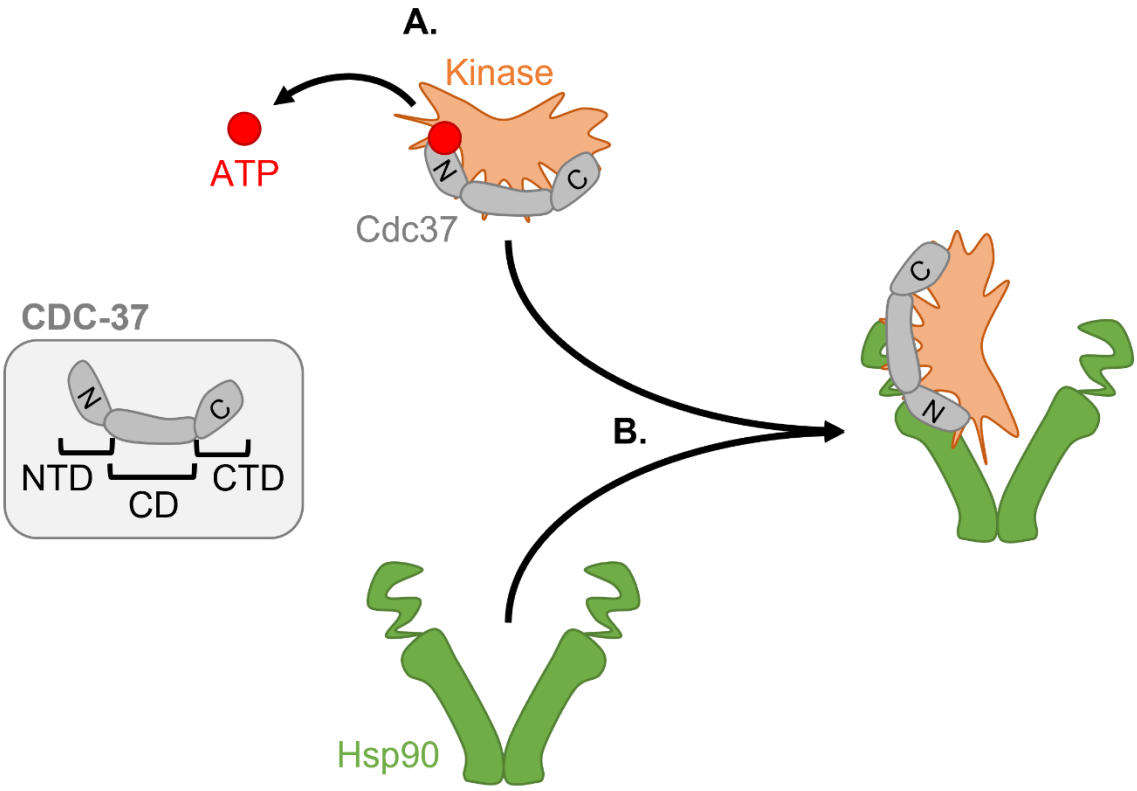

Figure 6: Schematic representation of Hsp90 kinase loading mediated by its nematode co-chaperone CDC-37. The structure of CDC-37 is schematically show in the gray box on the left and consists of a N-terminal (NTD / N), central (CD) and C-terminal domain (CTD / C). A) Kinase binding is mediated by the C-terminal domain of CDC-37, while the N-terminal domain can interfere with the nucleotide binding pocket of the kinase. B) Hsp90 is bound by the N-terminal domain of CDC-37, simultaneously inhibiting the ATPase activity of Hsp90 by blocking the N-terminal ATP binding site. This holds the chaperone in an open conformation, allowing the kinase substrate to be loaded onto Hsp90. Adapted from [125].

Whereas Cdc37 binds to the N-terminal domain of Hsp90 via its N-terminal domain, CDC-37 on the other hand binds to the middle domain [125,128,132]. Additionally, phosphorylation of the C-terminal domain of CDC-37 seems to play an important role in the binding of kinases, while no function is known for human Cdc37 [125].

Due to the therapeutic potential of Hsp90 [84-86] and the close relationship to Cdc37, Cdc37 itself might also be an important target in combating cancer or neurological diseases, like Alzheimer's disease and Parkinson's disease [87].

1.8. Heat shock protein 40

Hsp40, also called J-proteins, are co-chaperones of Hsp70 and play a crucial role for its function and the diversity of its clients [17,24]. The members of this family are historically divided based on their structure into three subclasses, which can all interact with Hsp70, but do not relate to their biochemical function (Figure 7) [133]. They are defined by the J-domain, an approximately 70 amino acid long domain, sharing a high similarity with *E. coli* DnaJ [134]. Apart from this domain they show a strong divergence in both sequence and resulting structure, leading to versatile and comprehensive functions in combination with Hsp70, for example the promotion of folding, assembly translocation and degradation of numerous substrate proteins [135].

Class I members, like nematode DNJ-12, share full domain conservation with DnaJ, including the N-terminal J-domain, a Glycine/Phenylalanine (Gly/Phe)-rich domain, a Cys-rich zinc finger motif, as well as the C-terminal extension [136]. They are also able to act independently from Hsp70, functioning as chaperones and suppressing the aggregation of clients [137-139]. Class II members, like nematode DNJ-13 in contrast, share only their N-terminal J-domain and the Gly/Phe-rich domain with DnaK, resulting in a strong dependence on the interaction with Hsp70, in order to function properly [140]. Lastly, class III consists of any J-protein which does not relate to the other two classes.

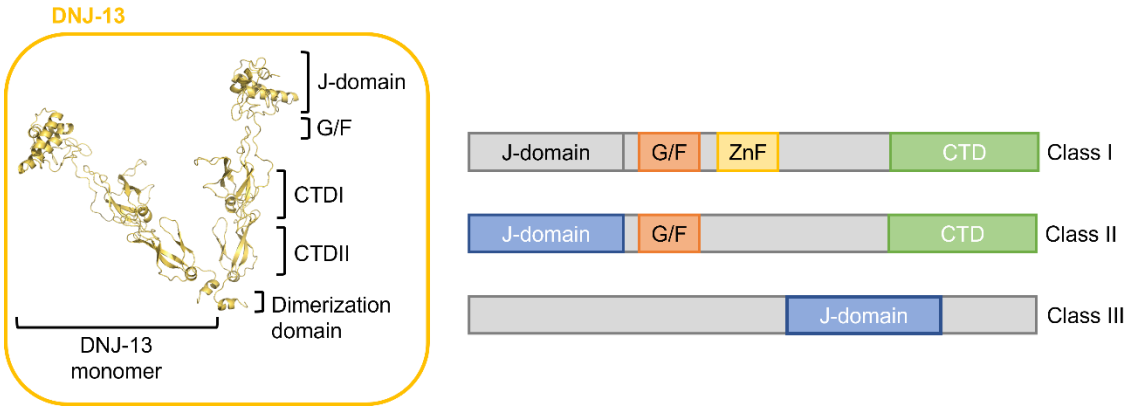

Figure 7: Structure of DNJ-13 and classification of J-domain containing proteins. The homology model of a DNJ-13 dimer, which is modeled after the amino acid sequence of *C. elegans* DNJ-13 and based upon the crystal structure of DnaJ from *Thermus thermophilus* (PDB 4J80) [141], is shown in the yellow box on the left. The schematic classification of J-domain containing proteins is adapted from [137] and differentiates the three distinct classes based upon their structural similarities to bacterial DnaJ. While all classes consist of the J-domain, only class I shares full domain conservation with DnaJ, including the J-domain, a Gly/Phe (G/F) domain and a zinc finger motif (ZnF). Despite both, class I and class II sharing their C-terminal domain (CTD), class II is lacking the ZnF and shares its J-domain and Gly/Phe (G/F) with DnaK, while class III consists of any J-protein which neither relates to class A or B.

In *C. elegans* exist three cytosolic and two Hsp40-like J-domain in mitochondria and endoplasmic reticulum. One of these cytosolic co-chaperones of HSC-70 is DNJ-13 (Figure 7) and like all class II J-proteins members, it shares its N-terminal J-domain with DnaK and, is known to form dimers, like all other J-proteins [135,142]. Its Gly/Phe-rich domain is involvement in the ATP-dependent substrate binding of HSP-70 [143,144] and the identical domain of DnaJ plays a crucial role in the conformational recognition of substrate proteins, as well as in the ability to interact with folded substrates [145]. Here the Cys-rich domain, which is replaced by a Met/Gly-rich domain in DNJ-13, both bind denatured substrates and improves the stability of the DnaK-substrate complex [139,146,147]. The Cys-rich domain most likely also supports further chaperone functions by controlling the J-protein interaction with other proteins [138,140,148]. Lastly, the C-terminus of DNJ-13 consists of two β-barrel-topology C-terminal domains CTDI and CTDII, and the affinity for client proteins is influenced by a separate C-terminal dimerization-domain [149,150]. Especially CTDI is thought to play an important role in client binding, due to the outbound Gly/Met-rich domain [139,146,147] and a hydrophobic pocket [140,151]. The deletion of the C-terminus of DnaJ-like proteins leads to non-viable mutants [152], thereby demonstrating the importance of client binding *in vivo*. However, no function is known for the CTDII of J-proteins yet, which precedes the C-terminal dimerization domain.

1.9. Uncoordinated mutant number cofactors

1.9.1. Uncoordinated mutant number 23

In *C. elegans* the gene for uncoordinated mutant number 23 (UNC-23) encodes a BAG domain-containing protein and represents an ortholog to the human Bag2 [112]. These BAG containing proteins share a conserved 45 amino acid long BAG domain near their C-terminus and are able to modulate the activity of the ATPase domain of Hsc70 post binding [111].

Interestingly mutations in the *unc-23* gene result in motility defects [113], due to the detachment of muscle cells from the hypodermis, thereby inducing a severe *head-bent* phenotype [112-114,153]. Despite its low affinity for Hsc70, the nucleotide exchange factor UNC-23 is thought to function together with Hsc70 and DNJ-13 in order to either maintain the stability of muscle cells or ultrastructure of myofilaments (Figure 8) [111]. Due to the similarity of UNC-23 and Bag2, respectively resembling the nematode and human system, a more solid understanding of this nucleotide exchange factor might help in mitigating or, at least, understanding hereditary forms of muscular dystrophy in humans.

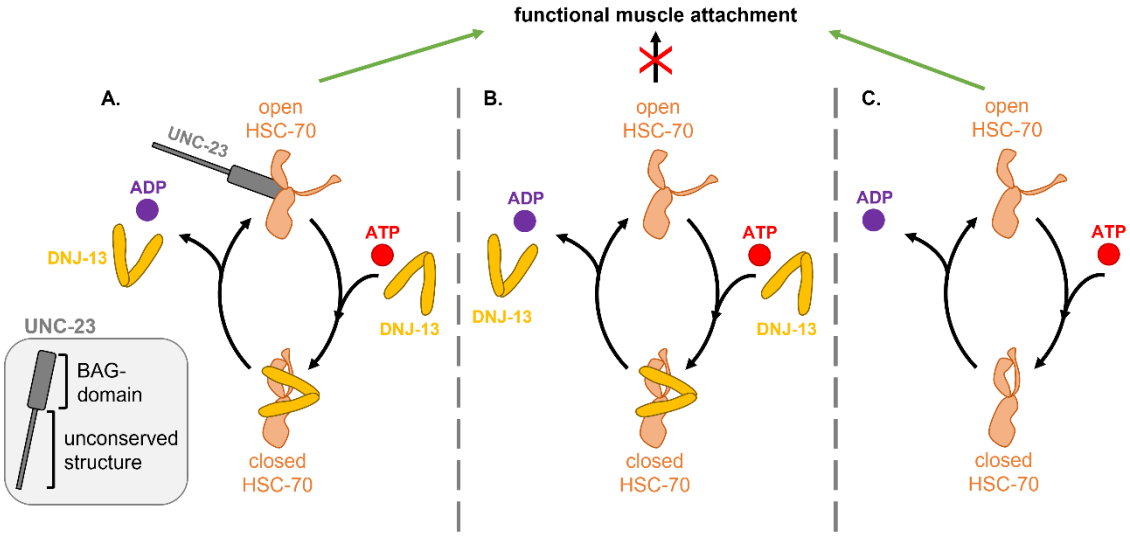

Figure 8: Structure and schematic role of UNC-23 during muscle maintenance. UNC-23 consists of a conserved C-terminal BAG domain which it shares with all BAG containing proteins and is schematically depicted in the grey box on the bottom left. **A)** Under physiological conditions UNC-23 binds to HSC-70 and promotes functional muscle attachment by antagonizing DNJ-13. **B)** Muscle attachment fails if UNC-23 is not present. **C)** However, muscle attachment is restored if both HSC-70 cofactors are missing. Adapted from [111].

1.9.2. Uncoordinated mutant number 45

The myosin chaperone uncoordinated mutant number 45 (UNC-45) on the other hand, is a cofactor of Hsp70 and Hsp90 [154], where it participates in the muscle-specific functions of the latter [155]. As actin filament-based cytoskeletal motors, myosins participate in a variety of cellular functions, including intracellular transport, signal transduction and cell migration [156]. During stress conditions HSP-90 and UNC-45 maintain the function of myosin filaments, mediated by folding of the myosin motor domain [157]. UNC-45 consists of three domains, the N-terminal tetratricopeptide (TPR), a middle domain, and an UNC-45/Cro1/She4p domain at the C-terminus. Interaction with Hsc70/Hsp90 is mediated by the N-terminal domain, whereas the C-terminus functions as a myosin-binding site [154,158]. Both domains are aligned by the middle domain, enabling the chaperone to form linear protein chains, thereby offering Hsp70/Hsp90 and its clients multiple binding sites [158]. Nematode UNC-45 is expressed from a single *unc-45* gene in muscle cells and in non-muscle tissues of early embryos [154,159].
Depletion of UNC-45 leads to rather specific and dramatic morphological changes, like paralysis due to muscle cell defects and sterility in *C. elegans*, demonstrating the essential role of UNC-45 *in vivo* [79].

1.10. Caenorhabditis elegans

Nematodes are among the most abundant and ubiquitous animals in existence. Of the many species belonging to the phylum of nematodes, *Caenorhabditis elegans* (*C. elegans*) is certainly the most intensively studied [160]. These roundworms are on average 1 mm long and consist mainly of hermaphrodites [161]. The life cycle of *C. elegans* divides into four larval stages (L1-L4), and the adult form, together covering a life span of 2-3 weeks (Figure 9). L2 larvae can form *dauer*-forms under nutrient restriction, enabling ten times longer survival under these conditions [162,163].

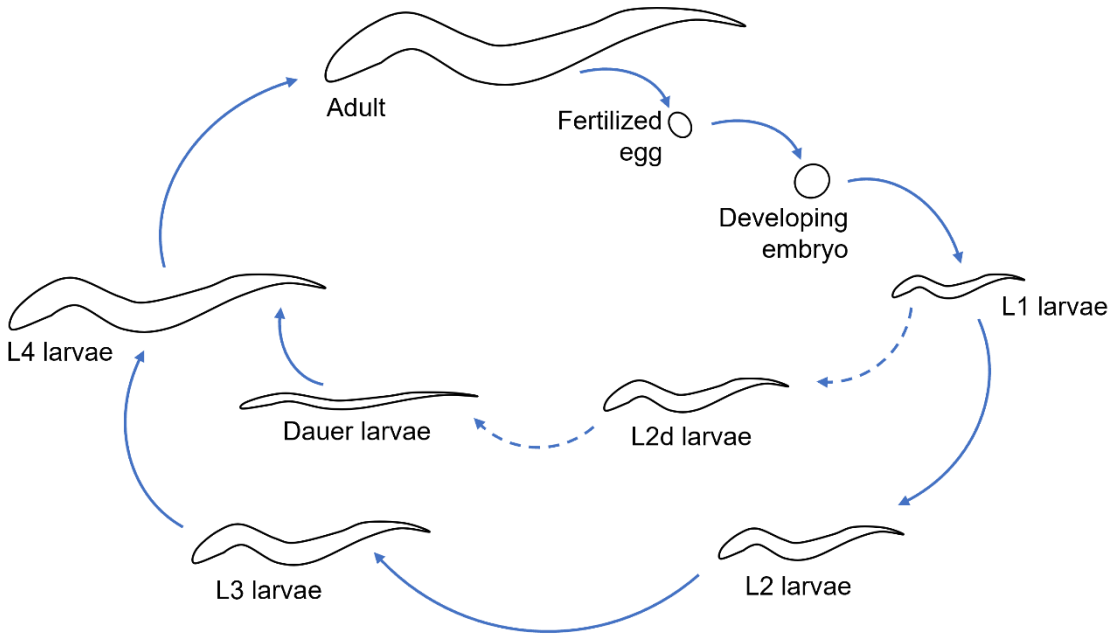

Figure 9: Schematic life cycle of *C. elegans*. Embryogenesis occurs after fertilization and eggs are laid by adult animals. Newly hatched larvae are called L1 and proceed to a further developed L2 stage under normal conditions. L2 larvae are then able to develop into the L4 stage and eventually reach the adult form, completing the life cycle. If food supply is limited (dashed lines) hatched L1 larvae can also enter a L2d stage, further developing into a stable *dauer* larvae form to increase their survivability. Under normal conditions, when the food supply is restored, *dauer* larvae can enter the L4 stage, enabling them to further mature into an adult. Figure adapted from [164].

During development the number of cells rises from 558 cells in L1 larvae to 959 somatic cells in hermaphrodites up to 1,031 in adult males with a largely invariant lineage of somatic cells [165,166]. The basic anatomy of *C. elegans* includes its skin, striated and nonstriated muscles, a nervous system dived into a pharynx and a central nervous system, a kidney, a digestive tract as well as gonads [160]. The genome of *C. elegans* contains approximately 20,100 encoding genes, with a total length of 100 million base pairs [167].

C. elegans strain Bristol N2 remains the standard laboratory strain by providing an inexpensive and simple tool of research [168]. Animals are either grown in liquid media or in petri dishes on agar, seeded with a lawn of *E. coli* as food source [169].

Despite the nematodes small genome and cell number, and the simplicity of its organs, there are many homologs to mammalian proteins sharing a multitude of functions [170-172]. This, together with its superior type of cultivation provides a more comprehensible and transferable experimental system, when compared to more complex eukaryotes like mammals.

1.11. Aims and scope of this PhD thesis

This thesis focuses on providing a more comprehensive view of *Caenorhabditis elegans* heat shock machinery by elaborating the role of both the HSC-70 and HSP-90 chaperone systems.

First, HSC-70 should be examined in greater detail. Thus, suppressor variants against the described severe *heat-bent* phenotype, induced by mutations in the nucleotide exchange factor UNC-23, should be investigated. To this effect, these four variants of HSC-70 should be purified together with some of its Hsp40 co-chaperones and nucleotide exchange factors. Next, these suppressor variants should then be characterized regarding their stability, interaction with these cofactors and overall function. Therefore, thermal shift assays should be performed to determine stability and binding to cofactors should be investigated with sedimentation velocity experiments. Then, NADH coupled regenerative assays together with luciferase refolding assays should be employed in order to determine the ATPase activity and refolding capacity respectively. Lastly, these combined findings could at one point yield resistant nematode strains against the *head-bent* phenotype, which might help in mitigating or, at least, understanding hereditary forms of muscular dystrophy in humans, due to the similarity of nematode and human system.

Next, the role of CDC-37, an important co-chaperone of HSP-90, should be examined regarding a potential cross-interaction between the HSP-90 and HSC-70 chaperone system. Since both systems are heavily involved in the specific folding of client proteins, as well as proteostasis control, their co-chaperones may even frequently interact with each other. While the co-chaperone Hop is already known to interact between both systems, no such interaction is known for CDC-37, a major co-chaperone of HSP-90. To this end, screening of CDC-37 together with prominent co-chaperones of HSC-70 should be performed and followed by the investigation of the potential interaction partners. For this, the respecting proteins should be purified, and the potential interaction partners should be thoroughly analyzed by a range of methods, to determine the stoichiometry, affinity, and interaction sites. This includes crosslinking, sedimentation velocity experiments as well as mass spectrometry of crosslinked species. The obtained

data should then be analyzed in order to generate a comprehensive model of the interaction partners. Lastly, the question remains if both potential interaction partners are still able to bind to HSP-90. To find an answer, the formation of a stable ternary complex should then be observed and ideally, both the HSP-90 and HSC-70 chaperone system can be linked by the found interaction. Eventually, these findings should contribute to the general understanding of both systems, which could even be of particular importance due to the interest in Hsp90 as a therapeutic target.

Additionally, the impact of the already mentioned HSP-90 on developmental processes in *C. elegans* should be investigated by a novel coexpression analysis, called clusterEX, initially developed for the simplified model system *Saccharomyces cerevisiae*. To this end, this analysis should be adapted for the GPL200 microarray platform in order to track gene expression changes, and later be validated against a state-of-the-art method for the analysis of microarray data. Based upon novel data, generated by using RNA interference against the chaperones HSP-90 and UNC-45, a clique map visualizing the co-regulation response, should be created with the *C. elegans* adapted clusterEX. In order to map these changes in the transcriptome on a developmental timeline, microarray datasets representing a time course ranging from early development up until adulthood should be obtained from the GEO repository, and likewise be analyzed. The clique maps of HSP-90 and UNC-45 depleted nematodes should then be compared to these generated developmental clique maps, each representing the different stages of nematode development. This should provide a transcriptional context to the observed phenotypes upon depletion of HSP-90 or UNC-45, while at the same time offer valuable insights into the role of both chaperones during the development of *C. elegans*. Furthermore, the adapted clusterEX could serve as a powerful tool for the scientific community for the analysis of microarray data.

Finally, structural and cellular mechanisms of the upstream regulation factor of HSP-90 and most prominent transcription factor of the heat-shock response, HSF-1, should be investigated. To this end, the adapted coexpression analysis clusterEX should be used to uncover induced clusters upon heat-shock. Next, heat-shock elements should be detected in the promoter regions of these highly induced genes and DNA probes representing the found sequences should be created. The stability of the DNA binding domain of HSF-1

should then be analyzed by both circular dichroism spectroscopy and thermal shift assays, prior to further analysis. Electrophoretic-mobility shift assays and sedimentation velocity experiments should be employed to investigate the interaction between the DBD of HSF-1 and the created DNA probes, representing the induced heat-shock elements and a global fit of the derived data should be analyzed in order to quantify the binding event. This approach might magnify the field of application of the adapted clusterEX, since the generated coexpression cliques provide a reference for the prediction of transcription factor binding sites, which could assist in gaining further insight into complex multi-step binding reactions in general.

In toto, these goals should provide novel findings regarding the heat shock response in *C. elegans* and therefore help with a better understanding of this model system, and eventually might be even transferable to the human system.

1.12. Overview of Methods

Cloning, protein expression and purification. cDNAs were cloned into bacterial expression vectors after a N-terminal His_6 tag. Site-directed mutagenesis was employed to generate mutants. Sequencing was used as method for verification.
These constructs were then transformed into *Escherichia coli* and expression of the respective proteins was induced. Cells were harvested and proteins were purified using affinity, ion exchange and size exclusion chromatography. Protein quality and quantity was determined by SDS-PAGE and UV/Vis spectroscopy, and the identity of the proteins was confirmed with mass spectrometry.

Structure and stability experiments. Circular dichroism spectroscopy was used to obtain information about both structure and stability of the proteins, while thermal shift assays were performed to analyze the stability of the folded structure.

Determination of chaperone activity. NADH coupled regenerative assays and luciferase refolding assays were performed, in order to respectively determine the ATPase activity as well as the refolding capacity.

Fluorescence labeling. To increase specificity, proteins were labeled with fluorescence dyes. The respective degree of labeling was determined with UV/Vis spectroscopy.

Analytical ultracentrifugation. Sedimentation velocity experiments were performed to derive molecular weights, sedimentation coefficients and diffusion coefficients, to get information on the heterogeneity of the sample, as well as to analyze possible binding between interaction partners.

Protein-protein crosslinking. Crosslinking of proteins was done to both analyze the interaction between binding partners and to generate samples for mass spectrometry experiments, conducted at the Ruhr-Universität Bochum.

Molecular modeling and docking. Homology modeling was performed when no protein structure was available. Possible protein interaction interfaces were identified based on the mass spectrometry experiments. This information was then used for molecular docking calculations.

Handling maintenance of *C. elegans* N2. Nematodes were grown on NGM plates seeded with *E. coli* OP50 bacteria at 20 °C. In order to maintain the culture, worms were also periodically picked and transferred to fresh NGM plates.

RNAi knock-down experiments. To induce gene-expression changes in, RNAi was used to deplete the respective mRNAs of *C. elegans*. Treated nematodes were washed off, shock frozen and used for microarray experiments, performed at the Zentrum für Fluoreszente Proteinanalytik in Regensburg.

Analysis of microarray data. Microarray data was analyzed both a commercial software as well as the in-house software clusterEX. Clique maps were generated, and GO-term,

phenotype and tissue enrichment were performed to obtain a genome-wide nematode gene network and to visualize gene-expression changes.

Quantification and statistics. Experiments were repeated, quantified, and statistically analyzed, as indicated.

The Materials and Method section of the included papers provides more information of the employed methods.

2. Results

2.1. *head-bent* resistant Hsc70 variants show reduced Hsp40 affinity and altered protein folding activity

Published in Scientific Reports, 2019 Aug 16; 9: 11955. doi: 10.1038/s41598-019-48109-0

Published by Katharina Papsdorf[1], Siyuan Sima[1], Lukas Schmauder[1], Sebastian Peter, Lisa Renner, Patricia Hoffelner and Klaus Richter[2]

PhD candidate

[1] these authors contributed equally

[2] corresponding author

2.1.1. Summary

The molecular chaperone Hsc70 plays an essential role in proteostasis and is driven by both the hydrolysis of ATP and the association with various cofactors. A mutation in the nematode nucleotide exchange factor UNC-23, resembling one of these cofactors, disrupts the muscle attachment of muscle cells, thereby inducing a severe *head-bent* phenotype in *C. elegans*. Four suppressor variants of HSC-70, D233N, S321F, A379V and D384N were found to suppress this phenotype.

In order to unravel the underlying molecular mechanism behind this suppression, these suppressor variants, together with the nucleotide exchange factors UNC-23 and BAG-1, as well as the Hsp40-like J-domain containing proteins DNJ-12 and DNJ-13 were purified and their interaction was characterized.

First, the stability of the HSC-70 variants was investigated by thermal shift assays, sedimentation velocity analysis and size-exclusion HPLC and the impact of nucleotide presence was determined. While most variants performed similar in terms of thermal stability and quaternary structure, S321F on the other hand showed both a reduced nucleotide response and an increase in oligomerization.

Next, the interaction of cofactors was investigated in terms of ATPase activity, luciferase refolding ability and their impact of binding on sedimentation velocity. Here the interactions between D233N and A379V showed a strong reduction with the two Hsp40-like cofactors, while the binding of nucleotide exchange factors was barely influence in both variants, together with D384N.

While molecular dynamics simulations suggest that D233N disrupts a salt bridge, which is important for the nucleotide-induced conformational changes of HSC-70, both changes of S321F and A379V, from wildtype HSC-70, lead to steric clashes near the mutation site.

Since reduced DNJ-13 binding was observed for most of the HSC-70 variants, it was interesting to see, whether interference with DNJ-13 could potentially rescue the *head-bent* phenotype *in vivo*. For this, DNJ-13 was depleted by using RNA interference in nematodes carrying the respective *unc-23* mutation, significantly improving the locomotion, while RNAi against other Hsp40-like proteins did not result in any effect. This potentially explains why HSC-70 variants with diminished DNJ-13 binding are able to suppress this phenotype after all.

2.1.2. Contribution of the PhD candidate

Katharina Papsdorf[1], Siyuan Sima[1] and Klaus Richter designed the experiments. Lukas Schmauder[1], Katharina Papsdorf[1], Sebastian Peter, Lisa Renner and Patricia Hoffelner performed the experiments. Siyuan Sima[1] and Klaus Richter performed the simulations. Lukas Schmauder[1], Katharina Papsdorf[1], Siyuan Sima[1] and Klaus Richter analyzed the data and wrote the manuscript.

2.1.3. Manuscript

SCIENTIFIC REPORTS
nature research

OPEN

head-bent resistant Hsc70 variants show reduced Hsp40 affinity and altered protein folding activity

Received: 28 August 2018
Accepted: 25 July 2019
Published online: 16 August 2019

Katharina Papsdorf[1,2], Siyuan Sima[1], Lukas Schmauder[1], Sebastian Peter[1], Lisa Renner[1], Patrica Hoffelner[1] & Klaus Richter[1]

The molecular chaperone Hsc70 performs essential tasks by folding proteins. Hsc70 is driven by the hydrolysis of ATP and tuned by the association with various co-chaperones. One such cofactor is the nematode nucleotide exchange factor UNC-23, whose mutation disrupts muscle attachment and induces a severe *head-bent* phenotype in *C.elegans*. Interestingly, four mutations in Hsc70 can suppress this phenotype, but the molecular mechanism underlying this suppression is unknown. Here we characterize these four suppressor variants, Hsc70 D233N, S321F, A379V and D384N. *In vitro* only Hsc70 S321F shows reduced stability and altered nucleotide interaction, but all mutations affect the ATPase stimulation. In particular, Hsc70 D233N and Hsc70 A379V show strongly reduced interactions with DNJ-12 and DNJ-13. Nucleotide exchange factor binding instead is barely influenced in Hsc70 D233N, A379V and D384N and their chaperone activity is preserved. Molecular dynamics simulations suggest that effects in Hsc70 S321F and Hsc70 A379V originate from steric clashes in the vicinity of the mutation site, while D233N disrupts a salt bridge that contributes to Hsc70's nucleotide-induced conformational changes. In summary, the analyzed mutants show altered ATPase and refolding activity caused by changes in Hsp40 binding.

The highly conserved molecular chaperone Hsc70 assists client protein folding in bacteria, fungi and higher eukaryotes. It promotes *de novo* folding of a diverse client set under physiological and stress conditions[1,2] ensuring general protein homeostasis[3,4]. Hsc70 is an ATPase with an N-terminal nucleotide binding domain (NBD) and a C-terminal substrate binding domain (SBD), which is covered by a flexible substrate lid. Hsc70 interacts with various cofactors that modulate client interaction and tune ATP hydrolysis. For example, Hsp40 proteins present the client protein to Hsc70 and accelerate ATP hydrolysis by interaction with the ATP bound Hsc70 conformation[5]. The co-chaperone group of Nucleotide Exchange Factors (NEF) instead compete with Hsp40 proteins to access Hsc70 and subsequently initiate the release of nucleotide and client from the complex[6]. In *C. elegans* Hsc70's ATP turnover is influenced by the Hsp40-like J-domain cofactors DNJ-13 and DNJ-12 and the NEFs UNC-23 and BAG-1[7–9]. The combination of Hsp40s and NEFs synergistically dramatically increases Hsc70's ATP turnover and client folding in all organisms studied to date[8,10–12].

The *hsp-1* gene encodes the sole functional Hsc70-like protein in the nematode's genome. This stands in contrast to many other organisms, such as yeast, where several functional homologs exist[13,14]. This offers the unique possibility to study the involvement of this essential chaperone in physiological processes. Knockdown experiments and homozygous deletion of *hsp-1* in *C. elegans* show that nematode Hsc70 is critically required already during early larval development[15,16]. Interestingly, overexpression of a fluorescently tagged HSP-1 leads to locomotion defects that are related to defects in the muscular attachment sites such as the *head-bent* phenotype[7]. This locomotion defect is phenocopied by mutations of the Hsc70 co-chaperone *unc-23*[17,18]. Here, degeneration of the head muscle cells leads to the failure of forward movements and conditions that resemble variations of muscular dystrophy[17,19]. This implies that Hsc70 complexes are influencing the attachment of muscle cells possibly by providing protection against shear stress[17,19]. Interestingly, mutation of multiple loci of *unc-23* induce this strong detrimental phenotype such as *unc-23(e25)*, which encodes the point mutation UNC-23 E297K, and *unc-23(ok1408)*

[1]Center for integrated protein research at the Department of Chemie, Technische Universität München, Lichtenbergstr. 4, 85748, Garching, Germany. [2]Present address: Stanford University School of Medicine, Department of Genetics, 300 Pasteur Drive, Stanford, CA, 94305, USA. Katharina Papsdorf, Siyuan Sima and Lukas Schmauder contributed equally. Correspondence and requests for materials should be addressed to K.R. (email: klaus.richter@richterlab.de)

which is characterized by a large deletion within *unc-23*. Recently four viable mutations in the ATPase domain of *C. elegans* Hsc70 were uncovered, which confer resistance to the *unc-23* mutation induced *head-bent* phenotype[17,20]. Two such mutations, Hsc70 D233N and Hsc70 A379V, were identified in a mutagenesis screen with the *unc-23(e25)*-allele encoding UNC-23 E297K[17]. In an independent study, two other mutations, Hsc70 S321F and Hsc70 D384N, were identified to confer resistance to the deletion allele *unc-23(ok1408)*[20]. However, the underlying molecular mechanism of how the point mutations in the essential chaperone Hsc70 can rescue the drastic locomotion phenotype is not understood.

While all these Hsc70 mutants are localized in the NBD (see Fig. 1A) it is not understood which changes in the cofactor interaction pattern they induce and if potentially they result in changes in Hsc70's activity. Here we characterize the Hsc70 mutations to understand, how phenotypic suppression could originate in this system. We find mechanistic changes during the ATPase cycle of these Hsc70 suppressor mutations likely driven by reduced cofactor binding. This largely correlates with the genetic interaction between Hsc70 and its cofactors UNC-23 and DNJ-13 *in vivo*.

Materials and Methods

Nematode handling. Nematodes were handled according to standard procedures[21]. *unc-23(e25)*, *unc-23(e324)* and *unc-23(ok1408)* strains (CB25, CB324, RB1301) were obtained from the CGC and were grown on NGM plates seeded with OP50 bacteria at 20 °C. For RNAi experiments HTT15(DE3) bacteria were freshly transformed with the dsRNA-encoding plasmids and then used as sole feeding source on RNAi plates. In these experiments synchronized L1 nematodes were transferred to plates containing NGM supplemented with 100 µg/ml ampicillin, 6 µg/ml tetracycline and 1 mM IPTG. Genes targeted by this approach were *dnj-13*, *dnj-12* and *dnj-19*[15,22] and the results were compared to empty L4440 vector control plasmid. To measure the nematode's motility thrashing assays were performed by transferring nematodes at adult day 1 to a droplet of M9. The thrashing movements per minute at 20 °C were recorded for 20 animals.

Protein expression. Wild type Hsc70 was expressed from a pET28b-Hsc70 expression plasmid and purified as described[8]. All mutations in nematode Hsc70 were generated by QuickChange PCR using the plasmid pET28b-Hsc70 and primers designed with the help of NEBaseChanger (https://nebasechanger.neb.com/). Resulting plasmids were sequenced to confirm the mutation (GATC-Biotech, Konstanz, Germany). Protein expression was performed in 5 L flasks at 20 °C for 16 h and protein purification was performed as previously described for Hsc70[7,8]. In brief, His-tagged proteins were purified by affinity purification via a Ni-NTA column, followed by ion-exchange and size exclusion chromatography. Hsc70 variants were stored in 40 mM HEPES/KOH pH 7.5, 50 mM KCl at −80 °C. Protein identity and purity were confirmed by mass spectrometry and SDS-PAGE. Hsc70 co-chaperones were purified as reported[8]. Purified co-chaperones were stored in 40 mM HEPES/KOH, pH 7.5, 150 mM KCl, 1 mM DTT, 1 mM EDTA. Ydj1 was purified as a His-SUMO-tagged protein. Here, after Ni-NTA affinity purification, the His-SUMO tag was cleaved by SUMO-protease and removed via Ni-NTA affinity purification followed by size exclusion chromatography. Luciferase was expressed in autoinduction medium[23] and purified using DEAE-Sephadex and size exclusion chromatography. Luciferase activity assays were employed to select the luciferase-containing fractions. Purified luciferase stocks were stored in PBS at −80 °C.

ATPase assay. The ATPase activity of Hsc70 was determined using an NADH coupled regenerative assay with 3 µM Hsc70 as described[24]. Measurements were performed at 25 °C in 120 µL cuvettes in 40 mM HEPES/KOH pH 7.5, 150 mM KCl, 5 mM $MgCl_2$. Baseline activity was determined and the assay started by addition of 2 mM ATP. The ATPase activity was determined in OriginPro 8.6 (OriginLabs, Northampton, USA) with the following equation, in which $\varepsilon(NAD^+) - \varepsilon(NADH) = -6200/(\mathrm{M} * \mathrm{cm})$.

$$Activity = \frac{\frac{\triangle A_{340}}{\triangle t}}{(\varepsilon(NAD^+) - \varepsilon(NADH)) \cdot c\ (ATPase)}$$

To determine the stimulation of the ATPase activity by co-chaperones, DNJ-13, DNJ-12, BAG-1 and Δ258-UNC-23 were added before the addition of ATP at the indicated concentrations. The extent of stimulation was calculated by subtracting the not stimulated ATPase rates of Hsc70s from the stimulated rates. This yields a value, which is free from potential non-Hsc70 related background, even if the background originates from the Hsc70-preparations. In cases, where the co-chaperone preparations showed ATPase activity, this additional background activity was also subtracted. Standard deviations were combined as required for subtraction of error-containing data. Each assay was measured three times and the average stimulation with standard deviation is plotted. Comparison of two sample t-test was performed to analyze statistical significance.

Analytical ultracentrifugation. Sedimentation velocity experiments were carried out in a Beckman XL-A analytical ultracentrifuge equipped with an AVIV AU-FDS fluorescence detection unit (AVIV Biomedical, New Jersey) as described[8]. To this end *BAG-1 was generated by fluorescently labeling BAG-1 at its cysteine residue with ATTO 488 C_5-maleimide (ATTO-TEC GmbH, Siegen, Germany). DNJ-13 was expressed with an additional cysteine in the His-tag linker and selectively labeled with ATTO 488 C_5-maleimide at this position. Δ258-UNC-23 was labeled with Alexa Fluor 488 C_5-maleimide (Thermo Fisher Scientific) and DNJ-12 was labeled with ATTO-488-NHS (*DNJ-12) for 2 hours at room temperature. Proteins were subsequently dialyzed to remove the free label. For binding analyses 300 nM of *BAG-1 or *DNJ-12 or *600 nm of DNJ-13 were sedimented at 42,000 rpm, 20 °C in the absence or presence of binding partners. Sedimentation velocity experiments were performed in 40 mM HEPES/KOH pH 7.5, 150 mM KCl, 1 mM DTT and 5 mM $MgCl_2$. 1 mM of nucleotides were added as indicated. dc/dt distributions were visualized with the program Sedview[25] and

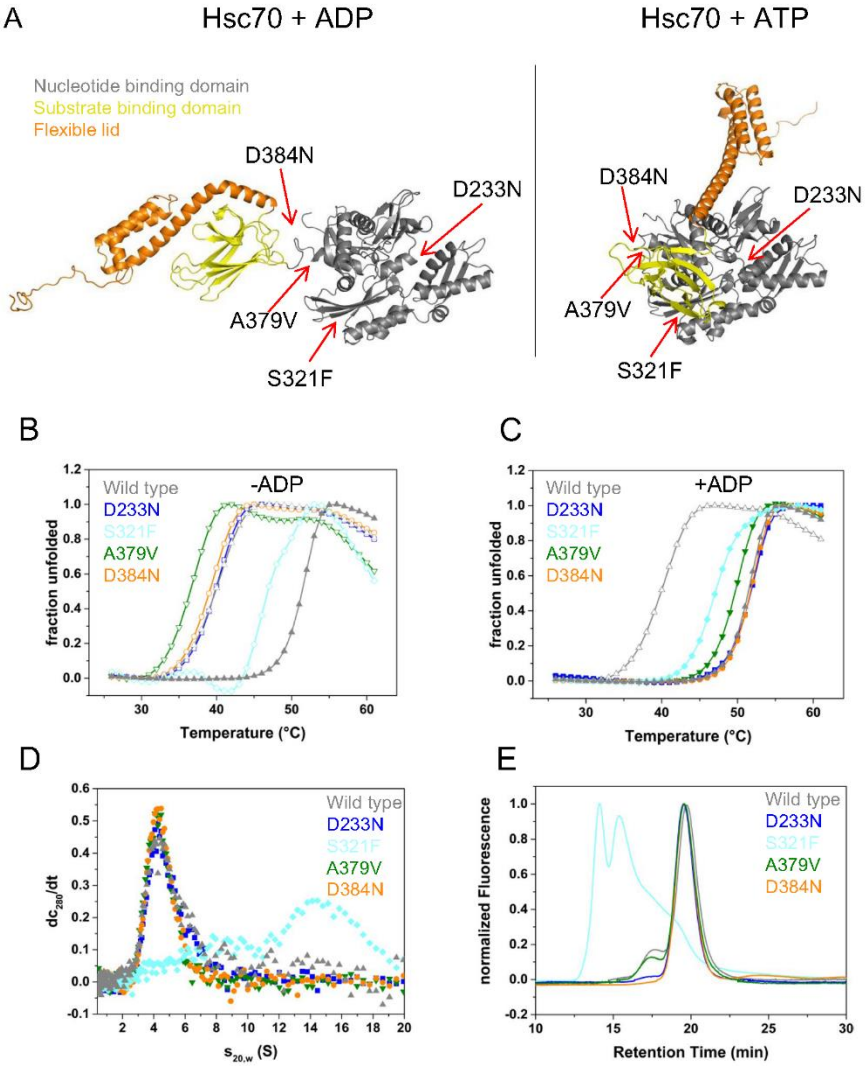

Figure 1. Structure and Stability of the Hsc70 mutants. (**A**) Closed Hsc70 structure with the four mutation sites indicated as D233N, S321F, A379V and D384N. ADP bound DnaK (PDB: 2KHO) with closed substrate binding domain served as template for the model. The NBD is shown in grey, the SBD in yellow, the lid domain in orange. Mayor rearrangements of the domains towards each other in ATP bound BIP (PDB: 5E84) with the same color code as before. (**B**) Structure and stability of Hsc70 mutants in the absence of nucleotide. Tertiary structure determination was performed using the thermal shift assay (TSA). Samples contained Hsc70 with (gray ▲) and without ADP (gray △) and Hsc70 D233N (blue □), Hsc70 S321F (cyan ◇), Hsc70 A379V (olive ▽) and Hsc70 D384N (orange ○) in standard buffer. (**C**) Structure and stability of the Hsc70 mutants in the presence of ADP. Samples contained Hsc70 with and without ADP and the variants Hsc70 D233N (blue ■), Hsc70 S321F (cyan ♦), Hsc70 A379V (olive ▼) and Hsc70 D384N (green ●) in standard buffer with 1 mM ADP. (**D**) Analytical ultracentrifugation reporting on the quaternary structure of the variants. Sedimentation velocity experiments were performed and dc/dt plots were generated as outlined in the Material and Methods section. Identical concentrations of Hsc70 (gray), Hsc70 D233N (blue), Hsc70 S321F (cyan), Hsc70 A379V (olive) and Hsc70 D384N (orange) were used. (**E**) SEC-HPLC was performed in standard buffer as described in the Material and Methods section. Line colors are as described in (**D**).

the customized script diffUZ was used for flexible scan range selection, for normalization of the data and for generation of the plots as described previously[7,8]. Fits to Gaussian functions were made in OriginPro 8.6 (OriginLabs, Northampton, USA). Each assay was measured in triplicates and a representative graph is plotted.

Characterization of the oligomerization status of Hsc70 variants was performed with the UV/VIS optical system (Beckman Coulter). Protein samples containing 0.5 mg/mL protein were used to determine the sedimentation coefficients of the Hsc70 variants. Data analysis was based on the generation of dc/dt plots with customized scripts. UltraScan II[26] was used to get information on the heterogeneity of the sample and to derive diffusion coefficients and molecular weights for the species.

Size-Exclusion HPLC. Size-Exclusion HPLC was performed on a HPLC system consisting of a Jasco PU-980 pump coupled to a Jasco UV-975 detector. A Superdex 200HR (GE Amersham) column was used to perform the separation in a buffer of 40 mM HEPES, pH 7.5, 150 mM KCl. 10 µg of Hsc70 variants were injected and the elution was recorded. Data was exported and plotted with Origin 8.6 (OriginLabs, Northampton, USA).

Thermal shift analysis. The melting temperature of the Hsc70 variants was determined in thermal shift assays (TSA). To this end, a 1:1000 fold dilution of SYPRO Orange (Thermo Fisher) was added to 0.2 mg/ml sample protein in 20 µL 40 mM HEPES/KOH pH 7.5, 150 mM KCl, 2 mM $MgCl_2$, 1 mM DTT. Fluorescence was measured in a fluorescence plate reader (Agilent Stratagene Mx3005P, excitation filter: 470 nm, emission filter: 570 nm) at an 1 °C/min heating rate. Nucleotides were added as indicated. Data analysis was performed with OriginPro 8.6 (OriginLabs, Northampton, USA). Each assay was measured in triplicates and a representative graph is plotted.

Luciferase refolding. The refolding capacity of the Hsc70 variants was investigated in a luciferase refolding assay[12,27]. To this end luciferase was chemically denatured in 25 mM HEPES/KOH pH 7.5, 50 mM KCl, 15 mM $MgCl_2$, 10 mM DTE, 1 mM ATP, 50 µg/mL BSA, 5 M urea for 45 minutes. Refolding was initiated by 125-fold dilution into 25 mM HEPES/KOH pH 7.5, 50 mM KCl, 15 mM $MgCl_2$, 2 mM DTE, 240 µM CoA, 1 mM ATP, 50 µg/ml BSA, 100 µM luciferin, 10 mM PEP, 50 µg/ml pyruvate kinase. The regained luciferase activity was measured continuously by recording luminescence in 96-well plates (Greiner Microlon, Solingen, Germany) in a PHERAstar^{Plus} (BMG LabTech) for 4 hours at 25 °C. If not indicated otherwise 3.2 µM of wild type and mutant Hsc70 were used with 0.8 µM of the Hsp40-like cofactors Ydj1, Hdj1, DNJ-12 or DNJ-13. Due to much lower activity, the DNJ-13 and DNJ-12 containing assays had to be corrected by subtracting the background signal of the respective Hsc70 variant, which were not identical. This effect is neglectable for the highly active Ydj1 and Hdj1 proteins, but becomes relevant, when comparing the Hsc70 variants with DNJ-13 and DNJ-12.

Influence of mutations on Hsc70 protein stability. Homology modeling was applied to generate the structures of docked and undocked nematode Hsc70 based on crystal structures of the respective Hsc70 conformations from other organisms. We used the ATP-bound state of human BIP (PDB: 5E84)[28] and yeast Sse1 (PDB: 2QXL)[29] and Sse1 bound to bovine Hsc70 (PDB: 3C7N) as "docked" conformations and we used *E.coli* DnaK (PDB: 2KHO)[30] and bovine Hsc70 bound to yeast Sse1 (PDB: 3C7N) as "undocked" conformation[31]. For homology modeling a sequence alignment was generated with ClustalOmega[32] based on Hsc70, Hsp70, BIP and Hsp110 proteins from *E. coli*, *S. cerevisiae*, *C. elegans*, *B. tauris* and *H. sapiens*. This alignment was used in Chimera Modeller[33] to calculate the structural coordinates of nematode Hsc70 in the docked (ATP bound) and undocked (ADP bound) conformation. Chimera Modeller generated an ensemble of five independent structures for each starting structure, yielding 15 structures for the docked state and 10 structures for the undocked state altogether. In the undocked models, the distance between the NBD and SBD differed, which is caused by the flexibility of the ~10 amino acid linker connecting the two domains. The ATPase domains of all generated structures were visually compared in PyMol[34] to assess whether they had converged similarly. Indeed within the docked ensemble the root mean square deviation (RMSD) of the ATPase domains was found to be between 0.5 Å (modeled homologs of the same PDB structure) and 1.6 Å (models with different PDB starting structure), while significant differences were visible towards the undocked models (RMSD >4 Å). As all investigated mutations reside in the NBD of Hsc70, only the modeled ATPase domains up to position 389 were used for further computational analysis.

To compare the influence of the mutations, single amino-acid mutations were introduced with Chimera[33] and with the FoldX BuildModel tool[35]. This way each mutation yielded an energetic penalty value relative to the wild type protein. This analysis was performed for the modeled structures generated. Thus, each mutation was quantified 25 times, with 5 calculations derived from the same PDB starting structure. These values were used to calculate the standard deviations depicted in the respective figures. The BuildModel tool displayed contributions to stability from different biophysical parameters, including electrostatic and hydrophobic contributions. The electrostatic values were used to plot the contribution of charged interactions to overall stability.

Simulation of the influence of mutations on the Hsc70 dynamics. Molecular dynamics simulations were performed to visualize the influence of the mutations onto the structure and stability of the respective Hsc70 variant. To this end the isolated ATPase domains were used. For simulations, the homology model of the undocked conformation was based on the PDB-coordinates of the human Hsc70 (PDB: 3C7N), which contains the highest sequence homology to the nematode Hsc70. The docked conformation was based on the BiP structure (PDB: 5B84), which contains the highest sequence homology to the nematode Hsc70. Simulations were performed in a water box with the equivalent of 40 mM NaCl. After minimizing the water energy and temperature and pressure adaptation of the system, the molecular dynamics simulation was run to yield 1 ns trajectories according to the described procedure for Gromacs[36]. This calculation was performed on an Intel Core i7-6800K CPU @ 3.40 GHz with support of a NVIDIA GeForce GTX 1080 graphics chip using Gromacs 5.1.4 built in the 64 bit environment of Windows 10. This system was capable of producing 30 ns/day. Alternatively the CoolMUC linux cluster of the Leibnitz-Rechenzentrum (LRZ) Garching was used with Gromacs 2016. Calculations were

performed systematically from customized *sbatch* scripts and usually employed 56 cores (2 nodes), capable of producing ~50 ns/day.

Initial trajectory analysis was performed with the Gromacs *energy* and *distance* tools. Simultaneous comparison of many 1 ns trajectories regarding distances between specific atoms for different Hsc70 variants in the two conformations were done by the customized script dynaMIX, which added the targeted atoms to each index.ndt file and initiated the distance determination for each time point with the Gromacs *distance* tool or with VMD[37]. Data points for distance histograms summarizing 30 1 ns time courses were collected from the last 20 frames of each trajectory. Resulting distance data were then plot in Origin 8.6. Images of specific amino acid positions were generated in VMD.

Results

Hsc70 S321F shows increased oligomerization and reduced nucleotide responses. Several mutations in Hsc70 were reported to suppress the *unc-23(e25)* and *unc-23(ok1408)* locomotion phenotype *in vivo*[17,20]. All these mutant sites (D233N, S321F, A379V and D384N) reside in the ATPase domain and the neighboring linker of Hsc70 (Fig. 1A). To obtain information on the mechanism of suppression, we purified these Hsc70 variants and performed biochemical characterization. Interestingly, all mutations support viability of *C. elegans*, which provides the powerful opportunity to biochemically characterize these non-lethal Hsc70 mutations and their molecular function.

Of the four mutants, only Hsc70 S321F showed an increased aggregation propensity during protein purification, while the other mutations behaved wild type like. To test, whether the mutations affect the stability of Hsc70 we performed thermal stability assays (Fig. 1B). Melting temperature for wild type Hsc70, Hsc70 D233N and D384N were observed at 39 °C, 39 °C and 38 °C respectively. Thus, thermal stability in these two mutants is not affected. Hsc70 A379V was slightly destabilized and already unfolded at 36 °C. Interestingly, the S321F mutation showed an increased melting temperature at 46 °C. Addition of nucleotides has been shown to exert a strong stabilizing effect on Hsc70 before[8]. Indeed, the melting temperature of Hsc70 increased to 51 °C after addition of 1 mM ADP. To test the response of the Hsc70 mutations to addition of nucleotides the thermal stability was assessed. Hsc70 D233N and D384N unfold at the same temperature as the wild type protein at 51 °C (Fig. 1C). Hsc70 A379V again is slightly destabilized unfolding at 49 °C. The ATP-induced stabilization suggests that the interaction with nucleotides is maintained in the three mutants (D233N, D384N and A379V) despite the mutations being in the nucleotide binding domain (see Fig. 1A). The only mutation that behaved differently was Hsc70 S321F. The addition of ADP did not result in any additional stabilization of the protein. As the melting temperature of Hsc70 S321F was higher than that of Hsc70 in the absence of nucleotides this protein appears more stable than Hsc70 in the absence and less stable in the presence of nucleotide (Fig. 1B,C).

We next tested the quaternary structure of the Hsc70 mutants. To this end we performed sedimentation velocity experiments with analytical ultracentrifugation (Fig. 1D). Here, wild type Hsc70 as well as Hsc70 D233N, A379V and D384N sediment with an identical sedimentation coefficient of 4.3 S ± 0.2 S. UltraScan-analysis suggests a molecular mass of roughly 70 kDa for the main species, showing that these purified proteins are mostly monomers in solution. A sedimentation coefficient of 4.3 S also matches values reported for the human Hsc70 protein in the past[38]. Hsc70 S321F, instead, sediments with 14 S, which reflects the formation of oligomers. The width of the distribution function in the dc/dt plots suggests the presence of diverse oligomeric forms. We performed SEC-HPLC to confirm this result. Indeed, for the variants with normal stability properties we observed a retention time of 19.5 minutes. Instead two distinct peaks with retention times of 14 and 15.5 minutes imply heterogeneous oligomers for Hsc70 S321F (Fig. 1E). In summary, the mutations D233N, A379V and D384N do not abolish nucleotide binding capacity and maintain oligomerization properties of wild type Hsc70. In contrast, Hsc70 S321F affects oligomerization, stability and possibly nucleotide binding suggesting large conformational rearrangements.

ATP hydrolysis is inhibited in Hsc70 mutants. A central question is if essential functions of Hsc70 are affected by the mutations as all four mutations are able to suppress the strong locomotion phenotype induced by *unc-23* mutations *in vivo*[17,20]. The mutations are localized in the ATPase domain of Hsc70, thus we tested if ATP hydrolysis is affected leading to modified ATPase cycles. Wild type Hsc70 exhibits ATP turnover rates of 0.07 min^{-1}. The mutation D233N showed significantly decreased ATP turnover to 0.02 min^{-1} (Fig. 2A), while S321F, A379V and D384N Hsc70 preparations showed slightly increased ATP hydrolysis.

In the presence of Hsp40 proteins and nucleotide exchange factors (NEFs) the ATP turnover of wild type Hsc70 can be strongly stimulated[8]. Individual cofactors stimulate the ATPase activity of the Hsc70 variants only mildly (Table 1). The strongest ability to stimulate the ATPase activity of Hsc70 is seen by combining the NEF BAG-1 and the Hsp40 like protein DNJ-12. Indeed, wild type Hsc70 can be stimulated approximately 10-fold, increasing its ATPase activity to 0.74 min^{-1} (ΔATPase = 0.67 min^{-1}, Fig. 2B). While Hsc70 and Hsc70 D384N exhibited a similar stimulation, the ATPase activity of Hsc70 D233N and Hsc70 A379V was only mildly accelerated. In fact, the observed stimulation was only 0.08 min^{-1} and 0.12 min^{-1} respectively and thus much lower than that for wild type Hsc70 (Fig. 2B). Also, the S321F mutation was weakly stimulated upon addition of DNJ-12 and BAG-1, implying that under the conditions of the ATPase assay, this variant shows some functionality.

An interesting question is how other cofactor combinations affect the ATPase activity. We next tested the influence of UNC-23 in combination with DNJ-12. We previously purified and characterized a stable fragment of UNC-23, termed Δ258-UNC-23[7], which binds to Hsc70 and performs the nucleotide exchange reaction[7]. This fragment was now used in ATPase assays alongside DNJ-12. Hsc70 wild type was stimulated by 0.40 min^{-1} and all mutants were stimulated to a similar extend with the exception of Hsc70 D233N, which showed significantly reduced stimulation (Fig. 2C). To test the ability of different co-chaperones to stimulate the ATPase activity, the Hsc70 mutants were also subjected to the J-domain protein DNJ-13. ATPase cycle acceleration in combination

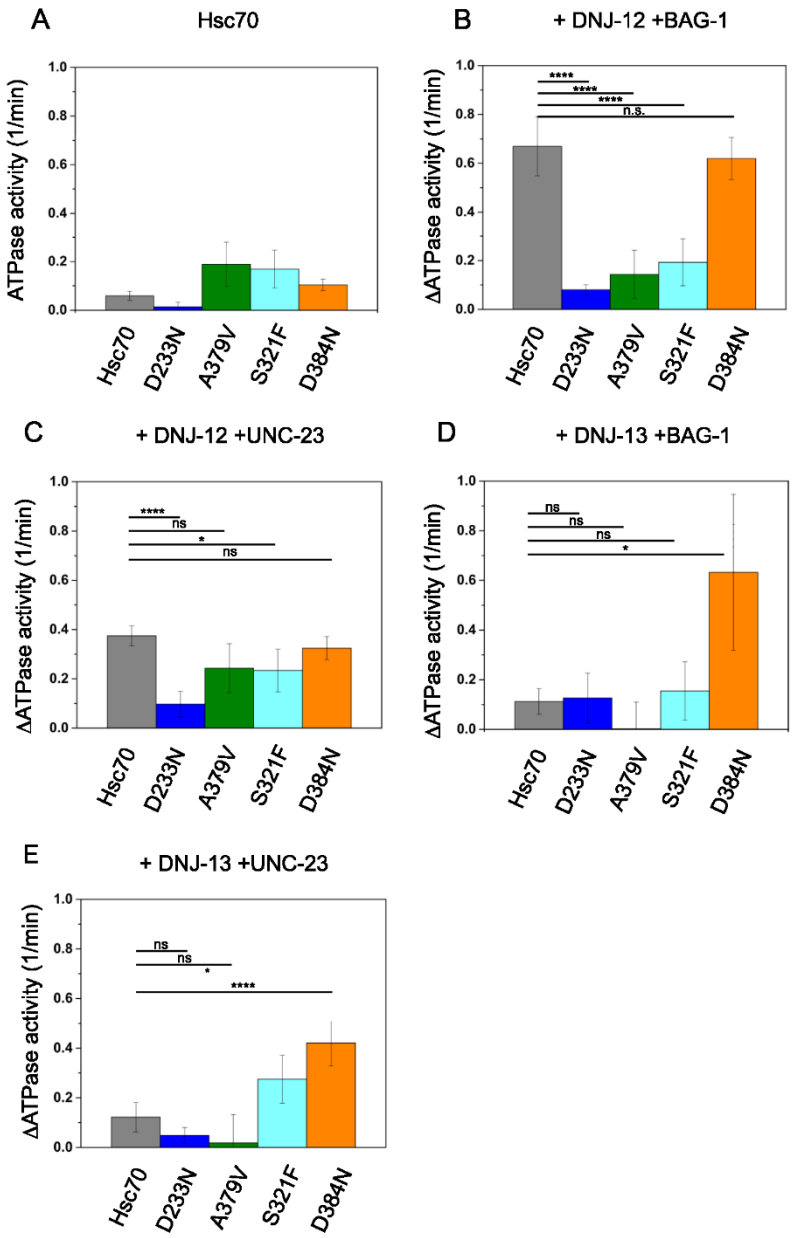

Figure 2. Stimulation of ATPase activity of Hsc70 variants. The ATPase activity of Hsc70 and mutant versions of it was determined in a regenerative ATPase assay as described in the Materials and Methods section. 3 µM Hsc70 were analyzed in standard buffer at 25 °C. (**A**) ATPase activity of the Hsc70 wildtype and mutants. (**B**) The Hsc70 ATPase stimulation after addition of DNJ-12 and BAG-1. The unstimulated ATPase activity was subtracted to provide a background-free value. 1 µM DNJ-12 and 3 µM BAG-1 was added to the Hsc70 mutants. (**C**) The Hsc70 ATPase stimulation after addition of 1 µM DNJ-12 and 3 µM △258 UNC-23. (**D**) The Hsc70 ATPase stimulation after addition of 1 µM DNJ-13 and 3 µM BAG-1. (**E**) The Hsc70 ATPase stimulation of 1 µM DNJ-13 and 3 µM △258 UNC-23. ****Indicates $p < 0.001$, *indicates $p < 0.01$, n.s. is not significant.

	BAG-1	DNJ-12	DNJ-13	UNC-23
Hsc70	0.61 ± 0.05	0.29 ± 0.03	0.56 ± 0.06	0.18 ± 0.03
Hsc70 D233N	0.14 ± 0.06	0.33 ± 0.05	0.08 ± 0.04	0.12 ± 0.00
Hsc70 S321F	N.A.	N.A.	N.A.	N.A.
Hsc70 A379V	0.21 ± 0.15	0.07 ± 0.01	0.19 ± 0.13	0.02 ± 0.00
Hsc70 D384N	0.11 ± 0.03	0.34 ± 0.03	0.39 ± 0.18	0.24 ± 0.02

Table 1. ATPase turnover measured for mutated Hsc70 variants in combination with excess with 3 µM BAG-1, 1 µM DNJ-12, 1 µM DNJ-13 or 3 µM UNC-23. Activity values are derived from replicates and depicted values are given in min^{-1}. Only the extent of stimulation is shown, as the unstimulated activity of the respective mutant and the background activity of the cofactor are subtracted as described in Materials and Methods section. Hsc70 S321F was omitted due to very high background activity.

with DNJ-13 yields in lower stimulation[7]. Interestingly, in combination with the NEF BAG-1, all mutants behave similar except for Hsc70 D384N. Here, the ATPase cycle is strongly stimulated in the presence of DNJ-13 and BAG-1 (△ATPase = 0.64 min^{-1}) while the other mutations, including Hsc70, Hsc70 D233N and Hsc70 S321F show only weak increases in ATP turnover (Fig. 2D). The strong stimulation of Hsc70 D384N is again observed with DNJ-13 and UNC-23 as NEF (Fig. 2E). These results show that all identified *unc-23* suppressor mutations in Hsc70 exhibit an altered functional interaction with Hsc70 co-chaperones despite being stable proteins with mostly normal nucleotide binding capabilities. This is observable as a mostly decreased stimulation for Hsc70 D233N and Hsc70 A379V and an increased stimulation of Hsc70 D384N. Thus, Hsc70 ATPase cycle regulation is differentially affected in the mutations while general ATP hydrolysis is possible in all mutants.

NEF binding is conserved in Hsc70 mutants. We next asked where the influences on the ATP turnover originate. To scrutinize, which of the co-chaperones is responsible for the observed changes, we tested their binding capability to Hsc70 individually. To this end we first employed analytical ultracentrifugation with fluorescently labeled BAG-1 (*BAG-1). *BAG-1 alone sediments at 2.2 S and in the presence of Hsc70 its sedimentation coefficient increased to 4.9 S. This indicates that *BAG-1 binds strongly to wild type Hsc70[8]. Likewise, all mutants bind *BAG-1 with the exception of Hsc70 S321F (Fig. 3A). This implies that the high affinity for BAG-1 is persevered in the three Hsc70 ATPase domain/linker mutations (D233N, D384N and A379V). To assess the full functionality of the *BAG-1/Hsc70-complex we tested if nucleotide addition reduces this protein-protein interaction. Indeed, after addition of ADP, the complex formation is diminished for all Hsc70 mutants similar to wild type Hsc70 (Fig. 3B). In conclusion, NEF interaction is functional and the response to nucleotide binding is mostly unaffected in the ATPase domain/linker mutations D233N, D384N and A379V (Fig. 3B).

In order to test for NEF specificity or if other NEFs behave similarly with respect to complex formation, we analyzed the binding of the Hsc70 mutants to the NEF *△258-UNC-23. To this end we employed analytical ultracentrifugation with fluorescently labeled UNC-23 (*△258-UNC-23). This fragment sediments with an $s_{20,w}$ of 3.5 S. After addition of Hsc70, the resulting protein complex can be observed with an increased sedimentation coefficient (4.2 S) (Fig. 3C). Here, as reported before, binding is much weaker compared to BAG-1[7], but detectable at Hsc70 concentrations of 3 µM. Hsc70 S321F again shows no binding to *△258-UNC-23, while the other mutants behave similar to wild type Hsc70 (Fig. 3C). All Hsc70 mutants similar to the Hsc70 wild type diminish their binding to *△258-UNC-23 in the presence of 2 mM ADP as to be expected for a nucleotide exchange factor interaction (Fig. 3D). Thus, while the ability of the Hsc70 mutants to increase their ATP turnover in the presence of co-chaperones is compromised, the binding of NEFs to the Hsc70 mutants is mostly conserved and still responsive to nucleotides in the mutants that are structurally least affected. This is particularly interesting, as NEFs as well as nucleotides bind the ATPase domain of Hsc70 and all mutations reside within this domain. Thus, the mutations do not induce large conformational rearrangements that abolish NEF binding.

J-protein binding is strongly reduced in Hsc70 mutants. The drastic changes and the failure to stimulate mutant Hsc70's ATPase activity by co-chaperones can barely be explained by the NEF interaction for three of the mutants as they behave very similar to wild type Hsc70. Thus, we next tested the binding of Hsp40-proteins to the Hsc70 mutants. We examined a labeled DNJ-13 (*DNJ-13) in analytical ultracentrifugation assays and tested its interaction with these Hsc70 mutants. We first addressed the formation of *DNJ-13/Hsc70 complexes in the absence of nucleotide for each Hsc70 mutant. Wild type Hsc70 does not form complexes with *DNJ-13 under these conditions (Fig. 4A). Similarly, no binding of Hsc70 S321F and A379V to *DNJ-13 was observed. Interestingly, some complex formation of Hsc70 D384N and very weak complex formation of Hsc70 D233N is detected (Fig. 4A). We previously reported very weak binding in the absence of ATP and strong formation of multimeric Hsc70/DNJ-13 complexes in the presence of ATP[8]. Indeed, in the presence of ATP, large *DNJ-13-containing complexes were formed with wild type Hsc70 (Fig. 4B). Hsc70 under these conditions showed distinct hetero oligomeric complexes at 8.4 S and 11.8 S. In turn, Hsc70 D384N formed one *DNJ-13-Hsc70 complex species sedimenting at 7.5 S. In both cases very little free *DNJ-13 at 4 S was observable (Fig. 4B). The interaction of *DNJ-13 with Hsc70 A379V and D233N was strongly reduced, resulting in a broad peak in the range of 6 to 8 S. In contrast to the strongly binding Hsc70 wild type and D384N, Hsc70 A379V retains a substantial amount of apparently free not complexed *DNJ-13. Interestingly, Hsc70 S321F showed no binding to *DNJ-13 in the presence of ATP (Fig. 4B). This demonstrates that DNJ-13 and the Hsc70 ATPase domain/linker mutants can form different oligomeric forms in the presence of ATP. However, the oligomer formation occurs most efficiently

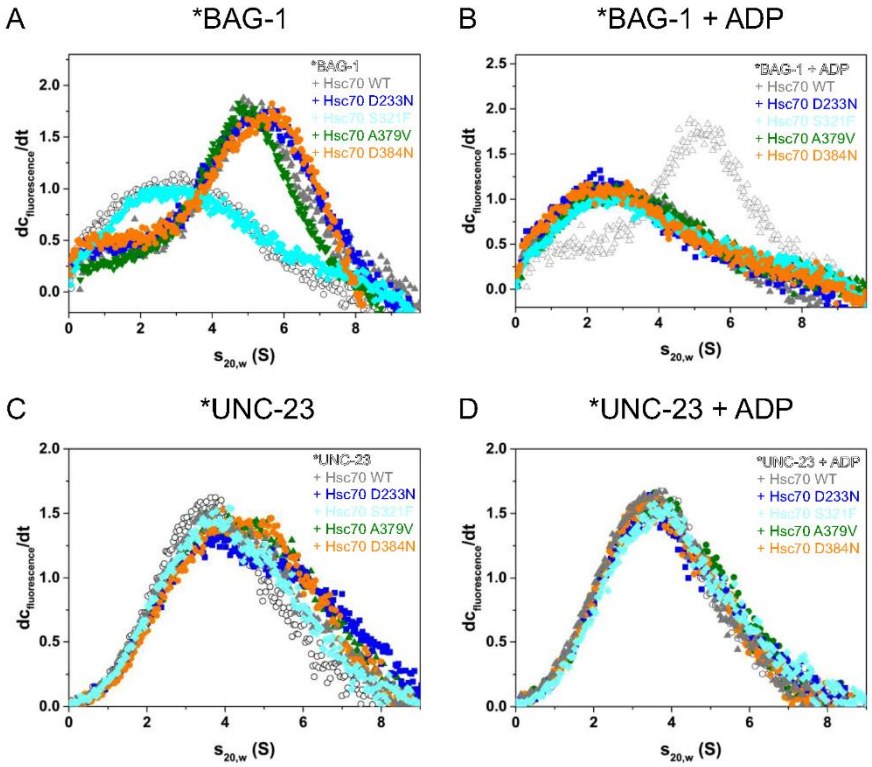

Figure 3. Influence of suppressor mutations on NEF interaction. Binding of Hsc70 mutants to co-chaperones via analytical ultracentrifugation. The conditions are listed in the Material and Method section. (**A**,**B**) Binding of *BAG-1 to wild type/mutant Hsc70 analyzed by analytical ultracentrifugation. *BAG-1 alone sediments at 2.2 S. Hsc70-bound *BAG-1 is observed at 4.9 S. (**A**) BAG-1 sedimentation either alone (open gray symbols) or in the presence of 2 µM Hsc70 (colored gray symbols), Hsc70 D233N (blue), Hsc70 S321F (cyan), Hsc70 A379V (olive) and Hsc70 D384N (orange). (**B**) Binding of *BAG-1 to wild type/mutant Hsc70 in the presence of ADP using the same color code as before. (**C**,**D**) Binding of *△258 UNC-23 to mutant/wild type Hsc70 analyzed by analytical ultracentrifugation. (**C**) Binding of 300 nM *△258 UNC-23 to wild type/mutant Hsc70 in the absence of nucleotides using the same color code as described above. (**D**) Binding of 300 nM *△258 UNC-23 to wild type/mutant Hsc70 in the presence of ADP using the same color code as above.

with wild type Hsc70. The interaction with DNJ-13 is reduced for all four Hsc70-variants. To test whether this effect is conserved in other Hsp40 proteins, we tested the binding to labeled DNJ-12 (*DNJ-12). Here no complex formation can be observed in the absence of nucleotide (Fig. 4C). In the presence of ATP instead, large protein complexes form at 9.9 S with Hsc70 wild type. Similarly, Hsc70 D384N is able to bind *DNJ-12 which results in complexes at 8.2 S. Again, the mutants A379V and D233N showed weak but reproducible binding to *DNJ-12, resulting in a shoulder of the dc/dt plot between 8 and 9 S. Nevertheless, in the presence of Hsc70 A379V and D233N most *DNJ-12 sediments with 4 S, representing unbound *DNJ-12 (Fig. 4D). Thus, complex formation between DNJ proteins and the Hsc70 ATPase domain mutations in the presence of ATP is decreased for all four mutations (Fig. 4D). Potentially, this highlights functional similarity between the different ATPase domain and linker mutations.

Hsc70 mutants refold luciferase at lower yields. We finally tested, whether the strong differences in cofactor binding are reflected in the capability of the Hsc70 mutants to actively refold substrates. This activity requires the close cooperation between Hsp40-proteins, substrate and Hsc70 *in vitro*, but no correlation exists between ATP turnover and efficiency of the folding process. Based on the observed viability of the nematodes harboring these mutations *in vivo*, it is to be expected that the essential functions of Hsc70 can be fulfilled despite the mutations. We performed luciferase refolding assays with Hsc70 and the yeast Hsp40-protein Ydj1, which is able to cooperate with higher eukaryotic Hsc70s[39,40]. Wild type Hsc70 efficiently refolds luciferase (Fig. 5A). Interestingly, Hsc70 D384N refolds even higher amounts of luciferase than the wild type protein. However, Hsc70 A379V and more strikingly Hsc70 D233N show diminished refolding capability (Fig. 5A). We then

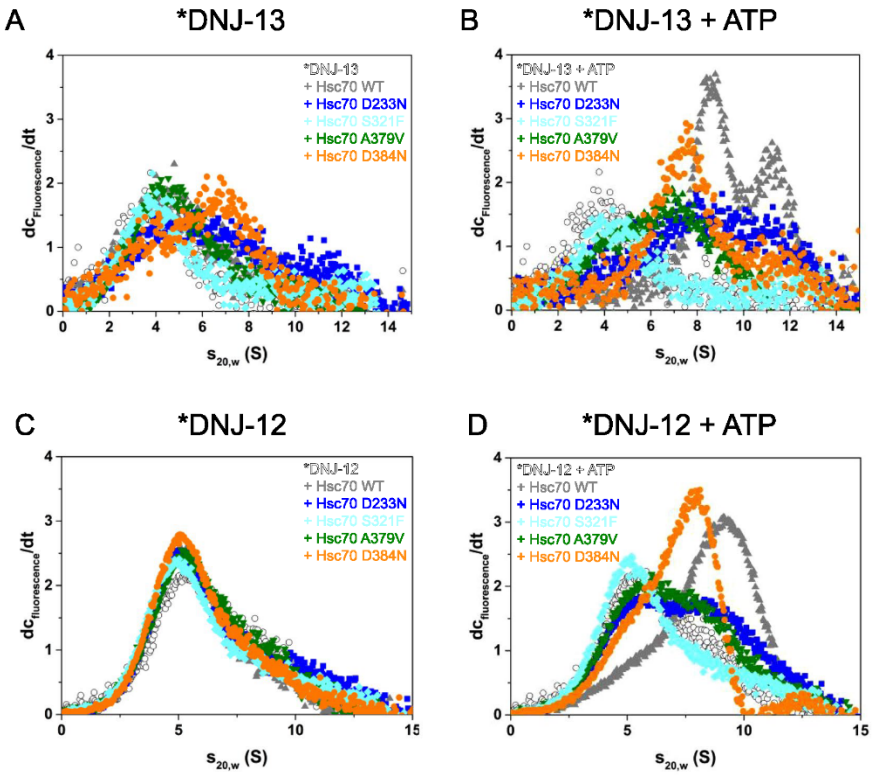

Figure 4. Influence of suppressor mutations on Hsp40-interaction. Binding of Hsc70 mutants to DNJ proteins via analytical ultracentrifugation. The conditions are as is listed in the Material and Method section. (**A**,**B**) Binding of *DNJ-13 to wild type/mutant Hsc70 analyzed by analytical ultracentrifugation. (**A**) Binding of 600 nM *DNJ-13 to wild type/mutant Hsc70 in the absence of nucleotides. DNJ-13 sedimentation was recorded either alone (open gray symbols) or in the presence of 4 µM Hsc70 wild type (gray), Hsc70 D233N (blue), Hsc70 S321F (cyan), Hsc70 A379V (olive) and Hsc70 D384N (orange). (**B**) Binding of *DNJ-13 in the presence of ATP to wild type/mutant Hsc70. Color code is as described above. (**C**,**D**) Binding of *DNJ-12 to wild type/mutant Hsc70 analyzed by analytical ultracentrifugation. (**C**) Binding of 300 nM *DNJ-12 to wild type/mutant Hsc70 in the absence of nucleotides using the same color code as described above. (**D**) Binding of 300 nM *DNJ-12 to wild type/mutant Hsc70 in the presence of ATP using the same color code as described above.

tested, whether the human Hsp40 protein Hdj1 and the nematode DNAJA-homolog DNJ-12 and the nematode DNAJB-homolog DNJ-13 also show differences in stimulating the luciferase refolding reaction. Together with Hdj1, Hsc70 D384N shows the highest refolding activity and Hsc70 D233N again the weakest. For DNJ-12 and DNJ-13, which are much less active this trend seems to not be conserved, as here the wild type Hsc70 shows the highest activity, indicating that the efficiency of the folding reaction is a product of each component and their interactions. In conclusion, the interaction with J-domain proteins is sufficient to allow some Hsc70 folding activity in these mutants. Given that *C. elegans* can live based on these mutant Hsc70-proteins, the residual folding activity apparently is sufficient to enable folding of Hsc70's essential clients *in vivo*.

Depletion of dnj-13 suppresses the phenotype of unc-23(e25). We have observed reduced DNJ-13 binding for most of the Hsc70 mutants in our study. An interesting question is whether the reduction of DNJ-13 and Hsc70 also rescues the strong locomotion phenotype in *C. elegans*. For the RB1301 strain we had previously observed that a reduction of cellular DNJ-13 levels is conferring resistance against the locomotion defect caused by the mutant allele *unc-23(ok1408)*, while reduction in *dnj-12* and *dnj-19* did not cause a change[7]. The Hsc70 S321F and Hsc70 D384N mutants were identified as suppressors of this allele. Despite the difficulty to compare *in vitro* and *in vivo* data, it is interesting to note that our *in vitro* data find that both mutants show decreased DNJ-13 affinity. In addition, especially Hsc70 D233N and Hsc70 A379V, which were identified to rescue the locomotion phenotype of *unc-23(e25)*, show diminished DNJ-13 binding. We thus tested, whether the *unc-23(e25)* allele's phenotype, which is based on a lysine to glutamate exchange in position 297 of UNC-23 in the strain CB25, can be suppressed by reducing cellular DNJ-13 levels *in vivo*. To this end we performed RNAi experiments with the

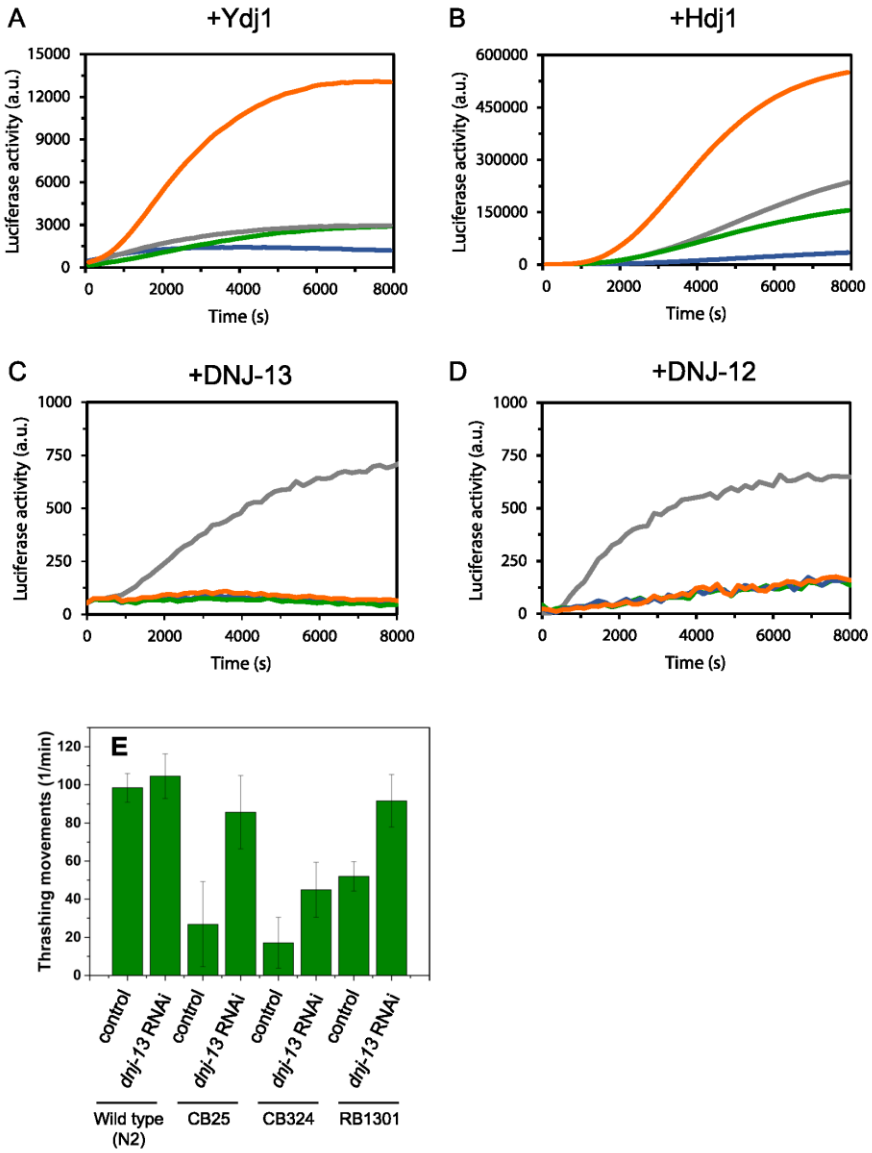

Figure 5. Influence of *Hsc70* ATPase domain mutation on refolding capacity. Refolding of denatured luciferase by mutant and wild type Hsc70s in the presence of the Hsp40-like cofactors Ydj1 (**A**), Hdj1 (**B**), DNJ-13 (**C**) as well as DNJ-12 (**D**). Luciferase is chemically denatured and refolded in refolding buffer as indicated in Material and Methods. Hsc70 wild type (gray), Hsc70 D233N (blue), Hsc70 A379V (olive) and Hsc70 D384N (orange) are shown. (**E**) *dnj-13* RNAi rescues the motility defect in three different *unc-23* mutations (CB25 *unc-23(e25)*, CB324 *unc-23(e324)*, RB1301 *unc-23(ok1408)*). Thrashing movements per minute of *unc-23* mutated nematodes in M9 buffer. Nematodes were grown on control and *dnj-13* RNAi conditions from hatching on and assessed at adult day 1. n = 20.

strain CB25 depleting *dnj-13* under the same conditions used to suppress the phenotype of the RB1301 strain. Nematodes harboring the *e25*-allele show progressively reduced motility at adult day 1. Applying *dnj-13* RNAi improved the locomotion significantly (Fig. 5B). RNAi against the homolog genes *dnj-12* and *dnj-19* on the other hand did not have an effect on the phenotype of CB25 nematodes (data not shown). We also tested the strain

CB324, harboring the allele *unc-23(e324)*. These nematodes showed a stronger phenotype compared to the other strains, but they likewise showed an improvement in motility, if DNJ-13 is depleted. This demonstrates that the genetic interaction between *unc-23* and *dnj-13* previously observed in *unc-23(ok1408)* nematodes[7] is preserved in other *unc-23* mutated strains. Thus, the positive impact of lower DNJ-13 levels is observable in several alleles of *unc-23* and potentially explains the selection of Hsc70 variants with diminished DNJ-13-binding as suppressors of this phenotype.

unc-23 suppressor mutations in Hsc70 affect the communication within the ATPase domain. Of the four Hsc70-variants the S321F-mutation appears most compromised in its biochemical function, while the other mutations do not affect stability and nucleotide binding to a great extent. Nevertheless, they also show striking changes to their interaction with DNJ-13. To estimate the impact of the mutations on protein structure and stability, we used molecular modeling. We determined structures for nematode Hsc70 in the two conformations of Hsc70: undocked/nucleotide-free/substrate-lid-closed and docked/ATP-bound/substrate-lid-open. Several publicly available structures for each conformation can be used for this. The docked Hsc70s were based on the crystal structures of human BIP in complex with ATP (PDB: 5E84, see Fig. 1A right) and on yeast Sse1 either alone (PDB: 2QXL) or in complex with bovine Hsc70 (PDB: 3C7N). In all these structures the Hsc70-like protein was crystallized in a conformation, where the substrate lid is docked onto the ATP-binding site and the SBD is accessible. The relaxed structures are based on bovine Hsc70 (PDB: 3C7N) and on *E. coli* DnaK (PDB: 2KHO, see Fig. 1A left), where the two domains of Hsc70 are separated and the SBD is closed by the substrate-lid. The similarities between the generated docked structures for nematode wild type Hsc70 are high (RMSD of 0.05 to 0.16 nm) and the modeled conformations are almost superimposable in the ATPase domain. This is similar for the undocked structures (RMSD of 0.09 to 0.3 nm). (Fig. 6).

We used the isolated ATPase domains to test for energetic influences that may originate from the four mutations. Based on the FoldX BuildModel tool, which we used to generate and characterize the mutations, the S321F ATPase domain is destabilized by roughly 20 kJ/mole in all five PDB-based model structures (Fig. 6A). In Hsc70 S321F the exchange from Ser321 to Phe321 may be so severe that several aspects of Hsc70 are affected including structure and stability. The fact that the nematodes can live based on the S321F mutation demonstrates a surprising plasticity apparently allowing *C. elegans* to complement such strong impairments to its sole and essential Hsc70 homolog.

The A379V-mutation is also destabilized but to a much lesser extent, while the other two mutations are almost neutral in all structures tested. Nevertheless, D233N in the ATP-induced conformation based on PDB: 5E84 shows a loss of electrostatic energy contribution, which implies that charged interactions at the mutation site could be affected (Fig. 6B). This is not observable to the same extent in the D384N mutation, which affects the same surrounding amino acids, but does so in a surface-exposed linker region. Thus, especially Hsc70 S321F and A379V are destabilized compared to the wild type protein, while D233N shows altered electrostatic interaction.

To get more information on structural influences of mutations that reside within the ATPase domain, we tested short molecular dynamics (MD) simulations. To this end we used the ATPase domain of the closed structure based on the human Hsc70 (PDB: 3C7N) and the ATPase domain of the docked structure based on BIP (PDB: 5E84). With each of the mutations we simulated short trajectories, which can provide insight into the local flexibility and structural deformation caused by the amino acid exchanges. We then analyzed the development of selected interatomic distances in the recorded trajectories. Indeed, we can see that based on the Cα-atoms of S321 (atom 4954 in Hsc70) and the nearby Cα of Thr223 (atom 3398 in Hsc70) a weak deformation of the beta sheet can be induced (Fig. 6C). We performed 30 such simulations with the first homologs of the modeled structures and compared the distance distributions. Indeed, a prominent difference can be observed in the histograms, as the S321F version generates higher distances within its structures during the simulation (Fig. 6D). The bulky Phe-residue introduced at position 321 differs drastically from the smaller Ser 321, which could account for these higher distances.

Likewise, the change of Ala to Val at position 379 induces local distortions that lead to a slightly increased distance between the Cα of Ala379 (atom 5841 of Hsc70) and the Cα of Phe21 (atom 286 in Hsc70), which is nearby (Fig. 7A). This is more obvious in histograms summarizing 30 trajectories (Fig. 7B). Thus, these mutations may induce local distortions of the packed structure surrounding the mutation site, which then could affect the protein's functionality as observed in our biochemical characterization.

In contrast, the changes caused by D233N appear more defined. No obvious structural effects are observable and there is no size difference between the original and replacing amino acid. Measuring the distance between the Cγ of D233 (atom 3525 in Hsc70) and the Cε of Arg72 (atom 1074 in Hsc70), it becomes obvious that these two side chains can form a salt bridge in the closed structure (Fig. 8A). The distance here fluctuates between 3 and 4 Å. In the open, nucleotide free structure the distance between these two side chain atoms is fluctuating between 16 and 20 Å, as they are residing now in opposite sides of the opened nucleotide binding region. In the closed state Asp233 is located in one lobe of the ATP-binding domain, while the acceptor of the negative charge, Arg72, resides in the other lobe and they approach each other once these lobes get closer after ATP-binding. It is interesting to note that Asp233 is conserved in Hsc70 proteins and also Arg72 is strictly conserved in all Hsc70 proteins tested here. It is obvious that this mutation site is far away from the proposed binding site of Hsp40's J-domain, thus most likely an indirect effect caused by altered conformational changes explains the weakened Hsp40 affinity observed *in vitro*. Even though the binding of the nucleotide appears to be uncompromised, the subsequent conformational changes might be affected due to the removal of the salt bridge. When the D233N variant is used in MD-simulations, the distance between Asn233 and Arg72 is increased to roughly 6–10 Å in many closed structures (Fig. 8B,C), implying that the Asn side chain is not able to contribute a similarly productive interaction. In the wild type Hsc70 the salt bridge instead is fairly stable (Fig. 8B,D). Given that Hsc70 D233N fails to generate the ATP-induced, J-domain binding conformation in our biochemical experiments, this mutation apparently

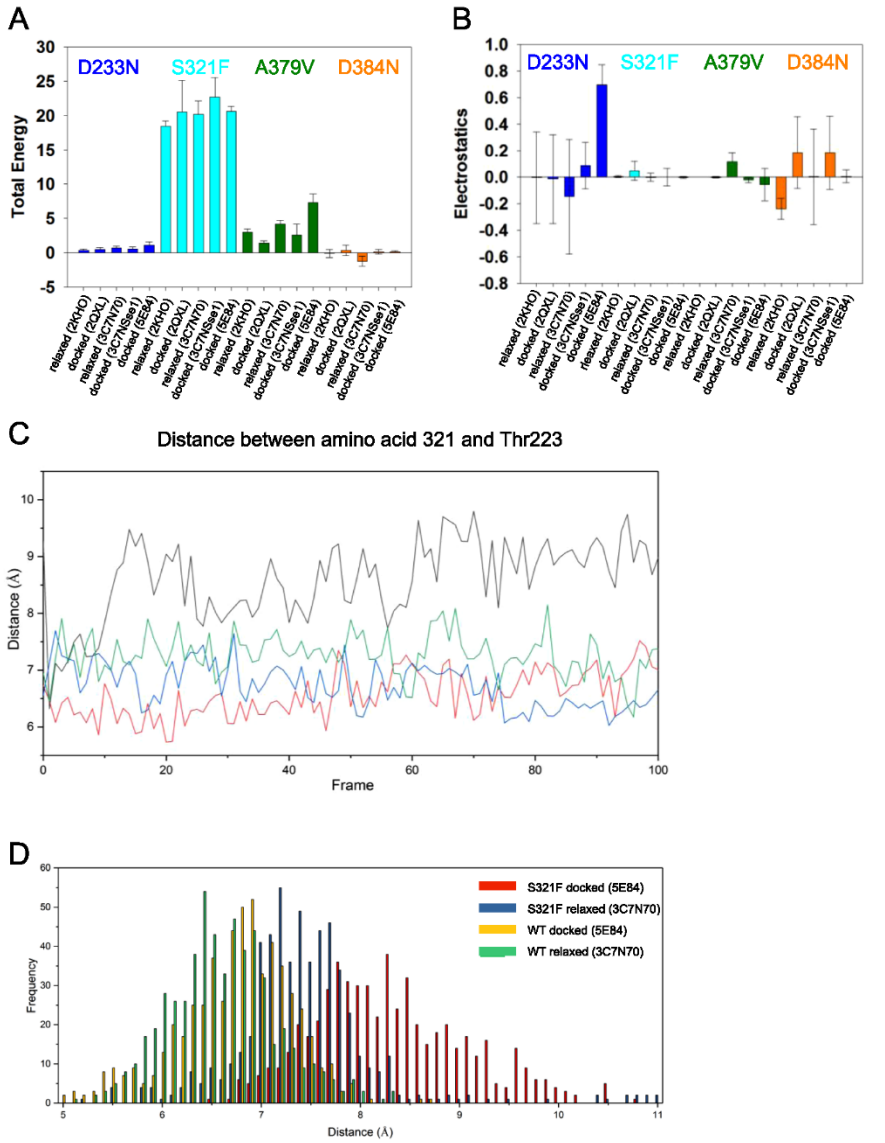

Figure 6. Simulated impact of the Hsc70 mutations on structure and stability. (**A**) Influence of the mutations on the stability of Hsc70 based on the FoldX BuildModel tool. An ensemble of 5 structures was generated by Chimera for each of the starting PDB structures. In each of these structures the amino acid exchanges were introduced and the FoldX tool returned estimated penalty values for the introduction of the mutation. The standard deviation results from differences within these 5 ensemble structures. (**B**) Influence of the mutation type on the charged interactions/electrostatics as indicated by FoldX. (**C**) Excerpt from molecular dynamics trajectories for Hsc70 S321F, representing the distance between the Cα of Thr223 and amino acid 321. Wild type Hsc70 open: green, wild type Hsc70 closed: red, Hsc70 S321F open: blue, Hsc70 S321F closed: black. (**D**) Average distances within the last 20 frames based on 30 simulations each. The plots show wild type Hsc70 and Hsc70 S321F (both either based on the ATP-complexed BIP or the uncomplexed Hsc70 structure).

leads to an Hsc70 variant, which has an altered ATPase cycle resulting from impeded conformational changes. These results provide rationality on how the mutation at the distant position 233 can alter the binding of the J-domain protein by reducing the closing efficiency of the ATPase lobe and thereby reducing the overall ATPase

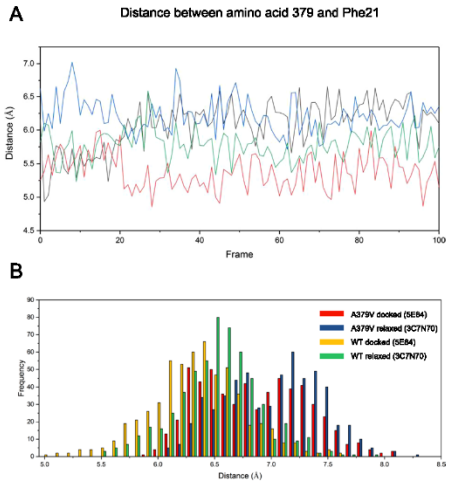

Figure 7. Simulated impact of the A379V mutation. (**A**) Excerpt from molecular dynamics trajectories for Hsc70 A379V, representing the distance between the Cα of amino acid 379 and Phe21. Wild type Hsc70 open: green, wild type Hsc70 closed: red, Hsc70 A397V open: blue, Hsc70 A397V closed: black. (**B**) Average distances between the Cα atoms of amino acid 379 and Phe21 within the last 20 frames in Hsc70 or Hsc70 A379V either based on the ATP-complexed BIP or Hsc70 alone.

rate and the affinity of the DNJ-cofactor requiring this conformation. This makes the Hsc70 D233N protein a very interesting mutant to further investigate the conformational mechanism of Hsc70 in a variant, which still is functional *in vivo* and supportive to life.

Discussion

In this study we characterize the biochemical properties of four Hsc70 mutations within the ATPase domain and neighboring linker mutations, which can act as suppressors of the *head-bent* phenotype in *C. elegans in vivo*. These four mutations show different biochemical properties regarding stability, cochaperone binding and activity (Fig. 8E) and the structural changes in these variants are sufficiently strong to induce energetic penalties in structural simulations. Based on our biochemical analysis, all these mutations cause changes to Hsc70's interaction with the J-domain proteins DNJ-13 and DNJ-12, in most cases by reducing the affinity (D233N, S321F and A379V, Fig. 8E). This might be caused by steric clashes in the ATPase domain in Hsc70 S321F and A379V. The D233N mutation possibly inhibits nucleotide-induced conformational changes which are required for Hsp40 binding. Thus, in Hsc70 D233N, S321F and A379V Hsp40 binding and subsequently the functional activities are inhibited.

This is not observed for the D384N mutant, where an increased ATPase stimulation is present. Interestingly, ATPase stimulation does not strictly correlate with refolding activity in this mutant. It is apparently possible that D384N becomes inactive when the ATPase activity is higher than usual. The mode of action to rescue the head-bent phenotype may be directly related to the changes of the analyzed Hsc70 cycle or may involve further interacting proteins. Previous studies have shown that cooperativity between nematode Hsp40 proteins increases refolding *in vitro* and decreases protein aggregation *in vivo*[9,41]. Thus, one exciting possibility is that cooperativity between Hsp40 proteins is altered in the Hsc70 mutants. Future studies which characterize the molecular mechanism of cooperation will shed light on this possibility.

Conditions which reduce the interaction with the DNJ-13 cofactor are helpful to overcome the severe phenotypes associated with *unc-23* mutations *in vivo*. This may be achieved by depleting *dnj-13* by RNA interference[7], or in cases where DNJ-13 is present this may also be achievable by modifications to Hsc70. The depletion of cellular *dnj-13* has been successful to suppress the *unc-23* deletion mutant allele *ok1408*[7]. Here we report that *dnj-13* depletion likewise rescues the single point-mutant allele *e25*, which harbors the mutated UNC-23 variant UNC-23 E297K and in addition the *unc-23(e324)* allele. Of note, while DNJ-12 and DNJ-13 interaction are reduced *in vitro* only *dnj-13* depletion *in vivo* rescues the muscular attachment phenotype. It is possible that DNJ-13 binds a specific client subset that directs Hsc70 away from the muscular attachment sites and that DNJ-12 would lack this feature.

Nevertheless, all Hsc70 mutants are still functional *in vivo*. The changes observed *in vitro* suggest that protein interactions are likewise going to be reshaped *in vivo*, but to an extent, which does not impede livability. The observed changes to the DNJ-13 interaction might be enough to generate a nematode strain, which is resistant to the *unc-23* mutation E297K and the debilitating phenotype associated with it. Thus, a diminished J-domain interaction of Hsc70 may reduce the detrimental muscular attachment phenotype. In this respect it is also interesting

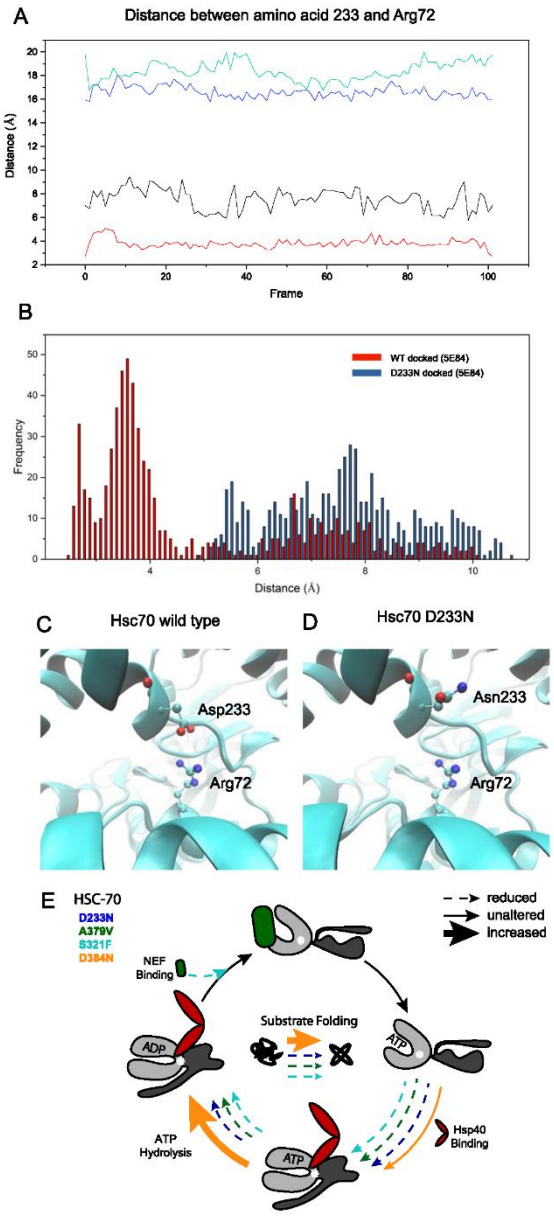

Figure 8. Simulated impact of the Hsc70 D233N mutation on the distance to Arg72. (**A**) Excerpt of the trajectories for Hsc70 D233N representing the distance between the Cγ of Glu/Gln233 and the Cε of Arg72. Wild type Hsc70 open: green, wild type Hsc70 closed: red, Hsc70 D233N open: blue, Hsc70 D233N closed: black. (**B**) Distances between the last 20 frames between Asp233 (Hsc70) or Asn233 (Hsc70 D233N) and Arg72 based on the ATP-complexed BIP structure. (**C**) Positioning of the salt bridge between Asp233 and Arg72 (CeHsc70 based on the structure PDB:5E84). (**D**) Positioning of the amino acids Asn233 and Arg72 in the D233N mutation of Hsc70. (**E**) Summary of the Hsc70 cycle. The colors reflect the respective mutants: Hsc70 D233N (blue), Hsc70 S321F (cyan), Hsc70 A379V (green) and Hsc70 D384N (orange). Solid arrow: not altered, dashed arrow: reduced, bold arrow: increased. Steps that are not analyzed are not represented by arrows. Summary is shown for the ATPase assay with DNJ-12 and Bag-1 as cofactors, which yields in the highest stimulation in wild type. Summary is shown for the luciferase refolding assay with Ydj-1 and Hdj-1, which yields in the highest activity in wild type.

to note, that in humans the Hsp40 protein DNAJB6 and the nucleotide exchange factor Bag3 are relevant in hereditary forms of muscular dystrophy[42–46]. Even though it is unclear, whether similar cellular mechanisms are responsible, this shows that in mammalian cells the Hsc70 system is participating in the development and suppression of related pathologies.

Data Availability

All data are fully available without restriction.

References

1. Mayer, M. P. Hsp70 chaperone dynamics and molecular mechanism. *Trends Biochem Sci* **38**, 507–514 (2013).
2. Clerico, E. M., Tilitsky, J. M., Meng, W. & Gierasch, L. M. How hsp70 molecular machines interact with their substrates to mediate diverse physiological functions. *J Mol Biol* **427**, 1575–1588 (2015).
3. Kim, Y. E., Hipp, M. S., Bracher, A., Hayer-Hartl, M. & Hartl, F. U. Molecular chaperone functions in protein folding and proteostasis. *Annu Rev Biochem* **82**, 323–355 (2013).
4. Mogk, A., Kummer, E. & Bukau, B. Cooperation of Hsp70 and Hsp100 chaperone machines in protein disaggregation. *Front Mol Biosci* **2**, 22 (2015).
5. Dekker, S. L., Kampinga, H. H. & Bergink, S. DNAJs: more than substrate delivery to HSPA. *Front Mol Biosci* **2**, 35 (2015).
6. Bracher, A. & Verghese, J. The nucleotide exchange factors of Hsp70 molecular chaperones. *Front Mol Biosci* **2**, 10 (2015).
7. Papsdorf, K., Sacherl, J. & Richter, K. The balanced regulation of Hsc70 by DNJ-13 and UNC-23 is required for muscle functionality. *J Biol Chem* **289**, 25250–25261 (2014).
8. Sun, L. *et al.* The lid domain of Caenorhabditis elegans Hsc70 influences ATP turnover, cofactor binding and protein folding activity. *PLoS One* **7**, e33980 (2012).
9. Nillegoda, N. B. & Bukau, B. Metazoan Hsp70-based protein disaggregases: emergence and mechanisms. *Front Mol Biosci* **2**, 57 (2015).
10. Genevaux, P., Georgopoulos, C. & Kelley, W. L. The Hsp70 chaperone machines of Escherichia coli: a paradigm for the repartition of chaperone functions. *Mol Microbiol* **66**, 840–857 (2007).
11. Hohfeld, J. & Jentsch, S. GrpE-like regulation of the hsc70 chaperone by the anti-apoptotic protein BAG-1. *EMBO J* **16**, 6209–6216 (1997).
12. Popp, S. L. & Reinstein, J. Functional characterization of the DnaK chaperone system from the archaeon Methanothermobacter thermautotrophicus DeltaH. *FEBS Lett* **583**, 573–578 (2009).
13. Heschl, M. F. & Baillie, D. L. Identification of a heat-shock pseudogene from Caenorhabditis elegans. *Genome* **32**, 190–195 (1989).
14. Heschl, M. F. & Baillie, D. L. Characterization of the hsp70 multigene family of Caenorhabditis elegans. *DNA* **8**, 233–243 (1989).
15. Kamath, R. S. *et al.* Systematic functional analysis of the Caenorhabditis elegans genome using RNAi. *Nature* **421**, 231–237 (2003).
16. Consortium, C. e. D.M. large-scale screening for targeted knockouts in the Caenorhabditis elegans genome. *G3 (Bethesda)* **2**, 1415–1425 (2012).
17. Rahmani, P., Rogalski, T. & Moerman, D. G. The C. elegans UNC-23 protein, a member of the BCL-2-associated athanogene (BAG) family of chaperone regulators, interacts with HSP-1 to regulate cell attachment and maintain hypodermal integrity. *Worm* **4**, e1023496 (2015).
18. Waterston, R. H., Thomson, J. N. & Brenner, S. Mutants with altered muscle structure of Caenorhabditis elegans. *Dev Biol* **77**, 271–302 (1980).
19. Plenefisch, J. D., Zhu, X. & Hedgecock, E. M. Fragile skeletal muscle attachments in dystrophic mutants of Caenorhabditis elegans: isolation and characterization of the mua genes. *Development* **127**, 1197–1207 (2000).
20. Fukuzono, T. *et al.* Chaperone complex BAG2-HSC70 regulates localization of Caenorhabditis elegans leucine-rich repeat kinase LRK-1 to the Golgi. *Genes Cells* **21**, 311–324 (2016).
21. Stiernagle, T. Maintenance of C. elegans. *WormBook*, 1–11 (2006).
22. Rual, J. F. *et al.* Toward improving Caenorhabditis elegans phenome mapping with an ORFeome-based RNAi library. *Genome Res* **14**, 2162–2168 (2004).
23. Studier, F. W. Protein production by auto-induction in high density shaking cultures. *Protein Expr Purif* **41**, 207–234 (2005).
24. Panaretou, B. *et al.* ATP binding and hydrolysis are essential to the function of the Hsp90 molecular chaperone *in vivo*. *EMBO J* **17**, 4829–4836 (1998).
25. Hayes, D. B. & Stafford, W. F. SEDVIEW, real-time sedimentation analysis. *Macromol Biosci* **10**, 731–735 (2010).
26. Demeler, B., Brookes, E. & Nagel-Steger, L. Analysis of heterogeneity in molecular weight and shape by analytical ultracentrifugation using parallel distributed computing. *Methods Enzymol* **454**, 87–113 (2009).
27. Szabo, A. *et al.* The ATP hydrolysis-dependent reaction cycle of the Escherichia coli Hsp70 system DnaK, DnaJ, and GrpE. *Proc Natl Acad Sci USA* **91**, 10345–10349 (1994).
28. Yang, J., Nune, M., Zong, Y., Zhou, L. & Liu, Q. Close and Allosteric Opening of the Polypeptide-Binding Site in a Human Hsp70 Chaperone BiP. *Structure* **23**, 2191–2203 (2015).
29. Liu, Q. & Hendrickson, W. A. Insights into Hsp70 chaperone activity from a crystal structure of the yeast Hsp110 Sse1. *Cell* **131**, 106–120 (2007).
30. Bertelsen, E. B., Chang, L., Gestwicki, J. E. & Zuiderweg, E. R. Solution conformation of wild-type E. coli Hsp70 (DnaK) chaperone complexed with ADP and substrate. *Proc Natl Acad Sci USA* **106**, 8471–8476 (2009).
31. Schuermann, J. P. *et al.* Structure of the Hsp110:Hsc70 nucleotide exchange machine. *Mol Cell* **31**, 232–243 (2008).
32. Sievers, F. *et al.* Fast, scalable generation of high-quality protein multiple sequence alignments using Clustal Omega. *Mol Syst Biol* **7**, 539 (2011).
33. Yang, Z. *et al.* UCSF Chimera, MODELLER, and IMP: an integrated modeling system. *J Struct Biol* **179**, 269–278 (2012).
34. Rigsby, R. E. & Parker, A. B. Using the PyMOL application to reinforce visual understanding of protein structure. *Biochem Mol Biol Educ* (2016).
35. Van Durme, J. *et al.* A graphical interface for the FoldX forcefield. *Bioinformatics* **27**, 1711–1712 (2011).
36. Van Der Spoel, D. *et al.* GROMACS: fast, flexible, and free. *J Comput Chem* **26**, 1701–1718 (2005).
37. Humphrey, W., Dalke, A. & Schulten, K. VMD: visual molecular dynamics. *J Mol Graph* **14**(33–38), 27–38 (1996).
38. Benaroudj, N., Batelier, G., Triniolles, F. & Ladjimi, M. M. Self-association of the molecular chaperone HSC70. *Biochemistry* **34**, 15282–15290 (1995).
39. Kirschke, E., Goswami, D., Southworth, D., Griffin, P. R. & Agard, D. A. Glucocorticoid receptor function regulated by coordinated action of the Hsp90 and Hsp70 chaperone cycles. *Cell* **157**, 1685–1697 (2014).
40. Morishima, Y. *et al.* The hsp90 cochaperone p23 is the limiting component of the multiprotein hsp90/hsp70-based chaperone system *in vivo* where it acts to stabilize the client protein: hsp90 complex. *J Biol Chem* **278**, 48754–48763 (2003).
41. Kirstein, J. *et al. In vivo* properties of the disaggregase function of J-proteins and Hsc70 in Caenorhabditis elegans stress and aging. *Aging cell* **16**, 1414–1424 (2017).

42. Ruggieri, A. *et al.* Complete loss of the DNAJB6 G/F domain and novel missense mutations cause distal-onset DNAJB6 myopathy. *Acta Neuropathol Commun* **3**, 44 (2015).
43. Harms, M. B. *et al.* Exome sequencing reveals DNAJB6 mutations in dominantly-inherited myopathy. *Ann Neurol* **71**, 407–416 (2012).
44. Sarparanta, J. *et al.* Mutations affecting the cytoplasmic functions of the co-chaperone DNAJB6 cause limb-girdle muscular dystrophy. *Nat Genet* **44**(450–455), S451–452 (2012).
45. Behin, A. *et al.* Myofibrillar myopathies: State of the art, present and future challenges. *Rev Neurol (Paris)* **171**, 715–729 (2015).
46. Selcen, D. *et al.* Mutation in BAG3 causes severe dominant childhood muscular dystrophy. *Ann Neurol* **65**, 83–89 (2009).

Acknowledgements

The authors like to thank the CGC for distributing the used nematode strains. K.R. also thanks the Deutsche Forschungsgemeinschaft for funding the research grant RI1873/1-4 and the Heisenberg position RI1873/5-1. We also thank the distributors of software that we could use during this study. This includes Microsoft Visual Studio Community Edition (Microsoft Corp.), NVIDIA CUDA 8.0 and Nsight libraries (NVIDIA Corp.), Gromacs 5.1.4 (http://www.gromacs.org/Downloads), Pymol Educational Edition (Schrodinger Int.) and Chimera 1.10.2 (www.gdfds.edu). We also like to thank Sebastian Jarosch, Julia Sacherl, Niyazi Umut Erdogdu, Eduard Kirchner, Lisa Brandmeier and Daniela Pachner for excellent practical assistance and Donald Moerman for fruitful discussions.

Author Contributions

K.P., S.S. and K.R. designed the experiments, S.P., L.R., P.H., L.S. and K.P. performed the experiments, S.S. and K.R. performed and analyzed the simulations, K.P., S.S., L.S. and K.R. wrote the manuscript.

Additional Information

Competing Interests: The authors declare no competing interests.

Publisher's note: Springer Nature remains neutral with regard to jurisdictional claims in published maps and institutional affiliations.

2.1.4. Permission to reprint the manuscript

CCC RightsLink®

Help Live Chat

SPRINGER NATURE

head-bent resistant Hsc70 variants show reduced Hsp40 affinity and altered protein folding activity

Author: Katharina Papsdorf et al
Publication: Scientific Reports
Publisher: Springer Nature
Date: Aug 16, 2019

Copyright © 2019, The Author(s)

Creative Commons

This is an open access article distributed under the terms of the Creative Commons CC BY license, which permits unrestricted use, distribution, and reproduction in any medium, provided the original work is properly cited.

You are not required to obtain permission to reuse this article.
To request permission for a type of use not listed, please contact Springer Nature

2.2. Nematode CDC-37 and DNJ-13 form complexes and can interact with HSP-90

Accepted manuscript, in press at Scientific Reports, 2021 Oct 18; doi: 10.1038/s41598-021-00885-4

Published by Lukas Schmauder, Eva Absmeier, Katalin Barkovits, Katrin Marcus and Klaus Richter[2]

PhD candidate

[2] corresponding author

2.2.1. Summary

Hsc70 and Hsp90 are important molecular chaperones, and both are required for proteostasis control and the specific folding of client proteins in eukaryotic and prokaryotic organisms. These two proteins interact with a large cohort of co-chaperones in order to specify their client spectrum and to coordinate the ATPase cycles and their co-chaperones may even frequently interact with each other.

Here CDC-37, an important co-chaperone of HSP-90, was examined regarding a potential cross-interaction between the HSP-90 and HSC-70 chaperone system. The Hsp40 like J-domain containing protein DNJ-13 was found to interact with CDC-37 in a crosslink screening, which was performed with prominent co-chaperones of HSC-70. This initial finding was then validated by sedimentation velocity analysis, where the addition of DNJ-13 to CDC-37 leads to strong shift in the sedimentation coefficient from 2.8 S to 5.3 S.

Next both the stoichiometry and affinity of the DNJ-13•CDC-37 complex was determined by sedimentation velocity analysis for fixed concentrations of CDC-37 and different concentrations of DNJ-13. Analysis of the data hinted at a complex consisting of one molecule CDC-37 and two molecules DNJ-13, resembled in a dimeric conformation, while an approximate K_D of 3 µM, indicating an intermediate affinity between the two proteins, could be determined.

Binding sites were then identified by analytical ultracentrifugation and crosslinking, using CDC-37 ΔN and ΔC fragments, together with full-length DNJ-13. Mass spectrometry of the crosslinked CDC-$37_{monomer}$•DNJ-13_{dimer} complex, concluded these experiments and a homology model was generated, showing the interaction between both N-termini as well as some interaction between the N-terminus of CDC-37 and the C-terminus of DNJ-13.

Lastly, sedimentation velocity analysis was once more employed to test if the complex is still able to interact with HSP-90, which indeed was the case. Furthermore, the presence of DNJ-13 even strengthens the complex formation between HSP-90 and CDC-37 and simultaneously modulates nucleotide-dependent effects.

Overall, these findings provide evidence for a more intricate interaction during client processing, between the HSP-90 and HSC-70 chaperone system, or at least their HSP-40 co-chaperones.

2.2.2. Contribution of the PhD candidate

Lukas Schmauder and Klaus Richter designed the experiments. Lukas Schmauder, Eva Absmeier, Katalin Barkovits and Katrin Marcus performed the experiments. Lukas Schmauder, Eva Absmeier analyzed the data. Lukas Schmauder and Klaus Richter wrote the manuscript.

2.2.3. Manuscript

Nematode CDC-37 and DNJ-13 form complexes and can interact with HSP-90

Lukas Schmauder[1], Eva Absmeier[1], Alexander Bepperling[1], Katalin Barkovits[2,3], Katrin Marcus[2,3] & Klaus Richter[1,*]

[1] Center for Integrated Protein Research at the Department of Chemistry, Technische Universität München, Lichtenbergstr. 4, 85748 Garching
[2] Medizinisches Proteom-Center, Ruhr-Universität Bochum, Gesundheitscampus 4, 44801, Bochum, Germany.
[3] Medical Proteome Analysis, Center for Protein Diagnostics (PRODI), Ruhr-University Bochum, Gesundheitscampus 4, 44801, Bochum, Germany.
[*] Corresponding author. E-Mail: klaus.richter@richterlab.de, Tel: +49-89-289-13342

Abstract

The molecular chaperones Hsc70 and Hsp90 are required for proteostasis control and specific folding of client proteins in eukaryotic and prokaryotic organisms. Especially in eukaryotes these ATP-driven molecular chaperones are interacting with cofactors that specify the client spectrum and coordinate the ATPase cycles.
Here we find that a Hsc70-cofactor of the Hsp40 family from nematodes, DNJ-13, directly interacts with the kinase-specific Hsp90-cofactor CDC-37. The interaction is specific for DNJ-13, while DNJ-12 another DnaJ-like protein of *C. elegans*, does not bind to CDC-37 in a similar manner. Analytical ultracentrifugation is employed to show that one CDC-37 molecule binds to a dimeric DNJ-13 protein with low micromolar affinity. We perform cross-linking studies with mass spectrometry to identify the interaction site and obtain specific cross-links connecting the N-terminal J-domain of DNJ-13 with the N-terminal domain of CDC-37. Further AUC experiments reveal that both, the N-terminal part of CDC-37 and the C-terminal domain of CDC-37, are required for efficient interaction. Furthermore, the presence of DNJ-13 strengthens the complex formation between CDC-37 and HSP-90 and modulates the nucleotide-dependent effects.
These findings on the interaction between Hsp40 proteins and Hsp90-cofactors provide evidence for a more intricate interaction between the two chaperone systems during client processing.

Introduction

Cdc37 is a well-known co-chaperone of Hsp90, which is required for the stable folding of many client kinases during their maturation. It consists of 3 structural domains, namely the N-terminal, central and C-terminal domain [1]. Crystal structures of Hsp90•Cdc37 and biochemical studies on the nematode HSP-90•CDC-37•kinase complexes reveal that the C-terminal domain of phosphorylated Cdc37 initiates the binding to a kinase-substrate, before the N-terminus of Cdc37 and the C-terminus of Hsp90 interact which each other [2-4]. During this process, the ATPase-activity of Hsp90 is inhibited by Cdc37, which blocks Hsp90's N-terminal ATP binding site thereby holding Hsp90 in an open conformation and assisting the loading of kinase clients onto the chaperone [5,6]. Binding of Aha1, another co-chaperone of Hsp90, leads to the dissociation of Cdc37 from the complex and Hsp90 is able to change into the closed ATPase active conformation, eventually leading to a mature kinase [3,7-9]. The detailed mechanism of kinase loading onto the Cdc37•Hsp90 complex still remains unknown.
Instead of forming a stable complex with Hsp90 and Cdc37, kinases can also associate with Hsc70 and Hsp40, leading to degradation by the proteasome if Cdc37 is depleted [10]. Here Hsp40 or in general J domain-containing proteins stimulate the hydrolysis activity of Hsc70 by binding to its ATP-bound state. Various nucleotide exchange factors like BAG domain-containing proteins then trigger nucleotide release by competing with the highly diverse J domain-proteins, leading to a strong ATP turnover if both are present [11].
In *Caenorhabditis elegans* (*C. elegans*), there are three cytosolic Hsp40-like J domain proteins, namely DNJ-12, DNJ-13 and DNJ-19 as well as the two Hsp40-like J-proteins DNJ-7 and DNJ-16 from mitochondria and ER, respectively. DNJ-12 and DNJ-19 share full domain conservation with *Escherichia coli* (*E. coli*) DnaJ, which is the namesake of the J-protein family.
DNJ-13 shares its N-terminal J-domain and its Gly/Phe-rich domain with DnaK, but the Cys-rich domain is replaced by a Met/Gly-rich domain [12]. The Gly/Phe-rich domain seems particularly interesting due to its involvement in the ATP-dependent substrate binding of HSP-70 [13,14]. A study by PERALES-CALVO *et al.* found that the Gly/Phe-rich domain of DnaJ plays a crucial role in the conformational recognition of substrate proteins [15], and in the ability of DnaJ to interact with folded substrates. Further, the Cys-rich domain of DnaJ binds denatured substrates and stabilizes the DnaK-substrate complex [16-18]. It is assumed that this domain also controls the J-protein interaction with other proteins, and thereby supports the chaperone functions [18-21].
The C-terminus contains two beta-barrel-topology domains CTD I and CTD II. In addition, a separate C-terminal dimerization-domain also influences the affinity for client proteins [22,23]. Especially CTD I is thought to play an important role in client binding, due to a hydrophobic pocket [21,24] and the outbound Gly/Met-rich domain [16-18]. Based on the importance of client binding *in vivo*, the deletion of the C-terminus of DnaJ-like proteins lead to non-viable mutants [25]. For the CTDII of J-proteins no function is known yet, but it precedes the C-terminal dimerization domain.

Both chaperone systems, Hsp70 and Hsp90, are involved in proteostasis control and specific folding of client proteins. Their cofactors may frequently interact during these functions within the large protein assemblies. To reveal potential interactions between cofactors, we employed protein cross-linking and analytical ultracentrifugation on the Hsp90-cofactor CDC-37 in order

to investigate possible interaction partners and further analyze the crosslinked proteins by mass spectrometry.

Material and Methods

Cloning, protein expression and purification

The pET28b plasmid was used as expression vector with the cDNA of either DNJ-13, CDC-37 and the respective fragments of CDC-37 (ΔN & ΔC), subcloned after the N-terminal His_6 tag. For expression, transformed *E. coli* BL21-CodonPlus(DE3)RIL cells were grown to an OD_{600} of 0.6 at 37 °C. Protein production was induced by adding 1 mM isopropyl 1-thio-β-D-galactopyranoside and further incubation at 20 °C. Cells were harvested and subsequently disrupted in a TS 0.75 cell disruption instrument (Constant Systems Ltd., Northants, UK). The His_6-tagged proteins were trapped on a HisTrap FF 5-mL affinity column (GE Healthcare) in 40 mM HEPES/KOH, pH7.5, 20 mM KCl, 1 mM DTT and eluted with buffer containing 300 mM imidazole. ResourceS ion-exchange chromatography and size exclusion chromatography on a 16/60 Superdex 75 HiLoad column (GE Healthcare) were subsequently performed. Proteins were stored and measured in a buffer containing 40 mM HEPES/KOH, pH7.5, 20 mM KCl, 1 mM DTT. The quality of each purified protein was confirmed by SDS-PAGE and mass spectroscopy on a Bruker UltraFlex III MALDI-TOF instrument (Bruker, Massachusetts, USA).

Fluorescence labeling of CDC-37

Labeled CDC-37 (*CDC-37) was generated by fluorescently labeling 0.5 mg CDC-37 at its cysteine residues with a 2-fold molar excess of ATTO 488 C_5-maleimide (ATTO-TEC, Germany) for 2 hours at room temperature in a buffer of 40 mM HEPES/KOH, pH7.5 and 20 mM KCl. The reaction was stopped by the addition of 20 mM DTT and *CDC-37 was subsequently dialyzed against the same buffer to remove free label. The degree of labeling as well as the concentration of the protein was determined by UV/VIS spectroscopy using the following equations:

$$A_{Protein} = A_{280} - A_{500} \cdot (CF_{280})$$

$$DOL = A_{500} \cdot MW / [protein] \cdot \varepsilon_{dye}$$

where $CF_{280} = 0.09$ and $\varepsilon_{dye} = 90{,}000\ M^{-1}\ cm^{-1}$ according to the manufacturer.

Analytical ultracentrifugation

Analytical ultracentrifugation (AUC) experiments were carried out in a Beckman ProteomeLab XL-A analytical ultracentrifuge (Beckman Coulter, Brea) equipped with an AVIV AU-FDS fluorescence detection system (Aviv Biomedical, Lakewood, NY) and a Ti-50 rotor (Beckman Coulter, Brea) as described previously [26]. For binding analyses, 300 nM of *CDC-37 were sedimented at 42,000 rpm and 20 °C in the absence or presence of 2 μM binding partners. Sedimentation experiments were performed in 40 mM HEPES/KOH pH 7.5, 20 mM KCl, 1 mM DTT and 5 mM $MgCl_2$. dc/dt distributions were visualized with the program Sedview [27] and the customized in-house script diffUZ was used for flexible scan range selection, for normalization of the data and for generation of the plots as described previously [11,28]. Fits to Gaussian functions were made in OriginPro (Version 2018b) (OriginLab Corporation, Northampton, MA, USA; https://www.originlab.com/origin). Each assay was measured in triplicates and a representative graph is plotted.

Sedimentation experiments of non-labeled proteins were performed in a similar manner using a concentration of 0.5 mg/ml protein and an UV/Vis optical system (Beckman Coulter, Brea). dc/dt plots were generated with the in-house script diffUZ as described in [29]. 2DSA analysis in UltraScan III Version 4.0 (https://ultrascan3.aucsolutions.com/) [30] was employed to get information on the heterogeneity of the sample and to derive sedimentation coefficients, diffusion coefficients and molecular weights for the species.

K_D determination

Fluorescence AUC was deployed to determine the approximate K_D of the DNJ-13•CDC-37 complex, using 100 nM *CDC-37 with increasing DNJ-13 concentrations (0-10 µM). Saturated complexes are represented by peaks with the highest sedimentation coefficients, which were plotted against the corresponding DNJ-13 concentrations. The K_D was then derived by fitting a Michaelis-Menten function in OriginPro (Version 2018b) (OriginLabs, Northampton, USA) onto the data points.

Crosslinking of DNJ-13•CDC-37 complexes

Crosslink experiments were performed using deuterium isotope labeled BS3-H_{12}/D_{12} and DSSG- H_6/D_6 (Creative Molecules Inc.) as crosslinking reagents. 16 µM DNJ-13 and 16 µM CDC-37 were mixed in a total volume of 50 µL (40 mM HEPES/KOH, pH7.5, 20 mM KCl) and crosslinked with a 32.5-fold molar excess of crosslinker. The reaction was stopped after 20 min at room temperature by the addition of 1 M Tris/HCl pH 8.0. As control, both proteins were also crosslinked alone. SDS-PAGE was used to analyze the crosslinked samples on pre-casted SERVAGel Neutral Gradient pH7.4 (SERVA, Heidelberg, Germany) according to the manufacturer's instruction. Images have not been cropped to remove lanes, as shown in Supplemental Figure 1-3. Bands of interest were then cut out and sent to the Medical Proteome Analysis Center for Protein Diagnostics (PRODI, Ruhr-University Bochum, Bochum).

Mass spectrometry

Gel pieces containing crosslinked protein bands were washed and digested in-gel as described previously [31,32]. The peptide concentration was then determined by amino acid analysis (AAA) as described by PLUM *et al.* [33].

Tryptic peptides were measured by nanoLC-ESI-MS/MS, also as described previously [32,34]. In short, an UltiMate 3000 RSLC nanoLC system (Thermo Scientific, Bremen, Germany) was used with the following solvent system: (A) 0.1% FA; (B) 84% ACN, 0.1% FA. For sample concentration and washing, loading on a trap column (Thermo, 100 µm × 2 cm, particle size 5 µm, pore size 100 Å, C18) at a flow rate of 30 µl/min with 0.1% TFA was performed. Afterwards, the trap column was serially connected to an analytical C18 column (Thermo, 75 µm × 50 cm, particle size 2 µm, pore size 100 Å), and the peptides were separated with a flow rate of 400 nl/min using a solvent gradient of 4% to 40% B for 95 min at 60 °C. 1 h of column washing was performed for equilibration after each sample measurement. The UltiMate 3000 RSLC nanoLC system was on-line connected to the nano-electrospray ionization source of a Q-Exactive HF (Thermo Scientific, Bremen, Germany).

Full MS spectra were scanned in the range 350–1400 m/z with a resolution of 60,000 at 200 m/z (AGC target 3e6, 80 ms maximum injection time). Capillary temperature was set to 275 °C and spray voltage to 1500 V (positive mode). Lock mass polydimethylcyclosiloxane (m/z 445.120) was used for internal recalibration. The m/z values initiating MS/MS were set on a dynamic exclusion list for 30 s and the 10 most intensive ions (charge 2+ to 6+) were selected for

fragmentation. MS/MS fragments were generated by higher-energy-collision-induced dissociation and the fragmentation was performed with 28% normalized collision energy. The fragment analysis was performed in an orbitrap analyzer with resolution 30,000 at 200 m/z (AGC 1e6, maximum injection time 120 ms).

Identification of crosslink sites

To confirm the presence of all proteins, the raw data was analyzed with MaxQuant 1.5 (https://maxquant.org/maxquant/) [35] and tables for the crosslinked proteins were obtained from all unmodified peptides and the complete peak lists. The peak lists also yielded intensity values and elution times for each peptide and were then imported into the in-house script xMASS [29] and analyzed as previously described [31].

A similar analysis on the same raw data was performed in pLink2.0 (http://pfind.ict.ac.cn) [36] with the following settings: Peptide mass range: 600–6000 Da; Peptide length: 6–60 AA; precursor tolerance: ± 15 ppm; fragment tolerance: ± 15 ppm; filter tolerance: ± 15 ppm; FDR < 5% at PSM level. Reported crosslinked spectra were filtered to a mass error < 2 ppm and then compared to the xMASS outputs. The most prominent confirmed hits are listed in Table 1. Sequence alignments of template and target proteins were performed in CLUSTALW (http://www.clustal.org/clustal2/) [37].

Molecular modelling and docking calculations

DnaJ of *Thermus thermophilus* (PDB 4J80) [38] served as homology template for DNJ-13 using the Chimera 1.13.1 interface to MODELLER (https://www.cgl.ucsf.edu/chimera/) [39,40]. Likewise for the generation of a CDC-37 homology model, human Cdc37 (PDB 5FWL) [41] was used. Docking of both homology models was performed in HADDOCK 2.4 (https://wenmr.science.uu.nl/haddock2.4/) [42]. Lysine residues, which were identified by crosslinking, were defined and a distance restraint of 30 Å was enforced on those residues in expert mode. PyMOL 2.5 (https://pymol.org/2/) was used to generate space-filling and ribbon models and crosslinks were visualized with the PyMOL plugin PyXlinkViewer (https://github.com/BobSchiffrin/PyXlinkViewer) [43].

Results

General interaction between CDC-37 and DNJ-13

Several interactions between Hsp90-cofactors had been observed in the yeast model system [44]. We aimed at identifying similar interactions of nematode CDC-37 and therefore investigated, whether the Hsp90-cofactor CDC-37 can potentially interact with other cofactors. We first performed a crosslink screening of several Hsc70 cofactors utilizing BS3 as a crosslinking reagent (Figure 1a). A potential interaction between CDC-37 and the J domain-containing protein DNJ-13 (bands marked by the two arrowheads in Figure 1a) was revealed, which to our knowledge was unknown until now. The upper band equals a molecular mass, comparable to one CDC-37 monomer and a DNJ-13 dimer, whereas the lower band compares to a CDC-37 monomer together with one DNJ-13 monomer. To confirm these findings, we then employed sedimentation velocity analytical ultracentrifugation (SV-AUC) of both proteins (Figure 1b). Fluorescently labeled CDC-37 had been generated before to investigate the interaction of CDC-37 with other cofactors of Hsp90 in the absence and presence of Hsp90 itself. During these studies, large parts of the Hsp90-cycle with Hsp90 could be reconstituted under experimental conditions [4,45]. We also investigated whether the addition of Hsp40 proteins influences the hydrodynamic properties of the fluorescently labeled *CDC-37. Indeed, DNJ-13 leads to a strong shift in sedimentation coefficient from 2.8 S to 5.3 S, implying an interaction between CDC-37 and DNJ-13 and the formation of a protein complex between these two proteins (Figure 1b). We aimed at understanding, whether this complex is specific to DNJ-13, or whether other Hsp40 proteins likewise form these assemblies. Addition of DNJ-12 instead did not lead to a likewise increase in size and therefore the formation of this complex appears to be specific for DNJ-13 as suggested by the crosslinking experiment.

Stoichiometry of one DNJ-13 dimer in complex with one CDC-37

While AUC with fluorescently labeled proteins is a powerful tool to analyze the oligomerization state as well as the association of labeled proteins with putative binding partners by determination of the hydrodynamic properties, complex formation best is confirmed with unmodified proteins. To ensure that the interaction between CDC-37 and DNJ-13 is not due to the attached label, an AUC experiment was performed with non-labeled CDC-37 and three different concentrations of DNJ-13 (Figure 2a). The complex was formed with the same sedimentation coefficient as in the fluorescence SV-AUC measurement (Figure 1b), confirming that the interaction is not caused by the labeling of CDC-37 with the fluorophore. The obtained sedimentation coefficients for CDC-37 alone and CDC-37 in complex with DNJ-13 were approximately the same as in the fluorescence experiments.

To determine the stoichiometry of the complex, absorbance AUC was employed. Three different conditions were compared: one with a substoichiometric concentration of CDC-37, one with an equal concentration of CDC-37 and DNJ-13 dimer, and one with a 2-fold excess of CDC-37 (Figure 2a). In the first case, all CDC-37 was bound in complex with the DNJ-13 dimer and a peak with the sedimentation coefficient of the DNJ-13 dimer was still visible (Figure 2a, black trace). The obtained mass for the second peak based on UltraScan 2DSA-analysis hinted at a complex of one molecule CDC-37 with a DNJ-13 dimer. The second condition showed almost solely a peak for the DNJ-13 dimer with one CDC-37 in complex. In the third condition a peak corresponding to free CDC-37 and a peak for the CDC-37•DNJ-13-dimer complex was visible (blue trace, Figure 2a).

Affinity of the complex between CDC-37 and DNJ-13

We next set out to determine the approximate K_D of the protein complex. To this end, we employed AUC with fluorescence detection, since the affinity of the protein complex may be too low for the fairly high protein concentrations needed for UV/Vis detection during AUC. The determination thus was carried out with 100 nM AlexaFluor 488-labeled CDC-37 (*CDC-37) and DNJ-13 protein at concentrations ranging from 0-10 µM (Figure 2b). The K_D was then estimated from the concentrations of free CDC-37 and CDC-37 in complex with DNJ-13 (Figure 2c). Saturation of complex formation could be obtained as no further increase in sedimentation coefficient was observed for the highest DNJ-13 concentrations employed. This also implies that the interaction is happening at a defined site and the complex was found to have an approximate K_D of 3 µM, which indicates an intermediate affinity between the two proteins.

Identification of binding sites with crosslinks and AUC for CDC-37 variants

Next, we aimed at addressing the binding sites of the two molecules. To confirm the relevance of individual domains for the interaction between the two proteins, deletion mutants of CDC-37 were made deleting either the N-terminus or the C-terminus of the Hsp90-cofactor. To investigate whether the CDC-37 variants are still able to bind full-length DNJ-13 the crosslinking reaction was repeated with CDC-37 and both fragments (Figure 3a). Several other bands were likewise observed in the isolated proteins and therefore only those bands were considered, that were specific for the setups, in which both proteins were mixed. The mixture, where a C-terminal deleted CDC-37 was used could still perform the cross-linking reaction, implying that the N-terminal part of CDC-37 is capable of performing this reaction. Furthermore, absorbance AUC experiments were performed with the fragments in similarity to the experiments with full-length CDC-37 (Figure 3b). Both fragments did not interact with the same strength as the full-length CDC-37 protein, implying that both termini may be involved in the binding reaction. However, a stronger increase in the sedimentation coefficient was observed for DNJ-13+CDC-37ΔN (5.2 S) compared to DNJ-13+CDC-37ΔC (4.2 S), which implies a stronger interaction as indicated by the titration of CDC-37 with DNJ-13 before. Nevertheless, for both deletion fragments, the peaks are fairly broad, indicating a dynamic binding mode and a weaker interaction. Based on the SV-AUC data most of the binding site seems to be located at the C-terminus of CDC-37, despite the identification of the crosslink at the N-terminus. Nevertheless, it is obvious from the AUC results that both regions contribute and the identification of the crosslink at the N-terminus may represent only one of the two binding sites.

CDC-37/DNJ-13 in complex with HSP90

We also aimed to determine, whether the CDC-37/DNJ-13 complex still can bind to HSP-90, for which CDC-37 acts as a co-chaperone during kinase maturation. Employing the fluorescently-labeled CDC-37 protein, AUC was performed to see whether the DNJ-13 complex binds to open or closed forms of HSP-90 (Figure 4a). To this end, ATPγS was supplemented into the binding reaction to induce the closed conformation of HSP-90 (Figure 4b). In the presence of ATPγS the equilibrium is shifted towards unbound CDC-37 as described previously. The equilibrium is shifted towards the ternary complex for the open form of HSP-90, but no influence of the nucleotide on the formation of the DNJ-13•CDC-37 complex is observed. The ternary complex between the three proteins can be clearly observed at 7 S, with only little residual CDC-37•DNJ-13 complexes left unbound at the employed concentration of

HSP-90. Addition of nucleotides to these complexes releases CDC-37•DNJ-13 complexes from HSP-90, indicating that the regulation of the CDC-37-Hsp90-interaction is still functional, when DNJ-13 is associated with CDC-37. Furthermore, no indication was seen that the presence of DNJ-13 dramatically changes the interaction between the complexed CDC-37 and Hsp-90. CDC-37 binds mainly the open form of HSP-90 but there is still unbound CDC-37 in the nucleotide-closed or the open state. In the presence of DNJ-13, all CDC-37 is bound to either the HSP-90 containing complex or to DNJ-13, indicating that CDC-37 has a stronger affinity to DNJ-13 than towards its chaperone HSP-90.

Structural organization of the CDC-37•DNJ-13 complex

Next, we analyzed the crosslinked binary complex of CDC-37 and DNJ-13 (Figure 5a and Figure 5b) by mass spectrometry to find key crosslink pairs in the complex, which would reveal more structural information.

Datasets generated by MS were analyzed by two independent programs, pLink2.0 and the in-house script xMASS, both yielding comparable results. We then obtained a schematic diagram of the relative protein arrangement in the complex (Figure 5c) based upon the identified intermolecular crosslinks (Table 1). 6 of the 10 intermolecular crosslinks could be obtained using DSSG as crosslinking compound, the 4 other pairs were linked by BS3. A major contact site was found between CDC-37 peptide MEQEKIDK (AA50) and DNJ-13 peptide YHPDKNK (35), occurring in both datasets. Another possible interaction site was identified between the N-terminus of CDC-37 (AA44) and in between the C-terminal domain I (CTDI) and II (CTDII) of DNJ-13 (AA235). The N-terminus of CDC-37 is known to be involved in client kinase binding and while CTDI is thought to play an important role in client binding, no function is known for the CTDII of J-proteins yet [1,21,24].

We then calculated a homology model for both nematode CDC-37 and DNJ-13, based on the human homolog Cdc37 (PDB: 5FWL) and bacterial DnaJ (PDB: 4J80) respectively. Finally, we performed an assembly of the proposed CDC-37•DNJ-13 complex, based upon the most prominent intermolecular crosslinks (Figure 6). Potential differences due to the limited sequence identity of both CDC-37 (37 %) and DNJ-13 (31 %) to their respective PDB templates, are not respected during homology modeling since most distances between crosslinked positions are in agreement with the 30 Å maximal length of the crosslinker. Crosslink pairs with a distance over 30 Å imply that minor rearrangements of the structure may have to be considered. Since a significant part of Cdc37 is not well resolved in PDB 5FWL further ambiguity exists. Nevertheless, the docking approach indicates that the two cofactors may interact alongside one DNJ-13 dimer with both domains of CDC-37 bound to that subunit.

Discussion

CDC-37 is known as HSP-90 co-factor during kinase maturation [46,47]. It arrests the ATP-driven molecular clamp mechanism of Hsp90 and thus has an inhibitory effect on the ATPase activity of HSP-90. Even though the partial crystal structure of the Cdc37•Hsp90 complex is solved [5] and parts of the kinase maturation cycle are understood [48,49], the question how the kinase is loaded onto the Cdc37•Hsp90 complex still remains unclear. We found that nematode DNJ-13, a well-described Hsc70 cofactor, interacts with the kinase specific Hsp-90 cofactor CDC-37 from nematodes. Altogether our results demonstrate an interaction between the Hsp90 co-chaperone CDC-37 and the J domain-containing protein DNJ-13 and the ability to form a stable complex *in vitro*. The complex has a K_D of approximately 3.4 µM and a stoichiometry of one CDC-37 monomer bound to a DNJ-13 monomer or dimer.

J-proteins, like DNJ-13, are known to form dimers [28] and CDC-37 interacts as a monomer in the CDC-37/HSP-90 kinase complex [48]. Interestingly, the complex of DNJ-13 and CDC-37 interacts with HSP-90, preferentially with the open state. In these assays, DNJ-13 binds stronger to CDC-37 than to HSP-90. It might be that the client kinase is further modulating the interaction affinities if present. The observed interaction between CDC-37 and DNJ-13 is interesting, as it links the CDC-37/HSP-90/Kinase system to the Hsc70/DNJ-13 chaperone machinery. Speculating on the relevance, this interaction might be important when transferring a kinase from the Hsc70 chaperone system to the Hsp90 chaperone system for further maturation. While this transfer process has been well established for the maturation of the GR receptor and other steroid binding receptors with the help of the cofactor Hop/STI-1 [50,51], it is less well established for the kinase clients.
Interestingly an interaction of DNJ-13s human orthologue DNAJB5 with Hop was identified before [50] and the relevance of Hsc70 for the maturation of kinases has been likewise observed [52]. A transfer of the client might therefore be required to coordinate the two chaperone systems. Alternatively, the interaction might be relevant for the degradation of the kinase after release from CDC-37, where likewise the Hsc70-system could participate. In any setting, the identification of this direct interaction between the two co-factors provides insight into the mechanisms of chaperone interaction during client processing.

We set out to define the interaction sites between CDC-37 and DNJ-13. To determine the interaction sites on DNJ-13 and CDC-37 an isotope-labeled crosslink for mass spectroscopy and deletion mutants of the two proteins were investigated. One single crosslink hints to an interaction of the C-terminal domain II of DNJ-13 with the N-terminus of CDC-37 (Figure 5). Analytical ultracentrifugation experiments with CDC-37ΔN and CDC-37ΔC mutants and full-length DNJ-13 show in contrast to the crosslink, that CDC-37ΔN binds stronger to DNJ-13 than CDC-37ΔC. This indicates that binding may occur on several sites with a stronger contribution coming from the C-terminus of CDC-37. This would contribute another complex interaction mode for CDC-37, which was found to interact with kinases and HSP-90 also via multiple interaction sites, despite the N-terminus being known as the kinase binding site [1].

Acknowledgements

K.R. and L.S. thank the Deutsche Forschungsgemeinschaft for funding the research grant RI1873/1-4 and the Heisenberg position RI1873/5-1. K.M. and K.B. were funded by P.U.R.E. (Protein Research Unit Ruhr within Europe), Ministry of Innovation, Science and Research of North-Rhine Westphalia, Germany. We also thank the distributors of free and open-source software that we could use during this study. This includes UltraScan III Version 4.0 (https://ultrascan3.aucsolutions.com/), MaxQuant (Computational Systems Biochemistry, Max-Planck Institute for Biochemistry), pLink 2.0 (Institute of Computing Technology, CAS), CLUSTALW (http://www.clustal.org/), Chimera 1.13.1 (https://www.cgl.ucsf.edu/), HADDOCK 2.4 (https://wenmr.science.uu.nl/) and PyMOL 2.5 (PyMOL Molecular Graphics System, Version 2.5 Schrödinger, LLC). We also thank the reviewers for their valuable suggestions.

Additional Information

Author contributions

L.S. and K.R. designed the experiments, L.S., E.A., A.B., K.B. and K.M. performed the experiments, L.S., E.A. and K.R. analyzed the data. L.S. and K.R. wrote the manuscript.

Competing Interests

The authors do not have competing interests in respect to this study.

Data Availability

All data are fully available without restriction.

References

1 Shao, J., Irwin, A., Hartson, S. D. & Matts, R. L. Functional dissection of cdc37: characterization of domain structure and amino acid residues critical for protein kinase binding. *Biochemistry* **42**, 12577-12588, doi:10.1021/bi035138j (2003).

2 Gray, P. J., Jr., Prince, T., Cheng, J., Stevenson, M. A. & Calderwood, S. K. Targeting the oncogene and kinome chaperone CDC37. *Nat Rev Cancer* **8**, 491-495, doi:10.1038/nrc2420 (2008).

3 Calderwood, S. K. Molecular cochaperones: tumor growth and cancer treatment. *Scientifica (Cairo)* **2013**, 217513, doi:10.1155/2013/217513 (2013).

4 Eckl, J. M. *et al.* Hsp90.Cdc37 Complexes with Protein Kinases Form Cooperatively with Multiple Distinct Interaction Sites. *J Biol Chem* **290**, 30843-30854, doi:10.1074/jbc.M115.693150 (2015).

5 Roe, S. M. *et al.* The Mechanism of Hsp90 regulation by the protein kinase-specific cochaperone p50(cdc37). *Cell* **116**, 87-98, doi:10.1016/s0092-8674(03)01027-4 (2004).

6 Siligardi, G. *et al.* Regulation of Hsp90 ATPase activity by the co-chaperone Cdc37p/p50cdc37. *J Biol Chem* **277**, 20151-20159, doi:10.1074/jbc.M201287200 (2002).

7 Taipale, M., Jarosz, D. F. & Lindquist, S. HSP90 at the hub of protein homeostasis: emerging mechanistic insights. *Nat Rev Mol Cell Biol* **11**, 515-528, doi:10.1038/nrm2918 (2010).

8 Taipale, M. *et al.* Quantitative analysis of HSP90-client interactions reveals principles of substrate recognition. *Cell* **150**, 987-1001, doi:10.1016/j.cell.2012.06.047 (2012).

9 Cox, M. B. & Johnson, J. L. The role of p23, Hop, immunophilins, and other co-chaperones in regulating Hsp90 function. *Methods Mol Biol* **787**, 45-66, doi:10.1007/978-1-61779-295-3_4 (2011).

10 Smith, J. R., Clarke, P. A., de Billy, E. & Workman, P. Silencing the cochaperone CDC37 destabilizes kinase clients and sensitizes cancer cells to HSP90 inhibitors. *Oncogene* **28**, 157-169, doi:10.1038/onc.2008.380 (2009).

11 Papsdorf, K., Sacherl, J. & Richter, K. The balanced regulation of Hsc70 by DNJ-13 and UNC-23 is required for muscle functionality. *J Biol Chem* **289**, 25250-25261, doi:10.1074/jbc.M114.565234 (2014).

12 Kampinga, H. H. & Craig, E. A. The HSP70 chaperone machinery: J proteins as drivers of functional specificity.

13 Cajo, G. C. *et al.* The role of the DIF motif of the DnaJ (Hsp40) co-chaperone in the regulation of the DnaK (Hsp70) chaperone cycle. *J Biol Chem* **281**, 12436-12444, doi:10.1074/jbc.M511192200 (2006).

14 Wall, D., Zylicz, M. & Georgopoulos, C. The conserved G/F motif of the DnaJ chaperone is necessary for the activation of the substrate binding properties of the DnaK chaperone. *J Biol Chem* **270**, 2139-2144, doi:10.1074/jbc.270.5.2139 (1995).

15 Perales-Calvo, J., Muga, A. & Moro, F. Role of DnaJ G/F-rich domain in conformational recognition and binding of protein substrates. *J Biol Chem* **285**, 34231-34239, doi:10.1074/jbc.M110.144642 (2010).

16 Linke, K., Wolfram, T., Bussemer, J. & Jakob, U. The roles of the two zinc binding sites in DnaJ. *J Biol Chem* **278**, 44457-44466, doi:10.1074/jbc.M307491200 (2003).

17 Banecki, B. *et al.* Structure-function analysis of the zinc finger region of the DnaJ molecular chaperone. *J Biol Chem* **271**, 14840-14848, doi:10.1074/jbc.271.25.14840 (1996).

18 Szabo, A., Korszun, R., Hartl, F. U. & Flanagan, J. A zinc finger-like domain of the molecular chaperone DnaJ is involved in binding to denatured protein substrates. *EMBO J* **15**, 408-417 (1996).

19 Ramos, C. H., Oliveira, C. L., Fan, C. Y., Torriani, I. L. & Cyr, D. M. Conserved central domains control the quaternary structure of type I and type II Hsp40 molecular chaperones. *J Mol Biol* **383**, 155-166, doi:10.1016/j.jmb.2008.08.019 (2008).

20 Lu, Z. & Cyr, D. M. Protein folding activity of Hsp70 is modified differentially by the hsp40 co-chaperones Sis1 and Ydj1. *J Biol Chem* **273**, 27824-27830, doi:10.1074/jbc.273.43.27824 (1998).

21 Lee, S., Fan, C. Y., Younger, J. M., Ren, H. & Cyr, D. M. Identification of essential residues in the type II Hsp40 Sis1 that function in polypeptide binding. *J Biol Chem* **277**, 21675-21682, doi:10.1074/jbc.M111075200 (2002).

22 Sha, B., Lee, S. & Cyr, D. M. The crystal structure of the peptide-binding fragment from the yeast Hsp40 protein Sis1. *Structure* **8**, 799-807, doi:10.1016/s0969-2126(00)00170-2 (2000).

23 Li, J., Qian, X. & Sha, B. The crystal structure of the yeast Hsp40 Ydj1 complexed with its peptide substrate. *Structure* **11**, 1475-1483, doi:10.1016/j.str.2003.10.012 (2003).

24 Li, J. & Sha, B. Structure-based mutagenesis studies of the peptide substrate binding fragment of type I heat-shock protein 40. *Biochem J* **386**, 453-460, doi:10.1042/BJ20041050 (2005).

25 Johnson, J. L. & Craig, E. A. An essential role for the substrate-binding region of Hsp40s in Saccharomyces cerevisiae. *J Cell Biol* **152**, 851-856, doi:10.1083/jcb.152.4.851 (2001).

26 Papsdorf, K. *et al.* head-bent resistant Hsc70 variants show reduced Hsp40 affinity and altered protein folding activity. *Scientific Reports* **9**, 11955, doi:10.1038/s41598-019-48109-0 (2019).

27 Hayes, D. B. & Stafford, W. F. SEDVIEW, real-time sedimentation analysis. *Macromol Biosci* **10**, 731-735, doi:10.1002/mabi.201000075 (2010).

28 Sun, L. *et al.* The lid domain of Caenorhabditis elegans Hsc70 influences ATP turnover, cofactor binding and protein folding activity. *PLoS One* **7**, e33980, doi:10.1371/journal.pone.0033980 (2012).

29 Haslbeck, V. *et al.* The activity of protein phosphatase 5 towards native clients is modulated by the middle- and C-terminal domains of Hsp90. *Sci Rep* **5**, 17058, doi:10.1038/srep17058 (2015).

30 Demeler, B., Brookes, E. & Nagel-Steger, L. Analysis of heterogeneity in molecular weight and shape by analytical ultracentrifugation using parallel distributed computing. *Methods Enzymol* **454**, 87-113, doi:10.1016/S0076-6879(08)03804-4 (2009).

31 Sima, S. *et al.* HSP-90/kinase complexes are stabilized by the large PPIase FKB-6. *Sci Rep* **11**, 12347, doi:10.1038/s41598-021-91667-5 (2021).

32 Kaziales, A., Barkovits, K., Marcus, K. & Richter, K. Glucocorticoid receptor complexes form cooperatively with the Hsp90 co-chaperones Pp5 and FKBPs. *Sci Rep* **10**, 10733, doi:10.1038/s41598-020-67645-8 (2020).

33 Plum, S. *et al.* Combined enrichment of neuromelanin granules and synaptosomes from human substantia nigra pars compacta tissue for proteomic analysis. *J Proteomics* **94**, 202-206, doi:10.1016/j.jprot.2013.07.015 (2013).

34 Barkovits, K. *et al.* Blood Contamination in CSF and Its Impact on Quantitative Analysis of Alpha-Synuclein. *Cells* **9**, doi:10.3390/cells9020370 (2020).

35 Tyanova, S., Temu, T. & Cox, J. The MaxQuant computational platform for mass spectrometry-based shotgun proteomics. *Nat Protoc* **11**, 2301-2319, doi:10.1038/nprot.2016.136 (2016).

36 Chen, Z. L. *et al.* A high-speed search engine pLink 2 with systematic evaluation for proteome-scale identification of cross-linked peptides. *Nat Commun* **10**, 3404, doi:10.1038/s41467-019-11337-z (2019).

37 Larkin, M. A. *et al.* Clustal W and Clustal X version 2.0. *Bioinformatics* **23**, 2947-2948, doi:10.1093/bioinformatics/btm404 (2007).

38 Barends, T. R. *et al.* Combining crystallography and EPR: crystal and solution structures of the multidomain cochaperone DnaJ. *Acta Crystallogr D Biol Crystallogr* **69**, 1540-1552, doi:10.1107/s0907444913010640 (2013).

39 Pettersen, E. F. *et al.* UCSF Chimera--a visualization system for exploratory research and analysis. *J Comput Chem* **25**, 1605-1612, doi:10.1002/jcc.20084 (2004).

40 Webb, B. & Sali, A. Comparative Protein Structure Modeling Using MODELLER. *Curr Protoc Bioinformatics* **54**, 5.6.1-5.6.37, doi:10.1002/cpbi.3 (2016).

41 Verba, K. A. *et al.* Atomic structure of Hsp90-Cdc37-Cdk4 reveals that Hsp90 traps and stabilizes an unfolded kinase. *Science* **352**, 1542-1547, doi:10.1126/science.aaf5023 (2016).
42 Dominguez, C., Boelens, R. & Bonvin, A. M. HADDOCK: a protein-protein docking approach based on biochemical or biophysical information. *J Am Chem Soc* **125**, 1731-1737, doi:10.1021/ja026939x (2003).
43 Schiffrin, B., Radford, S. E., Brockwell, D. J. & Calabrese, A. N. PyXlinkViewer: A flexible tool for visualization of protein chemical crosslinking data within the PyMOL molecular graphics system. *Protein Sci* **29**, 1851-1857, doi:10.1002/pro.3902 (2020).
44 Abbas-Terki, T., Briand, P. A., Donzé, O. & Picard, D. The Hsp90 co-chaperones Cdc37 and Sti1 interact physically and genetically. *Biol Chem* **383**, 1335-1342, doi:10.1515/bc.2002.152 (2002).
45 Gaiser, A. M., Kretzschmar, A. & Richter, K. Cdc37-Hsp90 complexes are responsive to nucleotide-induced conformational changes and binding of further cofactors. *J Biol Chem* **285**, 40921-40932, doi:10.1074/jbc.M110.131086 (2010).
46 Pearl, L. H. Hsp90 and Cdc37 -- a chaperone cancer conspiracy. *Curr Opin Genet Dev* **15**, 55-61, doi:10.1016/j.gde.2004.12.011 (2005).
47 Grammatikakis, N., Lin, J.-H., Grammatikakis, A., Tsichlis, P. N. & Cochran, B. H. p50(cdc37) Acting in Concert with Hsp90 Is Required for Raf-1 Function. *Molecular and Cellular Biology* **19**, 1661-1672, doi:10.1128/mcb.19.3.1661 (1999).
48 Mayer, M. P., Prodromou, C. & Frydman, J. The Hsp90 mosaic: a picture emerges. *Nat Struct Mol Biol* **16**, 2-6, doi:10.1038/nsmb0109-2 (2009).
49 Gaiser, A. M., Brandt, F. & Richter, K. The non-canonical Hop protein from Caenorhabditis elegans exerts essential functions and forms binary complexes with either Hsc70 or Hsp90. *J Mol Biol* **391**, 621-634, doi:10.1016/j.jmb.2009.06.051 (2009).
50 Bhattacharya, K. *et al.* The Hsp70-Hsp90 co-chaperone Hop/Stip1 shifts the proteostatic balance from folding towards degradation. *Nat Commun* **11**, 5975, doi:10.1038/s41467-020-19783-w (2020).
51 Kirschke, E., Goswami, D., Southworth, D., Griffin, P. R. & Agard, D. A. Glucocorticoid receptor function regulated by coordinated action of the Hsp90 and Hsp70 chaperone cycles. *Cell* **157**, 1685-1697, doi:10.1016/j.cell.2014.04.038 (2014).
52 Diehl, J. A., Yang, W., Rimerman, R. A., Xiao, H. & Emili, A. Hsc70 regulates accumulation of cyclin D1 and cyclin D1-dependent protein kinase. *Mol Cell Biol* **23**, 1764-1774, doi:10.1128/mcb.23.5.1764-1774.2003 (2003).

Table legends

Table 1. Most prominent unique hits in the crosslinked sample. Grey colored parts are obtained from DSSG crosslinked samples while white parts are obtained from BS3 crosslinked samples. **a)** Intermolecular crosslink pairs of sample #4 (Complex at approx. 135 kDa). **b)** Intermolecular crosslink pairs of sample #5 (Complex >245 kDa). **c)** Both Inter- and intramolecular crosslinked pairs in the reference sample #3 (DNJ-13 dimer).

Tables

Table 1.

a.

Peptide 1	Peptide 2	Protein 1	Protein 2
EAGAENKFK	GTTSKK	DNJ-13 (44)	CDC-37 (60)
MEQEKIDK	YHPDKNK	CDC-37 (50)	DNJ-13 (35)
GKDYYKVLGISK	EKGTTSK	DNJ-13 (3)	CDC37 (55)
KMKITR	KPQAPK	DNJ-13 (179)	CDC-37 (132)
MEQEKIDK	YHPDKNK	CDC-37 (50)	DNJ-13 (35)
AYRKMALK	MEELEKK	DNJ-13 (26)	CDC-37 (67)
MGKDYYK	GTTSKK	DNJ-13 (1)	CDC-37 (60)
MPIDYSK	GTTKKMK	CDC-37 (1)	DNJ-13 (176)
AYRKMALK	GTTSKK	DNJ-13 (26)	CDC-37 (60)
GLPNPKSPSHR	PIDYSK	DNJ-13 (299)	CDC-37 (2)
KEAELEEK	MGKDYYK	CDC-37 (97)	DNJ-13 (3)
LERMAEKK	DKPHPK	CDC-37 (44)	DNJ-13 (235)

b.

Peptide 1	Peptide 2	Protein 1	Protein 2
KFEAAEPVYMK	MGKDYYK	CDC-37 (241)	DNJ-13 (1)
MEQEKIDK	YHPDKNK	CDC-37 (50)	DNJ-13 (35)
MEELEKKLAAADVTDK	KMALKYHPDK	CDC-37 (67)	DNJ-13 (30)
MEQEKIDK	YHPDKNK	CDC-37 (50)	DNJ-13 (35)

c.

Peptide 1	Peptide 2	Protein 1	Protein 2
DYYKVLGISK	GATDDEIKK	DNJ-13 (7)	DNJ-13 (21)
GATDDEIKK	YHPDKNK	DNJ-13 (21)	DNJ-13 (35)
GLPNPKSPSHR	GATDDEIKK	DNJ-13 (299)	DNJ-13 (21)
KVMTDNAQR	EAGAENKFK	DNJ-13 (183)	DNJ-13 (44)
DYYKVLGISK	EAGAENKFK	DNJ-13 (7)	DNJ-13 (44)
NKEAGAENK	GKDYYK	DNJ-13 (37)	DNJ-13 (3)
KIYDQFGEEGLK	GATDDEIKK	DNJ-13 (62)	DNJ-13 (21)
VLGISKGATDDEIKK	EAGAENKFK	DNJ-13 (13)	DNJ-13 (44)
EIAEAYDVLSDDKKK	KIYDQFGEEGLK	DNJ-13 (59)	DNJ-13 (62)
VEKISLK	EGSDIKR	DNJ-13 (252)	DNJ-13 (248)
EAGAENKFK	GATDDEIKK	DNJ-13 (44)	DNJ-13 (21)
DYYKVLGISK	EGSDIKR	DNJ-13 (7)	DNJ-13 (248)

Figure Legends

Figure 1. Systematic cofactor CDC-37 interactions.
a) Interaction of CDC-37 (C) with and without the crosslinking reagent BS3, as indicated together with the cofactors Sti1, PPH-5, HSP-90, DNJ-12 and DNJ-13. The upper arrowhead indicates the observed crosslinked CDC-$37_{monomer}$•DNJ-13_{dimer} complex, whereas the lower arrowhead indicates a CDC-$37_{monomer}$•DNJ-$13_{monomer}$ complex. **b)** Sedimentation analysis of labeled CDC-37 (*CDC-37) together with the J domain-containing proteins DNJ-12 and DNJ-13. OriginPro (Version 2018b) was utilized for generating the graph.

Figure 2. KD and stoichiometry determination.
a) Absorbance sedimentation velocity analysis of CDC-37 titration to 10 µM DNJ-13 in substoichiometric, equal and excess concentrations, as indicated. CDC-37 (purple) and DNJ-13 (green) serve both as control, as well as assistance for the indication of unbound protein used in the titration. **b)** Titration of varying DNJ-13 concentrations in AUC experiments to 100 nM *CDC-37, as indicated. **c)** Kinetics of CDC-37/DNJ-13 binding based on titrated DNJ-13 concentrations and measured sedimentation coefficient. Graphs were generated in OriginPro (Version 2018b).

Figure 3. CDC-37 fragment interaction with DNJ-13.
a) SDS-PAGE of crosslinked DNJ-13 (D) together with CDC-37ΔN (ΔN), CDC-37ΔC (ΔC) or full-length CDC-37 (FL). Arrowheads indicate the observed complexes. **b)** Sedimentation analysis of DNJ-13 with either CDC-37ΔN, CDC-37ΔC or full-length CDC-37 as indicated. Shifting sedimentation coefficients are put into perspective by both controls, DNJ-13 (dashed grey) and CDC-37 (dashed yellow) respectively. OriginPro (Version 2018b) was utilized for generating the graph.

Figure 4. Interaction of HSP-90 with the CDC-37•DNJ-13 complex.
a) Sedimentation analysis of the binary complex, consisting of the either *CDC-37 and DNJ-13 (orange), *CDC-37 and HSP-90 (grey) or the ternary CDC-37•DNJ-13•HSP-90 complex (dashed green). **b)** Effect of ATPγS addition to both binary and ternary complex, similar to a). Graphs were generated in OriginPro (Version 2018b).

Figure 5. Mass spectrometry crosslink analysis.
a) Samples used for MS-analysis and crosslinked with DSSG. 1 = CDC-37 monomer, 2 = DNJ-13 monomer, 3 = DNJ-13 dimer, 4 = CDC37•DNJ13 complex made out of one CDC-37 and two DNJ-13 molecules, 5 = complex consisting of two CDC37•DNJ13 complexes. **b)** Samples used for MS-analysis, crosslinked with BS3, with the same naming scheme as in a). **c)** Visualization of the crosslinked pairs, obtained from MS-analysis (Table 1). Green lines indicate pairs crosslinked with DSSG; Yellow lines indicate pairs crosslinked with BS3; Red lines indicate the pair crosslinked by both DSSG and BS3.

Figure 6. Homology model of the CDC-37•DNJ-13 complex.
PDB structure 4J80 served as template for DNJ-13, monomers highlighted in cyan and brown; CDC-37 was modeled after PDB structure 5FWL, highlighted in magenta. Arrows indicate a rotation of the model and/or a swap between visualizations as either space-filling or ribbon model. Crosslinks are depicted as red lines between the ribbon models. Homology models were

generated in Chimera 1.13.1, docked with HADDOCK 2.4 and crosslinks were visualized in PyMOL 2.5.

Figures

Figure 1.

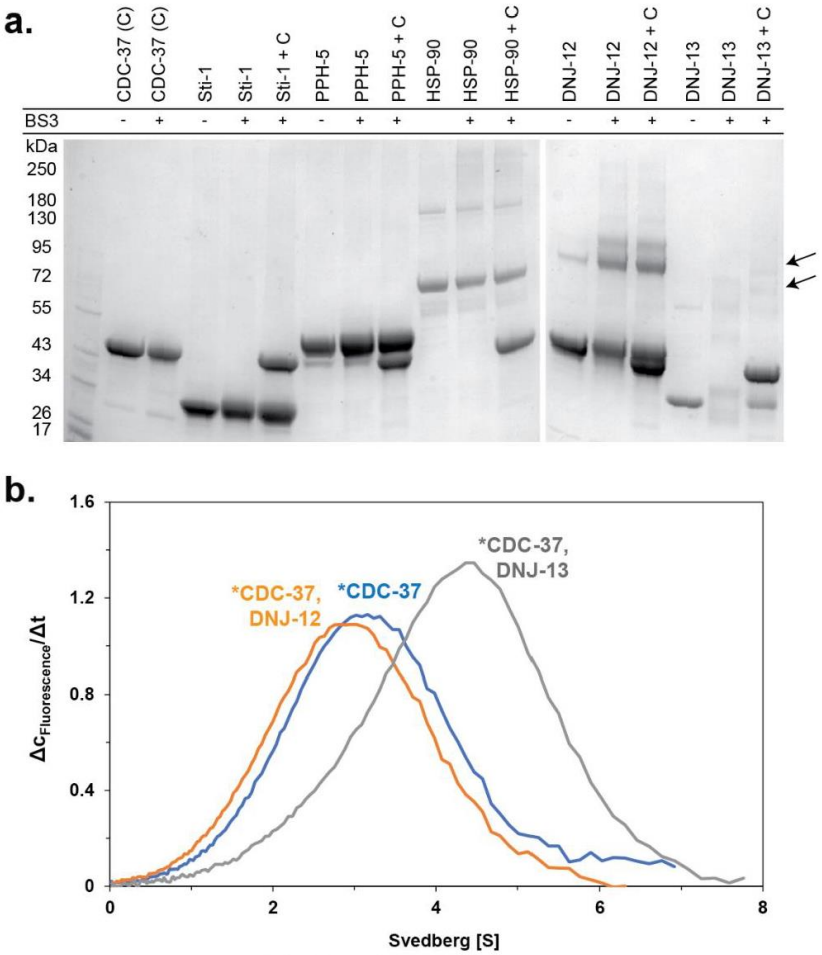

Figure 2.

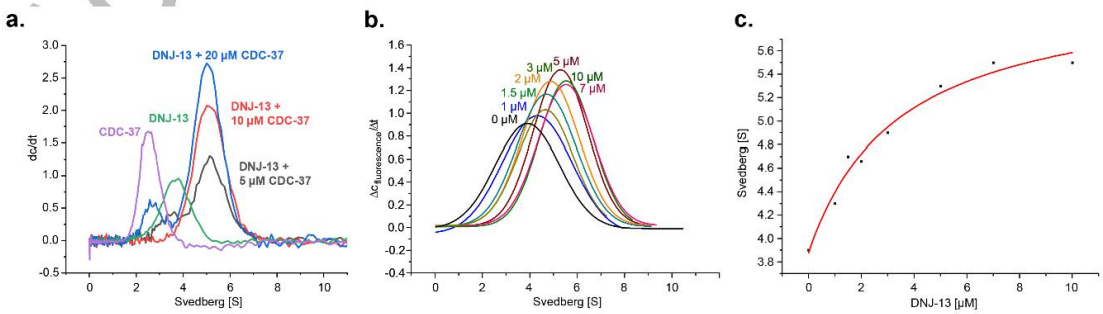

Figure 3.

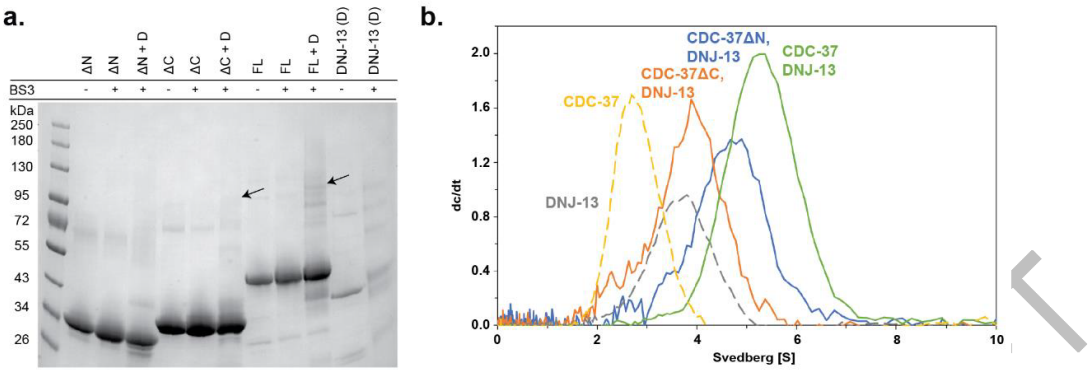

Figure 4.

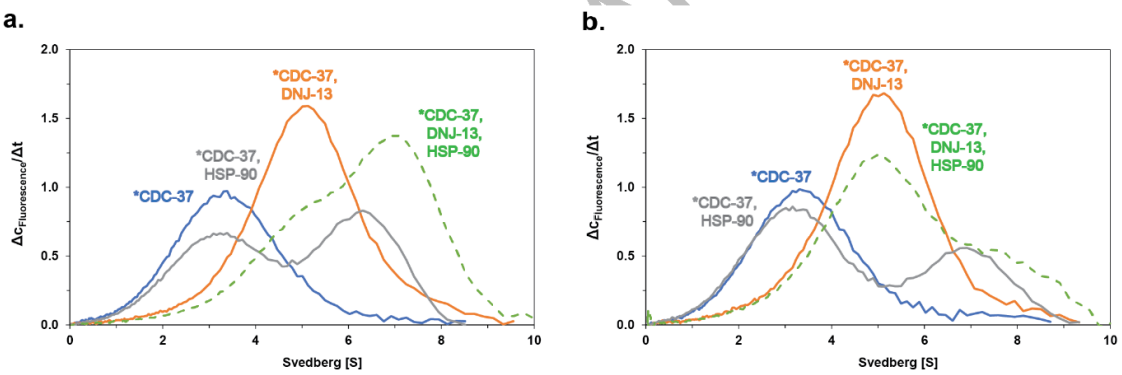

Figure 5.

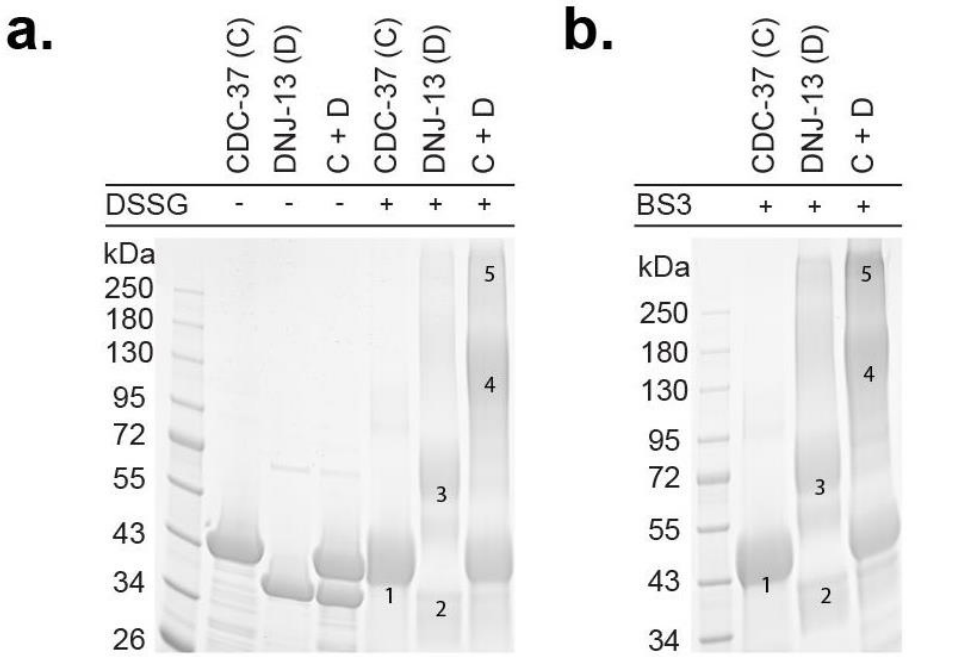

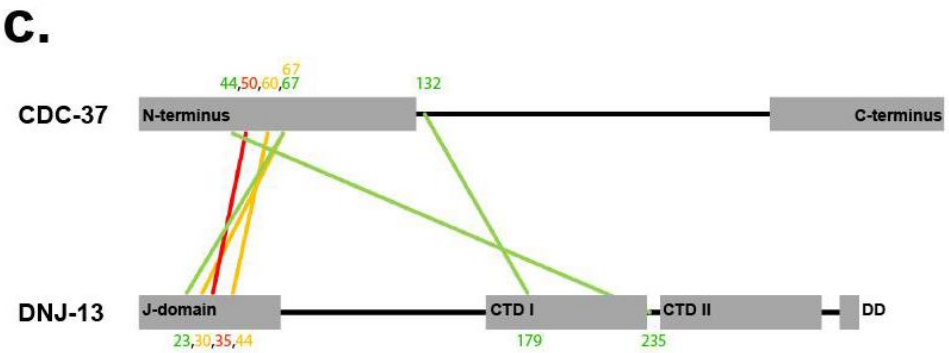

Figure 6.

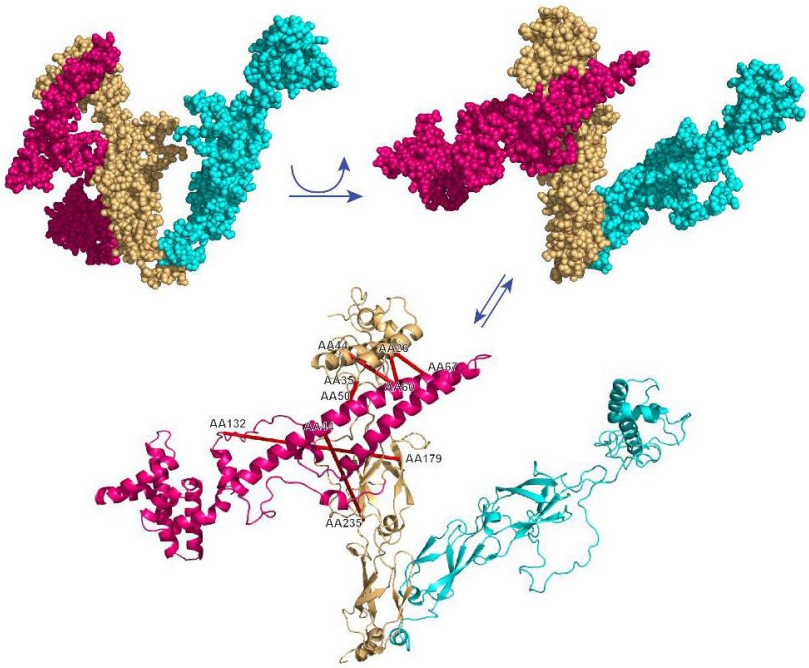

2.2.4. Permission to reprint the manuscript

nature.com

Licence to publish

Manuscript id:	bc26ed70-bc2a-474e-b1fc-db2cb83af19d
Proposed Title:	Nematode CDC-37 and DNJ-13 form complexes and can interact with HSP-90
The "Author(s)":	Lukas Schmauder, Eva Absmeier, Alexander Bepperling, Katalin Barkovits, Katrin Marcus, Klaus Richter
The "Journal":	Scientific Reports
The "Licensee":	Springer Nature Limited

Licence applicable to the Article: CC BY

The CC BY licence allows readers to copy, distribute and transmit the Article as long as it is attributed back to the author. Readers are permitted to alter, transform or build upon the Article, and to use the Article for commercial purposes. Please read the full licence for further details at - http://creativecommons.org/licenses/by/4.0/

The Licensee will consider publishing this article including any supplementary information and graphic elements therein (e.g. illustrations, charts, moving images) (the 'Article'), including granting readers rights to use the Article on an open access basis under the terms of the stated Creative Commons licence. Headings are for convenience only.

Grant of Rights

Subject to editorial acceptance of the Article, it will be published under the Creative Commons licence shown above. In consideration of the Licensee evaluating the Article for publication, the Author(s) grant the Licensee a non-exclusive, irrevocable and sub-licensable right, unlimited in time and territory, to copy-edit, reproduce, publish, distribute, transmit, make available and store the Article, including abstracts thereof, in all forms of media of expression now known or developed in the future, including pre- and reprints, translations, photographic reproductions and extensions. Furthermore, to enable additional publishing services, such as promotion of the Article, the Author(s) grant the Licensee the right to use the Article (including any graphic elements on a stand-alone basis) in whole or in part in electronic form, such as for display in databases or data networks (e.g. the Internet), or for print or download to stationary or portable devices. This includes interactive and multimedia use as well as posting the Article in full or in part on social media, and the right to alter the Article to the extent necessary for such use. Author(s) grant to Licensee the right to re-license Article metadata without restriction, including but not limited to author name, title, abstract, citation, references, keywords and any additional information as determined by Licensee.

Copyright

Ownership of copyright in the Article shall vest in the Author(s). When reproducing the Article or extracts from it, the Author(s) acknowledge and reference first publication in the Journal.

2.3. hsp-90 and *unc-45* depletion induce characteristic transcriptional signatures in coexpression cliques of *C. elegans*

Published in Scientific Reports, 2021 Jun 18; 11: 12852. doi: 10.1038/s41598-021-91690-6

Published by Lukas Schmauder and Klaus Richter[2]

PhD candidate

[2] corresponding author

2.3.1. Summary

During their development, nematodes progress through several larval stages, which can be arrested at certain steps through specific interference with the transcriptome. HSP-90 performs vital roles in a vast majority of proteostatic processes in *C. elegans*, while its co-chaperone UNC-45 participates in the muscle-specific functions. The depletion of both proteins leads to severe phenotypes, like sterility and paralysis, and it is possible, that both influence common pathways.

To see, whether this is case or not, a genome-wide coexpression clique map for the nematode *C. elegans* was created. Each of the 22,620 genes was assigned to exactly one clique and every gene was grouped into a coexpression clique. This resulted in a total of 307 coexpression cliques, which were visualized to represent the entire coexpression clique map for *C. elegans*. GO-term, phenotype and tissue enrichment analysis were employed to test whether the cliques resemble gene groups sharing a high level of functional similarity.

To see whether HSP-90 and UNC-45 influence common pathways in *C. elegans*, nematodes were treated with RNAi against *hsp-90* or *unc-45* respectively, and the depletion of both proteins was analyzed by the here described microarray analysis.

Overall, this allowed for the visualization and analysis of functional gene groups. Upregulated cliques contained “structural constituent of cuticle”, “response to unfolded protein”, “immune system response” and “cuticle development”. Downregulated cliques,

on the other hand, represent “embryo development”, “reproduction” and other many cliques implying stalled gonad development.
Next the transcriptional response in *unc-45* RNAi-treated nematodes was investigated with the same approach. The genome-wide coexpression clique approach yielded specific and significantly altered coexpression cliques. Upregulated cliques contained “produce cuticle collagens”, “linker cell movement” and “induction of heat response”, which is also reinforced by induction of heat-shock proteins, including *hsp-16.2* and *F44E5.4*. Interestingly, the depletion of HSP-90 also leads to a higher expression of *daf-16* target genes. In contrast, downregulated cliques contained “embryo development”, “cell membrane biogenesis”, “L1 larval development”, “linker-cell migration variant” and “spermatogenesis variant”, resulting in a stalled development of embryos, sperm, and vulva.
To understand, if these observed expression changes of *hsp-90* and *unc-45* RNAi are specific for one developmental transition at the time of arrest, a timeline representing the development of *C. elegans*, ranging from embryo to late adult and based on experimental microarray datasets retrieved from the GEO repository, was generated, and compared to the coexpression clique maps in HSP-90 and UNC-45 depleted nematodes. Here *hsp-90* RNAi arrested nematodes compared to the L4 state (both L4 and L4-letharghus), therefore implying that the chronological timing of events during development is misaligned when HSP-90 is depleted. For UNC-45 depleted animals on the other hand, a drop in the expression of normally upregulated genes between L4 and young adults was observed, thereby implying that a developmental delay occurs at a young adult stage.

These findings demonstrate the potential of the here developed coexpression analysis and could therefore provide a valuable tool in understanding concerted responses genome-wide level in *C. elegans*.

2.3.2. Contribution of the PhD candidate

Lukas Schmauder and Klaus Richter designed the experiments. Lukas Schmauder performed the experiments. Lukas Schmauder and Klaus Richter analyzed the data and wrote the manuscript.

2.3.3. Manuscript

scientific reports

OPEN

hsp-90 and *unc-45* depletion induce characteristic transcriptional signatures in coexpression cliques of *C. elegans*

Lukas Schmauder & Klaus Richter✉

Nematode development is characterized by progression through several larval stages. Thousands of genes were found in large scale RNAi-experiments to block this development at certain steps, two of which target the molecular chaperone HSP-90 and its cofactor UNC-45. Aiming to define the cause of arrest, we here investigate the status of nematodes after treatment with RNAi against *hsp-90* and *unc-45* by employing an in-depth transcriptional analysis of the arrested larvae. To identify misregulated transcriptional units, we calculate and validate genome-wide coexpression cliques covering the entire nematode genome. We define 307 coexpression cliques and more than half of these can be related to organismal functions by GO-term enrichment, phenotype enrichment or tissue enrichment analysis. Importantly, *hsp-90* and *unc-45* RNAi induce or repress many of these cliques in a coordinated manner, and then several specifically regulated cliques are observed. To map the developmental state of the arrested nematodes we define the expression behaviour of each of the cliques during development from embryo to adult nematode. *hsp-90* RNAi can be seen to arrest development close to the L4 larval stage with further deviations in *daf-16* regulated genes. *unc-45* RNAi instead leads to arrested development at young adult stage prior to the programmatic downregulation of sperm-cell specific genes. In both cases processes can be defined to be misregulated upon depletion of the respective chaperone. With most of the defined gene cliques showing concerted behaviour at some stage of development from embryo to late adult, the "clique map" together with the clique-specific GO-terms, tissue and phenotype assignments will be a valuable tool in understanding concerted responses on the genome-wide level in *Caenorhabditis elegans*.

Nematode-development is a highly complex process that is defined by temporal and spatial events in different tissues and cell types. Therefore simultaneous events are occurring in this process with chronological timing to enable the highly reproducible development program.

HSP-90 (DAF-21) is a molecular chaperone, crucial for the development of vulva, gonads and oocyte maturation as well as ensuring longevity of *C. elegans*[1–3]. It is an indispensable protein, activating and regulating many clients, for example protein kinases, and transcription factors, such as steroid receptors[4–6]. Inhibition of HSP-90, by either RNAi or specific compounds, therefore has the potential to interfere with several pathways. RNAi arrests the nematode development and reduces motility in later larval stages[7,8]. Prominent responses induced after *hsp-90*/*daf-21* RNAi include the heat-shock response, which is known to be suppressed by HSP-90 in most organisms[1,9,10]. Other affected responses are potentially regulated in a more organism-specific manner, like the innate immune response, which is coupled to the heat-shock response in nematodes[11,12]. Interestingly, both of these responses are also dependent on the developmental state of the nematode, with the heat-shock response being barely inducible in early larvae and also in adult aging nematodes[11]. The reason for these correlations is unclear, but it could be supported by assigning genes clearly to individual responses, so that the common principles and regulatory patterns become obvious.

The HSP-90 cofactor UNC-45 participates in the muscle-specific functions of HSP-90. Invertebrates possess a single *unc-45* gene, which is expressed in muscle cells, where UNC-45 performs HSP-90-dependet folding of the myosin motor domain. It further is expressed in non-muscle tissues of early embryos[13–15]. Depletion of the

Center for integrated protein research at the Department of Chemistry, Technische Universität München, Lichtenbergstr. 4, 85748 Garching, Germany. ✉email: klaus.richter@richterlab.de

HSP-90-cofactor UNC-45 leads to rather specific morphological changes, like paralysis due to muscle cell defects and sterility in *C. elegans*[7].

To see, whether these interacting factors influence common pathways, we compare the transcriptional response to depletion of these two proteins by microarray analysis. Microarrays are high-throuhgput analyses yielding a snapshot of the expression status of each represented gene[16]. For *C. elegans* a wealth of data exists, which link different sample conditions to the induction of certain marker genes. Here, as performed before for yeast[17], we derive and validate genome-wide coexpression cliques and use statistical analyses to define the cliques responding to *hsp-90* and *unc-45* RNAi treatment.

Material and methods

Clustering of genes and coexpression clique separation. Construction of the genome-wide coexpression "clique map" for the nematode GPL200 platform was performed as a stepwise procedure as described for the GPL2529 platform of yeast before[17]. In short, all available microarray datasets for the GPL200 platform (Affymetrix C. elegans Genome Array) were obtained from the GEO repository[18]. This included 2243 individual microarray experiments (Supplemental Table 1). These were normalized against each other with the software RMAexpress (Bolstad, 2014; http://rmaexpress.bmbolstad.com/[19]). Based on these normalized values, Pearson's correlation coefficients were obtained for each probe-probe pair of the 22,620 probes represented on this array type. The resulting list of correlation coefficients was then ranked to generate the ranked coexpression database with information on each probe represented on the GPL200 platform. The probes were then translated from ProbeSetIDs to the given *C. elegans* gene names. Genes, which were represented by more than one ProbeSetID on this array type, which is the case for 8052 ProbeSets, were specifically labelled to allow distinguishing these ProbeSetIDs in later evaluations. Confirming the quality of the ranked lists, in many cases the top coregulated ProbeSets are two ProbeSets reporting on the same gene (data not shown).

The database was then used to generate a network from these ranked lists by connecting the Top11 genes of each list and collecting these connections for all 22,620 genes employing the algorithm accessible on the webserver clusterEX.de[20]. In short, 121 connections were generated from the Top11 genes and added to an extensive list collecting all these pairwise interactions, thereby generating a network. The final network contained more than 600,000 unique gene–gene connections from about 2,700,000 gene–gene correlations. Thus on average a connection was obtained 4.5 times, leading to a network density almost on par with that of our previously generated network for yeast[17]. This genome-wide nematode gene network was then used to extract the individual cliques by isolating high density areas in an automated fashion from the network as described before[17]. Altogether 307 cliques were obtained, with the largest clique containing 1327 genes and the smallest clique containing 5 genes. The nematode analysis methods are added to the webserver functionality.

GO-term, phenotype and tissue enrichment. GO-term enrichment was analysed to test, whether some of the 307 aforementioned cliques enrich genes with functional similarity. To this end also published information from phenotype and tissue enrichment studies was used. As such the associations between genes and GO-terms were obtained from the "go_dictionary.csv" table available from https://github.com/dangeles/TissueEnrichmentAnalysis[21]. For phenotype enrichment the table "phenotype_ontology.csv" was employed (PEA[22]) and for tissue enrichment the tissue sets designated as "genesets_golden" were utilized. In all cases the calculation of the enrichment was performed as described[17] (Supplemental Table 2). 20 randomly scrambled clique sets were generated to determine, whether enrichment is considered relevant up to p-values of 1e-3, 1e-4 or beyond 1e-5.

Gene-expression changes after RNAi against *hsp-90* and *unc-45*. RNAi was used to deplete nematodes of *hsp-90* or *unc-45* mRNA and to induce the growth arrest and the transcriptomic responses of the nematodes. RNAi-treated nematodes were washed off the plates and were shock frozen immediately. Microarray experiments were performed at the Zentrum für Fluoreszente Proteinanalytik in Regensburg. To study the response to *hsp-90* RNAi or *unc-45* RNAi we analysed independent biological replicates. In these experiments, RNAi did not always yield the same level of growth arrest in the case of *hsp-90*, where the first microarray experiment produced a weaker response. We used each experiment sample/control-pair to assign all its differential expression values to the coexpression cliques and analysed those in respect to significant induction or repression. As the RNAi experiments were analysed on the more rarely employed GPL19230 Affymetrix platform (Affymetrix C. elegans Gene 1.0 ST Array), we bridged the cliques obtained from GPL200 ProbeSets to the GPL19230 ProbeSets. This bridging was performed by employing the given gene names without the ProbeSet-specific indexing. If a gene was represented by more than one ProbeSet in the cliques, then each of those instances was given the value determined from the GPL19230 expression data. If on the other hand, only one GPL200-derived ProbeSet was present in the cliques and several ProbeSets for this gene are recoded on the GPL19230 arrays, then the GPL19230-values were averaged and this value was used to color the clique map and to derive the statistical parameters for the clique. If the same gene contained two different probes on both platforms, then the averaged GPL19230-value was used in both occurences in the clique map. 1603 ProbeSets of the "clique map" did not receive data from GPL19230 this way and had to be omitted in the analysis. Despite these bridging needs between the platforms, significant changes in many cliques can be detected in each analysed RNAi experiment. The observed experiments were also analysed with the Transcriptome Analysis Console (TAC, Thermo Fisher Scientific) as a state-of-art method for analysis of microarray data.

Statistical analysis employing the clique map was done as described before[17]. In short, color coding of the clique set figures was done by determining the differential values for each gene and then assigning discrete values between −4 and +4 for the transcriptional changes of log2 < −1 to log2 > +1. For each discrete value a red tone

or blue tone was defined in Cytoscape (https://cytoscape.org/)[23]. In cases where responses were weak, like both *unc-45* experiments, the scale was adjusted to reach from log2 < −0.25 to log2 > +0.25. This analysis leads to information on most cliques as to whether they are induced or repressed with statistical significance as described before[17]. This method to evaluate nematode array data will be implemented for public use in the clusterEX.de webserver, which currently has this functionality only for yeast arrays.

Correlation analysis between different samples was made by plotting the cliques' expression values against each other and obtaining the coefficient of determination R^2 for the regression line. If R^2 was closer to 1, the correlation between the two sets was considered to be better. These results were compared to correlations on the gene level in cases where identical array types were utilized.

Analysis of microarray data on development. To define moments of clique relevance during development, time points from developmental series were used to determine a transcriptional status for each clique in the map. In many cases, cliques react to developmental steps as concerted units resulting in a non-random distribution of up- and downregulated hits throughout the 307 cliques. To cover several larval states, three published GPL200 series were obtained from the GEO repository. These represent a time course of early development with data from embryo, L1 and L4 larvae (GSE6547[24]) and a time course describing the aging process with time points at L4 larvae, and adults at day6 and day15 of development (GSE21784[25]). Lastly, a time-course was included describing different stages of larval development, composed of L3, L3-lethargus, L4, L4-lethargus and young adult (GSE46291[26]). Expression values were obtained from the normalized data table containing all public GPL200 experiments (see above).

Results

A genome-wide coexpression clique map for the nematode *C. elegans*. To obtain transcriptional units influenced by *hsp-90* and *unc-45* RNAi-treated nematodes, we first generated gene cliques that are coregulated in *C. elegans*, in which each of the 22,620 genes is assigned to exactly one clique. We had used the same procedure before to generate a coexpression clique map for *S. cerevisiae*[17]. Based on the same stepwise procedure, we grouped every gene reported on standard microarrays of the GPL200 platform into one coexpression clique of at least five genes. The procedure resulted in 307 coexpression cliques, which were visualized in Cytoscape to generate the "coexpression clique map" for *C. elegans*. We set out to test, whether these 307 coexpression cliques are gene groups with a high level of functional similarity, as it was observed for the yeast clique map before[17]. Therefore, we investigated all cliques by GO-term enrichment analysis. 220 of the 307 cliques show a GO-term enrichment with a p-value lower than 1e−3, 172 showed less than 1e−4, and 148 of the 307 cliques showed p-values of less than 1e−5 (Best results in Table 1). This is far better than 307 random cliques, which yielded these p-values 18 times, 2 times and zero times. We also found significant enrichments employing phenotype enrichment analysis (PEA[22]) and tissue enrichment analysis (TEA[21]) with 145, 106 and 81 cliques being enriched for the same phenotype (20, 3 and 0 times in random cliques) and 45, 37 or 29 cliques being enriched for tissue-specific expression in the three p-value categories (0, 0, and 0 times in random cliques). The values also are far better than cliques composed of random genes. In this way, roughly two thirds of the 307 coexpression cliques were assigned either a function, a related phenotype or a tissue-specific expression with acceptable significance criteria of below 1e−4 (Table 1).

***hsp-90* RNAi affects embryo development and induces stress responses.** Having confirmed that the "clique map" of coexpressed genes also holds information on functional, phenotypic and tissue-specific signatures, we set out to investigating the transcriptional response of *hsp-90* RNAi-treated nematodes. We previously had analysed these microarray data based on the Top250 differential regulated genes obtained from three experiments[11]. *hsp-90* depleted nematodes showed sterility, incomplete development of gonad arms and the formation of endomitotic oocytes[7,27]. Development is mostly blocked at a later larval stage. TAC analysis revealed many genes with substantially different expression levels and showed the strongest response in the experiment 1 (P152), while the experiment 2 (A966) and 3 (P062) showed a weaker response (Fig. 1a). Gene expression changes had implied the induction of the heat-shock response and the innate immune response in analyses before[11], but due to the focus on only 500 of the 22,620 genes measured with this array type, information from the many weaker affected genes could not be considered in this study[11].

The genome-wide gene expression cliques as defined here, instead allow visualization and analysis of all values. Significance analysis showed enrichment of up- and downregulation in many cliques for experiment 1 (Fig. 1b), but also for the other experiments 2 and 3 (Supplemental Fig. 1b and c). Indeed almost half of the cliques respond to the RNAi-treatment with a concerted response of their genes (Best cliques in Table 2). We first determined the upregulated cliques: these contain the clique col-138-col-49, which is holding genes related to the "structural constituent of cuticle" and the clique abu-7-abu-8_22491 related to the "response to unfolded protein". The largest upregulated clique, containing 209 genes, is mlt-9_22518-F33D4.6_14044 ("cuticle development" with phenotype of "molt variant" and localized in the "embryo hypodermis") and other cliques related to cuticle formation, including R12E2.14_75-R12E2.15, col-117-col-167_1015, col-146-col-133, col-128-cdh-10_9234 (enriched in "peptidase activity") and sqt-2-dpy-9. Cliques which are strongly upregulated also in experiment 2, include the cliques related to the "immune system response" C10C5.2-Y58A7A.3 and K08D10.9-F46A8.1. Based on the assignment of GO-terms, phenotypes and tissues, the largest and strongest downregulated cliques (Table 2) represent "embryo development" (T22D1.5-inx-14, enriched phenotype of "aneuploidy" and localized in "embryonic germline precursors"), "embryo development" (T24D1.3-egg-1, enriched phenotype of "polar body defective early embryo") and "reproduction" (puf-3-oma-2_18268, enriched phenotype "meiotic chromosome segregation variant" localized in the "germline_precursors") among many other cliques hinting at the stalled

Clusternumber	Cluster name	Clique position	Best GO-term	log10(pvalue)_GO	Enrichment-Fold_GO	Best PEA-Term	log10(pvalue)_PEA	Enrichment-Fold_PEA	Best TEA-Term	log10(pvalue)_TEA	Enrichment-Fold_TEA
80	rps-14_21270-rps-11_20714	R4 C17	Structural constituent of ribosome GO:0003735	189.66	83.29	Pleiotropic defects severe early emb WBPheno-type:0,000,270	120.69	43.09	WBPaper00026980_intestine_enriched_WBbt_0005772_1970	1.44	1.28
211	srj-42-srw-113	R1 C1	Sensory perception GO:0007600	143.77	6.31	Dauer metabolism variant WBPheno-type:0,001,547	10.86	2.84	WBPaper00040420_FLP_enriched_WBbt_0006828_288	0.00	0.46
282	srj-21-srh-32	R1 C3	Intrinsic component of membrane GO:0031224	128.75	2.29	Dauer metabolism variant WBPheno-type:0,001,547	7.14	3.04	WBPaper00040420_FLP_enriched_WBbt_0006828_288	0.00	0.37
187	F45H10.2-R53.4_21676	R3 C4	Organelle Inner membrane GO:0019866	74.24	34.23	Avoids bacterial lawn WBPheno-type:0,000,402	27.00	6.57	WBPaper00026980_intestine_enriched_WBbt_0005772_1970	3.37	1.50
93	flp-5-F17C11.2	R4 C4	Neuropeptide signaling pathway GO:0007218	56.65	67.09	Sinusoidal movement variant WBPheno-type:0,004,018	22.79	11.85	WBPaper00037950_all-neurons_larva_enriched_WBbt_0003679_1013	22.28	3.93
90	dkr-1-T09B9.3	R1 C5	Intrinsic component of membrane GO:0031224	52.94	1.97	Sinusoidal movement variant WBPheno-type:0,004,018	8.60	3.85	WBPaper00037950_all-neurons_larva_enriched_WBbt_0003679_1013	53.78	4.32
42	rab-28-Jbts-14_9542	R3 C5	Cell projection assembly GO:0030031	45.54	56.43	Amphid phasmid sensillum morphology variant WBPheno-type:0,001,527	16.40	17.48	WBPaper00037950_BAG-neuron_embryo_enriched_WBbt_0006825_454	42.10	7.48
203	sre-33-ZK1025.1_8337	R1 C2	Sensory perception GO:0007600	45.42	4.04	Dauer metabolism variant WBPheno-type:0,001,547	6.13	2.24	WBPaper00037950_coelomocytes_larva_enriched_WBbt_0005751_229	0.02	0.64
84	col-84-col-45	R9 C17	Collagen trimer GO:0005581	44.38	77.74	Dumpy WBPhenotype:0,000,583	3.04	8.11	WBPaper00040420_FLP_enriched_WBbt_0006828_288	0.00	0.20
41	col-117-col-167_1015	R9 C25	Structural constituent of cuticle GO:0042302	39.93	83.10	Dumpy WBPhenotype:0,000,583	5.47	7.68	WBPaper00037950_germline-precursors_embryo_enriched_WBbt_0006849_974	0.00	0.33
233	his-46_959-his-64	R10 C26	DNA packaging complex GO:0044815	39.57	191.32	Sister chromatid segregation defective early emb WBPheno-type:0,000,772	26.48	94.19	WBPaper00037950_germline-precursors_embryo_enriched_WBbt_0006849_974	0.00	0.07
215	col-138-col-49	R9 C23	Structural constituent of cuticle GO:0042302	35.30	87.06	Blistered WBPhenotype:0,000,025	5.77	41.59	WBPaper00037950_coelomocytes_larva_enriched_WBbt_0005751_229	0.07	0.60
80	rps-14_21270-rps-11_20714	R4 C17	Structural constituent of ribosome GO:0003735	189.66	83.29	Pleiotropic defects severe early emb WBPheno-type:0,000,270	120.69	43.09	WBPaper00026980_intestine_enriched_WBbt_0005772_1970	1.44	1.28
31	pbs-3_18439-rpn-5	R3 C7	Modification-dependent macromolecule catabolic process GO:0043632	23.08	13.30	Meiosis defective early emb WBPheno-type:0,001,041	32.03	23.37	WBPaper00031003_24hr_muscle_enriched_WBbt_0003675_918	2.78	1.65
187	F45H10.2-R53.4_21676	R3 C4	Organelle inner membrane GO:0019866	74.24	34.23	Avoids bacterial lawn WBPheno-type:0,000,402	27.00	6.57	WBPaper00026980_intestine_enriched_WBbt_0005772_1970	3.37	1.50
233	his-46_959-his-64	R10 C26	DNA packaging complex GO:0044815	39.57	191.32	Sister chromatid segregation defective early emb WBPheno-type:0,000,772	26.48	94.19	WBPaper00037950_germline-precursors_embryo_enriched_WBbt_0006849_974	0.00	0.07
93	flp-5-F17C11.2	R4 C4	Neuropeptide signaling pathway GO:0007218	56.65	67.09	Sinusoidal movement variant WBPheno-type:0,004,018	22.79	11.85	WBPaper00037950_all-neurons_larva_enriched_WBbt_0003679_1013	22.28	3.93
2	rps-5_2365-rpl-15_1655	R10 C23	Structural constituent of ribosome GO:0003735	24.02	68.88	Pleiotropic defects severe early emb WBPheno-type:0,000,270	19.08	40.82	WBPaper00037950_PVD-OLL-neurons_larva_enriched_WBbt_0006831_878	0.00	0.23
143	his-20_965-his-4	R11 C22	DNA packaging complex GO:0044815	30.10	191.32	Sister chromatid segregation defective early emb WBPheno-type:0,000,772	18.37	87.98	WBPaper00024505_pharyngeal_enriched_WBbt_0003681_329	0.00	0.18

Continued

Clusternumber	Cluster name	Clique position	Best GO-term	log10(pvalue)_GO	Enrichment-Fold_GO	Best PEA-Term	log10(pvalue)_PEA	Enrichment-Fold_PEA	Best TEA-Term	log10(pvalue)_TEA	Enrichment-Fold_TEA
96	mup-2-unc-87_284	R3 C13	Myofibril GO:0030016	31.32	27.72	Muscle system morphology variant WBPhenotype:0,000,603	17.34	8.57	WBPaper00031003_0hr_muscle_enriched_WBbt_0003675_761	20.71	3.64
218	H28G03.5_1027-H28G03.5_1042	R11 C24	Cell recognition GO:0008037	18.80	92.91	Axon fasciculation variant WBPhenotype:0,000,632	17.15	63.29	WBPaper00045521_Spermatogenic_WBbt_0005784_2743	0.00	0.33
42	rab-28-jbts-14_9542	R3 C5	Cell projection assembly GO:0030031	45.54	56.43	Amphid phasmid sensillum morphology variant WBPhenotype:0,001,527	16.40	17.48	WBPaper00037950_BAG-neuron_embryo_enriched_WBbt_0006825_454	42.10	7.48
234	pcn-1-cyb-3_17196	R7 C12	DNA replication GO:0006260	13.16	29.41	Cytokinesis variant WBPhenotype:0,002,408	16.17	11.19	WBPaper00037950_pharyngeal-muscle_embryo_enriched_WBbt_0005451_598	0.01	0.48
197	unc-11_429-unc-11_430	R12 C11	Phosphatidylinositol binding GO:0035091	15.76	172.19	Mid larval lethal WBPhenotype:0,000,116	15.12	160.50	WBPaper00037950_coelomocytes_embryo_enriched_WBbt_0005751_570	0.09	0.76
1	Y40H4A.2-ZK1053.2	R1 C6	Phosphorus metabolic process GO:0006793	17.12	3.03	Spermatogenesis variant WBPhenotype:0,000,670	1.48	4.25	WBPaper00045521_Spermatogenic_WBbt_0005784_2743	165.27	4.57
20	T22D1.5-inx-14	R2 C1	Embryo development GO:0009790	13.09	1.97	Aneuploidy WBPhenotype:0,001,882	11.50	6.39	WBPaper00037950_germline-precursors_embryo_enriched_WBbt_0006849_974	73.49	5.82
273	C01G10.14-dct-9_3227	R2 C3	Regulation of cell shape GO:0008360	20.29	18.38	Spermatogenesis variant WBPhenotype:0,000,670	2.62	7.10	WBPaper00045521_Spermatogenic_WBbt_0005784_2743	71.95	3.62
111	mlt-9_22518-F33D4.6_14044	R2 C6	Cuticle development GO:0042335	16.79	11.64	Molt variant WBPhenotype:0,002,041	12.53	5.66	WBPaper00037950_hypodermis_embryo_enriched_WBbt_0005733_734	56.15	6.08
90	dkr-1-T09B9.3	R1 C5	Intrinsic component of membrane GO:0031224	52.94	1.97	Sinusoidal movement variant WBPhenotype:0,004,018	8.60	3.85	WBPaper00037950_all-neurons_larva_enriched_WBbt_0003679_1013	53.78	4.32
42	rab-28-jbts-14_9542	R3 C5	Cell projection assembly GO:0030031	45.54	56.43	Amphid phasmid sensillum morphology variant WBPhenotype:0,001,527	16.40	17.48	WBPaper00037950_BAG-neuron_embryo_enriched_WBbt_0006825_454	42.10	7.48
213	xbx-3-DH11.5_20397	R1 C12	Signaling GO:0023052	15.19	2.38	Backward point velocity increased WBPhenotype:0,002,325	7.12	8.29	WBPaper00037950_all-neurons_larva_enriched_WBbt_0003679_1013	41.49	4.53
155	F42A9.7-T22B3.3	R3 C11	Regulation of cell shape GO:0008360	9.67	17.73	Dauer metabolism variant WBPhenotype:0,001,547	1.51	2.28	WBPaper00045521_Spermatogenic_WBbt_0005784_2743	25.38	2.62
83	sol-1-jnk-1_18695	R1 C9	Nervous system development GO:0007399	21.52	4.87	Synapse morphology variant WBPhenotype:0,000,616	10.59	8.04	WBPaper00031532_Larva_Pan_Neuronal_Enriched_WBbt_0003679_1603	25.10	2.45
93	flp-5-F17C11.2	R4 C4	Neuropeptide signaling pathway GO:0007218	56.65	67.09	Sinusoidal movement variant WBPhenotype:0,004,018	22.79	11.85	WBPaper00037950_all-neurons_larva_enriched_WBbt_0003679_1013	22.28	3.93
96	mup-2-unc-87_284	R3 C13	Myofibril GO:0030016	31.32	27.72	Muscle system morphology variant WBPhenotype:0,000,603	17.34	8.57	WBPaper00031003_0hr_muscle_enriched_WBbt_0003675_761	20.71	3.64
34	dhs-28_22199-acs-14	R4 C9	Oxoacid metabolic process GO:0043436	14.25	9.18	Lipid metabolism variant WBPhenotype:0,000,725	4.43	3.34	WBPaper00037950_intestine_embryo_enriched_WBbt_0005772_886	20.41	3.78

Table 1. Most relevant coexpression cliques of the clique map, their size and position, GO-term assignment, phenotype enrichment and tissue enrichment.

gonad development in agreement with the sterility phenotype observed. Comparing the three experiments a weak correlation can be found between experiment 2 and 1 ($R^2 = 0.148$) on a gene-by-gene level, which is increased, if cliques are compared ($R^2 = 0.307$, Fig. 1c). The same trend can be seen between experiments 3 and 1 correlating with $R^2 = 0.622$ for a gene-to-gene comparison, which increases to $R^2 = 0.764$, if cliques are compared (Fig. 1d). Moreover the significance analysis employing 20 random cliques shows that the most strongly up- and down-regulated cliques also are usually fulfilling the 1e-5 significance criterium in the compared experiments (Fig. 1c and d, colored in red).

Figure 1. *hsp-90* RNAi affects embryo development and induces stress responses. (**a**) Average gene expression difference of the experiments, determined with TAC, compared to the control RNAi. (**b**) Clique map for experiment 1 of *hsp-90* RNAi versus young adult of control RNAi. A more detailed description of the most strongly affected cliques can be found in Table 2 and corresponds to the positions in the clique map. (**c**) Comparison between experiment 1 and 3 on a gene-by-gene basis (left panel) and comparison between experiment 1 and 3 on a clique-by-clique basis (right panel). (**d**) Comparison between experiment 1 and 2 on a gene-by-gene basis (left panel) and comparison between experiment 1 and 2 on a clique-by-clique basis (right panel). The clique maps of experiment 3 and 2 are shown as Supplemental Fig. 1b and c. Cliques colored in red are induced upon RNAi while cliques in blue are repressed. The linear regression function was generated with Microsoft Excel without weighting, a square value of 1 would indicate a perfect correlation between the cliques.

unc-45 RNAi leads to delayed conclusion of sperm and vulva development. We then investigated the RNAi treatment against the HSP-90 cofactor *unc-45* with the same approach. *unc-45* RNAi-treatment leads to developmental disruptions and incomplete fertility at a more adult stage. To see, whether differences in the cliques can be observed we performed two independent RNAi-experiments with subsequent transcriptome analysis on DNA microarrays. Analysis with TAC showed a weaker response compared to the *hsp-90* RNAi in both experiments (Fig. 2a, Supplemental Fig. 2a). This also was evident in the analysis of the 307 expression cliques, where the color scheme had to be adjusted to visualize the concerted reactions (Fig. 2b and Supplemental Fig. 2b). Gene–gene comparisons showed a coefficient of determination of 0.15 between the experiments. When cliques were compared a coefficient of determination of 0.48 was obtained (Fig. 2c), confirming that also very weak responses can yield higher levels of repeatability by comparing matched groups of genes and not individual genes.

Like with *hsp-90* RNAi, specific cliques were found in all experiments to be significantly altered in their expression behavior. Upregulated are a few smaller cliques, like col-117-col-167_1015, msp-63-msp-33 and abu-7-abu-8_22491. These represent decisions to produce cuticle collagens, linker cell movement and induction of a response to heat. This also is reflected by the induction of hsp-16.2-F44E5.4_19238, a small clique containing the heat-shock proteins. This induction of the heat-shock response has been observed for *unc-45* RNAi before[7]. Downregulated cliques represent the large cliques ZK1053.4-C08F1.6 (embryo development), ZC373.2-Y62H9A.6_1596 (cell membrane biogenesis) and sdz-10-fbxb-62 (L1 larval development). The weak differences, while being statistically significant for the described cliques, correlate with the mostly adult state of the nematode after *unc-45* RNAi treatment and the observation that most developmental steps were performed, but the correct embryo development and the development of the vulva structure were affected[7].

A hint towards the lacking germ line development may be derived from the misregulation of the cliques msp-36_msp-63 (linker-cell migration variant), which contains several genes related to sperm development and the downregulation of nspc-1_614-nspc-10_22525 (spermatogenesis variant). Thus, while vulva development and sperm development are stalled, certain features of the regulatory pathways are not deviating from the control nematodes and only later stages of the programmatic decision process show deviations that could explain the mismanaged development in the absence of *unc-45*.

Expression in developmental stages is altered in similarity to the RNAi-induced arrest. Having observed cliques with altered expression, we aimed at understanding, whether these expression changes are specific for one developmental transition occurring at the time point of arrest. We thus generated a time series of development ranging from embryo to late adult and compared the expression of all 307 cliques and in particular of those found relevant for *unc-45* RNAi.

Striking differences were observed, when comparing the stages of each series (Supplemental Fig. 3), while differences between experiments of the same stage were small (Supplemental Figs. 4 and 5). Interestingly, also in these comparisons most of the isolated expression cliques showed coordinated expression differences, and also strong responses could be observed for the later developmental stages (Supplemental Fig. 6). In total more then 80% of the cliques show a statistically significant expression change during the development from embryo to 16 day adult and this also relates to most cliques found affected after *unc-45* RNAi (Fig. 2d, 2 cliques and their development). While only few cliques were affected upon *unc-45* RNAi treatment, *hsp-90* RNAi is expected to yield a much stronger response.

Indeed a drop is observed in the expression of most upregulated cliques between L4 and day6 adult. In these cases the developmental delay may be the reason of the observed higher expression. A opposite pattern is observed for the downregulated gene cliques, with the exception of two cliques, which are not appropriately regulated: T05E12.6_12439-T05E12.6_12396 and gpd-3_977-aldo-1_21168, both of which appear to regulate metabolism.

Expression in developmental stages is altered in similarity to the _hsp-90_ RNAi-induced arrest. We next tested, whether also for the *hsp-90* RNAi-treated nematodes developmental stages can be defined. The complexity of the differential expression between *hsp-90* RNAi arrested nematodes and young adults allow to compare the obtained expression patterns with know patterns from larval development. We thus were interested to see, whether the full extent of the transcriptional changes can be explained by the observed developmental delay. Therefore we utilized publicly available microarray experiments on nematode development to help identify transcriptional units in the clique map that report on comparable steps during

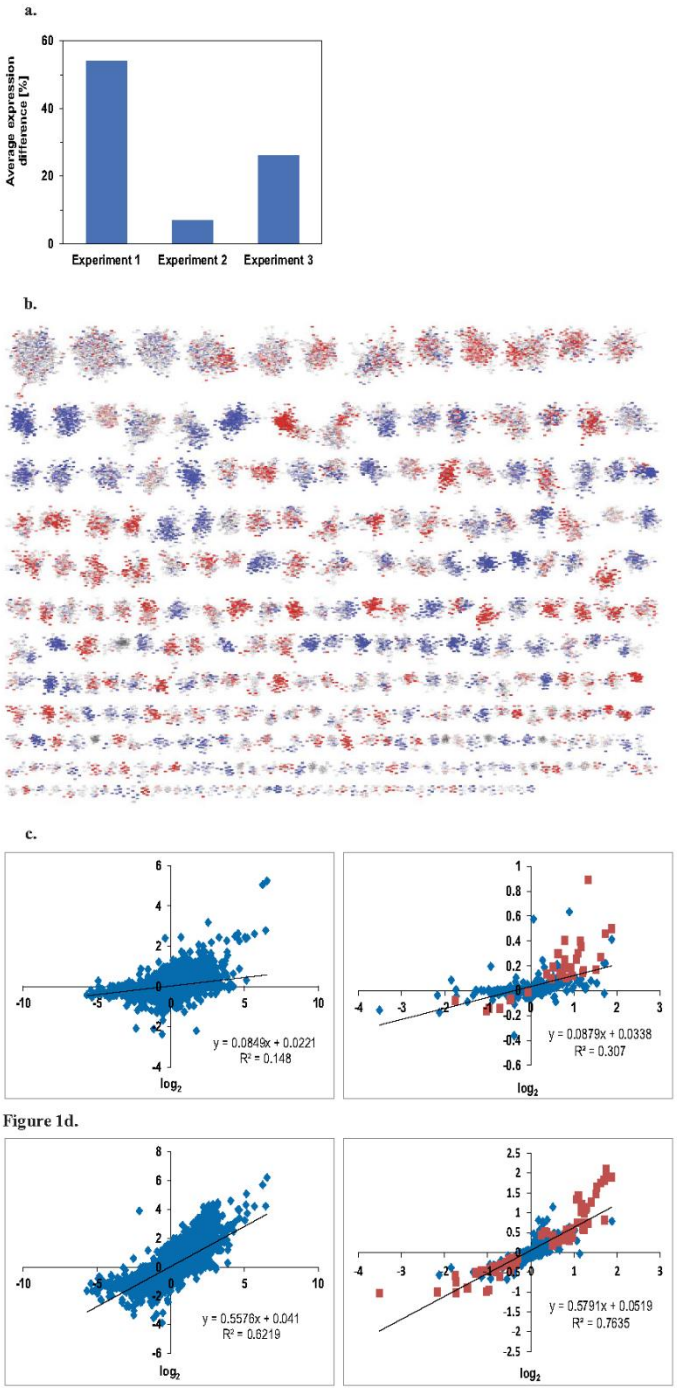
a.
Average expression difference [%]
60
40
20
0
Experiment 1
Experiment 2
Experiment 3
b.
c.
y = 0.0849x + 0.0221
R² = 0.148
log2
y = 0.0879x + 0.0338
R² = 0.307
log2

Figure 1d.

y = 0.5576x + 0.041
R² = 0.6219
log2
y = 0.5791x + 0.0519
R² = 0.7635
log2

Cluster name	Clique position	Best GO-Term	Best PEA-Term	Best TEA-Term	Mean STD	Log10(p) Exp 1	Log10(p) Exp 2	Log10(p) Exp 3
col-138-col-49	R9 C23	Structural constituent of cuticle GO:0042302	Blistered WBPhenotype:0000025	WBPaper00037950_coelomocytes_larva_enriched_WBbt_0005751_229	1.43 ± 0.71	28.5	35.6	70.2
abu-7-abu-8_22491	R8 C26	Response to unfolded protein GO:0006986	Dauer constitutive WBPhenotype:0000012	WBPaper00024505_pharyngeal_enriched_WBbt_0003681_329	1.43 ± 0.66	38.9	38.4	51.4
agmo-1_5527-F53B1.4	R10 C14	Pyridoxal phosphate binding GO:0030170	Molt variant WBPhenotype:0002041	WBPaper00037950_hypodermis_embryo_enriched_WBbt_0005733_734	1.29 ± 0.76	14.4	3.2	48.0
bus-8_3160-K04H4.2_2324	R9 C2	Amino sugar metabolic process GO:0006040	Molt variant WBPhenotype:0002041	WBPaper00024505_pharyngeal_enriched_WBbt_0003681_329	1.25 ± 0.73	30.4	3.5	103.9
R12E2.14_75-R12E2.15	R6 C9	Structural constituent of cuticle GO:0042302	Dumpy WBPhenotype:0,000,583	WBPaper00037950_germline-precursors_embryo_enriched_WBbt_0006849_974	1.22 ± 0.67	51.2	21.3	182.3
mlt-9_22518-F33D4.6_14044	R2 C6	Cuticle development GO:0042335	Molt variant WBPhenotype:0002041	WBPaper00037950_hypodermis_embryo_enriched_WBbt_0005733_734	1.08 ± 0.72	137.7	2.6	133.0
R12A1.3-M195.2	R6 C19	Amino sugar metabolic process GO:0006040	Dauer constitutive WBPhenotype:0000012	WBPaper00024505_pharyngeal_enriched_WBbt_0003681_329	1.05 ± 0.63	42.2	14.3	46.7
hsp-16.2-F44E5.4_19238	R12 C4	Response to heat GO:0009408	cadmium response variant WBPhenotype:0001653	WBPaper00037950_coelomocytes_larva_enriched_WBbt_0005751_229	1.03 ± 0.62	3.6	6.2	1.7
lys-3-tsp-1	R11 C40	Carbohydrate metabolic process GO:0005975	Male nervous system development variant WBPhenotype:0001008	WBPaper00040420_ALM_PLM_enriched_WBbt_0005406_198	0.99 ± 0.25	6.4	28.8	6.0
col-117-col-167_1015	R9 C25	Structural constituent of cuticle GO:0042302	Dumpy WBPhenotype:0000583	WBPaper00037950_germline-precursors_embryo_enriched_WBbt_0006849_974	0.94 ± 0.47	10.6	10.3	20.0
C38C6.3-acdh-6	R6 C14	Intrinsic component of membrane GO:0031224	Intestinal vacuole WBPhenotype:0001428	WBPaper00037950_hypodermis_embryo_enriched_WBbt_0005733_734	0.91 ± 0.59	71.0	1.4	59.3
pqn-54-abu-9	R6 C11	Response to unfolded protein GO:0006986	Shortened life span WBPhenotype:0001171	WBPaper00024505_pharyngeal_enriched_WBbt_0003681_329	0.91 ± 0.4	37.6	43.3	33.7
col-146-col-133	R9 C28	Structural constituent of cuticle GO:0042302	Dumpy WBPhenotype:0000583	WBPaper00037950_coelomocytes_larva_enriched_WBbt_0005751_229	0.89 ± 0.46	10.0	6.5	26.7
C36C5.12-F57G8.7	R11 C9	Negative regulation of proteolysis GO:0045861	Male tail morphology variant WBPhenotype:0000070	WBPaper00037950_coelomocytes_larva_enriched_WBbt_0005751_229	0.83 ± 0.71	13.9	1.3	5.0
col-128-cdh-10_9234	R3 C12	Peptidase activity GO:0008233	Molt variant WBPhenotype:0002041	WBPaper00037950_hypodermis_larva_enriched_WBbt_0005733_1250	0.82 ± 0.56	66.1	0.6	61.0
ptr-23_236-ptr-23_16340	R12 C6	Male sex differentiation GO:0046661	Developmental pigmentation variant WBPhenotype:0001009	WBPaper00037950_hypodermis_embryo_enriched_WBbt_0005733_734	0.79 ± 0.56	6.0	0.2	9.5
C10C5.2-Y58A7A.3	R4 C11	Immune system process GO:0002376	Cadmium response variant WBPhenotype:0001653	WBPaper00037950_coelomocytes_larva_enriched_WBbt_0005751_229	0.77 ± 0.31	36.6	83.0	39.9
sqt-2-dpy-9	R9 C6	Structural constituent of cuticle GO:0042302	Dumpy WBPhenotype:0000583	WBPaper00037950_hypodermis_larva_enriched_WBbt_0005733_1250	0.76 ± 0.48	13.0	1.0	18.9
dos-2-grd-2	R8 C7	Extracellular region GO:0005576	Pericellular component morphology variant WBPhenotype:0000912	WBPaper00037950_hypodermis_embryo_enriched_WBbt_0005733_734	0.75 ± 0.52	15.4	0.3	36.4

Continued

Cluster name	Clique position	Best GO-Term	Best PEA-Term	Best TEA-Term	Mean STD	Log10(p) Exp 1	Log10(p) Exp 2	Log10(p) Exp 3
K08D10.9-F46A8.1	R11 C42	Immune system process GO:0002376	Actin organization biogenesis variant WBPhenotype:0001587	WBPaper00037950_excretory-cell_larva_enriched_WBbt_0005812_528	0.72 ± 0.12	3.7	12.9	2.2
vit-2-vit-4_22519	R12 C22	Extracellular region GO:0005576	Pathogen susceptibility increased WBPhenotype:0001013	WBPaper00037950_pharyngeal-muscle_embryo_enriched_WBbt_0005451_598	− 1.57 ± 1.42	47.9	2.5	5.7
C17E7.4-T06D4.1	R5 C13	ribonucleoprotein granule GO:0035770	P granule defective WBPhenotype:0001301	WBPaper00037950_pharyngeal-muscle_embryo_enriched_WBbt_0005451_598	− 1.07 ± 0.87	168.7	1.2	72.1
171971_x_at-D1054.11_184	R11 C37	Cell GO:0005623	Egg laying defective WBPhenotype:0000006	WBPaper00037950_hypodermis_larva_enriched_WBbt_0005733_1250	− 0.96 ± 0.84	1.4	0.7	0.6
sea-1-R04D3.4	R7 C13	Nucleoside-triphosphatase regulator activity GO:0060589	Embryonic development variant WBPhenotype:0000749	WBPaper00037950_hypodermis_embryo_enriched_WBbt_0005733_734	− 0.93 ± 0.69	39.7	4.0	53.7
T24D1.3-egg-1	R7 C17	Embryo development GO:0009790	Polar body defective early emb WBPhenotype:0001147	WBPaper00037950_GABAergic-motor-neurons_larva_enriched_WBbt_0005190_132	− 0.82 ± 0.72	36.0	0.3	24.0
C46C2.5_15926-W03F11.1	R9 C22	Carbohydrate binding GO:0030246	Apoptosis increased WBPhenotype:0000183	WBPaper00037950_GABAergic-motor-neurons_embryo_enriched_WBbt_0005190_361	− 0.82 ± 0.57	15.7	2.5	13.8
ZC373.2-Y62H9A.6_1596	R3 C18	Flavonoid metabolic process GO:0009812	Cell membrane organization biogenesis variant WBPhenotype:0001982	WBPaper00037950_dopaminergic-neurons_larva_enriched_WBbt_0006746_1230	− 0.8 ± 0.7	53.5	6.0	32.5
ZK1053.4-C08F1.6	R4 C16	Embryo development GO:0009790	Embryonic development variant WBPhenotype:0000749	WBPaper00037950_hypodermis_embryo_enriched_WBbt_0005733_734	− 0.73 ± 0.4	70.9	12.9	40.5
T05E12.6_12439-T05E12.6_12396	R10 C3	Lipid catabolic process GO:0016042	Transgene expression increased WBPhenotype:0001236	WBPaper00037950_pharyngeal-muscle_embryo_enriched_WBbt_0005451_598	− 0.72 ± 0.82	28.7	2.8	3.3
fbxc-28-sdz-28	R7 C8	Modification-dependent macromolecule catabolic process GO:0043632	L1 larval development variant WBPhenotype:0000751	WBPaper00037950_hypodermis_embryo_enriched_WBbt_0005733_734	− 0.69 ± 0.39	26.3	23.5	41.6
K09D9.12-T10C6.10	R10 C7	Protein polyubiquitination GO:0000209	Fat content reduced WBPhenotype:0001183	WBPaper00037950_germline-precursors_embryo_enriched_WBbt_0006849_974	− 0.62 ± 0.54	7.6	1.2	3.8
puf-3-oma-2_18268	R5 C14	Reproduction GO:0000003	Meiotic chromosome segregation variant WBPhenotype:0001499	WBPaper00037950_germline-precursors_embryo_enriched_WBbt_0006849_974	− 0.6 ± 0.53	24.0	0.8	12.3
172276_x_at-Y116F11B.10_466	R12 C20	Chromosome segregation GO:0007059	Rachis wide WBPhenotype:0001943	WBPaper00036375_enriched_in_PVD_OLL_WBbt_0006831_2180	− 0.59 ± 0.47	1.2	0.2	1.0
C41G7.3_2766-ani-2_2946	R8 C2	Multi-organism reproductive process GO:0044703	Cytokinesis variant WBPhenotype:0002408	WBPaper00037950_germline-precursors_embryo_enriched_WBbt_0006849_974	− 0.59 ± 0.51	26.0	0.8	9.0
T22D1.5-inx-14	R2 C1	Embryo development GO:0009790	Aneuploidy WBPhenotype:0001882	WBPaper00037950_germline-precursors_embryo_enriched_WBbt_0006849_974	− 0.54 ± 0.48	122.7	2.0	60.1
let-99_22121-B0238.9_11154	R6 C21	Organelle fission GO:0048285	Embryonic development variant WBPhenotype:0000749	WBPaper00037950_germline-precursors_embryo_enriched_WBbt_0006849_974	− 0.52 ± 0.44	16.6	0.2	15.4
Y116A8C.19-F38C2.7	R10 C25	Poly(A) RNA binding GO:0044822	Dauer metabolism variant WBPhenotype:0001547	WBPaper00040420_FLP_enriched_WBbt_0006828_288	− 0.49 ± 0.25	4.8	5.5	4.5

Continued

Cluster name	Clique position	Best GO-Term	Best PEA-Term	Best TEA-Term	Mean STD	Log10(p) Exp 1	Log10(p) Exp 2	Log10(p) Exp 3
daf-18_2911-ced-2_4092	R8 C23	Nuclear transport GO:0051169	Cell death variant WBPhenotype:0000729	WBPaper00037950_GABAergic-motor-neurons_larva_enriched_WBbt_0005190_132	− 0.48 ± 0.4	6.9	0.6	10.0
pcn-1-cyb-3_17196	R7 C12	DNA replication GO:0006260	Cytokinesis variant WBPhenotype:0002408	WBPaper00037950_pharyngeal-muscle_embryo_enriched_WBbt_0005451_598	− 0.47 ± 0.38	17.2	1.5	5.3
C10C5.3-C10C5.5	R12 C40	Oxoacid metabolic process GO:0043436	Dauer constitutive WBPhenotype:0000012	WBPaper00037950_pharyngeal-muscle_embryo_enriched_WBbt_0005451_598	− 0.47 ± 0.48	2.6	5.1	2.2

Table 2. Most strongly affected cliques by *hsp-90* RNAi and their characteristics. Clique positions (letter = row, number = position from left to right) correspond to the clique map shown in Fig. 1b.

development. We employed microarray data from three experimental series (Table 4) and initially compared developmental transitions, showing similarity to the differences we observe in the RNAi-treated nematodes. These comparisons were L3/young adult, L4/young adult and L4let/young adult (Fig. 3a–c) as investigated in GSE46288/GSE46289[28]. Clearly similarities can be observed between the *hsp-90* RNAi treated nematodes and the L4 larvae, when each of them is compared to the young adult control. In fact, most of the cliques correlate in color and correlation analysis shows a coefficient of determination with these data of 0.4046, 0.5913 and 0.5915 (Fig. 3d). Based on these values, *hsp-90* RNAi-arrested nematodes best correspond to a L4-larval like state. Only few clear differences can be observed compared to L4 or L4-lethargus, while several cliques deviate from L3-like state. Judged from the few differences to L4 state, it might be that the chronological timing of the events during development is misaligned in *hsp-90* RNAi-arrested nematodes.

We further investigated, whether the expression behavior matches the known expression behavior during development and aging. To this end the cliques found relevant for *hsp-90* RNAi were investigated throughout development. While the strongly responsive upregulated cliques col-138_col-49, abu-7_abu-8, R12E2.14_75-R12E2.15, col-117_col-167, pqn-54_abu-9, col-146_col-133 already were found in context with the *unc-45* RNAi-arrested state (see Fig. 2d), further cliques are identificed as significantly upregulated in *hsp-90* RNAi treated nematodes (Fig. 3e). As for *unc-45* RNAi before the downregulated cliques vit-2_vit-4, C46C2.5_W03F11, ZC373.2-Y62H9A.6_1596, ZK1053.4-C08F1.6 were identified amid fbxc-28_sdz-28 (see Fig. 2d), plus additional ones not found significant before (Fig. 3e). Interestingly, in few cases, the directionality of the RNAi-induced response does not correlate with the expected behaviour during the arrested L4 state. This is evident for the cliques C17H1.6-C17H1.13, C32F10.4-D1086.2 and C10C5.2-Y58A7A.3.

***daf-16* target genes deviate from the developmental program in *hsp-90* RNAi.** We finally aimed at understanding the few cliques that deviate from the developmental progression and the explanation based on developmental delays. To this end we used the information gained previously that a fraction of the misregulated genes are *daf-16* targets[11]. We tested, which of the cliques from the clique map contain *daf-16* targets and then tested, whether those are regulated in coordance with developmental progress. Indeed, targets upregulated and suppressed by DAF-16 are enriched in several cliques (the 15 most prominent shown in Table 5, more information in Fig. 4a and b). Comparing the clusters identified in Eckl et al. (2017), with the current cliques we also observe a clear enrichment among several of the 307 cliques (Table 5). As spectulated in Eckl et al., among the cluster "Up1" there are many genes, which are regulated by DAF-16, while cluster "Up2" does not enrich *daf*-16 targets (Table 5). Mapping all cliques onto the network developed in Eckl et al. the enrichment of these cliques in certain parts of the network becomes evident. For the downregulated genes, also DAF-16 enriching cliques are among those containing these genes[11]. Therefore, especially among the upregulated genes, cliques are present, which contain an elevated level of *daf-16* target genes.

Interestingly, these cliques are upregulated despite their developmental program, which aims for downregulation. Thus, the presence of these cliques suggests a simultaneous modification to the dauer-program outside the developmental program after *hsp-90* RNAi induced growth arrest.

Discussion

In this study, we analysed microarray data from *C. elegans* based on preformed coregulated expression cliques. This approach has been applied successfully in the yeast model organism by us[17], but the applicability of this method to multicellular organisms has not been clear. We thus used the algorithms developed for yeast to also generate high quality coexpression cliques from nematode expression data and then validated them by GO-term enrichment, phenotype enrichment and tissue enrichment and by selective clique responses in individual microarray experiments. Based on our data from the developmental process of *C. elegans*, we believe that this analysis method could have broader use in the analysis of gene expression data from nematodes. This is evident from the correlated responses of cliques during nematode developmental transitions.

Recently also a different approach was reported to utilize genome-wide co-expression cliques for *C. elegans*[29]. In contrast to our appraoch, in this study an individual gene could be assigned to multiple cliques (on average 3) and also negative correlation was included. This makes the construction of a static clique map as used by us more difficult, but may include details missed by our approach. Both approaches will have their advantages. In the method described by us, we focus on the strongest connection and blank out those that might be secondary based on numbers, but still achieve very high levels of correlation with GO-terms, phenotypes and tissue specificity for most of the cliques.

One way to use the cliques could be by employing the popular GSEA platform[30], where our cliques can be either used as a single input file covering the whole genome or as part of the global collection of gene sets. Another way to use the cliques can also be via the clusterEX.de webserver that we have set up and will further develop for the purpose of gene expression analysis based on known co-expression relationships. It therefore will be interesting to see, how further useful applications will be developed based on these predefined gene sets.

Integrating *unc-45* into the developmental time line exposes distinct cliques for develeopmental stop. We first analysed *unc-45* depleted nematodes. In these nematodes, the depletion of *unc-45* leads to developmental arrest and paralysis in almost adult animals. Here the comparison with the young adult nematode shows that certain cliques are misregulated and some of those cliques also represent developmental marker cliques as suggested by our evaluation procedure. These marker genes help to map the developmental status of the *unc-45* depleted organisms. Clearly *unc-45* depleted nematodes are close to N2 nematodes in this approach, but defined changes in certain genes help to map the events that did not unfold during development.

To evaluate the disruption of vulva development, we individually tested the genes transcriptionally regulated during this process and their specific regulation (Table 3): *eff-1* (log2(dExp) = 0.185), *egl-18* (− 0.035), *egl-17* (0.000), *lin-3* (− 0.015), *lin-31* (0.00), *lin-39* (0.00), *egl-30* (0.02), *lag-2* (− 0.09), *apx-1* (0.055), *dsl-1* (− 0.085 as part of fbxc-28-sdz-28) and *elt-6* (-0.065), all of which are getting induced during vulva development[31]. In a critical step during vulva development the VPCs express LIN-39, which together with its cofactors CEH-20 and UNC-62, activates the expression of *ref-2*, which inhibits the expression of the fusogen EFF-1[32]). In UNC-45 depleted nematodes, *ref-2* is not yet upregulated compared to mock treated nematodes (− 0.675 and resides in clique cfz-2_18944-cfz-2_2268, which is downregulated twice significantly, but not very strongly) and also *ref-1* is lower expressed in *unc-45* RNAi-treated nematodes (− 0.46, ZK1053.4-C08F1.6), even though *lin-39* is expressed as in the control and *eff-1* is higher expressed (0.185, tnt-4-myo-1_2160), as expected for vulva development[33]. Thus, based on these expression patterns the induction to generate the vulva is not transmitted properly by the anchor cell from the developing gonad. Also *lin-12* (− 0.31, sol-1-jnk-1_18695), *cwn-1* (− 0.26, chd-7_16664-jmjd-3.1) and *vang-1* (− 0.175, nrde-3-tra-4_10484) are downregulated, further implying that central decisions to induce the vulva have not been made yet.

Regarding the germline, *asb-2* is reduced (− 0.21, tars-1-AFFX-r2-3026-5_at) and the nspd-proteins are still upregulated together with msp-proteins (Fig. 2d[34]), implying that sperm development is not completed yet, while the expression of the upstream regulators *spn-4* and *neg-1*[35] is at the same level as in the normally developed adult. Also the regulators of msp-expression *set-17* and *csr-1* are expressed at the level of the control nematodes[36], implying that sperm-development is almost finished[37,38].

Integrating *hsp-90* into the time line data exposes defined clusters for developmental stop. We used this clique map to also analyse the depletion of *hsp-90*. While depletion of *hsp-90* leads to developmental arrest and reduced motility in late larval stages, it also leads to defined transcriptional changes. To analyse the causes, we performed microarray experiments under wildtype conditions and under conditions, where the chaperone is depleted. Based on the clique analysis, it is obvious that certain developmental milestones are not reached yet in the HSP-90 depleted animals. Based on this analysis these nemtodes arrest in a late larval stage with additional misregulation of DAF-16 target genes.

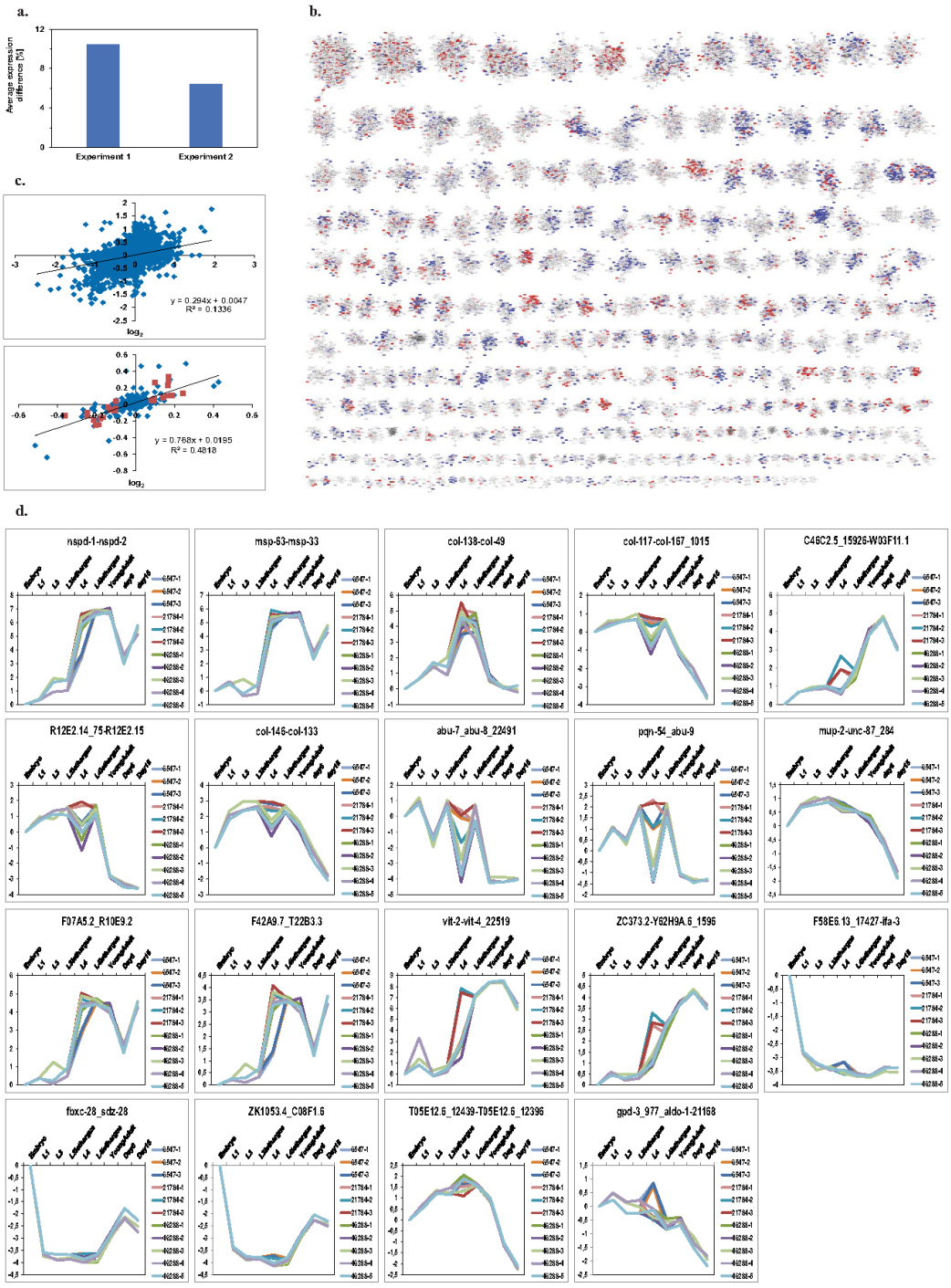
a.
Average expression difference [%]
Experiment 1
Experiment 2
b.
c.
y = 0.294x + 0.0047
R² = 0.1336
log2
y = 0.768x + 0.0195
R² = 0.4818
log2
d.
nspd-1-nspd-2
msp-53-msp-33
col-138-col-49
col-117-col-167_1015
C46C2.5_15926-W03F11.1
R12E2.14_75-R12E2.15
col-146-col-133
abu-7_abu-8_22491
pqn-54_abu-9
mup-2-unc-87_284
F07A5.2_R10E9.2
F42A9.7_T22B3.3
vit-2-vit-4_22519
ZC373.2-Y62H9A.6_1596
F58E6.13_17427-lfa-3
foxc-28_sdz-28
ZK1053.4_C08F1.6
T05E12.6_12439-T05E12.6_12396
gpd-3_977_aldo-1-21168

◂**Figure 2.** *unc-45* RNAi leads to delayed conclusion of sperm and vulva development. (**a**) Average gene expression difference of the experiments, determined with TAC, compared to the control RNAi. (**b**) Clique map for experiment 1 of *unc-45* RNAi versus young adult of control RNAi. A more detailed description of the most strongly affected cliques can be found in Table 3 and corresponds to the positions in the clique map. (**c**) Comparison between experiment 1 and 2 on a gene-by-gene basis (upper panel) and comparison between experiment 1 and 2 on a clique-by-clique basis (lower panel). The clique map of experiment 2 is shown as Supplemental Fig. 2b, d) Clique trends during development of *C. elegans*. Described interaction between genes involved in sperm development is shown as Supplemental Fig. 2c. Cliques colored in red are induced upon RNAi while cliques in blue are repressed. The linear regression function was generated with Microsoft Excel without weighting, a square value of 1 would indicate a perfect correlation between the cliques.

Previously it had been observed that the Top300 genes from the *hsp-90* RNAi analysis showed partial overlap with *daf-16* regulated genes. We thus employed the gene-list from this previous study to identify the cliques, which now represent these genes. Indeed the correlation is fairly clear, with the cliques C17H1.6-C17H1.13, C32F10.4-D1086.2 and C10C5.2-Y58A7A.3 being mostly overlapping with the previous cluster1_up and the cliques col-138-col-49, R12E2.14_75-R12E2.15, mlt-9_22518-F33D4.6_14044 being mostly overlapping with the cluster2_up. Utilizing the ranked list of *daf-16* target genes, we also determined which cliques most strongly are enriched in the Top750 and Bottom750 of this ranked list. These cliques are found mostly in cluster1_up confirming that the identification of this correlation also is visible from the clique map. Interestingly these cliques represent those that are differently regulated compared to the L4 larval stage. Thus the HSP-90 depletion leads to higher exression levles in a *daf-16* regulated cluster (cluster1_up) and a *daf-16* independent cluster (cluster2_up). With the *daf-16* independent cluster containing mostly cliques related to larval development, apparently the depletion of HSP-90 induces both of these processes. Whether they are connected via secondary effects is unclear to date, especially as the developmental timing of DAF-16 activity is a well described phenomenon.

Thus, based on several clearly regulated marker cliques, *hsp-90* arrested nematodes, like *unc-45* arrested nematodes, can be positioned in respect to a developmental time axis.

Cluster name	Clique position	Best GO-Term	Best PEA-Term	Best TEA-Term	Mean STD	Log10(p) Exp 1	Log10(p) Exp 2
nspd-1-nspd-2	R12 C1	Structural constituent of cuticle GO:0042302	Dumpy WBPhenotype:0000583	WBPaper00037950_coelomocytes_embryo_enriched_WBbt_0005751_570	0.38 ± 0.12	4.41	1.84
msp-36-msp-55	R10 C19	Lipid storage GO:0019915	Linker cell migration variant WBPhenotype:0001511	WBPaper00040420_FLP_enriched_WBbt_0006828_288	0.35 ± 0.08	1.15	2.54
msp-63-msp-33	R9 C14	Lipid storage GO:0019915	Linker cell migration variant WBPhenotype:0001511	WBPaper00040420_FLP_enriched_WBbt_0006828_288	0.31 ± 0.09	7.92	9.08
hsp-16.2-F44E5.4_19238	R12 C4	Response to heat GO:0009408	Cadmium response variant WBPhenotype:0001653	WBPaper00037950_coelomocytes_larva_enriched_WBbt_0005751_229	0.29 ± 0.17	16.49	1.60
abu-7-abu-8_22491	R8 C26	Response to unfolded protein GO:0006986	Dauer constitutive WBPhenotype:0000012	WBPaper00024505_pharyngeal_enriched_WBbt_0003681_329	0.25 ± 0.08	63.31	5.15
col-138-col-49	R9 C23	Structural constituent of cuticle GO:0042302	Blistered WBPhenotype:0000025	WBPaper00037950_coelomocytes_larva_enriched_WBbt_0005751_229	0.24 ± 0.22	34.90	0.93
col-117-col-167_1015	R9 C25	Structural constituent of cuticle GO:0042302	Dumpy WBPhenotype:0000583	WBPaper00037950_germline-precursors_embryo_enriched_WBbt_0006849_974	0.24 ± 0.06	29.40	5.29
pqn-54-abu-9	R6 C11	Response to unfolded protein GO:0006986	Shortened life span WBPhenotype:0001171	WBPaper00024505_pharyngeal_enriched_WBbt_0003681_329	0.2 ± 0.03	43.57	13.10
R12E2.14_75-R12E2.15	R6 C9	Structural constituent of cuticle GO:0042302	Dumpy WBPhenotype:0000583	WBPaper00037950_germline-precursors_embryo_enriched_WBbt_0006849_974	0.18 ± 0.08	47.12	8.99
lys-3-tsp-1	R11 C40	Carbohydrate metabolic process GO:0005975	Male nervous system development variant WBPhenotype:0001008	WBPaper00040420_ALM_PLM_enriched_WBbt_0005406_198	0.18 ± 0.22	27.93	1.06
C10C5.3-C10C5.5	R12 C40	Oxoacid metabolic process GO:0043436	Dauer constitutive WBPhenotype:0000012	WBPaper00037950_pharyngeal-muscle_embryo_enriched_WBbt_0005451_598	0.17 ± 0.05	4.43	2.28
F07A5.2-R10E9.2	R5 C7	Sodium ion transport GO:0006814	Nicotine response variant WBPhenotype:0001573	WBPaper00045521_Spermatogenic_WBbt_0005784_2743	0.15 ± 0.04	6.82	34.38
K11C4.1_20445-rnh-1.1	R8 C22	Regulation of cell shape GO:0008360	Fat content increased WBPhenotype:0001184	WBPaper00045521_Spermatogenic_WBbt_0005784_2743	0.14 ± 0.03	6.02	8.77
ssq-2_16507-ssq-3_1032	R12 C27	Response to hormone GO:0009725	Movement variant WBPhenotype:0001206	WBPaper00026980_intestine_enriched_WBbt_0005772_1970	0.13 ± 0	1.96	2.06
col-146-col-133	R9 C28	Structural constituent of cuticle GO:0042302	Dumpy WBPhenotype:0000583	WBPaper00037950_coelomocytes_larva_enriched_WBbt_0005751_229	0.12 ± 0.02	11.00	2.77
F42A9.7-T22B3.3	R3 C11	Regulation of cell shape GO:0008360	Dauer metabolism variant WBPhenotype:0001547	WBPaper00045521_Spermatogenic_WBbt_0005784_2743	0.11 ± 0.03	7.97	29.43
bus-8_3160-K04H4.2_2324	R9 C2	Amino sugar metabolic process GO:0006040	Molt variant WBPhenotype:0002041	WBPaper00024505_pharyngeal_enriched_WBbt_0003681_329	0.11 ± 0.08	8.94	0.92
R12A1.3-M195.2	R6 C19	Amino sugar metabolic process GO:0006040	Dauer constitutive WBPhenotype:0000012	WBPaper00024505_pharyngeal_enriched_WBbt_0003681_329	0.1 ± 0.04	6.65	3.63
T28A11.5-T06C12.14	R12 C14	Extracellular region GO:0005576	Dumpy WBPhenotype:0000583	WBPaper00037950_excretory-cell_larva_enriched_WBbt_0005812_528	0.1 ± 0.05	0.71	2.01
agmo-1_5527-F53B1.4	R10 C14	Pyridoxal phosphate binding GO:0030170	Molt variant WBPhenotype:0002041	WBPaper00037950_hypodermis_embryo_enriched_WBbt_0005733_734	0.1 ± 0.11	7.44	0.70
171971_x_at-D1054.11_184	R11 C37	Cell GO:0005623	Egg laying defective WBPhenotype:0000006	WBPaper00037950_hypodermis_larva_enriched_WBbt_0005733_1250	− 0.55 ± 0.09	3.70	0.66
gpd-3_977-aldo-1_21168	R9 C26	Glycosyl compound metabolic process GO:1901657	Fat content reduced WBPhenotype:0001183	WBPaper00031003_24hr_muscle_enriched_WBbt_0003675_918	− 0.51 ± 0.01	9.02	4.52
T05E12.6_12439-T05E12.6_12396	R10 C3	Lipid catabolic process GO:0016042	Transgene expression increased WBPhenotype:0001236	WBPaper00037950_pharyngeal-muscle_embryo_enriched_WBbt_0005451_598	− 0.29 ± 0.15	60.37	3.63

Continued

Cluster name	Clique position	Best GO-Term	Best PEA-Term	Best TEA-Term	Mean STD	Log10(p) Exp 1	Log10(p) Exp 2
ZK1053.4-C08F1.6	R4 C16	Embryo development GO:0009790	Embryonic development variant WBPhenotype:0000749	WBPaper00037950_hypodermis_embryo_enriched_WBbt_0005733_734	− 0.26 ± 0.12	26.51	73.26
C46C2.5_15926-W03F11.1	R9 C22	Carbohydrate binding GO:0030246	Apoptosis increased WBPhenotype:0000183	WBPaper00037950_GABAergic-motor-neurons_embryo_enriched_WBbt_0005190_361	− 0.24 ± 0.02	8.57	10.00
ZC373.2-Y62H9A.6_1596	R3 C18	Flavonoid metabolic process GO:0009812	Cell membrane organization biogenesis variant WBPhenotype:0001982	WBPaper00037950_dopaminergic-neurons_larva_enriched_WBbt_0006746_1230	− 0.22 ± 0.03	46.68	19.54
nspc-1_614-nspc-10_22525	R10 C12	Extracellular region GO:0005576	Spermatogenesis variant WBPhenotype:0000670	WBPaper00037950_coelomocytes_larva_enriched_WBbt_0005751_229	− 0.21 ± 0.06	5.62	5.79
C46C2.5_15925-F17E9.2	R10 C8	Hydrolase activity—acting on glycosyl bonds GO:0016798	Embryonic development variant WBPhenotype:0000749	WBPaper00037950_coelomocytes_larva_enriched_WBbt_0005751_229	− 0.2 ± 0.01	6.65	6.25
C03B1.14-F46C3.2	R8 C21	Membrane GO:0016020	Chemical hypersensitive WBPhenotype:0001918	WBPaper00037950_intestine_larva_enriched_WBbt_0005772_946	− 0.19 ± 0	9.53	10.38
fbxc-28-sdz-28	R7 C8	Modification-dependent macromolecule catabolic process GO:0043632	L1 larval development variant WBPhenotype:0000751	WBPaper00037950_hypodermis_embryo_enriched_WBbt_0005733_734	− 0.18 ± 0.08	10.65	27.90
fbxb-13-fbxb-24	R8 C18	Protein oligomerization GO:0051259	Cholinergic agonist resistant WBPhenotype:0001578	WBPaper00024505_pharyngeal_enriched_WBbt_0003681_329	− 0.17 ± 0.1	1.20	13.08
dsh-1_3575-C40A11.4	R5 C17	Protein oligomerization GO:0051259	Ectopic expression transgene WBPhenotype:0001276	WBPaper00037950_hypodermis_embryo_enriched_WBbt_0005733_734	− 0.14 ± 0.07	2.78	9.72
vem-1-ugt-58	R12 C35	Oxoacid metabolic process GO:0043436	Epithelial cell physiology variant WBPhenotype:0000986	WBPaper00037950_BAG-neuron_embryo_enriched_WBbt_0006825_454	− 0.14 ± 0.01	2.03	0.89
sdz-10-fbxb-62	R3 C17	Glycosylation GO:0070085	L1 larval development variant WBPhenotype:0000751	WBPaper00037950_hypodermis_embryo_enriched_WBbt_0005733_734	− 0.14 ± 0.09	2.82	41.16
Y41D4B.17-K10D11.6	R12 C32	Immune system process GO:0002376	Exploded through vulva WBPhenotype:0000038	WBPaper00037950_intestine_larva_enriched_WBbt_0005772_946	− 0.12 ± 0.03	0.84	0.77
fbxb-31-fbxb-119	R11 C28	Embryo development GO:0009790	Transgene expression reduced WBPhenotype:0001278	WBPaper00040420_FLP_enriched_WBbt_0006828_288	− 0.12 ± 0.09	0.64	4.30
R03E1.2_7363-ucr-2.1	R10 C30	Mitochondrion GO:0005739	mRNA levels increased WBPhenotype:0000136	WBPaper00037950_excretory-cell_larva_enriched_WBbt_0005812_528	− 0.12 ± 0.03	0.98	2.14
C35C5.8_15869-best-1	R10 C21	Transmembrane transport GO:0055085	Fat content increased WBPhenotype:0001184	WBPaper00037950_excretory-cell_larva_enriched_WBbt_0005812_528	− 0.12 ± 0.03	4.11	1.04
pek-1_22220-pek-1_33	R11 C12	Aging GO:0007568	Sluggish WBPhenotype:0000646	WBPaper00037950_GABAergic-motor-neurons_embryo_enriched_WBbt_0005190_361	− 0.11 ± 0	1.85	1.69
iff-2_18754-rpl-25.1	R12 C37	Amide biosynthetic process GO:0043604	Hermaphrodite fertility reduced WBPhenotype:0001259	WBPaper00037950_PVD-OLL-neurons_larva_enriched_WBbt_0006831_878	− 0.11 ± 0.03	0.65	1.39

Table 3. Most strongly affected cliques by *unc-45* RNAi and their characteristics. Clique positions (letter = row, number = position from left to right) correspond to the clique map shown in Fig. 2b.

Series	Sample	Description	Replicate
GSE6547	GSM146422	N2 worms at L1 stage	1
	GSM146423	N2 worms at L1 stage	2
	GSM147330	N2 worms at L1 stage	3
	GSM147334	N2 worms at L4 stage	1
	GSM147335	N2 worms at L4 stage	2
	GSM147336	N2 worms at L4 stage	3
	GSM147340	N2 worms at embryonic stage	1
	GSM147341	N2 worms at embryonic stage	2
	GSM147342	N2 worms at embryonic stage	3
GSE21784	GSM542652	L4 larvae	1
	GSM542653	L4 larvae	2
	GSM542654	L4 larvae	3
	GSM542655	Day 6 adult	1
	GSM542656	Day 6 adult	2
	GSM542657	Day 6 adult	3
	GSM542658	Day 15 adult	1
	GSM542659	Day 15 adult	2
	GSM542660	Day 15 adult	3
GSE46288	GSM1128166	L3	1
	GSM1128167	L3	2
	GSM1128168	L3	3
	GSM1128169	L3-lethargus	1
	GSM1128170	L3-lethargus	2
	GSM1128171	L3-lethargus	3
GSE46289	GSM1128172	L4	1
	GSM1128173	L4	2
	GSM1128174	L4	3
	GSM1128175	L4	4
	GSM1128176	L4	5
	GSM1128177	L4-lethargus	1
	GSM1128178	L4-lethargus	2
	GSM1128179	L4-lethargus	3
	GSM1128180	L4-lethargus	4
	GSM1128181	L4-lethargus	5
	GSM1128182	Adult	1
	GSM1128183	Adult	2
	GSM1128184	Adult	3
	GSM1128185	Adult	4
	GSM1128186	Adult	5

Table 4. Experiments used for the analysis of the developmental time line of *C. elegans*, obtained from the GEO expression data repository.

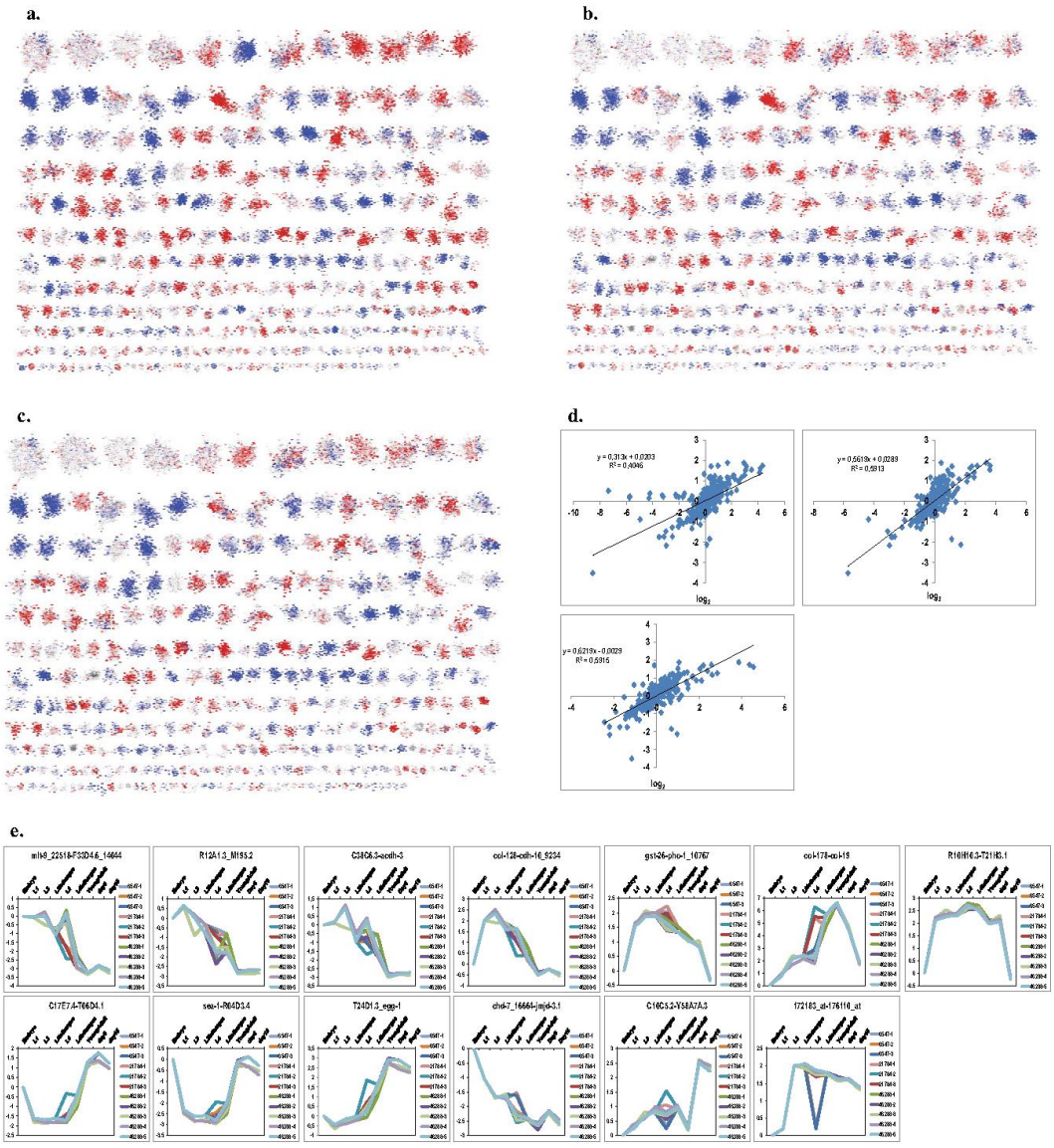

Figure 3. Expression in developmental stages is altered in similarity to the RNAi-induced arrest. (**a**) L3 comparison to young adult. (**b**) L4 comparison to young adult and (**c**) L4 lethargus to young adult. Other stepwise comparisons, like that of embryo to L1 or that of day6 nematode to day 16 adult nemtode are shown in the Supplemental Figures section as Supplemental Fig. 3, 4, 5 and 6. (**d**) Clique responses throughout development shown for selected cliques with significant change pattern. Cliques colored in red are induced compared to the earlier developmental stage, while cliques colored in blue are repressed. The linear regression function was generated with Microsoft Excel without weighting, a square value of 1 would indicate a perfect correlation between the cliques.

Up1	Up2	Down1	Down2	Down3	Down4
C10C5.2-Y58A7A.3	col-138-col-49	C46C2.5_15926-W03F11.1	C17E7.4-T06D4.1	vit-2-vit-4_22519	C17H12.6-swt-6
K08D10.9-F46A8.1	R12E2.14_75-R12E2.15	ZC373.2-Y62H9A.6_1596	fbxc-28-sdz-28	C10A4.6-C01A2.6	F55G11.8-dod-17
hsp-16.2-F44E5.4_19238	mlt-9_22518-F33D4.6_14044	C10C5.3-C10C5.5	sea-1-R04D3.4	fbxc-28-sdz-28	R10H10.3-T21H3.1
lys-3-tsp-1	col-117-col-167_1015	171971_x_at-D1054.11_184	ZK1053.4-C08F1.6	C17E7.4-T06D4.1	
hpo-6-C49C3.9	col-146-col-133	C46C2.5_15925-F17E9.2	F11A3.2-F47G3.3	R07E4.5-skp-1_1608	
C32F10.4-D1086.2	bus-8_3160-K04H4.2_2324	C03B1.14-F46C3.2	K09D9.12-T10C6.10	R10H10.3-T21H3.1	
F13E6.1_2090-C35C5.3_1843	sqt-2-dpy-9	col-178-col-19	K05C4.4-fbxc-46	sre-33-ZK1025.1_8337	
Y6G8.2_5650-F17B5.1	abu-7-abu-8_22491	T24D1.3-egg-1	fbxb-31-fbxb-119		
fbxa-35-Y39A3A.3	agmo-1_5527-F53B1.4		Y116A8C.19-F38C2.7		
C17H1.6-C17H1.13	dos-2-grd-2		npp-8_4368-E01B7.1_7741		
ccg-1_12351-ZC410.5	R12A1.3-M195.2		sdz-10-fbxb-62		
C17H12.6-swt-6	pqn-54-abu-9		fbxb-13-fbxb-24		
F58F9.3_11574-R07B7.6	col-128-cdh-10_9234		skr-16-F37B4.10		
T12G3.1_17-T12G3.1_18846	C38C6.3-acdh-6		dsh-1_3575-C40A11.4		
W01F3.2_1554-Y106G6D.8	C36C5.12-F57G8.7		dos-2-grd-2		

Table 5. HSP-90-responsive cliques with highest enrichment of *daf-16* supported (red) and suppressed (blue) genes. Sorted according to the nomenclature estabilshed in Eckl et al., 2017, which grouped the *hsp-90* responsive genes in two major groups for upregulation and four groups for downregulation based on co-expression network analysis. Cliques enriched within these groups are listed under the group names (Up1, Up2, Down1, Down2, Down3 and Down4). The groups are labeled in bold, if enrichment reaches the significance level of 1e-5 and they are colored, if the same group is found within the top *daf-16* regulated groups. Coloring is red, if it is among upregulated DAF-16 targets and blue if, it is among down regulated DAF-16 targets.

a.

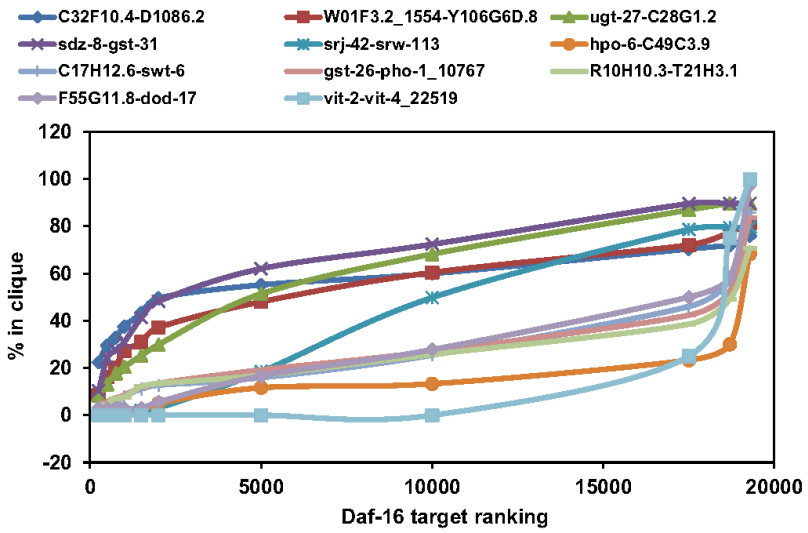

b.

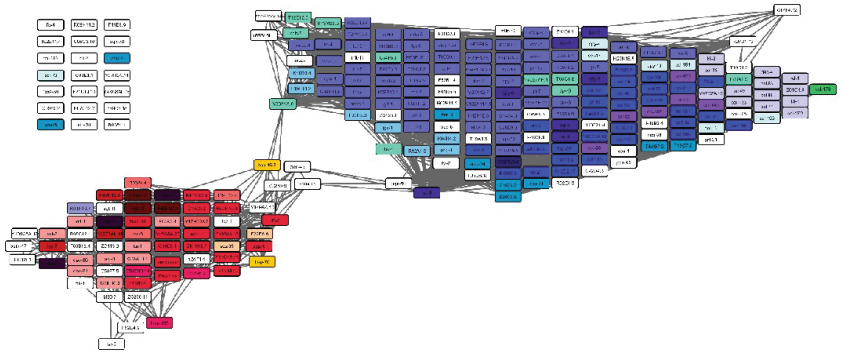

C10C5.2-Y58A7A.3		R:255 G:0 B:51	#FF0033	col-146-col-133		R:204 G:255 B:255	#CCFFFF
C17H1.6-C17H1.13		R:255 G:0 B:102	#FF0066	fbxa-35-Y39A3A.3		R:255 G:204 B:153	#FFCC99
C32F10.4-D1086.2		R:255 G:153 B:153	#FF9999	fbxb-5-fbxb-106		R:153 G:153 B:255	#9999FF
C36C5.12-F57G8.7		R:0 G:204 B:102	#00CC66	hpo-6-pho-1_10767		R:255 G:102 B:102	#FF6666
C38C3.6-npr-7		R:153 G:153 B:255	#9999FF	hsp-16.2F44E5.4_19238		R:255 G:204 B:0	#FFCC00
F54D5.3_7003-F54D5.3_7004		R:204 G:0 B:0	#CC0000	mlt-9_22518-F33D4.6_14044		R:102 G:102 B:255	#6666FF
F58F9.3_11574-R07B7.6		R:102 G:0 B:0	#660000	npp-8_4368-E01B7.1_7741		R:0 G:153 B:204	#0099CC
R10H10.3-T21H3.1		R:102 G:255 B:255	#66FFFF	nrde-3-tra-4_10484		R:102 G:51 B:255	#6633FF
R12A1.3-M195.2		R:102 G:204 B:255	#6668FF	pch-2-B0393.3		R:204 G:51: B:255	#CC33FF
R12E2.14_75-R12E2.15		R:0 G:0 B:255	#0000FF	puf-3-oma-2_18268		R:153 G:0 B:153	#990099
W01F3.2_1554-Y106G6D.8		R:51 G:0 B:51	#330033	sdz-10-fbxb-62		R:255 G:51 B:255	#FF33FF
ZC373.2-Y62H9A.6_1596		R:255 G:102 B:102	#FF6666	sea-1-R04D3.4		R:153 G:153 B:255	#9999FF
abu-7-abu-8_22491		R:0 G:153 B:204	#0099CC	skr-16-F37B4.10		R:0 G:0 B:51	#000033
col-117-col-167_1015		R:153 G:51 B:255	#9933FF	sqt-2-dpy-9		R:51 G:0 B:153	#330099
col-128-cdh-10_9234		R:51 G:255 B:204	#33FFCC	tnt-4-myo-1_2160		R:0 G:0 B:102	#000066
col-138-col-49		R:204 G:204 B:255	#CCCCFF				

Figure 4. Correlation between *daf-16* target genes and identified cliques for those genes most clearly enriched in *daf-16* targets. (**a**) Enrichted target cliques of DAF-16. The plot shows how many genes per clique are derived from the indicated range of the DAF-16 ranking. Cliques with high percentage values on the left side reflect cliques that are considered to be DAF-16 activatable while cliques with a low percentage up to the bottom to the DAF-16 ranking are considered repressed. (**b**) Most strongly enriched cliques in the Top750 and Bottom750 of the ranked *daf-16* target list.

Data availability

All data will be made fully available without restriction at http://www.richterlab.de/DataSets and on the GEO repository. Tables containing GO terms, PEA and TEA enrichment results for all cliques can be obtained from the authors.

Received: 31 January 2021; Accepted: 21 May 2021
Published online: 18 June 2021

References

1. Somogyvari, M., Gecse, E. & Soti, C. DAF-21/Hsp90 is required for C. elegans longevity by ensuring DAF-16/FOXO isoform A function. *Sci. Rep.* **8**, 12048. https://doi.org/10.1038/s41598-018-30592-6 (2018).
2. Inoue, T. *et al.* Cell cycle control by daf-21/Hsp90 at the first meiotic prophase/metaphase boundary during oogenesis in Caenorhabditis elegans. *Dev. Growth Differ.* **48**, 25–32. https://doi.org/10.1111/j.1440-169X.2006.00841.x (2006).
3. Gillan, V., Maitland, K., McCormack, G., Him, N. A. & Devaney, E. Functional genomics of hsp-90 in parasitic and free-living nematodes. *Int. J. Parasitol.* **39**, 1071–1081. https://doi.org/10.1016/j.ijpara.2009.02.024 (2009).
4. McClellan, A. J. *et al.* Diverse cellular functions of the Hsp90 molecular chaperone uncovered using systems approaches. *Cell* **131**, 121–135. https://doi.org/10.1016/j.cell.2007.07.036 (2007).
5. Nathan, D. F. & Lindquist, S. Mutational analysis of Hsp90 function: interactions with a steroid receptor and a protein kinase. *Mol. Cell Biol.* **15**, 3917–3925. https://doi.org/10.1128/mcb.15.7.3917 (1995).
6. Pratt, W. B. & Toft, D. O. Regulation of signaling protein function and trafficking by the hsp90/hsp70-based chaperone machinery. *Exp. Biol. Med. (Maywood)* **228**, 111–133. https://doi.org/10.1177/153537020322800201 (2003).
7. Gaiser, A. M., Kaiser, C. J., Haslbeck, V. & Richter, K. Downregulation of the Hsp90 system causes defects in muscle cells of Caenorhabditis elegans. *PLoS ONE* **6**, e25485. https://doi.org/10.1371/journal.pone.0025485 (2011).
8. Roe, S. M. *et al.* Structural basis for inhibition of the Hsp90 molecular chaperone by the antitumor antibiotics radicicol and geldanamycin. *J. Med. Chem.* **42**, 260–266. https://doi.org/10.1021/jm980403y (1999).
9. Sreedhar, A. S., Kalmar, E., Csermely, P. & Shen, Y. F. Hsp90 isoforms: functions, expression and clinical importance. *FEBS Lett.* **562**, 11–15. https://doi.org/10.1016/s0014-5793(04)00229-7 (2004).
10. Picard, D. Heat-shock protein 90, a chaperone for folding and regulation. *Cell Mol. Life Sci.* **59**, 1640–1648. https://doi.org/10.1007/pl00012491 (2002).
11. Eckl, J., Sima, S., Marcus, K., Lindemann, C. & Richter, K. Hsp90-downregulation influences the heat-shock response, innate immune response and onset of oocyte development in nematodes. *PLoS ONE* **12**, e0186389. https://doi.org/10.1371/journal.pone.0186386 (2017).
12. Prithika, U., Deepa, V. & Balamurugan, K. External induction of heat shock stimulates the immune response and longevity of Caenorhabditis elegans towards pathogen exposure. *Innate. Immun.* **22**, 466–478. https://doi.org/10.1177/1753425916654557 (2016).
13. Barral, J. M., Hutagalung, A. H., Brinker, A., Hartl, F. U. & Epstein, H. F. Role of the myosin assembly protein UNC-45 as a molecular chaperone for myosin. *Science* **295**, 669–671. https://doi.org/10.1126/science.1066648 (2002).
14. Liu, L., Srikakulam, R. & Winkelmann, D. A. Unc45 activates Hsp90-dependent folding of the myosin motor domain. *J. Biol. Chem.* **283**, 13185–13193. https://doi.org/10.1074/jbc.M800757200 (2008).
15. Kachur, T., Ao, W., Berger, J. & Pilgrim, D. Maternal UNC-45 is involved in cytokinesis and colocalizes with non-muscle myosin in the early Caenorhabditis elegans embryo. *J. Cell Sci.* **117**, 5313–5321. https://doi.org/10.1242/jcs.01389 (2004).
16. Zhao, S., Fung-Leung, W. P., Bittner, A., Ngo, K. & Liu, X. Comparison of RNA-Seq and microarray in transcriptome profiling of activated T cells. *PLoS ONE* **9**, e78684. https://doi.org/10.1371/journal.pone.0078644 (2014).
17. Sima, S., Schmauder, L. & Richter, K. Genome-wide analysis of yeast expression data based on a priori generated co-regulation cliques. *Microb. Cell* **6**, 160–176. https://doi.org/10.15698/mic2019.03.671 (2019).
18. Edgar, R., Domrachev, M. & Lash, A. E. Gene Expression Omnibus: NCBI gene expression and hybridization array data repository. *Nucl. Acids Res.* **30**, 207–210. https://doi.org/10.1093/nar/30.1.207 (2002).
19. Bolstad, B. M., Irizarry, R. A., Astrand, M. & Speed, T. P. A comparison of normalization methods for high density oligonucleotide array data based on variance and bias. *Bioinformatics* **19**, 185–193. https://doi.org/10.1093/bioinformatics/19.2.185 (2003).
20. Papsdorf, K., Sima, S., Richter, G. & Richter, K. Construction and evaluation of yeast expression networks by database-guided predictions. *Microb Cell* **3**, 236–247. https://doi.org/10.15698/mic2016.06.505 (2016).
21. Angeles-Albores, D., Lee, R. Y., Chan, J. & Sternberg, P. W. Tissue enrichment analysis for C. elegans genomics. *BMC Bioinform.* **17**, 366. https://doi.org/10.1186/s12859-016-1229-9 (2016).
22. Angeles-Albores, D., Lee, R., Chan, J. & Sternberg, P. Two new functions in the WormBase Enrichment Suite. *MicroPubl. Biol.* https://doi.org/10.17912/W25Q2N (2018).
23. Shannon, P. *et al.* Cytoscape: a software environment for integrated models of biomolecular interaction networks. *Genome Res.* **13**, 2498–2504. https://doi.org/10.1101/gr.1239303 (2003).
24. Kirienko, N. V. & Fay, D. S. Transcriptome profiling of the C. elegans Rb ortholog reveals diverse developmental roles. *Dev. Biol.* **305**, 674–684. https://doi.org/10.1016/j.ydbio.2007.02.021 (2007).
25. Youngman, M. J., Rogers, Z. N. & Kim, D. H. A decline in p38 MAPK signaling underlies immunosenescence in Caenorhabditis elegans. *PLoS Genet.* **7**, e1002082. https://doi.org/10.1371/journal.pgen.1002082 (2011).
26. George-Raizen, J. B., Shockley, K. R., Trojanowski, N. F., Lamb, A. L. & Raizen, D. M. Dynamically-expressed prion-like proteins form a cuticle in the pharynx of Caenorhabditis elegans. *Biol. Open* **3**, 1139–1149. https://doi.org/10.1242/bio.20147500 (2014).
27. Gaiser, A. M., Brandt, F. & Richter, K. The non-canonical Hop protein from Caenorhabditis elegans exerts essential functions and forms binary complexes with either Hsc70 or Hsp90. *J. Mol. Biol.* **391**, 621–634. https://doi.org/10.1016/j.jmb.2009.06.051 (2009).
28. Trojanowski, N. F., Nelson, M. D., Flavell, S. W., Fang-Yen, C. & Raizen, D. M. Distinct mechanisms underlie quiescence during two caenorhabditis elegans sleep-like states. *J. Neurosci.* **35**, 14571–14584. https://doi.org/10.1523/JNEUROSCI.1369-15.2015 (2015).
29. Cary, M., Podshivalova, K. & Kenyon, C. Application of transcriptional gene modules to analysis of caenorhabditis elegans' gene expression data. *G3 (Bethesda)* **10**, 3623–3638. https://doi.org/10.1534/g3.120.401270 (2020).
30. Subramanian, A. *et al.* Gene set enrichment analysis: a knowledge-based approach for interpreting genome-wide expression profiles. *Proc. Natl. Acad. Sci. USA.* **102**, 15545–15550. https://doi.org/10.1073/pnas.0506580102 (2005).
31. Sternberg, P. W. Vulval development. *WormBook* https://doi.org/10.1895/wormbook.1.6.1 (2005).
32. Weinstein, N. & Mendoza, L. A network model for the specification of vulval precursor cells and cell fusion control in Caenorhabditis elegans. *Front. Genet.* **4**, 112. https://doi.org/10.3389/fgene.2013.00112 (2013).
33. Shemer, G. & Podbilewicz, B. LIN-39/Hox triggers cell division and represses EFF-1/fusogen-dependent vulval cell fusion. *Genes Dev.* **16**, 3136–3141. https://doi.org/10.1101/gad.251202 (2002).
34. Ma, X. *et al.* Characterisation of Caenorhabditis elegans sperm transcriptome and proteome. *BMC Genom.* **15**, 168. https://doi.org/10.1186/1471-2164-15-168 (2014).

35. Tsukamoto, T. *et al.* LIN-41 and OMA ribonucleoprotein complexes mediate a translational repression-to-activation switch controlling oocyte meiotic maturation and the oocyte-to-embryo transition in Caenorhabditis elegans. *Genetics* **206**, 2007–2039. https://doi.org/10.1534/genetics.117.203174 (2017).
36. Engert, C. G., Droste, R., van Oudenaarden, A. & Horvitz, H. R. A Caenorhabditis elegans protein with a PRDM9-like SET domain localizes to chromatin-associated foci and promotes spermatocyte gene expression, sperm production and fertility. *PLoS Genet.* **14**, e1007295. https://doi.org/10.1371/journal.pgen.1007295 (2018).
37. LaMunyon, C. W. *et al.* A new player in the spermiogenesis pathway of Caenorhabditis elegans. *Genetics* **201**, 1103–1116. https://doi.org/10.1534/genetics.115.181172 (2015).
38. Campbell, A. C. & Updike, D. L. CSR-1 and P granules suppress sperm-specific transcription in the C. elegans germline. *Development* **142**, 1745–1755. https://doi.org/10.1242/dev.121434 (2015).

Acknowledgements
The authors would like to thank Deutsche Forschungsgemeinschaft for funding the research grant RI1873/1-4 and the Heisenberg position RI1873/5-1. We also thank the distributors of free and open source software that we could use during this study. This includes Cytoscape (Cytoscape Consortium), RMAexpress (Ben Bolstad) and Transcriptome Analysis Console (Thermo Fisher Scientific).

Author contributions
L.S. and K.R. designed the experiments. L.S. performed the experiments. L.S. and K.R. analyzed the data and wrote the manuscript.

Funding
Open Access funding enabled and organized by Projekt DEAL.

Competing interests
The authors declare no competing interests.

Additional information
Supplementary Information The online version contains supplementary material available at https://doi.org/10.1038/s41598-021-91690-6.

Correspondence and requests for materials should be addressed to K.R.

Reprints and permissions information is available at www.nature.com/reprints.

Publisher's note Springer Nature remains neutral with regard to jurisdictional claims in published maps and institutional affiliations.

2.3.4. Permission to reprint the manuscript

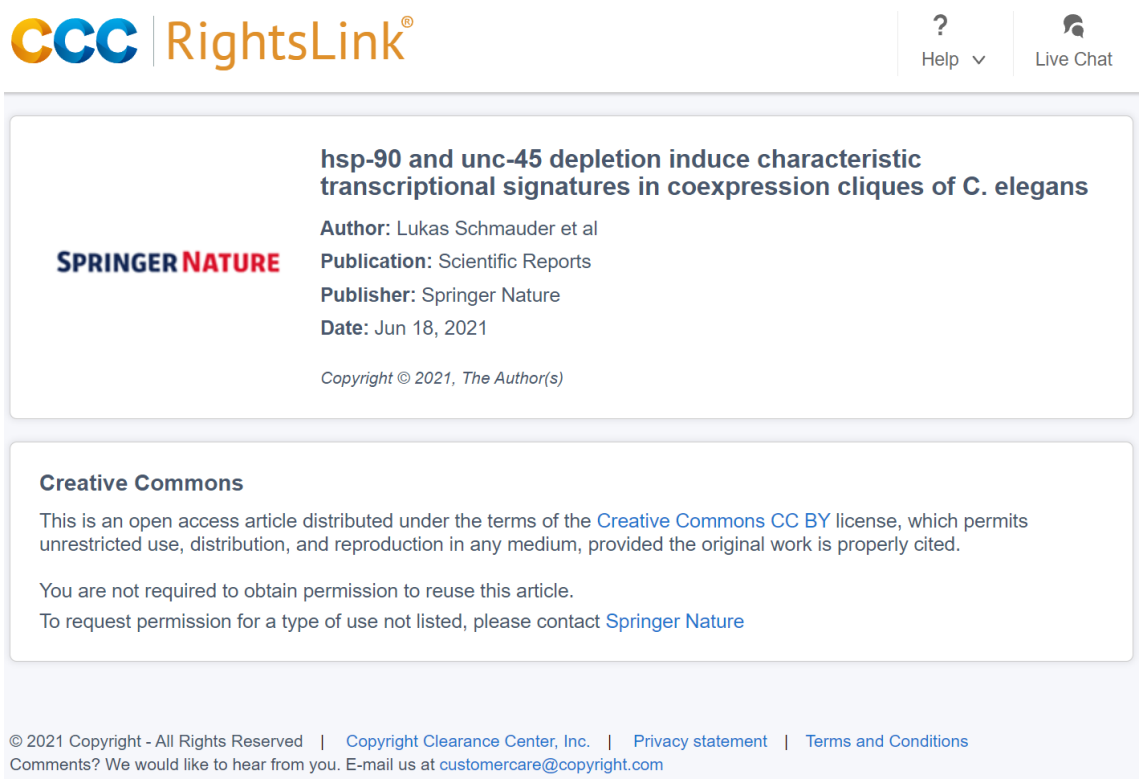

CCC RightsLink®

Help Live Chat

hsp-90 and unc-45 depletion induce characteristic transcriptional signatures in coexpression cliques of C. elegans

SPRINGER NATURE

Author: Lukas Schmauder et al
Publication: Scientific Reports
Publisher: Springer Nature
Date: Jun 18, 2021

Copyright © 2021, The Author(s)

Creative Commons

This is an open access article distributed under the terms of the Creative Commons CC BY license, which permits unrestricted use, distribution, and reproduction in any medium, provided the original work is properly cited.

You are not required to obtain permission to reuse this article.
To request permission for a type of use not listed, please contact Springer Nature

2.4. Binding of the HSF-1 DNA-binding domain to multimeric *C. elegans* consensus HSEs is guided by cooperative interactions.

Submitted manuscript currently in revision at Scientific Reports, 2021 Oct 20

Submitted by Lukas Schmauder[1], Siyuan Sima[1], Amira Ben Hadj, Ricardo Cesar and Klaus Richter[2].

PhD candidate

[1] these authors contributed equally

[2] corresponding author

2.4.1. Summary

The highly conserved HSF-1 coordinates the induction and expression of molecular chaperons, by binding to HSEs throughout the genome. Together with heat shock proteins it forms a densely linked interaction network upon heat-shock. In *C. elegans*, there are more than 4000 HSEs in the promoter regions of genes, containing a HSF-1 binding consensus region. It is therefore interesting to see how HSF-1 exactly interacts with this huge amount of target genes.

Therefore, a genome-wide coexpression analysis was employed to define upregulated genes during heat-shock conditions. This was achieved by harnessing the previously developed microarray analysis tool clusterEX, astonishingly revealing that most of the 4000 HSE-containing genes are unaffected during these conditions. Instead, only few of these genes are specifically upregulated, some of which, like F44E5.4, HSP-16.2, HSP-1, HSP-70, DNJ-12 and DNJ-13 are related to the HSP chaperone system.

Based on this finding, dsDNA probes resembling the promoter region and thereby containing the HSEs of the so found genes were created. In order to investigate if HSF-1 binding to these probes is possible *in vitro*, the DBD of HSF-1 was expressed and its stability was analyzed by both circular dichroism spectroscopy and thermal shift assays.

Next, electrophoretic-mobility shift assays and sedimentation velocity experiments were performed to determine the binding, affinity, and stoichiometry between both HSF-1 DBD and dsDNA probes representing the HSEs. Here, HSF-1 interacts with most of these probes, albeit with apparently different characteristics. A global fit of the derived data revealed, that despite the proposed trimeric binding mode for HSEs, also tetra- and pentameric HSEs exist, which were found to lead to additional cooperativity, while cooperativity is less pronounced for the common trimeric HSEs.

Here, the generated coexpression cliques were able to provide a tool for prediction of HSF-1 biding sites, which was then validated *in vitro*. This approach could therefore be of valuable assistance in the investigation of complex multi-step binding reactions.

2.4.2. Contribution of the PhD candidate

Siyuan Sima[1] and Klaus Richter designed the experiments. Lukas Schmauder[1], Siyuan Sima[1], Amira Ben Hadj and Ricardo Cesar performed the experiments. Lukas Schmauder[1], Siyuan Sima[1] and Klaus Richter analyzed the data and wrote the manuscript.

2.4.3. Manuscript

Binding of the HSF-1 DNA-binding domain to multimeric *C. elegans* consensus HSEs is guided by cooperative interactions.

Lukas Schmauder[1], Siyuan Sima[1], Amira Ben Hadj[1], Ricardo Cesar[1] and Klaus Richter[1,*]

[1] Center for Integrated Protein Research at the Department of Chemistry, Technische Universität München, Lichtenbergstr. 4, 85748 Garching
[*] Corresponding author. E-Mail: klaus.richter@richterlab.de, Tel: +49-89-289-13342

Abstract

The protein HSF-1 is the controlling transcription factor of the heat-shock response (HSR). Its binding to the heat-shock elements (HSEs) induces the strong upregulation of conserved heat-shock proteins, including Hsp70s, Hsp40s and small HSPs. Next to these commonly known HSPs, more than 4000 other HSEs are found in the promoter regions of *C. elegans* genes. From microarray experiments it is obvious that only few of the HSE-containing genes are specifically upregulated during the heat-shock response. Most of the 4000 HSE-containing genes instead are unaffected by elevated temperatures and coexpress with genes unrelated to the HSR. This is also the case for several genes related to the HSP chaperone system, like *dnj-12, dnj-13,* and *hsp-1*. Interestingly, several promoters of the dedicated HSR-genes, like *F44E5.4*p, *hsp-16.48*p or *hsp-16.2*p, contain extended HSEs in their promoter region, composed of four or five HSE-elements instead of the common trimeric HSEs.
We here aim at understanding how HSF-1 interacts with the different promoter regions. To this end we purify the nematode HSF-1 DBD and investigate the interaction with DNA sequences containing these regions. EMSA assays suggest that the HSF-1 DBD interacts with most of these HSE-containing dsDNAs, but with apparently different characteristics. We further employ sedimentation analytical ultracentrifugation (SV-AUC) to determine stoichiometry, affinity, and cooperativity of HSF-1 DBD binding to these HSEs. Interestingly, most HSEs show cooperative binding of the HSF-1 DBD with up to five DBDs being bound. In most cases binding to the HSEs of inducible promoters is stronger, even though the consensus scores are not always higher. The observed high affinity of HSF-1 to some non-inducible HSEs, like that of *dnj-12* or *hsp-1*, suggest that constitutive expression may be driven from some promoter regions, a fact that is evident for this transcription factor, that is essential also under non-stress conditions.

Introduction

The heat shock transcription factor (Hsf) is the essential transcriptional activator of the heat-shock response (HSR). It activates the genes of the classical HSR like Hsp70, small HSPs and Hsp40s [1-3]. Hsf proteins are further involved in many developmental processes, like embryonic placenta development [4], female meiotic division [5], and general transcription [6]. Hsf proteins are also reported as negative regulators of RNA polymerase II promoters and modulate protein homeostasis, cellular proliferation [7,8] and the regulation of multicellular organism growth [9,10]. In the mammalian genome several Hsf-like genes are encoded that have individual sets of target genes. In nematodes, only one Hsf-like gene (HSF-1) is encoded so the interaction between HSF-1 and the many detected HSEs can be investigated without the necessity to differentiate between several Hsf-proteins [11,12].

Despite this, the regulation of the heat-shock response in nematodes is complex, being influenced by the age of the animal and active mostly in muscular and intestinal tissues [13]. Further, larvae up to the L2 stage show a reduced expression of the HSR in contrast to older larval forms. The aging adult then is characterized by lower inducibility of the HSR [14]. These differences imply a complex regulation of HSF-1 activity during aging, which is thought to ensure that the nematode's reproductive phase is best protected from stressful events. Beyond that, nematode HSF-1 is participating in the innate immune response by upregulating specific target genes and in aging, where HSF-1 cooperates with the transcription factor DAF-16 [12,15-18]. The observation that several thousand of HSEs are present in the promoter regions throughout the nematode genome, even though the canonical HSR seems to be restricted to few genes [19,20], is puzzling. Surprisingly, several of the canonical heat-shock proteins, like HSP-90 are not even heat-inducible in *C. elegans* and also the canonical Hsp40-like proteins are not upregulated strongly upon heat-shock [16,21].

HSF-1 in nematodes is a protein of 671 amino acids. Like other Hsf proteins, HSF-1 consist of several conserved domains, including the N-terminal DNA-binding domain (DBD), an oligomerization domain and a carboxyl-terminal regulatory domain. Nematode HSF-1 further contains an 82-amino-acids extension of unknown function at its N-terminus. Under normal growth conditions Hsf proteins are monomeric and form cytosolic complexes with Hsp90 and Hsc70. This interaction prevents the trimerization and activation of Hsf proteins. Under heat-stress or other inducing conditions, Hsf proteins are released from the protecting chaperons and oligomerize. In most cases Hsf binds as a trimeric protein to the HSE-containing DNA sequences. The phosphorylation of Hsf proteins triggers the translocation to the nucleus and initiates the transcription [6,22-24]. Despite these regulatory events, the interaction of Hsf proteins with consensus dsDNA is observable also for the non-activated Hsf. In this respect, it is mostly unclear, how Hsf proteins distinguish the various HSE-containing target genes.

Here we focus on the DNA binding domain of HSF-1 from *C. elegans* and aim at resolving its interaction with differently regulated HSEs from the nematode genome. To this end we first define the HSE-containing genes that are upregulated upon heat-shock. We then use HSE-containing dsDNA constructs from these HSE regions to investigate to what extent the interaction parameters of the HSF-1 DBD with dsDNA are influenced by HSEs of different sequences and structural organization.

Material and Methods

Analysis of microarray data

Genome-wide coexpression clique separation had been performed with the subsequent production of a genome-wide network used to extract the obvious cliques as described before [25,26]. Further information is available under (www.richterlab.de/DataSets/ and https://github.com/klarichter/clusterEX_cliques_Celegans).

The three microarray data sets investigating the heat-shocked (GSM62937, GSM62941, GSM62945) versus non-shocked condition (GSM62936, GSM62940, GSM62944) were used to obtain the genes with highest overexpression, which can be obtained from the GEO microarray depository under the GSE2862 tag [27]. As expected, and previously published [12], the strongest upregulated genes were *hsp-16.1*, *hsp-16.48* and *F44E5.4* and their duplicated loci. Individual genes that show elevated expression under heat-shock conditions were determined. To obtain information on whether these genes commonly express together, the genome-wide clique set analysis was performed as described [25,26]. The heat-shock data sets were used together with the publicly available coexpression cliques. Altogether 307 cliques had been obtained before, with the largest clique containing 1200 genes and the smallest clique containing 6 genes and the publicly available information was used (www.richterlab.de/DataSets/ and https://github.com/klarichter/clusterEX_cliques_Celegans) [25,26]. We then used each of the three microarray replicates to assign their values to the genes in the coexpression cliques and analyzed those in respect to significant induction or repression as previously described for yeast and nematode expression studies [25,26]. As the publicly available heat-shock experiments were also performed on the GPL200 platform (Affymetrix C. elegans genome st-1.0), each Probe Set ID was represented by exactly one value in the described clique set. Analyses were performed for each replicate and average values for each clique were calculated to rank the cliques according to their average induction and p-values for induction significance as described [25,26].

HSE-detection in the promoter regions

HSE-detection in the promoter region 1000 bp upstream of the ATG was performed based on the PWM-models published for the human Hsf1's DNA binding sequence [28], which is represented by the following PWM pattern:

A	0.41	-3.20	1.13	1.05	-0.86	-0.55	-2.10	-1.61	-0.17	-1.28	0.58	-5.77	1.14	1.11	0.26
C	-0.57	-5.19	-5.19	-3.58	0.84	0.73	0.02	0.34	1.14	0.06	-0.53	-5.19	-5.19	-5.19	-0.21
G	0.84	1.70	-3.11	-1.20	-0.18	0.37	-0.70	-4.50	-0.27	-2.63	0.58	1.71	-5.19	-1.83	0.23
T	-5.77	-5.77	-5.77	-2.37	-0.08	-0.58	0.77	0.76	-2.40	0.79	-5.77	-5.77	-5.77	-5.77	-0.41

The 1000 bp promoter regions were obtained from Wormbase (www.wormbase.org) [29] and searched with this HSF-1 consensus description. As recommended, a threshold level of 9 was used as lower limit for detection [30]. In several cases HSEs were detected in the same promoter and located only 5 bp from each other, which implies that the investigated HSE actually is a tetrameric HSE. If this pattern is observed a second time, a pentameric HSE-element was detected or in rare cases even larger arrays of HSEs were detected.

HSF-1 fragmentation and purification

The N- and C-terminus of C. elegans HSF-1 were determined by comparing both hydropathy plots and sequence alignments of different Hsf proteins from diverse species. This yielded the fragment AA82-AA198 which was subcloned into the pGATE vector (HSF-1 DBD) and fused with a GST-tag. A GST-trap column was used for purification and the GST-tag was cleaved off by the TEV-protease before it was further purified via ion exchange chromatography and size-exclusion chromatography (all columns from GE Healthcare, Chicago, USA). Purity was determined by SDS-PAGE and peptide fingerprinting using mass spectrometry on a Bruker ultra-flex III MALDI-TOF/TOF instrument (Bruker, Billerica, USA) was employed to confirm the identity of the protein.

Circular Dichroism Spectroscopy

CD-spectroscopy on a Jasco J-715 was performed to obtain information on the structure and stability of the HSF-1 fragment. The folding state and the thermal stability of the expressed HSF-1 fragment was assessed at a concentration of 0.2 mg/mL in storage buffer (40 mM K_2HPO_4, 150 mM KCl). CD-spectra were recorded in the Far-UV region between 215 and 260 nm. To analyze the thermal stability of the fragment an unfolding transition was recorded at 220 nm in a temperature range between 25-95 °C.

Thermal shift assays

The stability of the folded structure was analyzed with thermal shift assays in a MxP3005 qPCR cycler (Stratagene, La Jolla, USA). Thermal shift assays were performed at a protein concentration of 0.2 mg/mL after addition of SYPRO orange (Invitrogen, Waltham, USA) at a dilution of 1:1000. The total volume was adjusted to 20 µL with storage buffer. The emission of SYPRO orange is recorded by excitation at 470 nm at a wavelength of 570 nm to monitor the temperature induced transition in the temperature range of 25 to 95 °C.

EMSA shift assays

ssDNA probes representing the promoter regions of *F44E5.5*, *Hsp-16.2a*, *Hsp16.2b*, *hsp-1*, *hsp-70*, *dnj-12 and dnj-13* were obtained from Eurofins MWG Biotech (Eurofins MWG Biotech, Ebersberg, Germany). An equal amount of forward and reverse complementary strand was incubated at 95 °C and aligned at room temperature. The interaction between these dsDNAs and the HSF-1 DBD was then monitored by EMSA shift assays, by performing a native PAGE after DBD was added to the dsDNA. Gels were incubated in SYBR green for DNA detection and analyzed in a Typhoon Fluorescence Scanner (GE Healthcare, Chicago, USA) using the Alexa Fluor filter at 532 nm and stained with Coomassie for visualization of the protein complex.

Analytical ultracentrifugation and determination of species distributions

Analytical ultracentrifugation was performed in a ProteomeLab XL-A analytical ultracentrifuge (Beckman-Coutler, Brea, USA) to determine the binding of HSF-1 DBD to dsDNA sequences. To this end single strand DNA sequences from different promoter regions of the same length were mixed with equal amounts of their complement strand in storage buffer, heated up to 95 °C and then cooled to RT to generate the double stranded DNA product that represents the promoter region. HSF-1 DBD was added to 1.5 µM dsDNA at different concentrations (0 µM, 2.25 µM, 4.5 µM, 7.5 µM, 10.5 µM, 15 µM and 22.5 µM) and the absorbance of these samples

was detected in analytical ultracentrifugation sedimentation velocity experiments at 260 nm and 280 nm at 42,000 rpm.

Data analysis of individual samples was performed with UltraScan III Version 4.0 (https://ultrascan3.aucsolutions.com/) [31]. All experiments were analyzed with the 2DSA-IT model employing the same settings (s-value range from 0 to 10 and f/f0 range from 1 to 4). This way two species distributions were obtained for each experiment, one for the data at 280 nm and one for 260 nm. The complexity of these distributions did not allow a unanimous assignment of solutes to species, which suggests that for a unifying solution a further reduction in search space has to be enforced. A reduced model therefore contained only the most abundant species of the binding reaction (HSF-1 DBD, ssDNA, dsDNA, dsDNA+1 HSF-1, dsDNA + 2 HSF-1, dsDNA + 3 HSF-1, dsDNA + 4 HSF-1 and dsDNA + 5 HSF-1) at defined $s_{20,w}$ values. These values were known for HSF-1 DBD, dsDNA and ssDNA from control experiments, while the other species were estimated from a stepwise optimization of these values. Given that all DNA strands were of the same size, a unique value for the sedimentation coefficient ($s_{20,w}$) of each assembly intermediate was assigned independent of the dsDNA used.

A custom grid model containing the species at the respective $s_{20,w}$ values was developed in UltraScan III and used to fit all data sets again. RMSD values of the unconstrained fit and the custom grid constrained fit were compared to verify that the fit quality despite the constraints is acceptable and the species $s_{20,w}$ values are sufficiently good estimates. To estimate the specific volume of each species and to confirm the MW of each obtained species the following equation was used:

$$\bar{v}_c = \sum_{i=1}^{N} f_i \bar{v}_i = f_p \bar{v}_p + \sum f_{np} \bar{v}_{np},$$

Value pairs for $D_{20,w}$ and $s_{20,w}$ were estimated and the extinction coefficients, specific volumes and molecular weights were calculated for each species in the custom grid model.

Estimation of interaction parameters for dsDNA-DBD interaction

Data analysis was finally performed using the species concentrations determined from UltraScan III in the first unconstrained 2DSA-IT analysis and data fitting was based on previously developed models. The fitting function was modified from an Origin DLL-file developed originally for the interaction of two proteins (PPH-5 and HSP-90) [32] to now describe the five-step binding process. Fitting was performed in analogy to the Nelder-Mead implementation for C# accessible at https://docs.microsoft.com/de-de/archive/msdn-magazine/2013/june/test-run-amoeba-method-optimization-using-csharp. Employing this function, K_D-values for each step could be estimated. Cooperativity was observed, if K_D-values for later assembly steps showed higher affinity than K_D-values for early binding steps. Despite the constrained model the obtained K_D-values contain large error intervals and are therefore considered as estimations due to the complexity of the binding events and the differences within the individual binding sites on the DNA.

Results

The heat-shock response is represented by a small set of genes in C. elegans

To distinguish heat shock inducible and non-inducible HSE-sites in the promoter regions, we aimed at defining the coregulated set of genes that represents the standard heat-shock response. To this end, we used a method previously described [26] to determine significant coregulation units responding to heat shock. The procedure employs 307 predefined coexpression cliques and overlays an actual experiment onto them to define responsive and non-responsive cliques. To identify the cliques that most strongly react to heat-shock, we used microarray data of experiments, which targeted this condition [27]. In all three replicates, in particular one small cluster was highly induced ($\log_2 > 2$), which contains the well described heat-shock genes *hsp-16.1*, *hsp-16.2*, *hsp-16.48*, *hsp-16.41*, *hsp-70*, *F44E5.4* and *F44E5.5* and in addition *unc-23* and *lact-4* (replicate 1 in Figure 1a, Summary of the three replicates in Table 1). While *unc-23* and *lact-4* were not significantly upregulated in the three microarray experiments, the other genes indeed represent this generally coregulated clique. Other cliques do not show a similarly high level of upregulation and this cluster clearly stood out with its 4.2-fold average induction (Table 1). Several canonical chaperones, like *dnj-12* (two probes in cliques **cdc-42_17192-rab-5_18073** and **srj-42-srw-113**), *dnj-13* (two probes in cliques **unc-116_2109-zfp-1_3976** and **tars-1-AFFX-r2-3026-5_at**) and the constitutively expressed Hsc70-homolog *hsp-1* (clique **dld-1-skn-1_16701**) are not part of the HSR-clique and we individually tested their induction to confirm that indeed they are not induced (Table 2). As they indeed are not upregulated in either of the replicates, the assignment to other cliques is obviously in line with the analyzed heat-induced samples of this data set.

Nematode HSEs vary widely in size and co-expression clique affiliation

We aimed at understanding, whether different affinities of the heat-shock transcription factor HSF-1 for the promoter sequences can be observed. Previous reports had highlighted that large number of HSEs can be found in the nematode genome [20,33]. Apparently, most of these genes are not induced upon heat-shock. To obtain the HSEs of the genes of interest we searched the 1000 bp promoter regions of all genes of *C. elegans*. We identified 4120 HSE in genes, which contain a consensus sequence for HSF-1 in their promoter region. Despite not being induced upon heat-shock, several genes related to the chaperone system were found to contain HSE-like sequences in the promoter region, like *dnj-12*, *dnj-13,* and *hsp-1*. These HSEs apparently are not used more strongly under heat-shock conditions to initiate an induction of the gene. Many other genes containing HSEs enrich in different cliques, which obviously also are not upregulated under heat-stress conditions. We then compared the sequence and structure of the HSEs in the promoter region of the chaperone proteins. Surprisingly, several promoters in the HSR-cluster contain more HSEs than the usually expected trimeric DNA-binding sequence, like *hsp-16.2a* and *F44E5.4*, which contain four or five HSF-1 binding sites in close vicinity (Figure 1b).

The isolated DBD of HSF-1 shows affinity to the F44E5.4 inducible promoter.

To test, to what extent binding differences correlate with expression differences and structural differences of the HSE we set out to determine *in vitro*, how the interaction of HSF-1 DBD is at these differently structured HSEs. To this end the isolated DNA binding domain of nematode

HSF-1 was purified, containing the DBD and omitting the nematode-specific sequences at the N-terminus and the further regulatory domains at the C-terminus. The structure of the purified DNA-binding domain was investigated by far-UV CD-spectroscopy. The spectra revealed a mostly α-helical structure (Figure 2a). To confirm the stability of the domain, we performed a thermal transition in the Far-UV CD-range and obtained a temperature midpoint of the unfolding transition of 55 °C (Figure 2b). We also performed a stability investigation employing the TSA assay, where no obvious differences were observed regarding the melting point (Figure 2c). Thus, all spectroscopic methods imply that the isolated DNA-binding domain of *C. elegans* HSF-1 is a stable and structured protein.

dsDNA probes generated by us from the heat-shock responsive cluster, in order to gain a better insight into the differential expression form the chaperone-gene derived HSEs. *F44E5.4* features a high consensus score pentameric site, both *hsp-70* and *unc-23* consist of only one trimeric site, while *hsp-16.2* has a high consensus score tetrameric site plus an additional trimeric site. Probes of equal length were also made for *hsp-1, dnj12* (trimeric HSE-site) and *dnj-13* (tetrameric site) representing the non-induced heat-shock related proteins. Since both sequence and position in the promoter region of the following genes are identical the probe for *F44E5.4* also represents *F44E5.5*, while *hsp-16.2* represents *hsp-16.11*, *hsp-16.41*, *hsp-16.48*. The sequences of the probes were obtained from the respective promoter regions. Here only HSEs were considered that locate within 1000 bps upstream of the starting point of transcription (Table 3). *F44E5.4*p contains more HSEs in its sequence than synthesized in this study (comparison of the promoter regions), but here likewise the probes with the highest consensus score were synthesized.

EMSA-assays imply differences between the chaperone-gene derived HSEs

Electrophoretic-mobility shift assays (EMSA) were performed to test the interaction between purified HSF-1 DBD and dsDNAs (Figure 3a). We set out to perform an initial binding analysis HSF-1 DBD to the promotor of *F44E5.4*, which also contains the highest amount of HSEs compared to the promoters used in this study. To this end, we titrated the DBD of HSF-1 with concentrations ranging from 0-22.5 µM to 1.5 µM of promoter DNA, which represents a 15-fold molar excess at the highest concentration. Notably a saturated complex of protein and DNA was reached at a concentration of 10 µM HSF1-DBD, at which the complex bands could be observed on the Coomassie stained gel, while at the same time no further reduction in free DNA was visible. Following this initial analysis, we also tested the dsDNA probes of *hsp-70, hsp-1, hsp-16.2, unc-23, dnj-12* and *dnj-13* under the same conditions. 10 µM HSF-1 DBD was added to each probe to determine the formation of the respective protein-DNA complex (Figure 3b), which showed depending on the probe used, a highly variable reduction in migration speed. While probes derived from the promoter of *dnj-13, unc-23* and *hsp-1* hardly showed any interaction with the DBD of HSF-1, *F44E5.4*, *hsp-70*, *hsp16.2* and *dnj-12* derived probes appeared to interact strongly, thereby forming intense bands with HSF-1 DBD, representing the dsDNA-protein complex. These results indicate that the HSF-1 DBD alone can interact with the different promoter-derived HSEs to a different extent.

Analytical ultracentrifugation confirms the binding differences at the various HSE-sites.

To unravel the interaction patterns, we performed SV-AUC under the condition employed for the gel-based assay. To this end, a titration with the DNA probe representing *F44E5.4*p was

performed. Addition of HSF-1 DBD resulted in an increase in the sedimentation coefficient, indicating the binding of HSF-1 DBD to dsDNA (Figure 4). In the titration, the progressive binding of HSF-1 DBD molecules increases the $s_{20,w}$ of the main species and indicates further complex formation at higher protein:DNA ratios. The complex with *F44E5.4*p appears to reach a saturated level when a 10-fold excess of HSF-1 DBD is added. At this point, the presence of remaining unbound HSF-1 DBD becomes clearly visible, which is in agreement to the EMSA binding assay.
Having investigated the promoter region with 5 potential binding sites, we tested, whether the promoter regions with less binding sites, show a similar response. Thus, the same approach was chosen for a DNA with only 3 binding sites derived from the promoter of *hsp-70*. Clearly the saturation point of the binding reaction was shifted to lower $s_{20,w}$ values in both wavelength detection modes, suggesting that in this case less HSF-1 DBD molecules bind to the promoter (Figure 5a). This behavior therefore appears to be a sequence-specific property. Further analog experiments were performed with all the other dsDNA strands and initially the highest $s_{20,w}$ values were noted (Figure 5b-g).

SV-AUC fitting to defined species reveals potential differences in occupation of complex binding sites.
The apparently very weak interaction at several consistent – at least on a monomeric level – HSE sites, questions the independent interaction of monomeric units at these sites. UltraScan III was employed to analyze the data from these experiments and to obtain information on the binding equilibrium in solution. To this end we compared the general ability to fit the data with a very flexible model (2DSA-IT) and with a very constrained model, where a custom grid was designed containing one $s_{20,w}$ value (Table 4) for each species to be considered (2DSA-CG-IT). This method reveals available free protein concentration dependent changes in complex species distributions and offers the opportunity to fit distributions of DNA/protein complex obtained directly from raw data to hypothetical species, thus, to obtain the concentration of each potential complex species and to describe the composition of the complex mixture in each sample. The comparison of RMSD values from 2DSA-IT and the much more restricted 2DSA-CG-IT of each complex species formed with different DNAs is shown in Figure 6 for *F44E5.4*p and in Figure 7, as well as in Supplement Figures 1-6 for the remaining DNA constructs. It is very clear from these data that different assembly mechanisms are happening in different probes and different stoichiometries must be assumed. In the UltraScan III analysis, the higher order complexes are only populated when using larger HSEs and in all cases the buildup of the free HSF-1 DBD can be observed at the higher concentrations employed in each titration. Furthermore, almost no binding was observed for the constructs of *hsp-1, dnj-13,* and *unc-23.* (Figure 7d, 7e and 7f)

Global fitting of stepwise binding models implies cooperative action at later binding steps.
We then set out to globally fit one titration to a predefined set of species, which is kept invariant throughout all the DNA probes analyzed. This is possible, as the dsDNA strands are of equal length and the binding sites are engineered to be in the middle of each dsDNA scaffold. Indeed, for each of the stronger binding species, the second binding step is exposing a lower dissociation constant compared to the first binding steps and similar relationships occur at the later binding steps at probes that harbor more than three binding sites. In fact, the four strongly interacting

systems (*hsp-70*, *hsp-16.2a*, *hsp-16.2b* and *F44E5.4*) show a second binding step with submicromolar affinity, while the first binding step is weaker (Table 5). Thus, it is indeed to be expected that cooperative actions increase the binding affinity and interactions between the occupied binding sites modulate and potentially coordinate the binding of HSF-1 at these HSEs.

Discussion

In the nematode genome there are 4120 HSEs, which contain HSF-1 binding consensus regions in the 500 bp upstream of their start codon. It is very surprising that despite these many HSF-1 regulated genes the canonical heat-shock response only represents a clique of 8 genes, 7 of which are regulated by HSF-1 binding promoter regions. Thus, the extent of regulation resulting from HSF-1's actions is clearly well beyond the induction of stress genes under stress conditions and reaches far into the normal growth cycle of the nematode under non-stressed conditions. The ability to resolve the clique membership based on coexpression analysis shows that also in larger organisms this approach may be successful and able to connect different cliques to different tissues and developmental states.

We here tested the binding of the HSF-1 DBD to some of the likely interacting promoter regions. From these studies we can find that the HSF-1 DBD alone can bind the HSE-regions originated from the genome with certain selectivity based on its affinity. Despite this, the affinities correlate to some extent with the calculated consensus score and with the inducibility of the respective gene. It is interesting to note, that despite the proposed trimeric binding mode, tetrameric and pentameric HSEs exist and that binding to those sites is driven by additional cooperativity. Among the probes we investigate in this study, the tetrameric and pentameric sites represent those, which are inducible upon heat-shock.

One exception among the probes studied here is formed by *dnj-12*, which is not inducible but well capable of binding to the HSF-1 DBD and given the ubiquitous expression of this protein it might be envisioned that its binding to HSF-1 is constitutive, and the induced expression therefore is not increased upon heat-shock, but these correlations need to be confirmed in subsequent studies. This logic may be relevant for many of the 4120 HSE-binding sites found in promoter regions. Nevertheless, it is important to note, that our approach solely considers the DBD of HSF-1 and that HSF-1 HSE binding as a whole is further regulated by posttranslational modifications, like phosphorylation [34,35] and deacetylation [36].

In general, the developed AUC assay to test the binding of several proteins to one DNA strand is very valuable in quantifying the binding events and may represent an opportunity to study the many interactions occurring on dsDNA with different binding sites for individual transcription factors. While the sedimentation coefficients for the custom grid are an assumption, they provide a rational to obtain stepwise binding information from the SV-AUC titration data. The absolute values of the obtained stepwise dissociation constants are to be used with care, but trends can be derived from these values with good confidence.

The ability to resolve different intermediate assembly steps may be further increased by using direct interaction models for the fitting, but the stepwise procedure shown here already represents the chance to quantify these events. Nevertheless, the grouping of the genes into coexpression cliques, the identification of common transcription factors for these cliques and the analysis of binding events to the predicted transcription factor binding sites opens possibilities to gain further insight into the complex relationships leading to the spatio-temporal expression of genes during development and aging of *C. elegans*, or complex multi-step binding reactions in general.

Acknowledgements

K.R., L.S. and S.S. thank the Deutsche Forschungsgemeinschaft for funding the research grant RI1873/1-4 and the Heisenberg position RI1873/5-1. We also thank the distributors of free and open-source software that we could use during this study. This includes This includes UltraScan III Version 4.0 (https://ultrascan3.aucsolutions.com/), RMAexpress 1.0.5 by Ben Bolstad (https://rmaexpress.bmbolstad.com/) and Cytoscape 3.8.2 (Cytoscape Consortium, https://cytoscape.org/).

Additional Information

Author contributions

S.S. and K.R. designed the experiments, S.S., L.S., A.B.H., R.C., performed the experiments, S.S., L.S. and K.R. analyzed the data and wrote the manuscript.

Competing interests

The authors do not have competing interests in respect to this study.

Data Availability

All data are fully available without restriction.

References.

1 Vihervaara, A. & Sistonen, L. HSF1 at a glance. *Journal of cell science* **127**, 261-266, doi:10.1242/jcs.132605 (2014).

2 Skaggs, H. S. *et al.* HSF1-TPR interaction facilitates export of stress-induced HSP70 mRNA. *The Journal of biological chemistry* **282**, 33902-33907, doi:10.1074/jbc.M704054200 (2007).

3 Williams, R. S. & Benjamin, I. J. Protective responses in the ischemic myocardium. *The Journal of clinical investigation* **106**, 813-818, doi:10.1172/JCI11205 (2000).

4 Xiao, X. *et al.* HSF1 is required for extra-embryonic development, postnatal growth and protection during inflammatory responses in mice. *The EMBO journal* **18**, 5943-5952, doi:10.1093/emboj/18.21.5943 (1999).

5 Kallio, M. *et al.* Brain abnormalities, defective meiotic chromosome synapsis and female subfertility in HSF2 null mice. *The EMBO journal* **21**, 2591-2601, doi:10.1093/emboj/21.11.2591 (2002).

6 Kaitsuka, T., Tomizawa, K. & Matsushita, M. Transformation of eEF1Bdelta into heat-shock response transcription factor by alternative splicing. *EMBO reports* **12**, 673-681, doi:10.1038/embor.2011.82 (2011).

7 Kubota, H., Matsumoto, S., Yokota, S., Yanagi, H. & Yura, T. Transcriptional activation of mouse cytosolic chaperonin CCT subunit genes by heat shock factors HSF1 and HSF2. *FEBS letters* **461**, 125-129 (1999).

8 Cahill, C. M., Waterman, W. R., Xie, Y., Auron, P. E. & Calderwood, S. K. Transcriptional repression of the prointerleukin 1beta gene by heat shock factor 1. *The Journal of biological chemistry* **271**, 24874-24879 (1996).

9 Pirkkala, L., Nykanen, P. & Sistonen, L. Roles of the heat shock transcription factors in regulation of the heat shock response and beyond. *FASEB journal : official publication of the Federation of American Societies for Experimental Biology* **15**, 1118-1131 (2001).

10 Gidalevitz, T., Prahlad, V. & Morimoto, R. I. The stress of protein misfolding: from single cells to multicellular organisms. *Cold Spring Harbor perspectives in biology* **3**, doi:10.1101/cshperspect.a009704 (2011).

11 Joutsen, J. & Sistonen, L. Tailoring of Proteostasis Networks with Heat Shock Factors. *Cold Spring Harb Perspect Biol* **11**, doi:10.1101/cshperspect.a034066 (2019).

12 Brunquell, J., Morris, S., Lu, Y., Cheng, F. & Westerheide, S. D. The genome-wide role of HSF-1 in the regulation of gene expression in Caenorhabditis elegans. *BMC Genomics* **17**, 559, doi:10.1186/s12864-016-2837-5 (2016).

13 Guisbert, E., Czyz, D. M., Richter, K., McMullen, P. D. & Morimoto, R. I. Identification of a tissue-selective heat shock response regulatory network. *PLoS Genet* **9**, e1003466, doi:10.1371/journal.pgen.1003466 (2013).

14 Li, J., Chauve, L., Phelps, G., Brielmann, R. M. & Morimoto, R. I. E2F coregulates an essential HSF developmental program that is distinct from the heat-shock response. *Genes & development* **30**, 2062-2075, doi:10.1101/gad.283317.116 (2016).

15 Hsu, A. L., Murphy, C. T. & Kenyon, C. Regulation of aging and age-related disease by DAF-16 and heat-shock factor. *Science* **300**, 1142-1145, doi:10.1126/science.1083701 (2003).

16 Morley, J. F. & Morimoto, R. I. Regulation of longevity in Caenorhabditis elegans by heat shock factor and molecular chaperones. *Mol Biol Cell* **15**, 657-664, doi:10.1091/mbc.e03-07-0532 (2004).

17 Brunquell, J., Snyder, A., Cheng, F. & Westerheide, S. D. HSF-1 is a regulator of miRNA expression in Caenorhabditis elegans. *PLoS One* **12**, e0183445, doi:10.1371/journal.pone.0183445 (2017).

18 Ben-Zvi, A., Miller, E. A. & Morimoto, R. I. Collapse of proteostasis represents an early molecular event in Caenorhabditis elegans aging. *Proc Natl Acad Sci U S A* **106**, 14914-14919, doi:10.1073/pnas.0902882106 (2009).

19 Morimoto, R. I. The heat shock response: systems biology of proteotoxic stress in aging and disease. *Cold Spring Harb Symp Quant Biol* **76**, 91-99, doi:10.1101/sqb.2012.76.010637 (2011).

20 GuhaThakurta, D. *et al.* Identification of a novel cis-regulatory element involved in the heat shock response in Caenorhabditis elegans using microarray gene expression and computational methods. *Genome Res* **12**, 701-712, doi:10.1101/gr.228902 (2002).

21 Gaiser, A. M., Kaiser, C. J., Haslbeck, V. & Richter, K. Downregulation of the Hsp90 system causes defects in muscle cells of Caenorhabditis elegans. *PLoS One* **6**, e25485, doi:10.1371/journal.pone.0025485 (2011).

22 Wang, X. *et al.* Phosphorylation of HSF1 by MAPK-activated protein kinase 2 on serine 121, inhibits transcriptional activity and promotes HSP90 binding. *The Journal of biological chemistry* **281**, 782-791, doi:10.1074/jbc.M505822200 (2006).

23 Xing, H., Mayhew, C. N., Cullen, K. E., Park-Sarge, O. K. & Sarge, K. D. HSF1 modulation of Hsp70 mRNA polyadenylation via interaction with symplekin. *The Journal of biological chemistry* **279**, 10551-10555, doi:10.1074/jbc.M311719200 (2004).

24 Guo, Y. *et al.* Evidence for a mechanism of repression of heat shock factor 1 transcriptional activity by a multichaperone complex. *The Journal of biological chemistry* **276**, 45791-45799, doi:10.1074/jbc.M105931200 (2001).

25 Sima, S., Schmauder, L. & Richter, K. Genome-wide analysis of yeast expression data based on a priori generated co-regulation cliques. *Microb Cell* **6**, 160-176, doi:10.15698/mic2019.03.671 (2019).

26 Schmauder, L. & Richter, K. hsp-90 and unc-45 depletion induce characteristic transcriptional signatures in coexpression cliques of C. elegans. *Sci Rep* **11**, 12852, doi:10.1038/s41598-021-91690-6 (2021).

27 Wang, P., Zhao, J. & Corsi, A. K. Identification of novel target genes of CeTwist and CeE/DA. *Developmental biology* **293**, 486-498, doi:10.1016/j.ydbio.2005.10.011 (2006).

28 Pachkov, M., Erb, I., Molina, N. & van Nimwegen, E. SwissRegulon: a database of genome-wide annotations of regulatory sites. *Nucleic Acids Res* **35**, D127-131, doi:10.1093/nar/gkl857 (2007).

29 Stein, L., Sternberg, P., Durbin, R., Thierry-Mieg, J. & Spieth, J. WormBase: network access to the genome and biology of Caenorhabditis elegans. *Nucleic Acids Res* **29**, 82-86, doi:10.1093/nar/29.1.82 (2001).

30 Wang, S., Cheng, X., Li, Y., Wu, M. & Zhao, Y. Image-based promoter prediction: a promoter prediction method based on evolutionarily generated patterns. *Sci Rep* **8**, 17695, doi:10.1038/s41598-018-36308-0 (2018).

31 Demeler, B., Brookes, E. & Nagel-Steger, L. Analysis of heterogeneity in molecular weight and shape by analytical ultracentrifugation using parallel distributed computing. *Methods Enzymol* **454**, 87-113, doi:10.1016/S0076-6879(08)03804-4 (2009).

32 Haslbeck, V. *et al.* The activity of protein phosphatase 5 towards native clients is modulated by the middle- and C-terminal domains of Hsp90. *Sci Rep* **5**, 17058, doi:10.1038/srep17058 (2015).

33 Garrigues, J. M., Tsu, B. V., Daugherty, M. D. & Pasquinelli, A. E. Diversification of the Caenorhabditis heat shock response by Helitron transposable elements. *eLife* **8**, e51139, doi:10.7554/eLife.51139 (2019).

34 Hietakangas, V. *et al.* Phosphorylation of serine 303 is a prerequisite for the stress-inducible SUMO modification of heat shock factor 1. *Mol Cell Biol* **23**, 2953-2968, doi:10.1128/MCB.23.8.2953-2968.2003 (2003).

35 Holmberg, C. I., Tran, S. E., Eriksson, J. E. & Sistonen, L. Multisite phosphorylation provides sophisticated regulation of transcription factors. *Trends Biochem Sci* **27**, 619-627, doi:10.1016/s0968-0004(02)02207-7 (2002).

36 Zelin, E. & Freeman, B. C. Lysine deacetylases regulate the heat shock response including the age-associated impairment of HSF1. *J Mol Biol* **427**, 1644-1654, doi:10.1016/j.jmb.2015.02.010 (2015).

Table Legends.

Table 1. Cliques identified as significantly up- or downregulated in the heat-shock experiments of WANG *et al.* (GSE2862) [27]. The average values for the three replicate experiments are shown together with the standard deviation and the clique size.

Table 2. Significantly enriched genes and their clique assignment, or number of HSEs in the promoter region of the included genes. Individual induced genes are shown and their association to cliques. Further the number of HSEs modules that can be found within 1000 bp of their upstream promoter sequence.

Table 3. HSE-containing probes designed from the promoter sequences of chaperone genes and used in the binding studies. The designed probes originate from the 1000 bp promoter sequence and are positioned as indicated. The strand and anti-sense strand were synthesized and combined to give the promoter sequence able to bind HSEs.

Table 4. Parameters used for custom grid fitting approach. Generally applicable sedimentation coefficients were obtained for this model system, where HSEs are embedded into probes of identical size. Extinction coefficients are also shown. f/f0 was kept floating during the fit with the custom grid model, while the $s_{20,w}$ was set to allow only the species mentioned in this table.

Table 5. Calculated K_D values derived from SV-AUC fitting. No color coding = cooperativity, orange color coding = weak cooperativity, red color coding = no cooperativity

Figure Legends.

Figure 1. Determined coexpression cliques and utilized promoter regions. a) Genome clustered in 307 expression groups derived from public expression experiments. The color code reflects the heat-shock response as determined by WANG *et al.* (GSE2862) [27]. The highly induced cluster is enlarged for better visualization (see blue box at the bottom left). b) Promoter region of inducible and non-inducible chaperones, relative to the ATG start codon.

Figure 2. Structure and stability of HSF-1 DBD fragment 82-198. a) CD-spectroscopy, b) thermal transition with CD-spectroscopy and c) TSA assay

Figure 3. EMSA shift of the DNA-HSF-1 complex. The DNAs were stained with the DNA stain (left gel) whereas proteins were stained with Coomassie Blue (right gel). a) Titration of HSF-1 DBD to the promotor F44E5.4; b) Comparison of selected DNA promotors.

Figure 4. Analysis of interaction between promotor F44E5.4 and Hsf-1 DBD via titration in SV-AUC. a) dc/dt plot of the absorbance measured at 260 nm and for b) at 280 nm at different concentrations of HSF-1 DBD, when added to 1.5 µM of HSE-containing DNA.

Figure 5. Analysis of interaction between selected promotors and Hsf-1 DBD via titration in SV-AUC. dc/dt plots of the absorbance measured at 260 nm (left panel) and at 280 nm (right panel). Respective promoters used: a) HSP16.2a; b) HSP16.2 b; c) HSP-70; d) HSP-1; e) DNJ-13; f) UNC-23; g) DNJ-12.

Figure 6. Custom grid fitting for F44E5.4-HSF-1 species. a) Average weight of DNA-HSF-1 complexes, b) Partial concentrations of used DNA and HSF-1 species c) Partial concentration of F44E5.4-HSF-1 complex species.

Figure 7. Partial concentration of each species in DNA-HSF-1 samples, derived via custom grid fitting. Selected promoter = a) HSP16.2a; b) HSP16.2b; c) HSP-70; d) HSP-1; e) DNJ-13; f) UNC-23.

Tables 1.

Table 1.

Clique Number	Clique Name	Clique Size	Genes with Signal in Array	Average Log_2	STD Log2
268	hsp-16.2-F44E5.4_19238	10	10	2.06	0.37
5	Y73B3A.2_1097-Y73B3A.2_1130	17	2	0.33	0.71
104	C10A4.6-C01A2.6	16	16	0.27	0.14
291	fbxc-6-F09C6.1	8	8	0.24	0.36
163	R05H5.4-F22D6.9_20949	5	5	0.22	0.27
235	C10C5.3-C10C5.5	6	6	0.22	0.20
241	fbxa-154_11499-Y44A6D.1	74	67	0.22	0.12
250	K12H6.6_1575-C23H4.6	6	6	0.19	0.33
80	C17H1.6-C17H1.13	76	75	0.19	0.13
169	C33H5.1-F49C12.2	11	11	0.18	0.36

Table 2.

Gene Name	Average Expression Change log_2	STD	Member of Clique	Controlled by HSEs [number]
hsp-16.41	4.33964945	0.47257324	**hsp-16.2-F44E5.4_19238**	7
hsp-16.1	3.37025306	0.36880836	**hsp-16.2-F44E5.4_19238**	7
hsp-16.2	3.24598022	0.57114605	**hsp-16.2-F44E5.4_19238**	7
F44E5.4_221	2.43535939	0.6531605	**hsp-16.2-F44E5.4_19238**	10
hsp-16.48	2.43449799	0.26151971	**hsp-16.2-F44E5.4_19238**	7
F44E5.4_19238	2.42823859	0.70781857	**hsp-16.2-F44E5.4_19238**	10
C27D6.1	2.17492883	0.66776873	**176662_at-Y53F4B.16**	-
fbxb-22	2.1705405	1.27504799	**sdz-10-fbxb-62**	-
math-6	2.12527449	0.85966164	**srj-21-srh-32**	-
F20B6.7	1.95293402	0.75883293	**tub-2_4713-daf-2_5288**	-
C15B12.3	1.87784369	0.59022648	**172183_at-176110_at**	-
Y6B3B.2	1.79628476	1.35642504	**183712_at-srbc-74_8864**	-
F28A10.9	1.7697348	0.4485698	**srj-42-srw-113**	-
C01B4.2	1.74098252	0.42244849	**srj-21-srh-32**	-
str-243	1.72570157	0.42783197	**sre-33-ZK1025.1_8337**	-
hsp-70	1.69538497	0.43818876	**hsp-16.2-F44E5.4_19238**	3
C07A9.5_18941	1.68623723	1.47072224	**F28H1.5-T05D4.5**	-
Y16E11A.2	1.67500495	0.73573836	**fbxa-154_11499-Y44A6D.1**	12
C31G12.3	1.64731562	1.2334763	**srj-42-srw-113**	-
F07B7.8_11449	1.62495315	1.43400867	**183712_at-srbc-74_8864**	-
clec-142	1.61733446	1.76090815	**F28H1.5-T05D4.5**	-
srh-258	1.59055877	0.53259038	**srj-42-srw-113**	-
scl-19	1.59004684	1.03454503	**srj-42-srw-113**	3
Y68A4B.3	1.58552192	1.18455696	**C33H5.1-F49C12.2**	-
clec-20	1.58507895	0.97920764	**sre-33-ZK1025.1_8337**	-
wrt-7	1.58082879	0.50613839	**grl-19-C13A2.4**	-
C04H5.7	1.56608678	0.85708337	**C46C2.5_15926-W03F11.1**	-
fbxb-118	1.56221989	0.81840697	**sdz-10-fbxb-62**	-
pqn-16	1.5514195	1.07311037	**srj-42-srw-113**	-
srh-154_13942	1.53974391	1.00629988	**srj-21-srh-32**	2
...				
lact-4	0.48976226	0.47729707	**hsp-16.2-F44E5.4_19238**	-
bag-1	0.44163843	0.29340987	**F54E7.8-orc-5_6376**	3
dnj-12_21104	0.2791495	0.14801702	**cdc-42_17192-rab-5_18073**	3
hsp-1	0.23010296	0.59319525	**dld-1-skn-1_16701**	6
unc-23_16614	0.0047227	0.216626	**hsp-16.2-F44E5.4_19238**	6
unc-23_3327	-0.07377314	0.30315485	**hsp-16.2-F44E5.4_19238**	6
dnj-13_17082	-0.41124351	0.31596264	**tars-1-AFFX-r2-3026-5_at**	7
dnj-12_3674	-0.49049134	0.41234554	**srj-42-srw-113**	3
dnj-13_3319	-0.51080312	0.14089521	**unc-116_2109-zfp-1_3976**	7

Table 3.

	fwd	rev	Trimeric consensus scores	Orien-tation	Start Position relative to ATG
DNJ-12	aaaagtgtcgagaatgtt cacgaaaaatcgttaga	tctaacgatttttcgtgaa cattctcgacactttt	9.66	Fwd	-221
DNJ-13	agtaaatagaacgctctg gaaagttccgcactctt	aagagtgcggaactttc cagagcgttctatttact	13.01, 9.1	Fwd, Rev	-205
F44E5.4	gcagtggaatattccag aagcttctagaagaagtt	aacttcttctagaagctt ctggaatattccactgc	11.59, 12.43, 13.07	Fwd, Rev, Fwd	-124 (also *F44E5.5*)
HSP-1	tgacgaaattcgaattttc tagaatcccgccacgc	gcgtggcgggattctag aaaattcgaatttcgtca	10.24	Fwd	-150
Hsp-16.2a	gccttacagaatgttcta gaaggtcctagatgcat	atgcatctaggaccttct agaacattctgtaaggc	9.41, 12.81	Rev, Fwd	-117 (*hsp-16.49* and *hsp-16.41*) -253 (*hsp-16.11* and *hsp-16.2*)
Hsp-16.2b	acaagcagctcgaatgtt ctagaaaaaggtggaaa	tttccacctttttctagaa cattcgagctgcttgt	11.86	Fwd	-104
Hsp-70	agtaaattgtagaaggtt ctagaagatgccagagg	cctctggcatcttctaga accttctacaatttact	12.71	Fwd	-112
Unc-23	acggagcctcggattctt ccagaaaattgagtctc	gagactcaattttctgga agaatccgaggctccgt	9.48	Fwd	-573

Table 4.

	$s_{20,w}$ (S)	E_{260} ($M^{-1}cm^{-1}$)	E_{280} ($M^{-1}cm^{-1}$)
HSF-1 DBD	1.75	8,388	13,980
dsDNA	3.15	563,198	304,431
ssDNA (residual from mixing)	1.75	355,400	192,108
dsDNA+1 DBD	3.9	571,586	318,411
dsDNA+2 DBD	4.65	579,974	332,391
dsDNA+3 DBD	5.35	588,362	346,371
dsDNA+4 DBD	5.95	596,750	360,351
dsDNA+5 DBD	6.55	605,138	374,331

Table 5.

	K_D1	K_D2	K_D3	K_D4	K_D5
Hsp1	12.25 ± 1.88	4.00 ± 2.64	0.23 ± 0.25	2.12 ± 2.03	4.21 ± 1.15
Unc23	8.71 ± 6.88	2.36 ± 4.81	5.82 ± 5.51	11.03 ± 6.99	17.50 ± 9.28
F44E5.4	7.48 ± 2.13	0.12 ± 0.05	2.9 ± 2.68	0.28 ± 0.31	18.15 ± 3.20
Hsp70	2.56 ± 0.75	0.91 ± 0.14	8.87 ± 0.46	400.19 ± 171.32	395.13 ± 26.33
Hsp16.2a	4.57 ± 0.83	0.70 ± 0.07	5.29 ± 0.26	35.39 ± 6.55	65.23 ± 20.42
Hsp16.2b	3.47 ± 2.15	0.90 ± 0.39	18.75 ± 7.52	21.32 ± 12.25	18.05 ± 8.57
Dnj13	6.66 ± 1.93	9.70 ± 2.85	25.26 ± 18.36	36.93 ± 15.79	9.42 ± 4.65

Figures.

Figure 1.

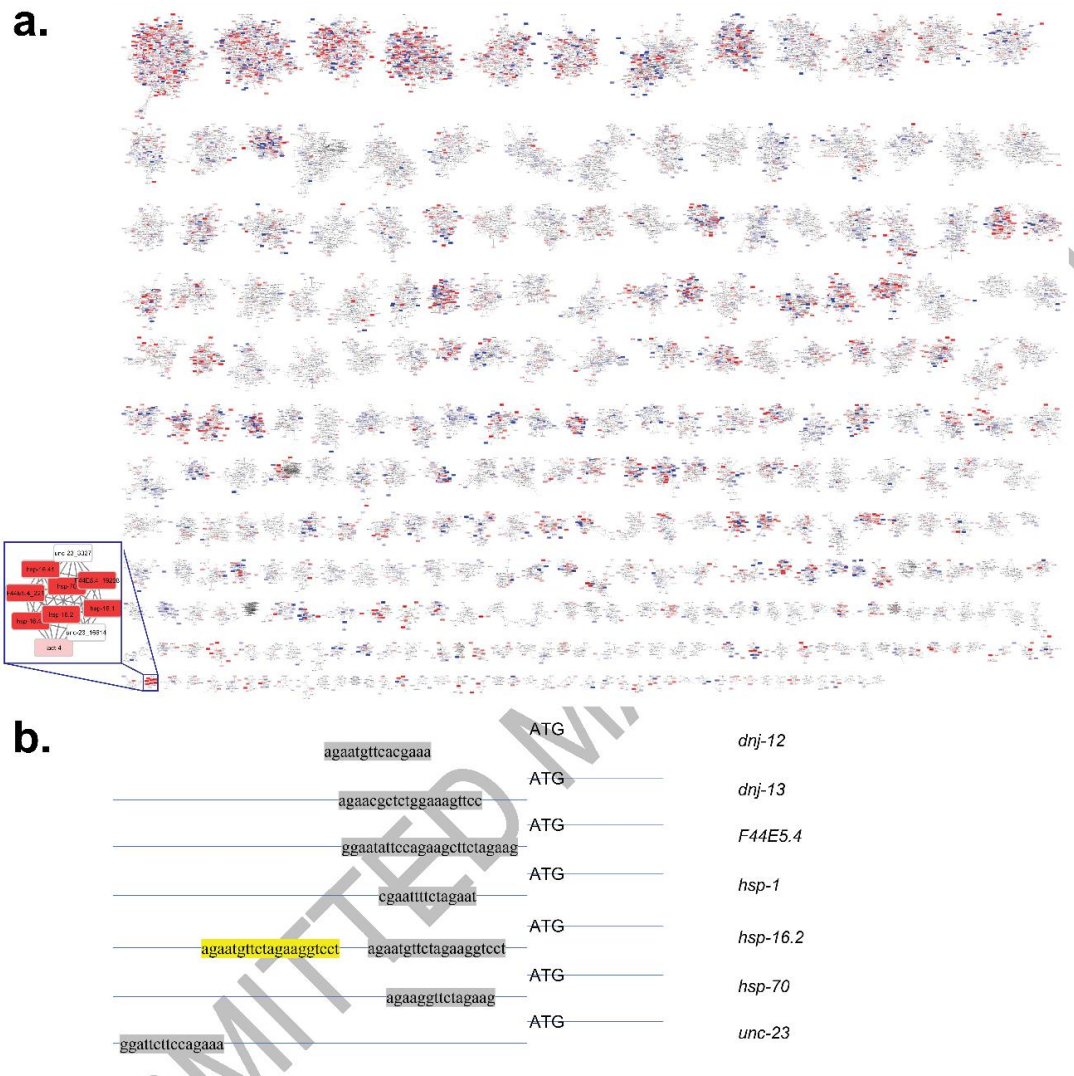

Figure 2.

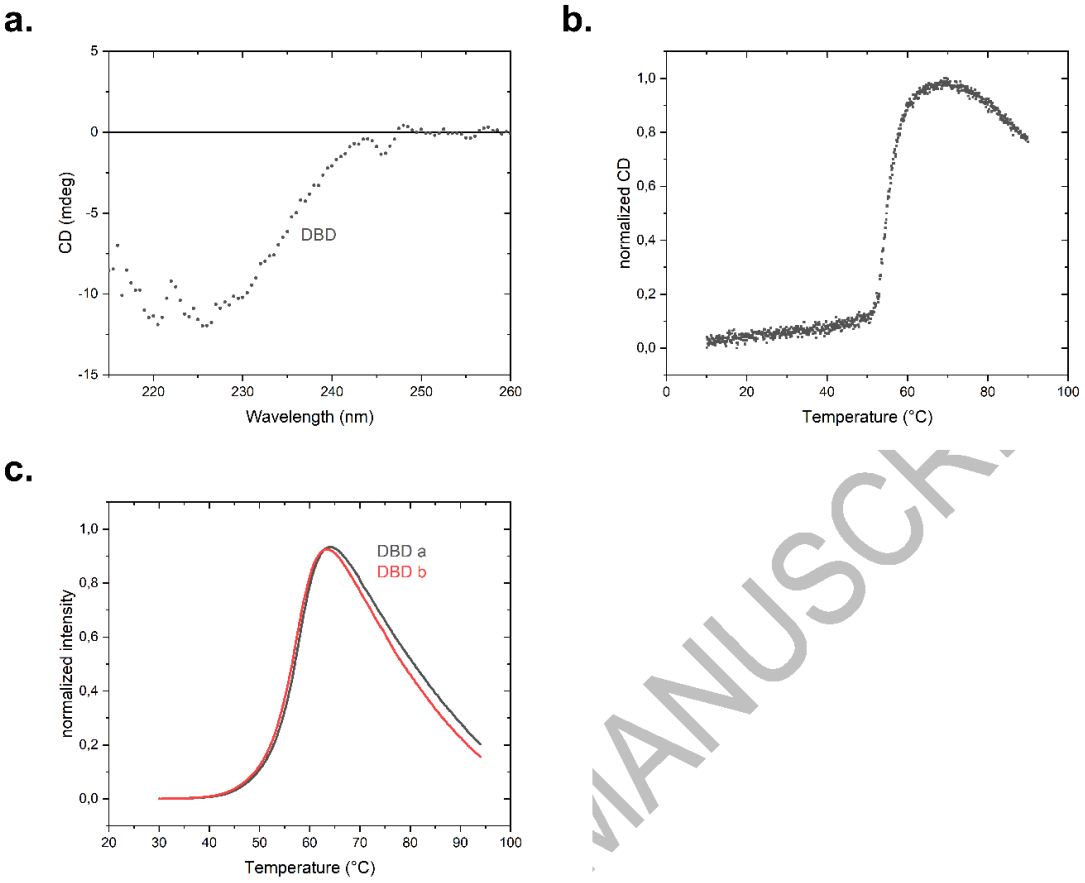

Figure 3.

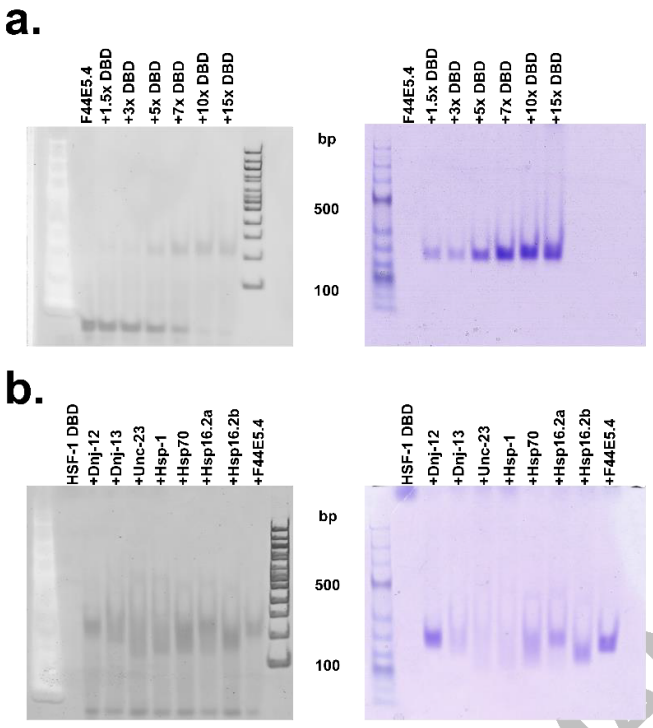

Figure 4.

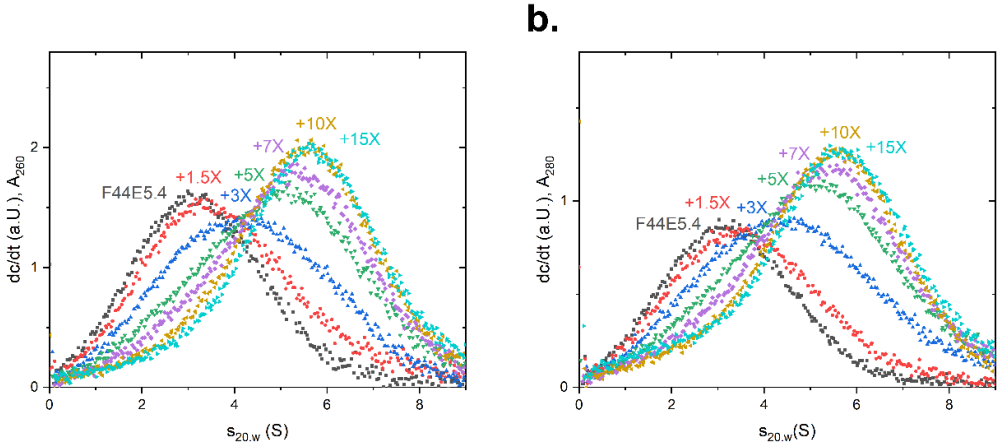

Figure 5.

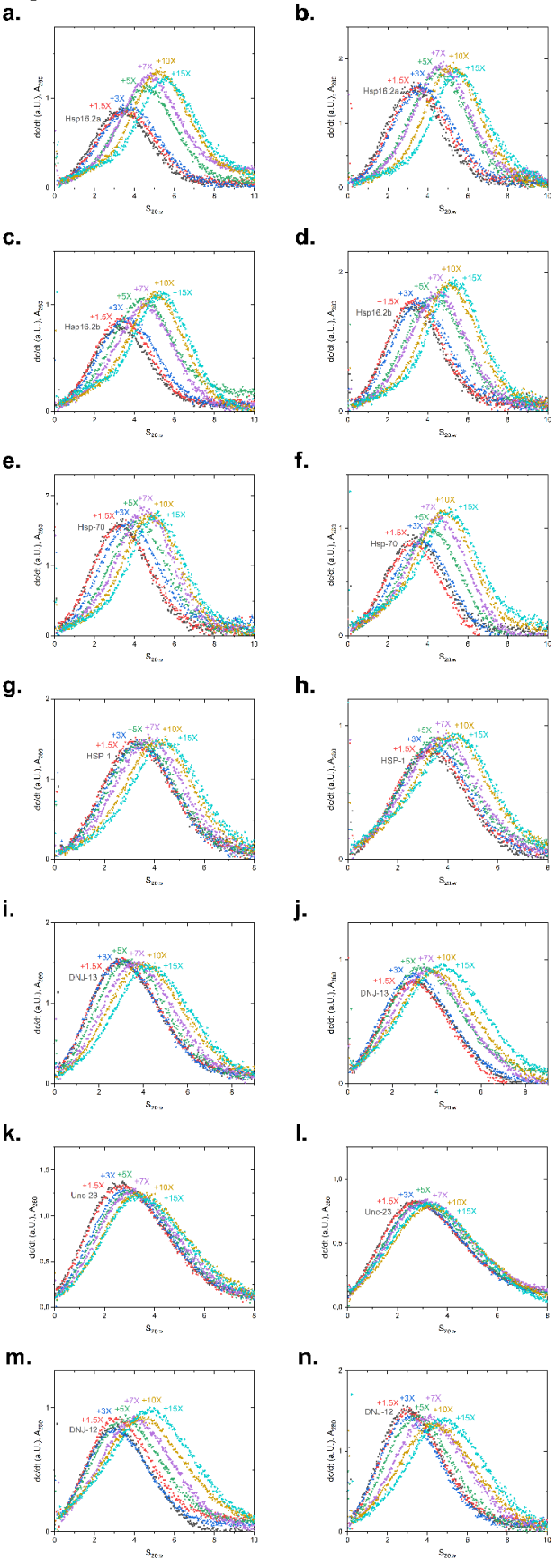

Figure 6.

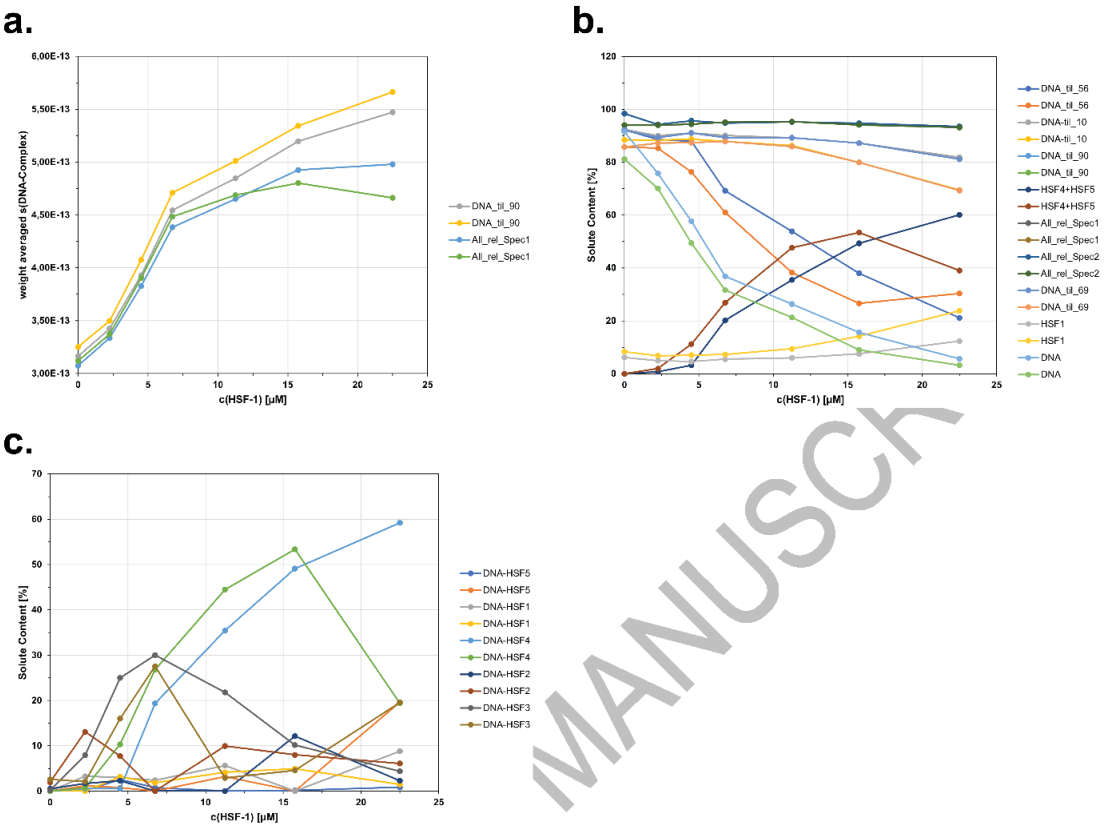

Figure 7.

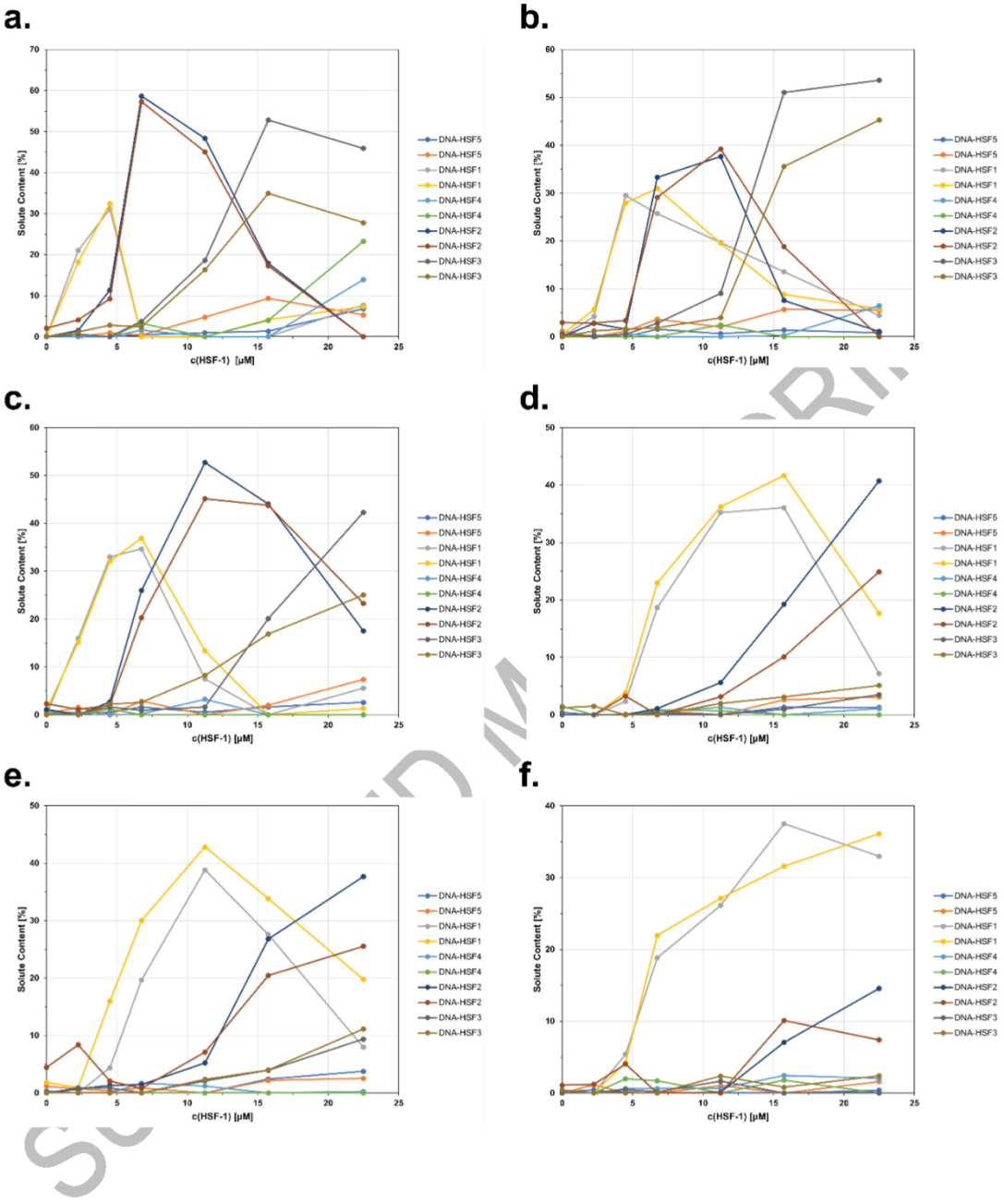
a.
b.
c.
d.
e.
f.
Solute Content [%]
c(HSF-1) [µM]
DNA-HSF5
DNA-HSF5
DNA-HSF1
DNA-HSF1
DNA-HSF4
DNA-HSF4
DNA-HSF2
DNA-HSF2
DNA-HSF3
DNA-HSF3

3. Summary and outlook

This thesis provides a more comprehensive view of the heat-shock machinery of the model nematode *Caenorhabditis elegans*.

First, the biochemical properties of four variants of HSC-70, which were found to suppress a severe *head-bent* phenotype of *C. elegans* [112,115], were investigated. These four variants, D233N, S321F, A379V and D384N were purified and characterized regarding their stability, activity and specific binding to co-chaperones and nucleotide exchange factors.

Compared to wildtype HSC-70, most variants showed similar stability and quaternary structure. However, variant S321F deviated in terms of a reduced nucleotide response and increased oligomerization, compared to the wildtype. Although the interaction with the nucleotide exchange factors BAG-1 and UNC-23 had almost no influence on the activity of most HSC-70 variants, D233N and A379V showed a strong reduction when paired with DNJ-12 and DNJ-13. Here, the structural deviation from wildtype HSC-70 induces energetic penalties, caused by steric clashes in both S321F and A379V, and a disrupted salt bridge in variant D233N.

Interestingly, HSC-70 variant D384N showed an increase in ATPase activity, which, on the other hand, did not correlate with its refolding activity. This leads to the assumption, that due to a significantly increased ATPase activity, this mutant becomes inactive, and thereby rescues the *head-bent* phenotype. Nematode J-proteins are known to both enforce refolding *in vitro*, while they circumvent aggregation *in vivo*. Altogether, this leads to the assumption, that the interaction of these co-chaperones with the suppressor variants of HSC-70, is altered in comparison to wildtype HSC-70.

Further, a reduced DNJ-13 interaction was observed for most of the HSC-70 variants. Therefore, it was interesting to see, whether interference with DNJ-13, could potentially rescue the *head-bent* phenotype *in vivo*. DNJ-13 was depleted as a result of specific RNAi in nematodes carrying the respective *unc-23* mutation. This depletion proofed to be sufficient to significantly improve the locomotion. Interestingly RNAi against *dnj-12* did not result in any effect. In contrast to DNJ-12, DNJ-13 might bind to client proteins *in vivo*, and thereby diverting HSC-70 from muscular attachment sites. This could also

potentially explain why HSC-70 variants with diminished DNJ-13 binding are able to suppress this phenotype after all.
Nevertheless, by investigating the four HSC-70 suppressor variants of *C. elegans head-bent* phenotype, a connection to DNJ-13 was proposed which, could yield a resistant nematode strain against this severe *head-bent* phenotype. Due to the relevance of Hsp40 co-chaperones, like DnaJB6, and nucleotide exchange factors, such as Bag3, in both systems [173-177], this might be of help in mitigating, or at least aid in understanding hereditary forms of muscular dystrophy in humans.

HSC-70 and HSP-90 are both heavily involved in the specific folding of client proteins, as well as proteostasis control [99,111,120,178]. Therefore, their co-chaperones may even frequently interact with each other. While the co-chaperone Hop is already known to interact between both systems [179,180], no such interaction was known for CDC-37, a major co-chaperone of HSP-90. To this end, the role of CDC-37 was examined, regarding a potential cross-interaction between the HSP-90 and HSC-70 chaperone system.
Therefore, a crosslink screening was performed and an interaction between DNJ-13 and CDC-37 was unraveled. Further, the protein complex showed a stoichiometry of one CDC-37 monomer interacting with either a DNJ-13 monomer or dimer, as a result of an intermediate affinity with a K_D of approximately 3.4 µM between the two proteins. This is in agreement with previous findings, showing CDC-37 to interact as a monomer in a HSP-90•CDC-37•kinase complex [142], while J-proteins like DNJ-13 are known to form dimers [97].
In order to define the binding interface between both proteins, sedimentation velocity analysis as well as mass spectrometry analysis were employed. Even though both methods yielded different binding sites, it is not entirely contradicting and indicates that an interaction might occur on several sites throughout both proteins. Overall, the N-terminus of CDC-37 was found to bind predominantly to the N-terminal J-domain of DNJ-13, while one particular interesting crosslink connected the N-terminus of CDC-37 to the C-terminal domain II of DNJ-13, for which no function is yet known. This finding implies an additional binding mode for the N-terminus of CDC-37, which is hitherto known as kinase binding site [124], and might be comparable to the interaction with both kinases and HSP-90.

Strikingly, CDC-37•DNJ-13 is still able to interact preferentially with the open state of HSP-90. This interaction could be further modulated by the presence of client kinases, however, it connects the HSP-90•CDC-37•kinase system to the HSC-70•DNJ-13 system. This might come into play for the coordinated transfer of kinases between both systems, that has already been established for the co-chaperone Hop and some steroid binding receptors, like GR [179-181]. In contrast, this transfer could also be of importance in the degradation of kinases, in which the HSC-70 system then participates [182]. Nevertheless, a similar interaction between Hop and DnaJB5, a human orthologue of DNJ-13 was found before [179], while Hsc70 was observed to also play a role in kinase maturation [183].
In any case, these findings should contribute to a general understanding of both systems, which could be of particular importance due to the interest in Hsp90 as a therapeutic target in humans.

Next, the impact of the molecular chaperone HSP-90 and its cofactor UNC-45, which participates in the muscle-related folding of HSP-90, was investigated by a novel genome-wide coexpression analysis. To this end, a preceding microarray analysis script, initially developed for coexpression analysis in the simplified model system *Saccharomyces cerevisiae* [184], was adapted to fit the far more complex nematode *C. elegans*. Based on more than 2243 individual microarray experiments, a universal clique map containing 307 distinct co-regulated cliques was generated, representing the entirety of *C. elegans* genes. Further, a timeline was created, ranging from embryo to late adult, and thereby enabling the comparison of transcriptional changes during development. This greatly supports the ability to discriminate if these changes in expression are specific to one developmental stage.
Using RNAi against *unc-45*, changes in the transcriptome of *C. elegans* were induced and the respective microarray data was analyzed and mapped to the generated timeline. Here, the depletion of UNC-45 leads to a delay in the completion of sperm and the development of the vulva, while the transcriptome relates strongly to the young adult stage. Usually, during the development of the vulva, a critical step occurs where LIN-39 together with its cofactors UNC-62 and CEH-20 induces the expression of *ref-2* [185-187]. Here, *ref-2* is not upregulated, which should then, in turn, inhibit the fusogen EFF-1 as an expected factor for vulva development [186]. These findings, together with the downregulation of additional genes involved in the vulva development, imply that the induction of vulva

development is impeded in UNC-45 depleted nematodes. Further, a combination of upregulated nspd- and msp-proteins [188,189], together with the downregulation of *asb-2* [190], leads to a halt in sperm development prior to completion [191,192].

hsp-90 RNAi on the other hand was found to have a more diverse effect on the transcriptome. Nematodes arrest in their development close to the L4 larval stage and genes of the immune response, unfolded protein response, and cuticle development were strongly upregulated, while genes for embryo development and reproduction were downregulated. This is in agreement with the observed phenotype after the depletion of HSP-90, and since the innate immune response in nematodes is coupled to the heat-shock response [83,193], an upregulation of both was already expected. Interestingly *daf-16* regulated genes were found to be significantly misregulated with respect to their original developmental program [76,194,195]. These genes were clustered into up- and downregulated genes, which revealed a simultaneous modification to the *dauer*-program upon *hsp-90* RNAi. Still, it remains unclear if this misregulation might be connected to the depletion of HSP-90 via secondary effects.

Offering a powerful tool for the genome-wide coexpression analysis in *C. elegans*, this approach was then employed for the detection of HSF-1 regulated genes in heat stressed nematodes, thereby demonstrating its methodical power again. Here, the nematode genome which harbors over 4120 HSEs containing HSF-1 binding consensus regions, was narrowed down to a surprisingly small clique of 8 genes. Therefore, HSF-1 seems to control a vast majority of these genes during non-stressed conditions, while only a few are explicitly upregulated during heat-shock.

To validate these 8 found genes, dsDNA probes were created, resembling their promoter regions including the HSEs, and the DNA binding domain of HSF-1 was expressed, in order investigate the interaction of both, HSF-1 and dsDNA probes. Additionally, a custom grid sedimentation velocity analysis was employed to quantify the binding event, thus providing an opportunity to study multiple interactions between transcription factors and dsDNA binding sites. Here, the DBD of HSF-1 was able to bind to the HSE-regions of the probes with a certain selectivity based on its affinity. Further, tetrameric and pentameric HSEs were discovered in addition to the trimeric binding mode, simultaneously increasing the cooperativity. Here, *F44E5.4* featured the only promoter

with a pentameric consensus score site, while both *hsp-16.2*p and *dnj-13*p contained a tetrameric site.
Despite this HSE being not inducible by HSF-1 *in vivo*, the dsDNA probe of *dnj-12* was efficiently bound by the HSF-1 DBD. This leads to the assumption that this binding event, instead of being exclusive to heat-shock, might be constitutive, which is also supported by the ubiquitous expression of DNJ-12, and might apply to many of the found HSEs in *C. elegans*. Nevertheless, further research is needed, since only the DBD of HSF-1 was utilized and posttranslational modifications of full-length HSF-1, like phosphorylation [56,196] or deacetylation [57,197], are known to contribute to the binding of HSEs by HSF-1. Nevertheless, this approach as a whole provides a reference for the prediction of transcription factor binding sites, which can assist in gaining further insight into complex multi-step binding reactions in general.

In any case, these findings demonstrate both, the functionality of this genome-wide co-expression analysis functionality, as well as a superior form of visualization of large data when compared to an already existing state-of-the-art analysis program. Interestingly, a different approach utilizing transcriptional genome-wide modules, was recently reported, enabling individual genes to be assigned into multiple cliques. While this expands the possibilities to detect genes, which are connected to more than one functional clique, it also complicates the generation of a static clique map. However, both approaches provide a potent tool for the genome-wide analysis of coexpressed genes in *C. elegans* and are thereby of significant scientific value.

In toto, this thesis provides novel findings regarding the heat-shock response in *C. elegans*, therefore assisting in a better understanding of this model system and might even be partly transferable to the human system.

4. References

1 Labbadia, J. & Morimoto, R. I. The biology of proteostasis in aging and disease. *Annu Rev Biochem* **84**, 435-464, doi:10.1146/annurev-biochem-060614-033955 (2015).

2 Hipp, M. S., Kasturi, P. & Hartl, F. U. The proteostasis network and its decline in ageing. *Nat Rev Mol Cell Biol* **20**, 421-435, doi:10.1038/s41580-019-0101-y (2019).

3 Kim, Y. E., Hipp, M. S., Bracher, A., Hayer-Hartl, M. & Hartl, F. U. Molecular chaperone functions in protein folding and proteostasis. *Annu Rev Biochem* **82**, 323-355, doi:10.1146/annurev-biochem-060208-092442 (2013).

4 Anckar, J. & Sistonen, L. Regulation of HSF1 function in the heat stress response: implications in aging and disease. *Annu Rev Biochem* **80**, 1089-1115, doi:10.1146/annurev-biochem-060809-095203 (2011).

5 Haynes, C. M. & Ron, D. The mitochondrial UPR - protecting organelle protein homeostasis. *J Cell Sci* **123**, 3849-3855, doi:10.1242/jcs.075119 (2010).

6 Walter, P. & Ron, D. The unfolded protein response: from stress pathway to homeostatic regulation. *Science* **334**, 1081-1086, doi:10.1126/science.1209038 (2011).

7 Ellis, R. J. & Minton, A. P. Protein aggregation in crowded environments. *Biol Chem* **387**, 485-497, doi:10.1515/BC.2006.064 (2006).

8 Chiti, F. & Dobson, C. M. Protein misfolding, functional amyloid, and human disease. *Annu Rev Biochem* **75**, 333-366, doi:10.1146/annurev.biochem.75.101304.123901 (2006).

9 Kim, Y. E. *et al.* Soluble Oligomers of PolyQ-Expanded Huntingtin Target a Multiplicity of Key Cellular Factors. *Mol Cell* **63**, 951-964, doi:10.1016/j.molcel.2016.07.022 (2016).

10 Guo, J. L. *et al.* Unique pathological tau conformers from Alzheimer's brains transmit tau pathology in nontransgenic mice. *J Exp Med* **213**, 2635-2654, doi:10.1084/jem.20160833 (2016).

11 Brundin, P., Melki, R. & Kopito, R. Prion-like transmission of protein aggregates in neurodegenerative diseases. *Nat Rev Mol Cell Biol* **11**, 301-307, doi:10.1038/nrm2873 (2010).

12 Li, J. Y. *et al.* Lewy bodies in grafted neurons in subjects with Parkinson's disease suggest host-to-graft disease propagation. *Nat Med* **14**, 501-503, doi:10.1038/nm1746 (2008).

13 Gidalevitz, T., Prahlad, V. & Morimoto, R. I. The stress of protein misfolding: from single cells to multicellular organisms. *Cold Spring Harb Perspect Biol* **3**, doi:10.1101/cshperspect.a009704 (2011).

14 Nillegoda, N. B., Wentink, A. S. & Bukau, B. Protein Disaggregation in Multicellular Organisms. *Trends Biochem Sci* **43**, 285-300, doi:10.1016/j.tibs.2018.02.003 (2018).

15 Balchin, D., Hayer-Hartl, M. & Hartl, F. U. In vivo aspects of protein folding and quality control. *Science* **353**, aac4354, doi:10.1126/science.aac4354 (2016).

16 Frydman, J. Folding of newly translated proteins in vivo: the role of molecular chaperones. *Annu Rev Biochem* **70**, 603-647, doi:10.1146/annurev.biochem.70.1.603 (2001).

17 Hartl, F. U. & Hayer-Hartl, M. Molecular chaperones in the cytosol: from nascent chain to folded protein. *Science* **295**, 1852-1858, doi:10.1126/science.1068408 (2002).
18 Balch, W. E., Morimoto, R. I., Dillin, A. & Kelly, J. W. Adapting proteostasis for disease intervention. *Science* **319**, 916-919, doi:10.1126/science.1141448 (2008).
19 Li, J., Labbadia, J. & Morimoto, R. I. Rethinking HSF1 in Stress, Development, and Organismal Health. *Trends Cell Biol* **27**, 895-905, doi:10.1016/j.tcb.2017.08.002 (2017).
20 Zaher, H. S. & Green, R. Fidelity at the molecular level: lessons from protein synthesis. *Cell* **136**, 746-762, doi:10.1016/j.cell.2009.01.036 (2009).
21 Picard, D. Heat-shock protein 90, a chaperone for folding and regulation. *Cell Mol Life Sci* **59**, 1640-1648, doi:10.1007/pl00012491 (2002).
22 Dobson, C. M., Sali, A. & Karplus, M. Protein Folding: A Perspective from Theory and Experiment. *Angew Chem Int Ed Engl* **37**, 868-893, doi:10.1002/(SICI)1521-3773(19980420)37:7<868::AID-ANIE868>3.0.CO;2-H (1998).
23 Anfinsen, C. B. Principles that govern the folding of protein chains. *Science* **181**, 223-230, doi:10.1126/science.181.4096.223 (1973).
24 Hartl, F. U. Molecular chaperones in cellular protein folding. *Nature* **381**, 571-579, doi:10.1038/381571a0 (1996).
25 Young, J. C., Hoogenraad, N. J. & Hartl, F. U. Molecular chaperones Hsp90 and Hsp70 deliver preproteins to the mitochondrial import receptor Tom70. *Cell* **112**, 41-50, doi:10.1016/s0092-8674(02)01250-3 (2003).
26 Biebl, M. M. & Buchner, J. Structure, Function, and Regulation of the Hsp90 Machinery. *Cold Spring Harb Perspect Biol* **11**, doi:10.1101/cshperspect.a034017 (2019).
27 Schopf, F. H., Biebl, M. M. & Buchner, J. The HSP90 chaperone machinery. *Nat Rev Mol Cell Biol* **18**, 345-360, doi:10.1038/nrm.2017.20 (2017).
28 Gragerov, A. I., Martin, E. S., Krupenko, M. A., Kashlev, M. V. & Nikiforov, V. G. Protein aggregation and inclusion body formation in Escherichia coli rpoH mutant defective in heat shock protein induction. *FEBS Lett* **291**, 222-224, doi:10.1016/0014-5793(91)81289-k (1991).
29 Kerner, M. J. *et al.* Proteome-wide analysis of chaperonin-dependent protein folding in Escherichia coli. *Cell* **122**, 209-220, doi:10.1016/j.cell.2005.05.028 (2005).
30 Mayer, M. P. Gymnastics of molecular chaperones. *Mol Cell* **39**, 321-331, doi:10.1016/j.molcel.2010.07.012 (2010).
31 Richter, K., Haslbeck, M. & Buchner, J. The heat shock response: life on the verge of death. *Mol Cell* **40**, 253-266, doi:10.1016/j.molcel.2010.10.006 (2010).
32 Kiefhaber, T., Rudolph, R., Kohler, H. H. & Buchner, J. Protein aggregation in vitro and in vivo: a quantitative model of the kinetic competition between folding and aggregation. *Biotechnology (N Y)* **9**, 825-829, doi:10.1038/nbt0991-825 (1991).
33 Jahn, M., Buchner, J., Hugel, T. & Rief, M. Folding and assembly of the large molecular machine Hsp90 studied in single-molecule experiments. *Proc Natl Acad Sci U S A* **113**, 1232-1237, doi:10.1073/pnas.1518827113 (2016).
34 Cox, M. B. & Johnson, J. L. Evidence for Hsp90 Co-chaperones in Regulating Hsp90 Function and Promoting Client Protein Folding. *Methods Mol Biol* **1709**, 397-422, doi:10.1007/978-1-4939-7477-1_28 (2018).

35 Vihervaara, A. & Sistonen, L. HSF1 at a glance. *J Cell Sci* **127**, 261-266, doi:10.1242/jcs.132605 (2014).
36 Akerfelt, M., Morimoto, R. I. & Sistonen, L. Heat shock factors: integrators of cell stress, development and lifespan. *Nat Rev Mol Cell Biol* **11**, 545-555, doi:10.1038/nrm2938 (2010).
37 Solis, E. J. *et al.* Defining the Essential Function of Yeast Hsf1 Reveals a Compact Transcriptional Program for Maintaining Eukaryotic Proteostasis. *Mol Cell* **69**, 534, doi:10.1016/j.molcel.2018.01.021 (2018).
38 Skaggs, H. S. *et al.* HSF1-TPR interaction facilitates export of stress-induced HSP70 mRNA. *J Biol Chem* **282**, 33902-33907, doi:10.1074/jbc.M704054200 (2007).
39 Kubota, H., Matsumoto, S., Yokota, S., Yanagi, H. & Yura, T. Transcriptional activation of mouse cytosolic chaperonin CCT subunit genes by heat shock factors HSF1 and HSF2. *FEBS Lett* **461**, 125-129, doi:10.1016/s0014-5793(99)01437-4 (1999).
40 Cahill, C. M., Waterman, W. R., Xie, Y., Auron, P. E. & Calderwood, S. K. Transcriptional repression of the prointerleukin 1beta gene by heat shock factor 1. *J Biol Chem* **271**, 24874-24879 (1996).
41 Kallio, M. *et al.* Brain abnormalities, defective meiotic chromosome synapsis and female subfertility in HSF2 null mice. *EMBO J* **21**, 2591-2601, doi:10.1093/emboj/21.11.2591 (2002).
42 Kaitsuka, T., Tomizawa, K. & Matsushita, M. Transformation of eEF1Bdelta into heat-shock response transcription factor by alternative splicing. *EMBO Rep* **12**, 673-681, doi:10.1038/embor.2011.82 (2011).
43 Xiao, X. *et al.* HSF1 is required for extra-embryonic development, postnatal growth and protection during inflammatory responses in mice. *EMBO J* **18**, 5943-5952, doi:10.1093/emboj/18.21.5943 (1999).
44 Pirkkala, L., Nykanen, P. & Sistonen, L. Roles of the heat shock transcription factors in regulation of the heat shock response and beyond. *FASEB J* **15**, 1118-1131, doi:10.1096/fj00-0294rev (2001).
45 Vuister, G. W. *et al.* Solution structure of the DNA-binding domain of Drosophila heat shock transcription factor. *Nat Struct Biol* **1**, 605-614 (1994).
46 Wu, C. Heat shock transcription factors: structure and regulation. *Annu Rev Cell Dev Biol* **11**, 441-469, doi:10.1146/annurev.cb.11.110195.002301 (1995).
47 Wang, X. *et al.* Phosphorylation of HSF1 by MAPK-activated protein kinase 2 on serine 121, inhibits transcriptional activity and promotes HSP90 binding. *J Biol Chem* **281**, 782-791, doi:10.1074/jbc.M505822200 (2006).
48 Xing, H., Mayhew, C. N., Cullen, K. E., Park-Sarge, O. K. & Sarge, K. D. HSF1 modulation of Hsp70 mRNA polyadenylation via interaction with symplekin. *J Biol Chem* **279**, 10551-10555, doi:10.1074/jbc.M311719200 (2004).
49 Guo, Y. *et al.* Evidence for a mechanism of repression of heat shock factor 1 transcriptional activity by a multichaperone complex. *J Biol Chem* **276**, 45791-45799, doi:10.1074/jbc.M105931200 (2001).
50 Orosz, A., Wisniewski, J. & Wu, C. Regulation of Drosophila heat shock factor trimerization: global sequence requirements and independence of nuclear localization. *Mol Cell Biol* **16**, 7018-7030, doi:10.1128/MCB.16.12.7018 (1996).
51 Jaeger, A. M., Makley, L. N., Gestwicki, J. E. & Thiele, D. J. Genomic heat shock element sequences drive cooperative human heat shock factor 1 DNA binding and

selectivity. *J Biol Chem* **289**, 30459-30469, doi:10.1074/jbc.M114.591578 (2014).
52 Guertin, M. J. & Lis, J. T. Chromatin landscape dictates HSF binding to target DNA elements. *PLoS Genet* **6**, e1001114, doi:10.1371/journal.pgen.1001114 (2010).
53 Newton, E. M., Knauf, U., Green, M. & Kingston, R. E. The regulatory domain of human heat shock factor 1 is sufficient to sense heat stress. *Mol Cell Biol* **16**, 839-846, doi:10.1128/MCB.16.3.839 (1996).
54 Xie, Y., Zhong, R., Chen, C. & Calderwood, S. K. Heat shock factor 1 contains two functional domains that mediate transcriptional repression of the c-fos and c-fms genes. *J Biol Chem* **278**, 4687-4698, doi:10.1074/jbc.M210189200 (2003).
55 Joutsen, J. & Sistonen, L. Tailoring of Proteostasis Networks with Heat Shock Factors. *Cold Spring Harb Perspect Biol* **11**, doi:10.1101/cshperspect.a034066 (2019).
56 Holmberg, C. I. *et al.* Phosphorylation of serine 230 promotes inducible transcriptional activity of heat shock factor 1. *EMBO J* **20**, 3800-3810, doi:10.1093/emboj/20.14.3800 (2001).
57 Zelin, E. & Freeman, B. C. Lysine deacetylases regulate the heat shock response including the age-associated impairment of HSF1. *J Mol Biol* **427**, 1644-1654, doi:10.1016/j.jmb.2015.02.010 (2015).
58 Dayalan Naidu, S. & Dinkova-Kostova, A. T. Regulation of the mammalian heat shock factor 1. *FEBS J* **284**, 1606-1627, doi:10.1111/febs.13999 (2017).
59 Jin, X., Eroglu, B., Moskophidis, D. & Mivechi, N. F. Targeted Deletion of Hsf1, 2, and 4 Genes in Mice. *Methods Mol Biol* **1709**, 1-22, doi:10.1007/978-1-4939-7477-1_1 (2018).
60 Li, J., Chauve, L., Phelps, G., Brielmann, R. M. & Morimoto, R. I. E2F coregulates an essential HSF developmental program that is distinct from the heat-shock response. *Genes Dev* **30**, 2062-2075, doi:10.1101/gad.283317.116 (2016).
61 Brunquell, J., Morris, S., Lu, Y., Cheng, F. & Westerheide, S. D. The genome-wide role of HSF-1 in the regulation of gene expression in Caenorhabditis elegans. *BMC Genomics* **17**, 559, doi:10.1186/s12864-016-2837-5 (2016).
62 Taipale, M., Jarosz, D. F. & Lindquist, S. HSP90 at the hub of protein homeostasis: emerging mechanistic insights. *Nat Rev Mol Cell Biol* **11**, 515-528, doi:10.1038/nrm2918 (2010).
63 Lai, B. T., Chin, N. W., Stanek, A. E., Keh, W. & Lanks, K. W. Quantitation and intracellular localization of the 85K heat shock protein by using monoclonal and polyclonal antibodies. *Mol Cell Biol* **4**, 2802-2810, doi:10.1128/mcb.4.12.2802-2810.1984 (1984).
64 Didenko, T., Duarte, A. M., Karagoz, G. E. & Rudiger, S. G. Hsp90 structure and function studied by NMR spectroscopy. *Biochim Biophys Acta* **1823**, 636-647, doi:10.1016/j.bbamcr.2011.11.009 (2012).
65 Jackson, S. E. Hsp90: structure and function. *Top Curr Chem* **328**, 155-240, doi:10.1007/128_2012_356 (2013).
66 Calderwood, S. K. Molecular cochaperones: tumor growth and cancer treatment. *Scientifica (Cairo)* **2013**, 217513, doi:10.1155/2013/217513 (2013).
67 Cox, M. B. & Johnson, J. L. The role of p23, Hop, immunophilins, and other co-chaperones in regulating Hsp90 function. *Methods Mol Biol* **787**, 45-66, doi:10.1007/978-1-61779-295-3_4 (2011).

68 Caplan, A. J., Ma'ayan, A. & Willis, I. M. Multiple kinases and system robustness: a link between Cdc37 and genome integrity. *Cell Cycle* **6**, 3145-3147, doi:10.4161/cc.6.24.5147 (2007).

69 Verba, K. A. *et al.* Atomic structure of Hsp90-Cdc37-Cdk4 reveals that Hsp90 traps and stabilizes an unfolded kinase. *Science* **352**, 1542-1547, doi:10.1126/science.aaf5023 (2016).

70 Sima, S. *et al.* HSP-90/kinase complexes are stabilized by the large PPIase FKB-6. *Sci Rep* **11**, 12347, doi:10.1038/s41598-021-91667-5 (2021).

71 Guisbert, E., Czyz, D. M., Richter, K., McMullen, P. D. & Morimoto, R. I. Identification of a tissue-selective heat shock response regulatory network. *PLoS Genet* **9**, e1003466, doi:10.1371/journal.pgen.1003466 (2013).

72 Barna, J. *et al.* Heat shock factor-1 intertwines insulin/IGF-1, TGF-beta and cGMP signaling to control development and aging. *BMC Dev Biol* **12**, 32, doi:10.1186/1471-213X-12-32 (2012).

73 Kijima, T. *et al.* HSP90 inhibitors disrupt a transient HSP90-HSF1 interaction and identify a noncanonical model of HSP90-mediated HSF1 regulation. *Sci Rep* **8**, 6976, doi:10.1038/s41598-018-25404-w (2018).

74 David, C. L., Smith, H. E., Raynes, D. A., Pulcini, E. J. & Whitesell, L. Expression of a unique drug-resistant Hsp90 ortholog by the nematode Caenorhabditis elegans. *Cell Stress Chaperones* **8**, 93-104, doi:10.1379/1466-1268(2003)8<93:eoaudh>2.0.co;2 (2003).

75 Inoue, T. *et al.* Cell cycle control by daf-21/Hsp90 at the first meiotic prophase/metaphase boundary during oogenesis in Caenorhabditis elegans. *Dev Growth Differ* **48**, 25-32, doi:10.1111/j.1440-169X.2006.00841.x (2006).

76 Somogyvari, M., Gecse, E. & Soti, C. DAF-21/Hsp90 is required for C. elegans longevity by ensuring DAF-16/FOXO isoform A function. *Sci Rep* **8**, 12048, doi:10.1038/s41598-018-30592-6 (2018).

77 Gillan, V., Maitland, K., McCormack, G., Him, N. A. & Devaney, E. Functional genomics of hsp-90 in parasitic and free-living nematodes. *Int J Parasitol* **39**, 1071-1081, doi:10.1016/j.ijpara.2009.02.024 (2009).

78 Horikawa, M., Sural, S., Hsu, A. L. & Antebi, A. Co-chaperone p23 regulates C. elegans Lifespan in Response to Temperature. *PLoS Genet* **11**, e1005023, doi:10.1371/journal.pgen.1005023 (2015).

79 Gaiser, A. M., Kaiser, C. J., Haslbeck, V. & Richter, K. Downregulation of the Hsp90 system causes defects in muscle cells of Caenorhabditis elegans. *PLoS One* **6**, e25485, doi:10.1371/journal.pone.0025485 (2011).

80 Roe, S. M. *et al.* Structural basis for inhibition of the Hsp90 molecular chaperone by the antitumor antibiotics radicicol and geldanamycin. *J Med Chem* **42**, 260-266, doi:10.1021/jm980403y (1999).

81 Sreedhar, A. S., Kalmar, E., Csermely, P. & Shen, Y. F. Hsp90 isoforms: functions, expression and clinical importance. *FEBS Lett* **562**, 11-15, doi:10.1016/s0014-5793(04)00229-7 (2004).

82 Eckl, J., Sima, S., Marcus, K., Lindemann, C. & Richter, K. Hsp90-downregulation influences the heat-shock response, innate immune response and onset of oocyte development in nematodes. *PLoS One* **12**, e0186386, doi:10.1371/journal.pone.0186386 (2017).

83 Prithika, U., Deepa, V. & Balamurugan, K. External induction of heat shock stimulates the immune response and longevity of Caenorhabditis elegans towards

pathogen exposure. *Innate Immun* **22**, 466-478, doi:10.1177/1753425916654557 (2016).
84 Neckers, L. Hsp90 inhibitors as novel cancer chemotherapeutic agents. *Trends Mol Med* **8**, S55-61, doi:10.1016/s1471-4914(02)02316-x (2002).
85 Neckers, L. & Workman, P. Hsp90 molecular chaperone inhibitors: are we there yet? *Clin Cancer Res* **18**, 64-76, doi:10.1158/1078-0432.CCR-11-1000 (2012).
86 Neckers, L. *et al.* Methods to validate Hsp90 inhibitor specificity, to identify off-target effects, and to rethink approaches for further clinical development. *Cell Stress Chaperones* **23**, 467-482, doi:10.1007/s12192-018-0877-2 (2018).
87 Gracia, L., Lora, G., Blair, L. J. & Jinwal, U. K. Therapeutic Potential of the Hsp90/Cdc37 Interaction in Neurodegenerative Diseases. *Front Neurosci* **13**, 1263, doi:10.3389/fnins.2019.01263 (2019).
88 Palleros, D. R., Welch, W. J. & Fink, A. L. Interaction of hsp70 with unfolded proteins: effects of temperature and nucleotides on the kinetics of binding. *Proc Natl Acad Sci U S A* **88**, 5719-5723, doi:10.1073/pnas.88.13.5719 (1991).
89 Kabani, M. & Martineau, C. N. Multiple hsp70 isoforms in the eukaryotic cytosol: mere redundancy or functional specificity? *Curr Genomics* **9**, 338-248, doi:10.2174/138920208785133280 (2008).
90 Mayer, M. P. Hsp70 chaperone dynamics and molecular mechanism. *Trends Biochem Sci* **38**, 507-514, doi:10.1016/j.tibs.2013.08.001 (2013).
91 Finka, A., Sharma, S. K. & Goloubinoff, P. Multi-layered molecular mechanisms of polypeptide holding, unfolding and disaggregation by HSP70/HSP110 chaperones. *Front Mol Biosci* **2**, 29, doi:10.3389/fmolb.2015.00029 (2015).
92 Meimaridou, E., Gooljar, S. B. & Chapple, J. P. From hatching to dispatching: the multiple cellular roles of the Hsp70 molecular chaperone machinery. *J Mol Endocrinol* **42**, 1-9, doi:10.1677/JME-08-0116 (2009).
93 Dekker, S. L., Kampinga, H. H. & Bergink, S. DNAJs: more than substrate delivery to HSPA. *Front Mol Biosci* **2**, 35, doi:10.3389/fmolb.2015.00035 (2015).
94 Bracher, A. & Verghese, J. The nucleotide exchange factors of Hsp70 molecular chaperones. *Front Mol Biosci* **2**, 10, doi:10.3389/fmolb.2015.00010 (2015).
95 Genevaux, P., Georgopoulos, C. & Kelley, W. L. The Hsp70 chaperone machines of Escherichia coli: a paradigm for the repartition of chaperone functions. *Mol Microbiol* **66**, 840-857, doi:10.1111/j.1365-2958.2007.05961.x (2007).
96 Hohfeld, J. & Jentsch, S. GrpE-like regulation of the hsc70 chaperone by the anti-apoptotic protein BAG-1. *EMBO J* **16**, 6209-6216, doi:10.1093/emboj/16.20.6209 (1997).
97 Sun, L. *et al.* The lid domain of Caenorhabditis elegans Hsc70 influences ATP turnover, cofactor binding and protein folding activity. *PLoS One* **7**, e33980, doi:10.1371/journal.pone.0033980 (2012).
98 Popp, S. L. & Reinstein, J. Functional characterization of the DnaK chaperone system from the archaeon Methanothermobacter thermautotrophicus DeltaH. *FEBS Lett* **583**, 573-578, doi:10.1016/j.febslet.2008.12.062 (2009).
99 Stricher, F., Macri, C., Ruff, M. & Muller, S. HSPA8/HSC70 chaperone protein: structure, function, and chemical targeting. *Autophagy* **9**, 1937-1954, doi:10.4161/auto.26448 (2013).
100 Sondermann, H. *et al.* Structure of a Bag/Hsc70 complex: convergent functional evolution of Hsp70 nucleotide exchange factors. *Science* **291**, 1553-1557, doi:10.1126/science.1057268 (2001).

101 Popp, S. *et al.* Structural dynamics of the DnaK-peptide complex. *J Mol Biol* **347**, 1039-1052, doi:10.1016/j.jmb.2005.02.026 (2005).
102 Morshauser, R. C., Wang, H., Flynn, G. C. & Zuiderweg, E. R. The peptide-binding domain of the chaperone protein Hsc70 has an unusual secondary structure topology. *Biochemistry* **34**, 6261-6266, doi:10.1021/bi00019a001 (1995).
103 Zhang, P., Leu, J. I., Murphy, M. E., George, D. L. & Marmorstein, R. Crystal structure of the stress-inducible human heat shock protein 70 substrate-binding domain in complex with peptide substrate. *PLoS One* **9**, e103518, doi:10.1371/journal.pone.0103518 (2014).
104 Scheufler, C. *et al.* Structure of TPR domain-peptide complexes: critical elements in the assembly of the Hsp70-Hsp90 multichaperone machine. *Cell* **101**, 199-210, doi:10.1016/S0092-8674(00)80830-2 (2000).
105 Brinker, A. *et al.* Ligand discrimination by TPR domains. Relevance and selectivity of EEVD-recognition in Hsp70 x Hop x Hsp90 complexes. *J Biol Chem* **277**, 19265-19275, doi:10.1074/jbc.M109002200 (2002).
106 Radons, J. The human HSP70 family of chaperones: where do we stand? *Cell Stress Chaperones* **21**, 379-404, doi:10.1007/s12192-016-0676-6 (2016).
107 GuhaThakurta, D. *et al.* Identification of a novel cis-regulatory element involved in the heat shock response in Caenorhabditis elegans using microarray gene expression and computational methods. *Genome Res* **12**, 701-712, doi:10.1101/gr.228902 (2002).
108 Heschl, M. F. & Baillie, D. L. Identification of a heat-shock pseudogene from Caenorhabditis elegans. *Genome* **32**, 190-195, doi:10.1139/g89-428 (1989).
109 Heschl, M. F. & Baillie, D. L. Characterization of the hsp70 multigene family of Caenorhabditis elegans. *DNA* **8**, 233-243, doi:10.1089/dna.1.1989.8.233 (1989).
110 Nillegoda, N. B. & Bukau, B. Metazoan Hsp70-based protein disaggregases: emergence and mechanisms. *Front Mol Biosci* **2**, 57, doi:10.3389/fmolb.2015.00057 (2015).
111 Papsdorf, K., Sacherl, J. & Richter, K. The balanced regulation of Hsc70 by DNJ-13 and UNC-23 is required for muscle functionality. *J Biol Chem* **289**, 25250-25261, doi:10.1074/jbc.M114.565234 (2014).
112 Rahmani, P., Rogalski, T. & Moerman, D. G. The C. elegans UNC-23 protein, a member of the BCL-2-associated athanogene (BAG) family of chaperone regulators, interacts with HSP-1 to regulate cell attachment and maintain hypodermal integrity. *Worm* **4**, e1023496, doi:10.1080/21624054.2015.1023496 (2015).
113 Waterston, R. H., Thomson, J. N. & Brenner, S. Mutants with altered muscle structure of Caenorhabditis elegans. *Dev Biol* **77**, 271-302, doi:10.1016/0012-1606(80)90475-3 (1980).
114 Plenefisch, J. D., Zhu, X. & Hedgecock, E. M. Fragile skeletal muscle attachments in dystrophic mutants of Caenorhabditis elegans: isolation and characterization of the mua genes. *Development* **127**, 1197-1207 (2000).
115 Fukuzono, T. *et al.* Chaperone complex BAG2-HSC70 regulates localization of Caenorhabditis elegans leucine-rich repeat kinase LRK-1 to the Golgi. *Genes Cells* **21**, 311-324, doi:10.1111/gtc.12338 (2016).
116 Nollen, E. A. *et al.* Genome-wide RNA interference screen identifies previously undescribed regulators of polyglutamine aggregation. *Proc Natl Acad Sci U S A* **101**, 6403-6408, doi:10.1073/pnas.0307697101 (2004).

117 Kamath, R. S. *et al.* Systematic functional analysis of the Caenorhabditis elegans genome using RNAi. *Nature* **421**, 231-237, doi:10.1038/nature01278 (2003).

118 Reed, S. I. The selection of amber mutations in genes required for completion of start, the controlling event of the cell division cycle of S. cerevisiae. *Genetics* **95**, 579-588, doi:10.1093/genetics/95.3.579 (1980).

119 Caplan, A. J., Mandal, A. K. & Theodoraki, M. A. Molecular chaperones and protein kinase quality control. *Trends Cell Biol* **17**, 87-92, doi:10.1016/j.tcb.2006.12.002 (2007).

120 Pearl, L. H. Hsp90 and Cdc37 -- a chaperone cancer conspiracy. *Curr Opin Genet Dev* **15**, 55-61, doi:10.1016/j.gde.2004.12.011 (2005).

121 Gray, P. J., Jr., Prince, T., Cheng, J., Stevenson, M. A. & Calderwood, S. K. Targeting the oncogene and kinome chaperone CDC37. *Nat Rev Cancer* **8**, 491-495, doi:10.1038/nrc2420 (2008).

122 Taipale, M. *et al.* Quantitative analysis of HSP90-client interactions reveals principles of substrate recognition. *Cell* **150**, 987-1001, doi:10.1016/j.cell.2012.06.047 (2012).

123 Verba, K. A. & Agard, D. A. How Hsp90 and Cdc37 Lubricate Kinase Molecular Switches. *Trends Biochem Sci* **42**, 799-811, doi:10.1016/j.tibs.2017.07.002 (2017).

124 Shao, J., Irwin, A., Hartson, S. D. & Matts, R. L. Functional dissection of cdc37: characterization of domain structure and amino acid residues critical for protein kinase binding. *Biochemistry* **42**, 12577-12588, doi:10.1021/bi035138j (2003).

125 Eckl, J. M. *et al.* Hsp90.Cdc37 Complexes with Protein Kinases Form Cooperatively with Multiple Distinct Interaction Sites. *J Biol Chem* **290**, 30843-30854, doi:10.1074/jbc.M115.693150 (2015).

126 Calderwood, S. K. Cdc37 as a co-chaperone to Hsp90. *Subcell Biochem* **78**, 103-112, doi:10.1007/978-3-319-11731-7_5 (2015).

127 Siligardi, G. *et al.* Regulation of Hsp90 ATPase activity by the co-chaperone Cdc37p/p50cdc37. *J Biol Chem* **277**, 20151-20159, doi:10.1074/jbc.M201287200 (2002).

128 Roe, S. M. *et al.* The Mechanism of Hsp90 regulation by the protein kinase-specific cochaperone p50(cdc37). *Cell* **116**, 87-98, doi:10.1016/s0092-8674(03)01027-4 (2004).

129 Smith, J. R., Clarke, P. A., de Billy, E. & Workman, P. Silencing the cochaperone CDC37 destabilizes kinase clients and sensitizes cancer cells to HSP90 inhibitors. *Oncogene* **28**, 157-169, doi:10.1038/onc.2008.380 (2009).

130 Oberoi, J. *et al.* Structural and functional basis of protein phosphatase 5 substrate specificity. *Proc Natl Acad Sci U S A* **113**, 9009-9014, doi:10.1073/pnas.1603059113 (2016).

131 Vaughan, C. K. *et al.* Hsp90-dependent activation of protein kinases is regulated by chaperone-targeted dephosphorylation of Cdc37. *Mol Cell* **31**, 886-895, doi:10.1016/j.molcel.2008.07.021 (2008).

132 Eckl, J. M. *et al.* Cdc37 (cell division cycle 37) restricts Hsp90 (heat shock protein 90) motility by interaction with N-terminal and middle domain binding sites. *J Biol Chem* **288**, 16032-16042, doi:10.1074/jbc.M112.439257 (2013).

133 Cheetham, M. E. & Caplan, A. J. Structure, function and evolution of DnaJ: conservation and adaptation of chaperone function. *Cell Stress Chaperones* **3**, 28-36, doi:10.1379/1466-1268(1998)003<0028:sfaeod>2.3.co;2 (1998).

134 Pellecchia, M., Szyperski, T., Wall, D., Georgopoulos, C. & Wuthrich, K. NMR structure of the J-domain and the Gly/Phe-rich region of the Escherichia coli DnaJ chaperone. *J Mol Biol* **260**, 236-250, doi:10.1006/jmbi.1996.0395 (1996).

135 Kampinga, H. H. & Craig, E. A. The HSP70 chaperone machinery: J proteins as drivers of functional specificity. *Nat Rev Mol Cell Biol* **11**, 579-592, doi:10.1038/nrm2941 (2010).

136 Cyr, D. M. Cooperation of the molecular chaperone Ydj1 with specific Hsp70 homologs to suppress protein aggregation. *FEBS Lett* **359**, 129-132, doi:10.1016/0014-5793(95)00024-4 (1995).

137 Ajit Tamadaddi, C. & Sahi, C. J domain independent functions of J proteins. *Cell Stress Chaperones* **21**, 563-570, doi:10.1007/s12192-016-0697-1 (2016).

138 Lu, Z. & Cyr, D. M. Protein folding activity of Hsp70 is modified differentially by the hsp40 co-chaperones Sis1 and Ydj1. *J Biol Chem* **273**, 27824-27830, doi:10.1074/jbc.273.43.27824 (1998).

139 Szabo, A., Korszun, R., Hartl, F. U. & Flanagan, J. A zinc finger-like domain of the molecular chaperone DnaJ is involved in binding to denatured protein substrates. *EMBO J* **15**, 408-417 (1996).

140 Lee, S., Fan, C. Y., Younger, J. M., Ren, H. & Cyr, D. M. Identification of essential residues in the type II Hsp40 Sis1 that function in polypeptide binding. *J Biol Chem* **277**, 21675-21682, doi:10.1074/jbc.M111075200 (2002).

141 Barends, T. R. *et al.* Combining crystallography and EPR: crystal and solution structures of the multidomain cochaperone DnaJ. *Acta Crystallogr D Biol Crystallogr* **69**, 1540-1552, doi:10.1107/S0907444913010640 (2013).

142 Mayer, M. P., Prodromou, C. & Frydman, J. The Hsp90 mosaic: a picture emerges. *Nat Struct Mol Biol* **16**, 2-6, doi:10.1038/nsmb0109-2 (2009).

143 Wall, D., Zylicz, M. & Georgopoulos, C. The conserved G/F motif of the DnaJ chaperone is necessary for the activation of the substrate binding properties of the DnaK chaperone. *J Biol Chem* **270**, 2139-2144, doi:10.1074/jbc.270.5.2139 (1995).

144 Cajo, G. C. *et al.* The role of the DIF motif of the DnaJ (Hsp40) co-chaperone in the regulation of the DnaK (Hsp70) chaperone cycle. *J Biol Chem* **281**, 12436-12444, doi:10.1074/jbc.M511192200 (2006).

145 Perales-Calvo, J., Muga, A. & Moro, F. Role of DnaJ G/F-rich domain in conformational recognition and binding of protein substrates. *J Biol Chem* **285**, 34231-34239, doi:10.1074/jbc.M110.144642 (2010).

146 Linke, K., Wolfram, T., Bussemer, J. & Jakob, U. The roles of the two zinc binding sites in DnaJ. *J Biol Chem* **278**, 44457-44466, doi:10.1074/jbc.M307491200 (2003).

147 Banecki, B. *et al.* Structure-function analysis of the zinc finger region of the DnaJ molecular chaperone. *J Biol Chem* **271**, 14840-14848, doi:10.1074/jbc.271.25.14840 (1996).

148 Ramos, C. H., Oliveira, C. L., Fan, C. Y., Torriani, I. L. & Cyr, D. M. Conserved central domains control the quaternary structure of type I and type II Hsp40 molecular chaperones. *J Mol Biol* **383**, 155-166, doi:10.1016/j.jmb.2008.08.019 (2008).

149 Li, J., Qian, X. & Sha, B. The crystal structure of the yeast Hsp40 Ydj1 complexed with its peptide substrate. *Structure* **11**, 1475-1483, doi:10.1016/j.str.2003.10.012 (2003).

150 Sha, B., Lee, S. & Cyr, D. M. The crystal structure of the peptide-binding fragment from the yeast Hsp40 protein Sis1. *Structure* **8**, 799-807, doi:10.1016/s0969-2126(00)00170-2 (2000).
151 Li, J. & Sha, B. Structure-based mutagenesis studies of the peptide substrate binding fragment of type I heat-shock protein 40. *Biochem J* **386**, 453-460, doi:10.1042/BJ20041050 (2005).
152 Johnson, J. L. & Craig, E. A. An essential role for the substrate-binding region of Hsp40s in Saccharomyces cerevisiae. *J Cell Biol* **152**, 851-856, doi:10.1083/jcb.152.4.851 (2001).
153 Meissner, B. *et al.* An integrated strategy to study muscle development and myofilament structure in Caenorhabditis elegans. *PLoS Genet* **5**, e1000537, doi:10.1371/journal.pgen.1000537 (2009).
154 Barral, J. M., Hutagalung, A. H., Brinker, A., Hartl, F. U. & Epstein, H. F. Role of the myosin assembly protein UNC-45 as a molecular chaperone for myosin. *Science* **295**, 669-671, doi:10.1126/science.1066648 (2002).
155 Liu, L., Srikakulam, R. & Winkelmann, D. A. Unc45 activates Hsp90-dependent folding of the myosin motor domain. *J Biol Chem* **283**, 13185-13193, doi:10.1074/jbc.M800757200 (2008).
156 Krendel, M. & Mooseker, M. S. Myosins: tails (and heads) of functional diversity. *Physiology (Bethesda)* **20**, 239-251, doi:10.1152/physiol.00014.2005 (2005).
157 Hellerschmied, D. & Clausen, T. Myosin chaperones. *Curr Opin Struct Biol* **25**, 9-15, doi:10.1016/j.sbi.2013.11.002 (2014).
158 Gazda, L. *et al.* The myosin chaperone UNC-45 is organized in tandem modules to support myofilament formation in C. elegans. *Cell* **152**, 183-195, doi:10.1016/j.cell.2012.12.025 (2013).
159 Kachur, T., Ao, W., Berger, J. & Pilgrim, D. Maternal UNC-45 is involved in cytokinesis and colocalizes with non-muscle myosin in the early Caenorhabditis elegans embryo. *J Cell Sci* **117**, 5313-5321, doi:10.1242/jcs.01389 (2004).
160 Riddle, D. L., Blumenthal, T., Meyer, B. J. & Priess, J. R. in *C. elegans II* (eds nd *et al.*) (1997).
161 Brenner, S. The genetics of Caenorhabditis elegans. *Genetics* **77**, 71-94, doi:10.1093/genetics/77.1.71 (1974).
162 Patterson, G. I. & Padgett, R. W. TGF beta-related pathways. Roles in Caenorhabditis elegans development. *Trends Genet* **16**, 27-33, doi:10.1016/s0168-9525(99)01916-2 (2000).
163 Smeal, T. & Guarente, L. Mechanisms of cellular senescence. *Curr Opin Genet Dev* **7**, 281-287, doi:10.1016/s0959-437x(97)80139-6 (1997).
164 Strange, K. From genes to integrative physiology: ion channel and transporter biology in Caenorhabditis elegans. *Physiol Rev* **83**, 377-415, doi:10.1152/physrev.00025.2002 (2003).
165 Sulston, J. E. & Horvitz, H. R. Post-embryonic cell lineages of the nematode, Caenorhabditis elegans. *Dev Biol* **56**, 110-156, doi:10.1016/0012-1606(77)90158-0 (1977).
166 Sulston, J. E., Schierenberg, E., White, J. G. & Thomson, J. N. The embryonic cell lineage of the nematode Caenorhabditis elegans. *Dev Biol* **100**, 64-119, doi:10.1016/0012-1606(83)90201-4 (1983).
167 Dieterich, C. *et al.* The Pristionchus pacificus genome provides a unique perspective on nematode lifestyle and parasitism. *Nat Genet* **40**, 1193-1198, doi:10.1038/ng.227 (2008).

168 Jorgensen, E. M. & Mango, S. E. The art and design of genetic screens: caenorhabditis elegans. *Nat Rev Genet* **3**, 356-369, doi:10.1038/nrg794 (2002).
169 Lewis, J. A. & Fleming, J. T. Basic culture methods. *Methods Cell Biol* **48**, 3-29 (1995).
170 Brose, N., Hofmann, K., Hata, Y. & Sudhof, T. C. Mammalian homologues of Caenorhabditis elegans unc-13 gene define novel family of C2-domain proteins. *J Biol Chem* **270**, 25273-25280, doi:10.1074/jbc.270.42.25273 (1995).
171 Irie, M. *et al.* Isolation and characterization of mammalian homologues of Caenorhabditis elegans lin-7: localization at cell-cell junctions. *Oncogene* **18**, 2811-2817, doi:10.1038/sj.onc.1202652 (1999).
172 Johansson, A., Driessens, M. & Aspenstrom, P. The mammalian homologue of the Caenorhabditis elegans polarity protein PAR-6 is a binding partner for the Rho GTPases Cdc42 and Rac1. *J Cell Sci* **113 (Pt 18)**, 3267-3275 (2000).
173 Harms, M. B. *et al.* Exome sequencing reveals DNAJB6 mutations in dominantly-inherited myopathy. *Ann Neurol* **71**, 407-416, doi:10.1002/ana.22683 (2012).
174 Ruggieri, A. *et al.* Complete loss of the DNAJB6 G/F domain and novel missense mutations cause distal-onset DNAJB6 myopathy. *Acta Neuropathol Commun* **3**, 44, doi:10.1186/s40478-015-0224-0 (2015).
175 Selcen, D. *et al.* Mutation in BAG3 causes severe dominant childhood muscular dystrophy. *Ann Neurol* **65**, 83-89, doi:10.1002/ana.21553 (2009).
176 Behin, A. *et al.* Myofibrillar myopathies: State of the art, present and future challenges. *Rev Neurol (Paris)* **171**, 715-729, doi:10.1016/j.neurol.2015.06.002 (2015).
177 Sarparanta, J. *et al.* Mutations affecting the cytoplasmic functions of the co-chaperone DNAJB6 cause limb-girdle muscular dystrophy. *Nat Genet* **44**, 450-455, S451-452, doi:10.1038/ng.1103 (2012).
178 Grammatikakis, N., Lin, J. H., Grammatikakis, A., Tsichlis, P. N. & Cochran, B. H. p50(cdc37) acting in concert with Hsp90 is required for Raf-1 function. *Mol Cell Biol* **19**, 1661-1672, doi:10.1128/MCB.19.3.1661 (1999).
179 Bhattacharya, K. *et al.* The Hsp70-Hsp90 co-chaperone Hop/Stip1 shifts the proteostatic balance from folding towards degradation. *Nat Commun* **11**, 5975, doi:10.1038/s41467-020-19783-w (2020).
180 Gaiser, A. M., Brandt, F. & Richter, K. The non-canonical Hop protein from Caenorhabditis elegans exerts essential functions and forms binary complexes with either Hsc70 or Hsp90. *J Mol Biol* **391**, 621-634, doi:10.1016/j.jmb.2009.06.051 (2009).
181 Kirschke, E., Goswami, D., Southworth, D., Griffin, P. R. & Agard, D. A. Glucocorticoid receptor function regulated by coordinated action of the Hsp90 and Hsp70 chaperone cycles. *Cell* **157**, 1685-1697, doi:10.1016/j.cell.2014.04.038 (2014).
182 Fernandez-Fernandez, M. R., Gragera, M., Ochoa-Ibarrola, L., Quintana-Gallardo, L. & Valpuesta, J. M. Hsp70 - a master regulator in protein degradation. *FEBS Lett* **591**, 2648-2660, doi:10.1002/1873-3468.12751 (2017).
183 Diehl, J. A., Yang, W., Rimerman, R. A., Xiao, H. & Emili, A. Hsc70 regulates accumulation of cyclin D1 and cyclin D1-dependent protein kinase. *Mol Cell Biol* **23**, 1764-1774, doi:10.1128/MCB.23.5.1764-1774.2003 (2003).
184 Sima, S., Schmauder, L. & Richter, K. Genome-wide analysis of yeast expression data based on a priori generated co-regulation cliques. *Microb Cell* **6**, 160-176, doi:10.15698/mic2019.03.671 (2019).

185 Sommer, R. J. & Sternberg, P. W. Changes of induction and competence during the evolution of vulva development in nematodes. *Science* **265**, 114-118, doi:10.1126/science.8016644 (1994).
186 Shemer, G. & Podbilewicz, B. LIN-39/Hox triggers cell division and represses EFF-1/fusogen-dependent vulval cell fusion. *Genes Dev* **16**, 3136-3141, doi:10.1101/gad.251202 (2002).
187 Horvitz, H. R. & Sternberg, P. W. Multiple intercellular signalling systems control the development of the Caenorhabditis elegans vulva. *Nature* **351**, 535-541, doi:10.1038/351535a0 (1991).
188 Engert, C. G., Droste, R., van Oudenaarden, A. & Horvitz, H. R. A Caenorhabditis elegans protein with a PRDM9-like SET domain localizes to chromatin-associated foci and promotes spermatocyte gene expression, sperm production and fertility. *PLoS Genet* **14**, e1007295, doi:10.1371/journal.pgen.1007295 (2018).
189 Tsukamoto, T. *et al.* LIN-41 and OMA Ribonucleoprotein Complexes Mediate a Translational Repression-to-Activation Switch Controlling Oocyte Meiotic Maturation and the Oocyte-to-Embryo Transition in Caenorhabditis elegans. *Genetics* **206**, 2007-2039, doi:10.1534/genetics.117.203174 (2017).
190 Ma, X. *et al.* Characterisation of Caenorhabditis elegans sperm transcriptome and proteome. *BMC Genomics* **15**, 168, doi:10.1186/1471-2164-15-168 (2014).
191 LaMunyon, C. W. *et al.* A New Player in the Spermiogenesis Pathway of Caenorhabditis elegans. *Genetics* **201**, 1103-1116, doi:10.1534/genetics.115.181172 (2015).
192 Campbell, A. C. & Updike, D. L. CSR-1 and P granules suppress sperm-specific transcription in the C. elegans germline. *Development* **142**, 1745-1755, doi:10.1242/dev.121434 (2015).
193 Singh, V. & Aballay, A. Heat-shock transcription factor (HSF)-1 pathway required for Caenorhabditis elegans immunity. *Proc Natl Acad Sci U S A* **103**, 13092-13097, doi:10.1073/pnas.0604050103 (2006).
194 Mueller, M. M. *et al.* DAF-16/FOXO and EGL-27/GATA promote developmental growth in response to persistent somatic DNA damage. *Nat Cell Biol* **16**, 1168-1179, doi:10.1038/ncb3071 (2014).
195 Zecic, A. & Braeckman, B. P. DAF-16/FoxO in Caenorhabditis elegans and Its Role in Metabolic Remodeling. *Cells* **9**, doi:10.3390/cells9010109 (2020).
196 Hietakangas, V. *et al.* Phosphorylation of serine 303 is a prerequisite for the stress-inducible SUMO modification of heat shock factor 1. *Mol Cell Biol* **23**, 2953-2968, doi:10.1128/MCB.23.8.2953-2968.2003 (2003).
197 Boyault, C., Sadoul, K., Pabion, M. & Khochbin, S. HDAC6, at the crossroads between cytoskeleton and cell signaling by acetylation and ubiquitination. *Oncogene* **26**, 5468-5476, doi:10.1038/sj.onc.1210614 (2007).

5. Appendix

5.1. Supplemental information for "Nematode CDC-37 and DNJ-13 form complexes and can interact with HSP-90"

Nematode CDC-37 and DNJ-13 form complexes and can interact with HSP-90

Lukas Schmauder[1], Eva Absmeier[1], Alexander Bepperling[1], Katalin Barkovits[2,3], Katrin Marcus[2,3] & Klaus Richter[1,*]

[1] Center for Integrated Protein Research at the Department of Chemistry, Technische Universität München, Lichtenbergstr. 4, 85748 Garching
[2] Medizinisches Proteom-Center, Ruhr-Universität Bochum, Gesundheitscampus 4, 44801, Bochum, Germany.
[3] Medical Proteome Analysis, Center for Protein Diagnostics (PRODI), Ruhr-University Bochum, Gesundheitscampus 4, 44801, Bochum, Germany.
[*] Corresponding author. E-Mail: klaus.richter@richterlab.de, Tel: +49-89-289-13342

Supplemental Figures.

Supplemental Figure 1a.

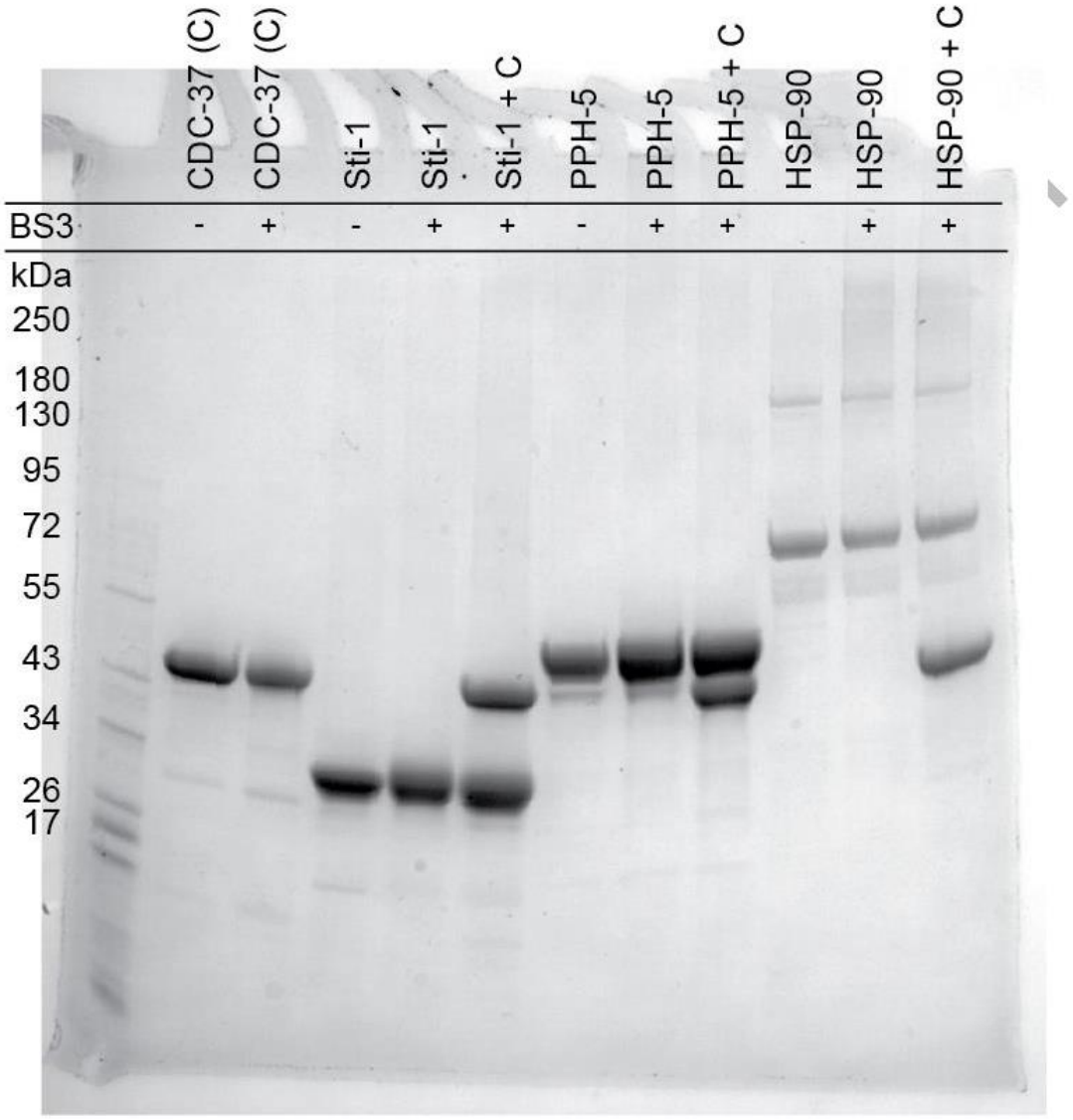

Supplemental Figure 1a.: Uncropped image of used for the creation of the left part Figure 1a. SDS-PAGE of CDC-37 (C) with and without the crosslinking reagent BS3, as indicated together with the cofactors Sti1, PPH-5, and HSP-90.

Supplemental Figure 1b.

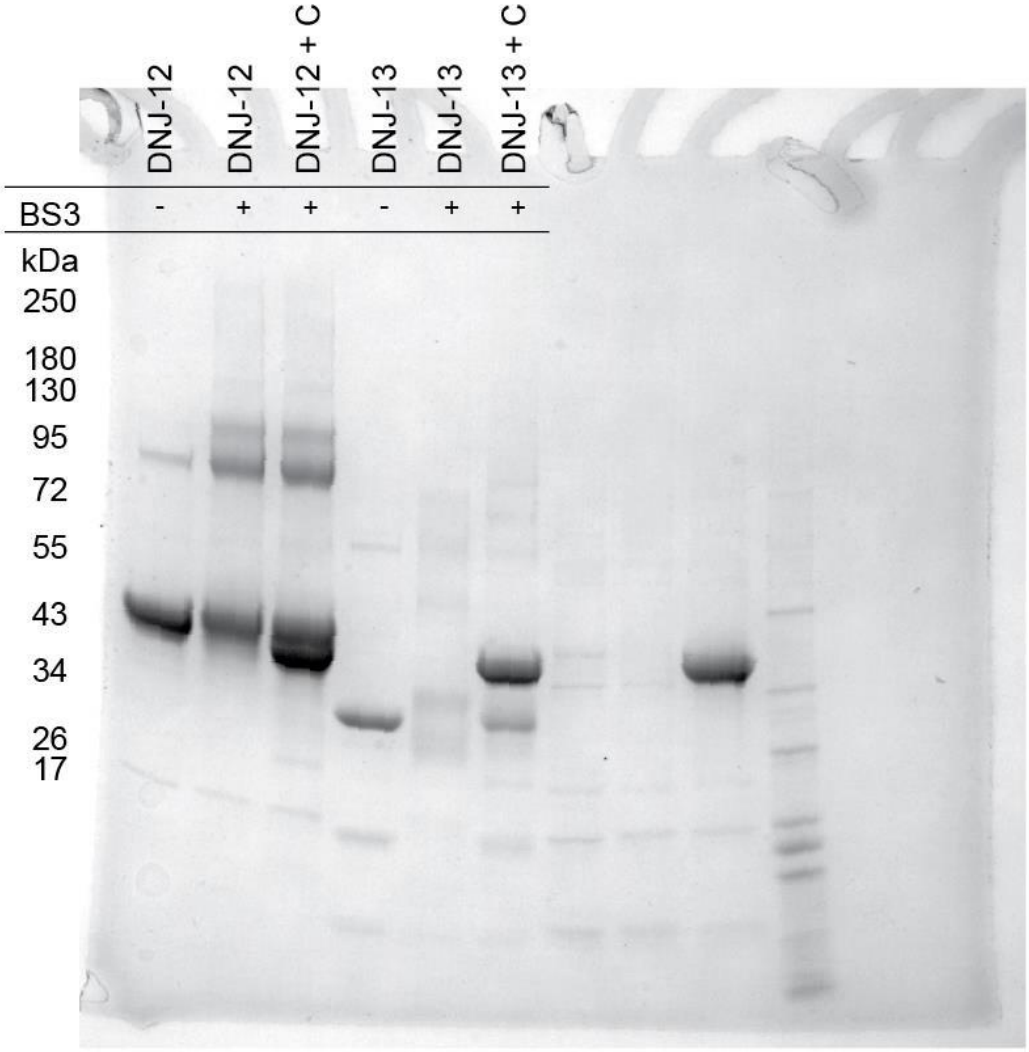

Supplemental Figure 1b.: Uncropped image of used for the creation of the right part of Figure 1a. SDS-PAGE of CDC-37 (C) crosslinked with and without the reagent BS3, as indicated together with the cofactors DNJ-12 and DNJ-13.

Supplemental Figure 2.

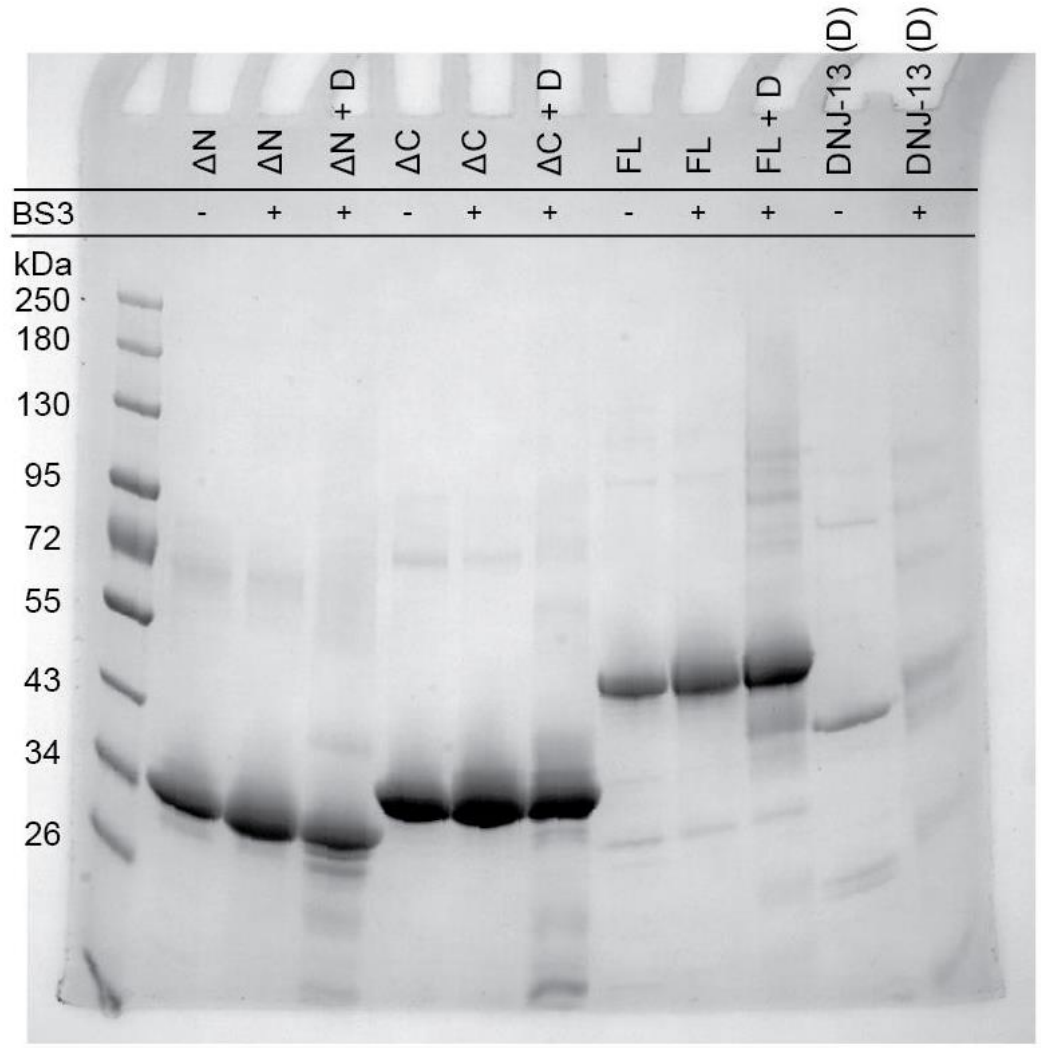

Supplemental Figure 2.: Uncropped image of used for the creation of Figure 3a. SDS-PAGE of crosslinked DNJ-13 (D) together with CDC-37ΔN (ΔN), CDC-37ΔC (ΔC) or full-length CDC-37 (FL).

Supplemental Figure 3.

Supplemental Figure 3.: Uncropped image of used for the creation of Figure 5a. Samples used for MS-analysis and crosslinked with DSSG are shown on the left side, whereas samples crosslinked with BS3 are shown on the right. 1 = CDC-37 monomer, 2 = DNJ-13 monomer, 3 = DNJ-13 dimer, 4 = CDC37•DNJ13 complex made of one CDC-37 and two DNJ-13 molecules, 5 = complex consisting of two CDC37•DNJ13 complexes.

Appendix

5.2. Supplemental information for "*hsp-90* and *unc-45* depletion induce characteristic transcriptional signatures in coexpression cliques of *C. elegans*"

The online version contains further supplementary material in the form of five supplementary figures and three supplementary tables, which due to their resolution and size could not be implemented into this thesis.

This supplementary material is made fully available at 10.1038/s41598-021-91690-6.

Appendix

5.3. Supplemental information for "Binding of the HSF-1 DNA-binding domain to multimeric *C. elegans* consensus HSEs is guided by cooperative interactions"

Binding of the HSF-1 DNA-binding domain to multimeric *C. elegans* consensus HSEs is guided by cooperative interactions.

Lukas Schmauder[1], Siyuan Sima[1], Amira Ben Hadj[1], Ricardo Cesar[1] and Klaus Richter[1,*]

[1] Center for Integrated Protein Research at the Department of Chemistry, Technische Universität München, Lichtenbergstr. 4, 85748 Garching
[*] Corresponding author. E-Mail: klaus.richter@richterlab.de, Tel: +49-89-289-13342

Supplemental Figure 1a.

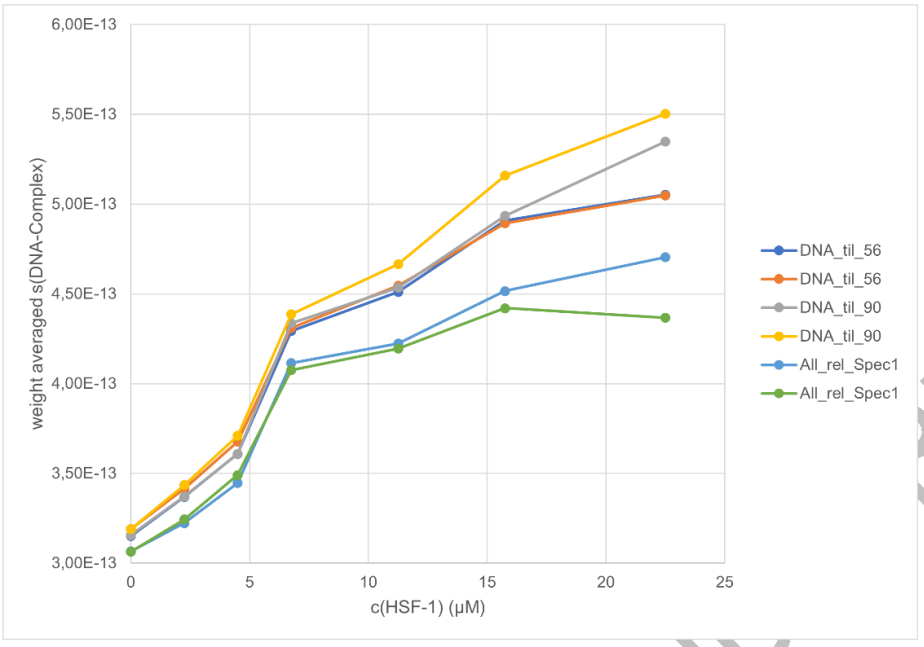

Average weight of HSP16.2a-HSF-1 complexes, derived from custom grid fitting

Supplemental Figure 1b.

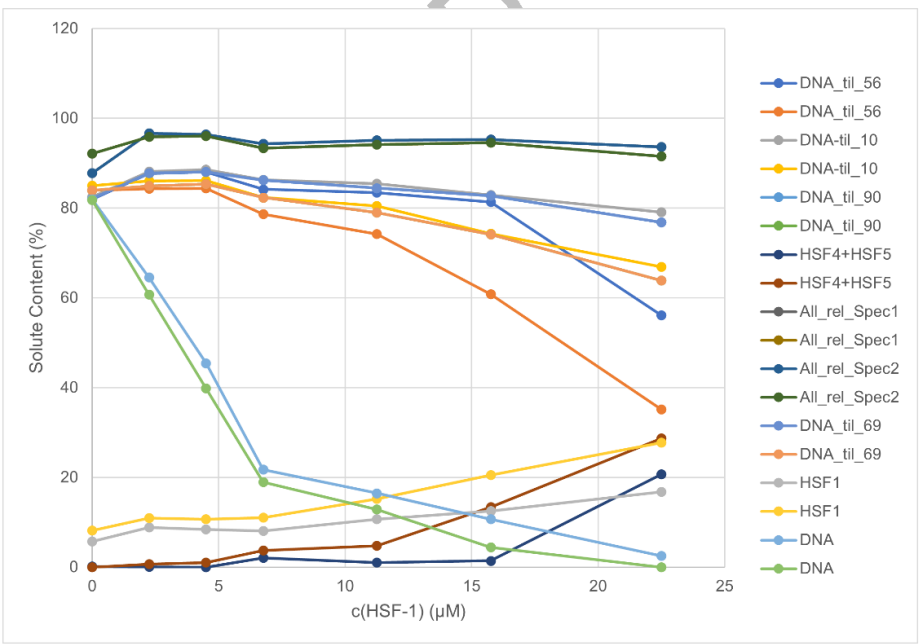

Partial concentrations of used Hsp16.2a DNA and HSF-1 species, derived from custom grid fitting.

Supplemental Figure 2a.

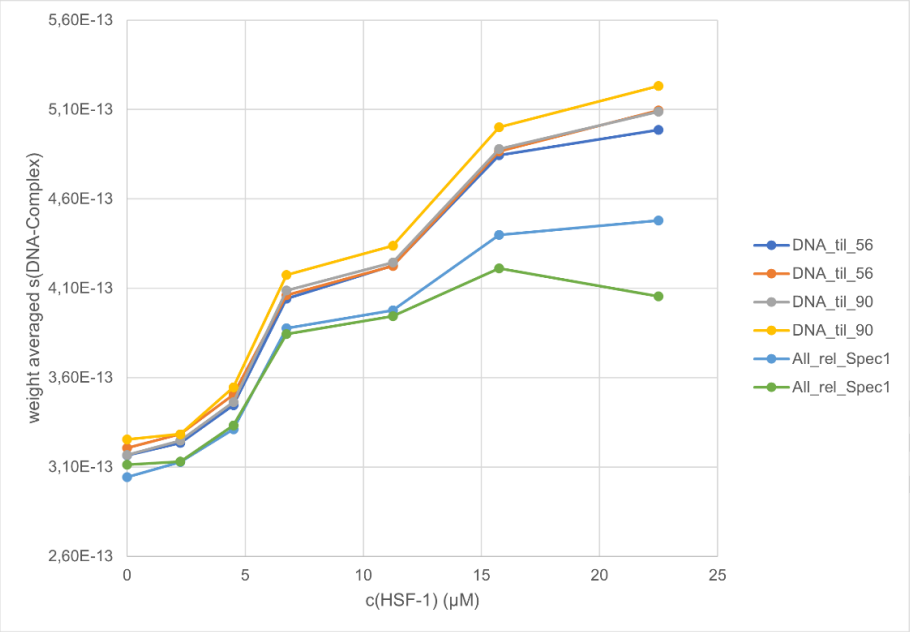

Average weight of HSP16.2b-HSF-1 complexes, derived from custom grid fitting

Supplemental Figure 2b.

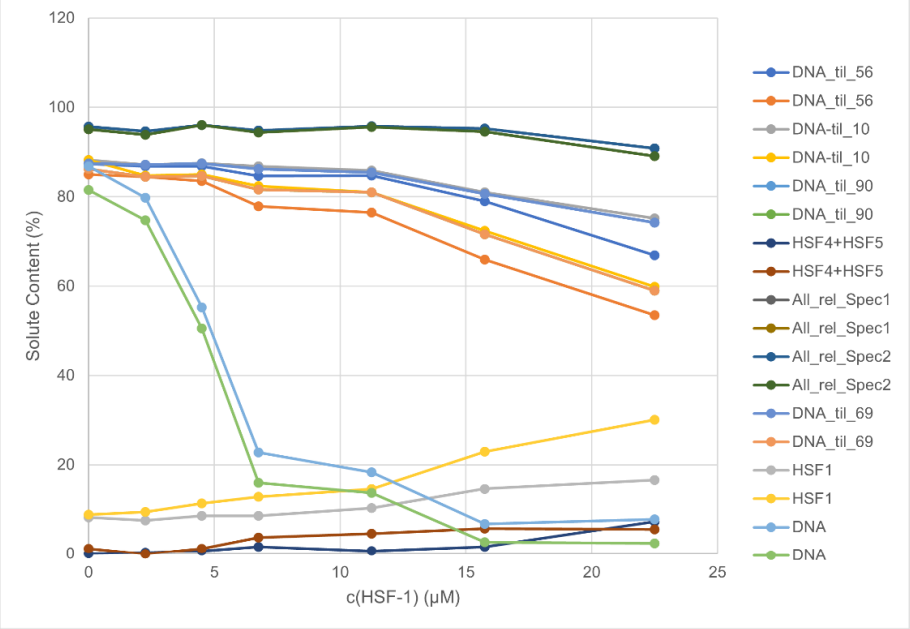

Partial concentrations of used Hsp16.2b DNA and HSF-1 species, derived from custom grid fitting.

Supplemental Figure 3a.

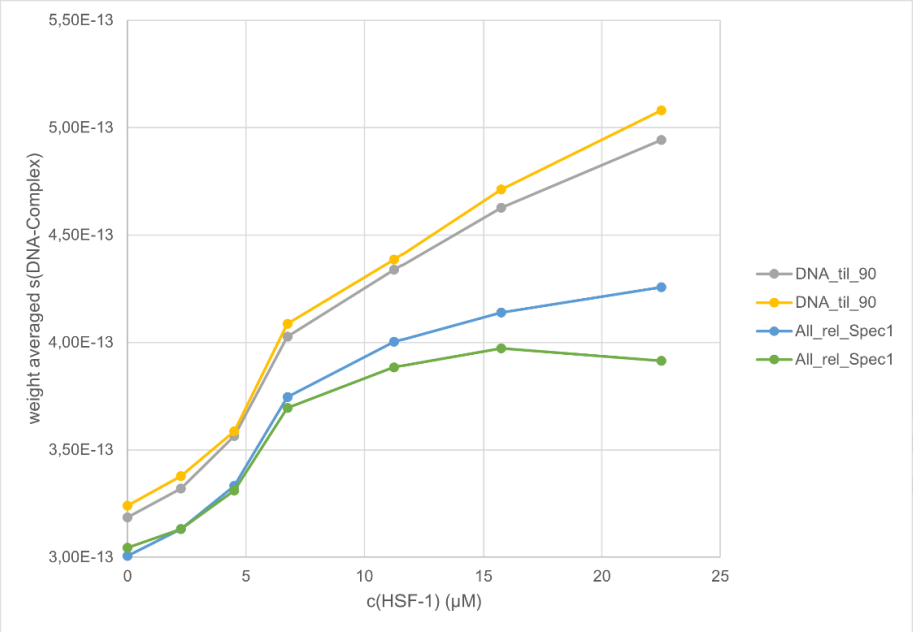

Average weight of HSP-70-HSF-1 complexes, derived from custom grid fitting

Supplemental Figure 3b.

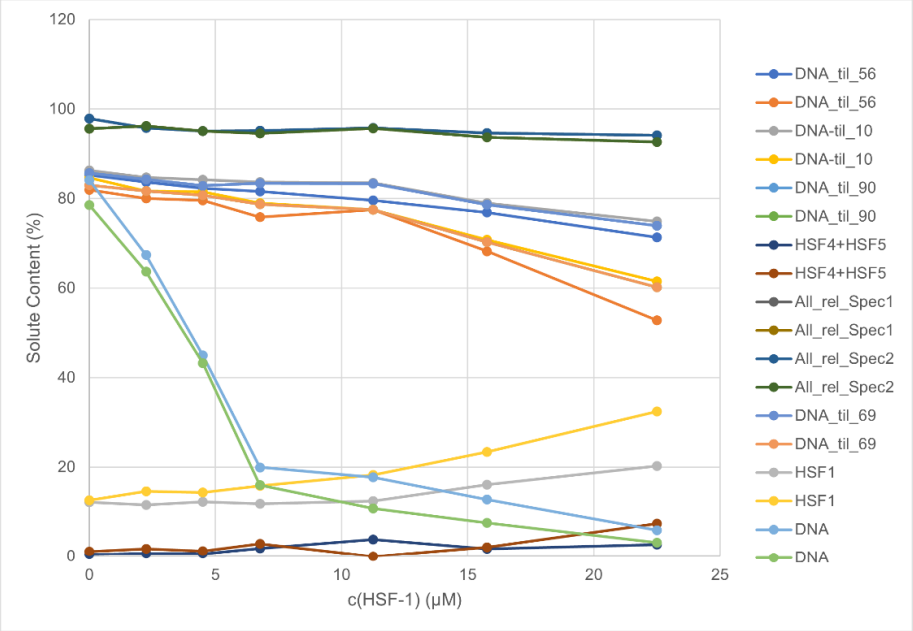

Partial concentrations of used HSP-70 DNA and HSF-1 species, derived from custom grid fitting.

Supplemental Figure 4a.

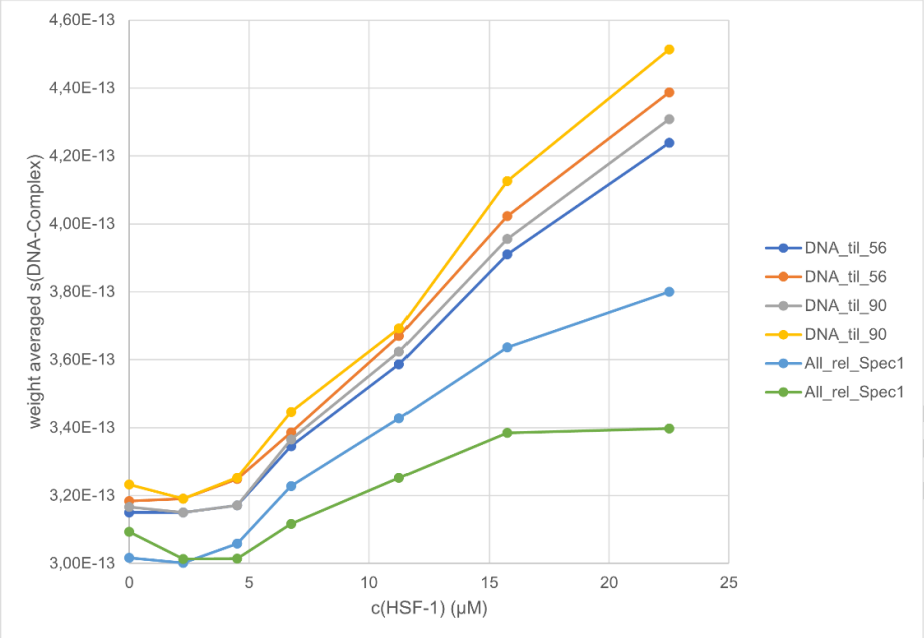

Average weight of HSP-1-HSF-1 complexes, derived from custom grid fitting

Supplemental Figure 4b.

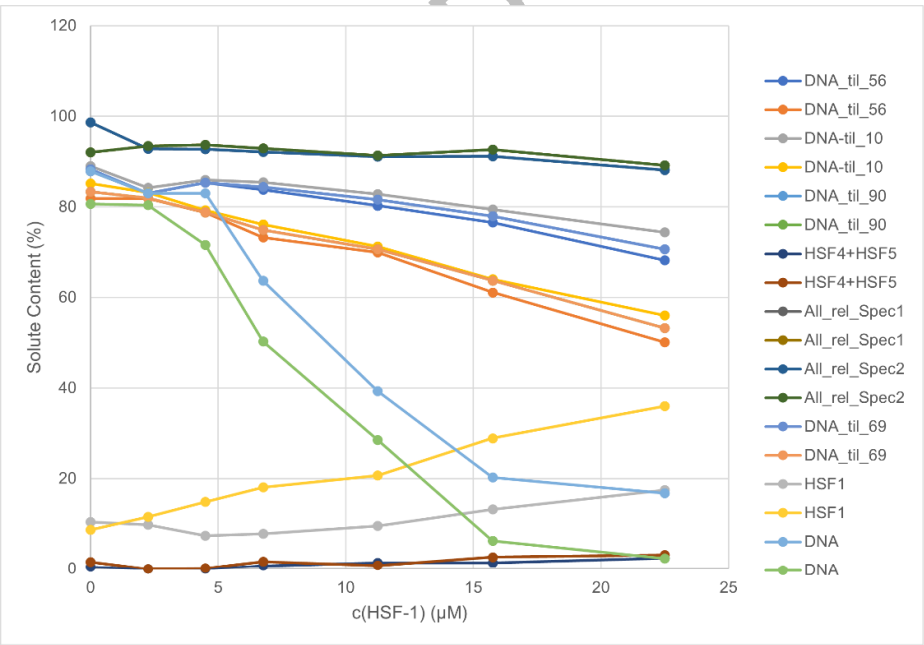

Partial concentrations of used HSP-1 DNA and HSF-1 species, derived from custom grid fitting.

Supplemental Figure 5a.

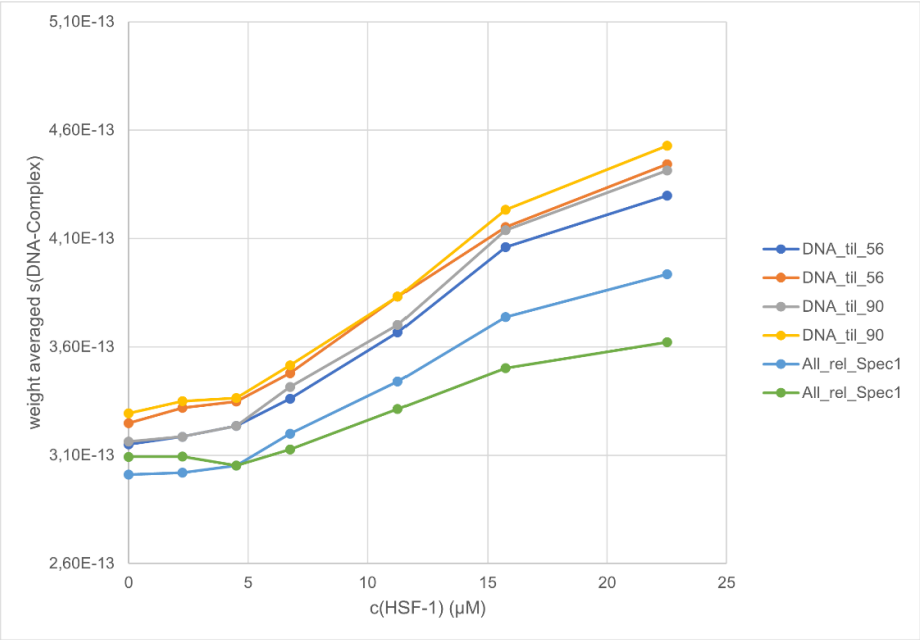

Average weight of DNJ-13-HSF-1 complexes, derived from custom grid fitting

Supplemental Figure 5b.

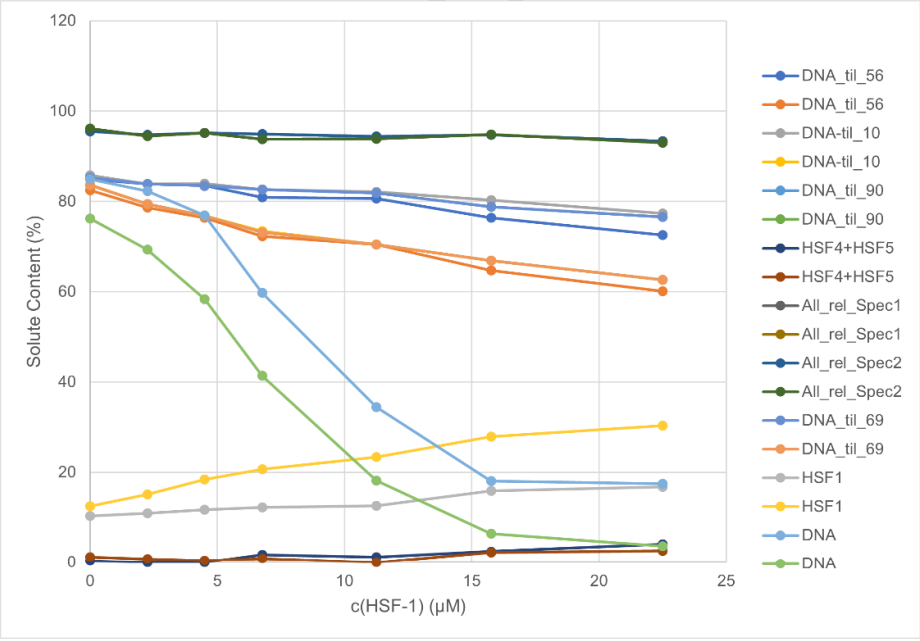

Partial concentrations of used DNJ-13 DNA and HSF-1 species, derived from custom grid fitting.

Supplemental Figure 6a.

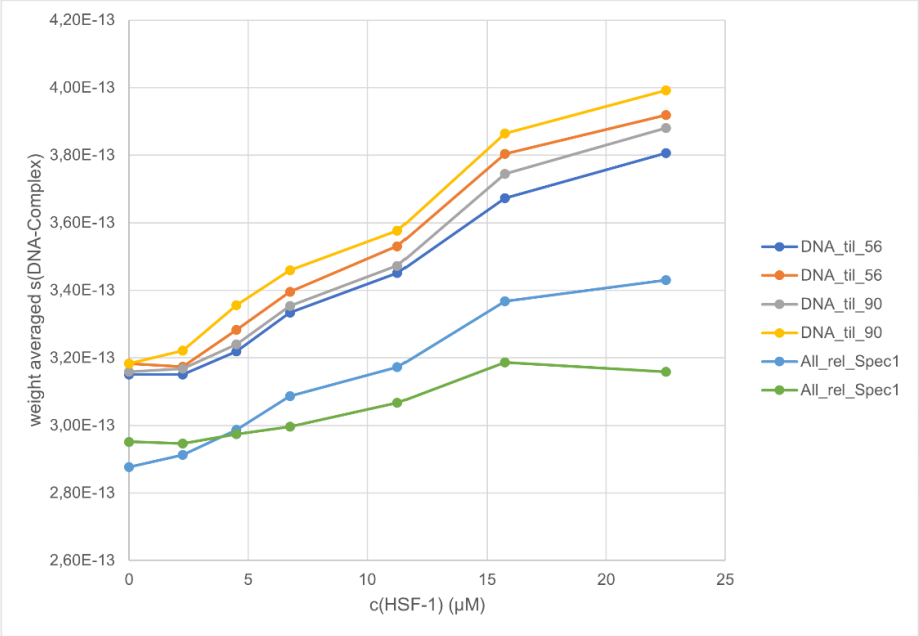

Average weight of UNC-23-HSF-1 complexes, derived from custom grid fitting

Supplemental Figure 6b.

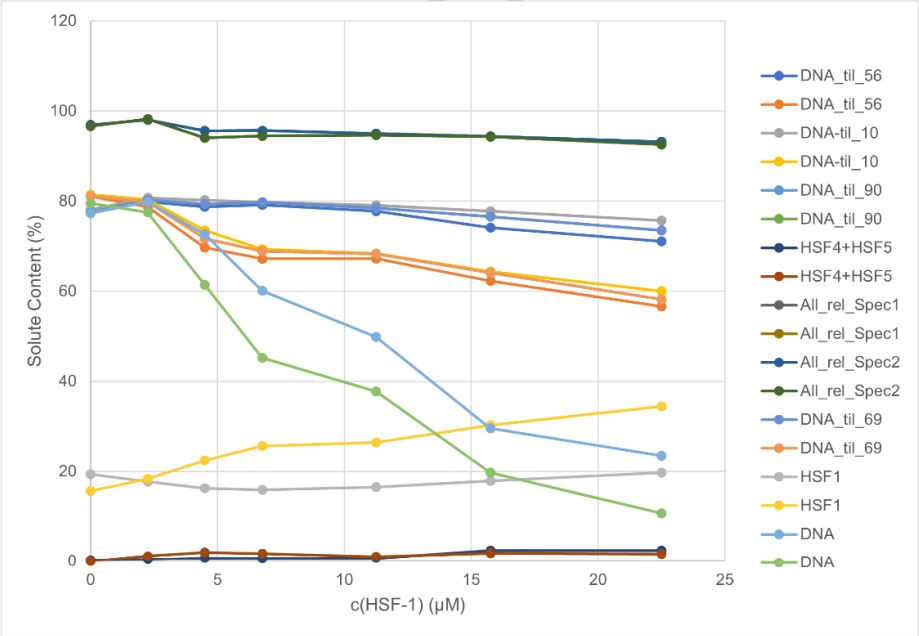

Partial concentrations of used UNC-23 DNA and HSF-1 species, derived from custom grid fitting.

Appendix

Abbreviations

Abbreviation	Description
%	Percent
°C	Degree Celsius
µM	Micromole [10^{-6} M]
ΔC	Truncated C-terminus
ΔG	Gibbs free energy [kg m² s^{-2}]
ΔN	Truncated N-terminus
AA	Amino acids
ADP	Adenosine diphosphate
ATP	Adenosine triphosphate
Bag/BAG	Bcl-2-associated athanogene
C	Carboxyl
C. elegans	*Caenorhabditis elegans*
Cdc	Mammalian cell division cycle protein
CDC	Nematode cell division cycle protein
cDNA	complementary DNA
Cdk4	Cyclin-dependent kinase 4
CTD	C-terminal domain
DAF-16	Nematode FOXO
DAF-21	Nematode Hsp90
DBD	DNA-binding domain
DD	Dimerization domain
DNA	Deoxyribonucleic acid
DnaK	Bacterial Hsp70
DNJ	DnaJ domain containing protein
dsDNA	Double strand DNA
E. coli	*Escherichia coli*
Fkbp51/52	FK506-binding protein

Appendix

FOXO	Forkhead box protein O
GEO	Gene expression omnibus
GO	Gene ontology
GR	Glucocorticoid receptor
His_6	Hexa histidine-tag
Hop	Hsp70-Hsp90 organizing protein
HPLC	High performance liquid chromatography
Hsc	Mammalian heat shock cognate
HSC	Nematode heat shock cognate
HSE	Heat shock element
HSF-1	Heat shock factor 1
Hsp	Mammalian heat shock protein
HSP	Nematode heat shock protein
HSR	Heat shock response
K_D	Dissociation equilibrium constant
M	Mole
MD	Middle domain
mRNA	Messenger RNA
N	Amine
NADH	Nicotinamide adenine dinucleotide
NBD	Nucleotide binding domain
NEF	Nucleotide exchange factor
NGM	Nematode growth media
NTD	N-terminal domain
PDB	Protein data bank
PEA	Phenotype enrichment analysis
PTM	Posttranslational modification
RD	Regulatory domain
RNA	Ribonucleic acid
RNAi	RNA interference

S	Sedimentation coefficient, Svedberg [10^{-13} s]
SBD	Substrate binding domain
SDS-PAGE	Sodium dodecyl sulfate polyacrylamide gel electrophoresis
Sti1	Stress-inducible protein 1
TAC	Transcriptome analysis console
TAD	Transactivation domain
TEA	Tissue enrichment analysis
TPR	Tetratricopeptide repeat
Unc	Mammalian uncoordinated mutant number
UNC	Nematode uncoordinated mutant number
UPR	Unfolded protein response
UV/Vis	Ultraviolet-visible spectroscopy

Appendix

Acknowledgements

Hereby I want to thank Prof. Dr. Johannes Buchner for the amazing possibility to create this PhD thesis, at the Lehrstuhl für Biotechnologie of the Technical University Munich and I furthermore want to declare my gratitude for his mentorship over the course of this work.
Most notably I want to thank my supervisor Dr. Klaus Richter, for the interesting topic, the excellent supervision, many precious tips, and tricks as well as guidance throughout the thesis.
Further I want to thank the DFG and CIPSM for financing the projects which eventually resulted in this thesis.
I also want to thank both Margot Rubinstein and Anna Semm for their support in all bureaucratic matters, and Martin Haslbeck who helped me a lot regarding all my questions when it came to the labs and equipment.
Furthermore, I want to thank Anja Osterauer, Bettina Richter, Florian Ruhrnößl, Laura Meier and Ruby Kahn for their technical support throughout the entirety of my PhD.
Very special thanks to my colleagues Anna Kaziales, Siyuan Sima, and Jasmin König for all the laughter, the nice and fruitful conversations and discussion, their help in the lab and in general the great time I had during my stay.
As well as all my students for their practical support in the lab, especially Lukas Sam und Nikolina Lipovcic who were helping me a lot during this work, but also Amira Ben Hadj and Tobias Steegmüller for all the nice discussions.
Further I want to thank all colleagues of the Lehrstuhl für Biotechnologie for the great time, knowledge sharing, interesting discussions, and festivities.
I´d also like to thank Katalin Barkovits and Katrin Marcus for the lovely collaboration, which yielded great results.
Eventually, I want to thank my family and all my friends for their support and great time throughout my whole PhD.

Appendix